



HAL
open science

Water and veterinary pharmaceutical transfer in an agricultural mesoscale catchment prone to flash floods

Nico Hachgenei

► **To cite this version:**

Nico Hachgenei. Water and veterinary pharmaceutical transfer in an agricultural mesoscale catchment prone to flash floods. Hydrology. Université Grenoble Alpes [2020-..], 2022. English. NNT: 2022GRALU007 . tel-04575517

HAL Id: tel-04575517

<https://theses.hal.science/tel-04575517>

Submitted on 15 May 2024

HAL is a multi-disciplinary open access archive for the deposit and dissemination of scientific research documents, whether they are published or not. The documents may come from teaching and research institutions in France or abroad, or from public or private research centers.

L'archive ouverte pluridisciplinaire **HAL**, est destinée au dépôt et à la diffusion de documents scientifiques de niveau recherche, publiés ou non, émanant des établissements d'enseignement et de recherche français ou étrangers, des laboratoires publics ou privés.



THÈSE

Pour obtenir le grade de

DOCTEUR DE L'UNIVERSITÉ GRENOBLE ALPES

Spécialité : Sciences de la Terre et de l'Univers et de l'Environnement

Arrêté ministériel : 25 mai 2016

Présentée par

Nico HACHGENEI

Thèse dirigée par **Céline DUWIG**, Chargée de recherche et co-encadrée par **Lorenzo SPADINI**, Maître de Conférence, UGA et **GUILLAUME NORD**, Enseignant-chercheur, UGA

préparée au sein du **Laboratoire Institut des Géosciences de l'Environnement**

dans **l'École Doctorale Sciences de la Terre de l'Environnement et des Planètes**

Transfert d'eau et de résidus pharmaceutiques vétérinaires dans un bassin versant agricole de méso-échelle soumis aux crues éclairs

Water and veterinary pharmaceutical transfer in an agricultural mesoscale catchment prone to flash floods

Thèse soutenue publiquement le **30 mars 2022**, devant le jury composé de :

Madame Céline DUWIG

CHARGÉE DE RECHERCHE HDR, IRD délégation Sud-Est, Directrice de thèse

Monsieur Markus HRACHOWITZ

PROFESSEUR ASSOCIÉ, Delft University of Technology, Rapporteur

Monsieur Christian STAMM

CHERCHEUR, Institut fédéral suisse des sciences et technologies aquatiques Eawag, Rapporteur

Madame Marina COQUERY

DIRECTRICE DE RECHERCHE, INRAE centre Lyon-Grenoble Auvergne Rhône-Alpes, Examinatrice

Monsieur Laurent CHARLET

PROFESSEUR DES UNIVERSITÉS, Université Grenoble Alpes, Président

Monsieur Jérôme MOLENAT

DIRECTEUR DE RECHERCHE, INRAE centre Occitanie-Montpellier, Examineur

Abstract

Our modern society has reached a high life expectancy and good health conditions. This is to a great extent due to our highly developed medical system including a large variety of drugs that can cure and prevent many deadly diseases. The backside of this diversity of highly effective chemical compounds are their diverse adverse effects. Many of them enter the environment through a variety of pathways. Here they can either create resistances or harm or kill non-target organisms.

This work focuses on residues of veterinary drugs entering the environment via dung from treated animals. Their environmental transfer is studied under the conditions of a meso-scale catchment under Mediterranean climate with extensive agriculture. The Mediterranean climate is characterized by a high temporal dynamic with elongated dry periods and intense storm events leading to particular conditions like intermittence of flow and flash floods. These conditions affect the fate of contaminants in the terrestrial and aquatic environment.

In a first step, interviews with livestock breeders were conducted to identify the treatment practices. 14 pharmaceutically active compounds (PhAC) were identified to be systematically used in the catchment, 10 of which antiparasitic drugs. Antibiotics were of significant use only for goats. We chose Ivermectin (IVM) as a representative molecule for those antiparasitic drugs and did further transfer experiments on this compound.

For these experiments, we developed a device to sample intact soil monoliths and subject them to simulated rainfall. Dung from untreated cows was spiked to a realistic concentration (3 mg kg^{-1}) as reported in literature in the dung of treated cows and placed on the soil in the shape of a cow pat. Consecutive intense rain events were simulated and surface runoff and drainage flow were measured and sampled at high frequency. Concentration values of up to 3855 ng L^{-1} were observed in overland flow (OF). The concentration in drainage flow was significantly reduced in soils from the sedimentary foothills part of the study site ($< 150 \text{ ng L}^{-1}$). On soils from the Coiron basaltic plateau, water repellency led to strong preferential flow and the concentration of IVM was not substantially reduced by leaching through the soil. On the other hand, higher initial soil moisture led to increased retention of IVM through both drainage and OF. Overall, up to 1% of the initial mass of IVM was exported during two consecutive rain events. In addition, we could show that drying of cow dung effectively reduces the mobilization of IVM. In general, more OF and a higher export of IVM were observed on soils from the Coiron plateau. On this scale, soil water repellency (SWR) seems to play a substantial role in the generation of OF and is generally higher in brunisol soils from the Coiron plateau.

Finally, in order to link those results to the catchment scale and the overall problematic of transfer of pharmaceutical residues to surface water bodies, a semi-distributed conceptual hydrological model was developed on the scale of the Claduègne catchment using SAS functions and age tracking in order to estimate transit time distributions (TTD) on an hourly time step. The model was forced with potential evapotranspiration, precipitation and precipitation deuterium signature and calibrated against observed discharge, silica concentration and deuterium isotope ratio of the water molecule at the outlet. The model predicts fractions of up to 60% of discharge at the outlet of an age below one

day during major flood events. Over the whole observation period, this fraction represents 8.4 % of the total runoff. 77 % of the time this fraction is zero. In average, 25 % of the discharge are less than 30 d old. This fraction is higher in winter and zero in the end of summer. This model however does not represent smaller flood events on dry soil sufficiently well to draw conclusions on the event water proportions under these conditions.

The analysis of a few stream water samples from the Claduègne catchment for three veterinary pharmaceuticals revealed that Fenbendazole (FBZ) and Mebendazole (MBZ) were only present at detectable concentrations throughout flood events, indicating a strong importance of preferential flow for their transfer into the streams. Concentrations of the pork antiparasitic FBZ of up to 28.4 ng L^{-1} were observed during a small flood event in summer, which is 355 time the predicted no effect concentration (PNEC) for fish.

This thesis shows that high amounts of IVM can be mobilized from cow dung and transferred through and over soil at the plot-scale, despite the fact that IVM is generally considered immobile due to its hydrophobicity and therefore strong adsorption to the soil's organic matter. The highest mobilization of IVM was observed under the condition of intense precipitation on dry soil due to water repellency causing strong preferential flow (including OF). Preliminary results on the catchment scale suggest that this mechanism may as well be effective on this scale, despite the smaller amplitude of the hydrological response. An age tracking model reveals a high fraction of event water in the discharge at the Claduègne outlet during major flood events.

Keywords: Veterinary pharmaceutical, Antiparasitic, Transfer, Preferential flow, Contaminant of emerging concern, SAS function, Water age tracking

Résumé

Notre société moderne a atteint une espérance de vie élevée et de bonnes conditions de santé. Cela est dû en grande partie à notre système médical hautement développé, qui comprend une grande variété de médicaments capables de guérir et de prévenir de nombreuses maladies mortelles. Le revers de la médaille de cette diversité de composés chimiques hautement efficaces est la diversité de leurs effets indésirables. Nombre d'entre eux pénètrent dans l'environnement par diverses voies. Là, ils peuvent soit créer des résistances, soit nuire ou tuer des organismes non ciblés.

Ce travail se concentre sur les résidus de médicaments vétérinaires qui pénètrent dans l'environnement via les excréments des animaux traités. Leur transfert environnemental est étudié dans les conditions d'un bassin versant à méso-échelle sous climat méditerranéen avec une agriculture extensive. Le climat méditerranéen est caractérisé par une dynamique temporelle élevée avec des périodes sèches prolongées et des événements orageux intenses conduisant à des conditions particulières comme l'intermittence du débit et les crues éclaircies. Ces conditions affectent le devenir des contaminants dans l'environnement terrestre et aquatique.

Dans un premier temps, des entretiens avec des éleveurs ont été menés pour identifier les pratiques de traitement. 14 composés pharmaceutiquement actifs (PhAC) ont été identifiés comme étant systématiquement utilisés dans le bassin versant, dont 10 antiparasitaires. Les antibiotiques n'étaient utilisés de manière significative que pour les chèvres. Nous avons choisi l'Ivermectine (IVM) comme molécule représentative de ces médicaments antiparasitaires et nous avons fait des expériences de transfert sur ce composé.

Pour ces expériences, nous avons mis au point un dispositif permettant de prélever des monolithes de sol intacts et de les soumettre à des pluies simulées. Des bouses de vaches non traitées ont été dopées à une concentration réaliste (3 mg kg^{-1}) telle que rapportée dans la littérature dans les bouses de vaches traitées et placées sur le sol sous la forme d'une bouse de vache. Des événements pluvieux intenses consécutifs ont été simulés et le ruissellement de surface (OF) ainsi que le flux de drainage ont été mesurés et échantillonnés à haute fréquence. Des valeurs de concentration allant jusqu'à 3855 ng L^{-1} ont été observées dans l'OF. La concentration dans le flux de drainage était significativement réduite dans les sols provenant de la partie sédimentaire du site d'étude ($< 150 \text{ ng L}^{-1}$). Sur les sols du plateau basaltique du Coiron, l'hydrophobicité du sol a conduit à un fort écoulement préférentiel et la concentration d'IVM n'a pas été substantiellement réduite au passage à travers le sol. D'un autre côté, une humidité initiale du sol plus élevée a conduit à une rétention accrue de l'IVM à la fois par le drainage et par l'OF. Dans l'ensemble, jusqu'à 1 % de la masse initiale d'IVM a été exportée au cours de deux événements pluvieux consécutifs. En outre, nous avons pu montrer que le séchage de la bouse de vache réduit efficacement la mobilisation de l'IVM. En général, plus d'OF et une plus grande exportation d'IVM ont été observées sur les sols du plateau du Coiron. A cette échelle, l'hydrophobicité du sol semble jouer un rôle important dans la génération de l'OF et est généralement plus élevée dans les brunisols du plateau du Coiron.

Enfin, afin de relier ces résultats à l'échelle du bassin versant et à la problématique globale de transfert des résidus pharmaceutiques vers les masses d'eau de surface, un modèle hydrologique

conceptuel semi-distribué a été développé à l'échelle du bassin versant de la Claduègne à l'aide de fonctions SAS et de suivi d'âge afin d'estimer les distributions de temps de transit (TTD) sur un pas de temps horaire. Le modèle a été forcé avec l'évapotranspiration potentielle, les précipitations et la signature en deutérium des précipitations et calibré par rapport au débit observé, à la concentration en silice et au rapport isotopique en deutérium de la molécule d'eau à l'exutoire. Le modèle prédit des fractions allant jusqu'à 60 % du débit à l'exutoire d'un âge inférieur à un jour pendant les événements de crue majeurs. Sur l'ensemble de la période d'observation, cette fraction représente 8.4 % de l'écoulement total. Pendant 77 % du temps, cette fraction est nulle. En moyenne, 25 % du volume d'eau sortant du bassin versant a un âge inférieur à 30 jours. Cette fraction est plus élevée en hiver et nulle à la fin de l'été. Ce modèle ne représente cependant pas suffisamment bien les petits événements de crue sur sol sec pour tirer des conclusions sur les proportions d'eau des événements dans ces conditions.

L'analyse de quelques échantillons d'eau de ruisseau de la Claduègne pour trois produits pharmaceutiques vétérinaires a révélé que le Fenbendazole (FBZ) et le Mebendazole (MBZ) étaient présents à des concentrations détectables uniquement en période de crue, ce qui indique une forte importance de l'écoulement préférentiel pour leur transfert dans les ruisseaux. Des concentrations de l'antiparasite porcin FBZ allant jusqu'à 28.5 ng L^{-1} ont été observées lors d'un petit événement de crue en été, ce qui correspond à 355 fois la concentration prédite sans effet (PNEC) pour les poissons.

Cette thèse montre que de grandes quantités d'IVM peuvent être mobilisées à partir de bouses de vache et transférées à travers et sur le sol à l'échelle décimétrique, malgré le fait que l'IVM est généralement considéré comme immobile en raison de son hydrophobie et donc de sa forte adsorption à la matière organique du sol. La mobilisation la plus élevée de l'IVM a été observée dans des conditions de précipitations intenses sur un sol sec en raison de la répulsion de l'eau qui provoque un fort écoulement préférentiel (y compris l'OF). Des résultats préliminaires à l'échelle du bassin versant suggèrent que ce mécanisme peut aussi bien être efficace à cette échelle, malgré la plus faible amplitude de la réponse hydrologique. Un modèle de suivi de l'âge révèle une fraction élevée d'eau événementielle lors des grandes crues du bassin versant de la Claduègne.

Mots-clés : Pharmaceutique vétérinaire, Antiparasite, Transfert, Flux préférentiel, Contaminant émergent, SAS function, Traçage de l'âge de l'eau

Acknowledgements

Foremost I would like to thank my three supervisors Céline Duwig, Guillaume Nord and Lorenzo Spadini for the opportunity to work on this very interesting subject of high importance. I would like to thank you for your support and for mobilizing the means necessary to realize the variable ideas developed throughout this PhD. I thank all of you also for your different ideas on how to reorient the subject and for your moral support. Thank you Céline for making so many things possible both by providing the financial means and supporting me hands-on during field and lab work. Thank you Guillaume for sharing your profound knowledge of the Claduègne catchment and all the different factors influencing the flow of water and matter through it both in theory and on the field. Thank you Lorenzo for sharing your broad knowledge on all the different aspects of geochemistry and so many ideas on the processes that could influence the observed concentrations of different ions and elements in the water.

I want to thank the members of the comité de thèse, Isabelle Braud, Emilie Jardé and Christelle Margoum who gave me valuable advice and motivation over the last three years.

I would like to thank the jury members Markus Hrachowitz, Christian Stamm, Marina Coquery, Laurent Charlet and Jérôme Molénat for investing the time to evaluate this work.

I would like to thank the OHM-CV for making this study possible by providing the valuable observation infrastructure including a large variety of instrumentation and a data history that built a solid base to construct hypotheses on the catchment functioning. I would like to thank especially Brice Boudevillain and Guillaume Nord who both put a large effort in sustaining this infrastructure without which studies like this would not be possible.

The technical service is thanked for support during field work and for the maintenance of the hydro-metric stations. Special thanks to Bernard Mercier for the development of a program for serial communication with the balances used during the rainfall simulation experiments, to Stéphane Boubkraoui for his help during field work and the setup of the precipitation samplers and to Hervé Denis for the laser granulometry analyses.

Thanks to Henri Mora for the broad support during the development of the soil sampling boxes and all technical aspects of the rainfall simulation experiments. Thanks to François Courvoisier who did a great contribution to the experiments during his Master thesis. Thanks to Jean-Marie Misciosa for the physical construction of the sampling frames.

I thank Nicolas Robinet for the help with the interviews and welcoming me at the CERMOSEM on many of my field trips.

I would like to thank Céline Voiron for her analytical support as well as the great effort put into the methodological development and the analysis of Ivermectin at the IGE. I would also like to thank Marie-Christine Morel for the development of this method and the quantification of the results, which represents a tremendous effort.

I thank Christine Baduel for her advise on solid phase extraction and field sampling for organic contaminants at trace levels as well as for quantifying the samples from the Claduègne catchment. I also thank Laure Jullien for the support in the solid phase extraction.

Jean-Francois Sutra and Anne Lespine are thanked for their advise and for analyzing the first series of samples from the mesocosms.

Laurent Oxarango is thanked for the advise and help regarding the X-ray tomography of soil samples. I would also like to thank the many other members of the HyDRIMZ team and the IGE lab who helped me through fruitful discussions, sharing their knowledge and experience and creative ideas.

Jean-Pierre Vandervaere is thanked for his valuable advise on the rainfall simulation experiments as well as field infiltration experiments.

The air-o-sol analytical platform is thanked for the analytical support.

Patrick Ginot is thanked for analyzing the water stable isotope samples.

The administrative service of IGE lab is thanked for making possible the countless fields trips, orders and other paper work while always being warm and friendly when I asked for help in the last minute. I would like to thank especially Odette Nave, Manon Garreau, Eric Chollet, Carmeline Meli and Valérie Lanari.

I would also like to thank Wajdi Nechba and Mondher Chekki from the IGE's informatics service for help with all sorts of computer problems and advice on accessing the universities computer cluster GRICAD.

Furthermore, I would like to thank the people working hard to improve the extremely helpful open-source tools *Python*, *LaTeX*, *QGIS*, *Fiji*, *Inkscape* and *R*.

I thank the different colleagues who I shared the office with for the nice atmosphere, especially An who was always there, but also Romane, Suffyian, Magdalena, Ranim, Joni and the others who spent some time with us in office 139. Thanks also to the other PhD students at IGE lab for the fun PhD weekends, BBQs and ultimate frisbee sessions, especially Antoine, Anil and Hannah. It was great to meet you guys.

I would like to thank my friends in Grenoble for making life in the Alps so much fun and adventure, especially Hermann, Seb, Julius, Paul, Andi, Mario and Alex. Thank you also to my new flying buddies Clément, Antoine, Pauline, Eloïse and the Duck for many nice moments to balance this theoretical work. Thank you to my old friends back in Germany and elsewhere, Fussel, Maria, Suse, Denis, Vera, Dave and Eva for keeping in touch.

Thank you Marie for your love, support and understanding, especially during these last months.

Finally, I would like to express my gratitude to my parents and my sister for all the support and love I get from them.

Contents

Abstract	i
Résumé	iii
Acknowledgements	iii
List of Figures	ix
List of Tables	xiii
Acronyms	xv
Symbols	xvii
1 Introduction	1
1.1 General introduction / context	1
1.2 Objectives	5
1.3 Approach, encountered problems and redefined goals	5
1.4 Manuscript organization	7
2 Study site: the Claduègne catchment	9
2.1 Context of the OHM-CV and previous studies	9
2.2 Land use	13
2.3 Hydro-meteorological monitoring	13
2.4 Meteorology	16
2.5 Hydrology	17
2.6 Geology	20
2.6.1 Coiron basaltic plateau	20
2.7 Topography	23
2.8 Pedology	24
3 Use of pharmaceuticals in extensive agriculture in the Ardèche region	27
3.1 Scientific context: Pharmaceuticals in the Environment	28
3.1.1 Sources of pharmaceutical products in the environment	29

3.1.2	Types of pharmaceuticals	29
3.1.2.1	Focus on antibiotics	30
3.1.3	Environmental effects of pharmaceuticals	30
3.1.4	Use of pharmaceuticals in livestock	31
3.1.5	Occurrence of veterinary pharmaceuticals in rivers	32
3.1.6	Occurrence of pharmaceuticals in Mediterranean rivers	32
3.1.6.1	Studies in the Claduègne catchment: Pharma BV	33
3.1.7	Knowledge gap	35
3.1.8	Objectives of this chapter	36
3.2	Methods	36
3.2.1	Interview methodology	36
3.2.2	Water sampling & chemical analysis	39
3.3	Results	42
3.3.1	Use of veterinary pharmaceutical products in the Claduègne catchment	42
3.3.2	Stream concentrations of selected pharmaceuticals	46
3.4	Discussion	52
3.4.1	Use of veterinary pharmaceuticals in the Claduègne catchment	52
3.4.2	Applicability of the results	53
3.4.3	Pharmaceuticals in the streams of the Claduègne Catchment	53
3.4.4	Lessons from the contact with farmers	55
4	Soil transfer study	57
4.1	Introduction	58
4.1.1	Flow of water through soil: basic concepts	59
4.1.2	Ivermectin	61
4.1.2.1	History & use	61
4.1.2.2	Mode of action	62
4.1.2.3	Environmental fate and effects	62
4.1.3	Knowledge gaps	67
4.2	Methods	67
4.2.1	Device to simulate contaminant transfer through intact soil (VZJ, 2022)	67
4.2.2	Additional methodological specifications	78
4.2.3	Soil sampling locations and experiments	78
4.2.4	Soil characterization	80
4.2.4.1	Grain size distribution	82
4.2.4.2	Soil organic carbon	82
4.2.4.3	Soil water repellency	83
4.2.4.4	Hydraulic conductivity	85
4.2.4.5	Structure: tomography	87
4.3	Results	92
4.3.1	Hydrological functioning	92
4.3.2	Ivermectin transfer	98

4.4	Discussion	105
4.4.1	Hydrological functioning	105
4.4.1.1	Solute transfer	111
4.4.2	Ivermectin transfer	113
4.4.2.1	Quantification problems and potential reasons	113
4.4.2.2	Factors controlling the transfer of Ivermectin	113
4.5	Conclusion	116
4.6	Link to the catchment scale	117
5	Solute transfer and water age tracking in the Claduègne catchment	119
5.1	Introduction	120
5.1.1	Transit time tracing in hydrology	120
5.1.2	Goals of transit time tracing within the PhD	122
5.2	Methods	124
5.2.1	Dataset description	124
5.2.1.1	Tracer choice and sampling strategy	124
5.2.1.2	Water analysis	127
5.2.1.3	Synthesis of results / data	129
5.2.2	The model	137
5.2.2.1	Forcing and calibration data	139
5.2.2.2	Model structure	139
5.2.2.3	Age of water	141
5.2.2.4	Tracers	149
5.2.2.5	Model calibration	151
5.2.2.6	Initial conditions	153
5.3	Results	153
5.3.1	Model fit	153
5.3.1.1	Goodness of fit interdependence	158
5.3.2	Transit times	158
5.4	Discussion	164
5.4.1	Calibrated parameters	164
5.4.1.1	Implications on catchment functioning	167
5.4.2	Discussion and implications of the modeled transit time distributions	168
5.4.3	Constraints, limitations and possible improvements	169
5.4.4	SAS functions and reactive transport	171
5.5	Conclusion	172
6	General conclusion & perspectives	175
6.1	Conclusion	175
6.2	Perspectives	177
	Glossary	181

References	183
A Interview guideline	A-1
B Additional pharmaceutical concentrations	B-1
C Supplemental material soil sampling device	C-1
D Additional element / ion concentrations	D-1
E Method article: Stable isotope memory effect correction (MEX, 2022)	E-1

List of Figures

2.1	OHM-CV sites	11
2.2	Study site location	12
2.3	Land use map	14
2.4	Measurement stations	15
2.5	Spatial distribution of extreme precipitation	17
2.6	Monthly precipitation & evapotranspiration	18
2.7	Monthly discharge distribution	19
2.8	Flood example	20
2.9	CLA dry vs. flood	21
2.10	Claduègne Geology	22
2.11	Source types Coiron plateau	23
2.12	Claduègne Topography	24
2.13	Claduègne Pedology	25
3.1	Contaminant dynamic Pharma BV	34
3.2	Interviewed parcels	37
3.3	POCIS locations	40
3.4	Livestock Claduègne catchment	45
3.5	Pharmaceutical detection frequencies	47
3.6	Mebendazole concentration Gazel	49
3.7	Fenbendazole concentration Gazel	50
3.8	Trimethoprim concentration Gazel	51
3.9	POCIS concentrations	52
4.1	Structure of avermectines	61
4.2	Mesocosm sampling locations	79
4.3	Event timeline	81
4.4	Cumulative grain size distribution & size classes	82
4.5	Soil OM with depth	83
4.6	Tension disc infiltration results Pradel	86
4.7	Tension disc infiltration results Coiron	87
4.8	Soil tomography	89
4.9	Soil tomography segmentation	90

4.10	Soil pore size distributions	91
4.11	Soil I & J flow	93
4.12	Soil I & J water content	94
4.13	Soil C, D & E flow	95
4.14	Soil C, D & E water content	96
4.15	Soil C water content (sensors)	98
4.16	Cumulative IVM outflux	99
4.17	IVM concentrations F, G, H	101
4.18	IVM concentrations C, D	102
4.19	IVM concentrations I, J	103
4.20	IVM concentrations E, B	104
4.21	Observed OF on the Coiron	105
4.22	Soil water repellency schema	106
4.23	Relations between event parameters	108
4.24	Cumulative solute outflux	112
5.1	Sampling sites	125
5.2	Concentration - discharge relationships	130
5.3	Claduègne concentration time-series	131
5.4	Silica concentration synthesis	132
5.5	Silica concentration time series	134
5.6	Stable isotope ratios - MWL	137
5.7	Precipitation stable isotope time series	138
5.8	Model reservoirs	140
5.9	Storage age illustration	142
5.10	SAS function illustration	144
5.11	SAS function young preference compensation	146
5.12	Time-variant SAS function illustration	147
5.13	Modeled Si time series	154
5.14	Modeled deuterium time series	155
5.15	Streamflow discharge residuals	156
5.16	Model vs. observations summarized	157
5.17	Overall vs. individual goodness of fit	158
5.18	Modeled nwf and ywf	159
5.19	Hydrograph separation	161
5.20	Transit time distribution time series	162
5.21	Residence and transit time distributions	163
5.22	NSE dependence on W_s	165
5.23	NSE dependence on k_{diss}	166
5.24	Relation between NSE values	167
A.1	Interview guideline	A-2

B.1	Sulfamethoxazole concentration Gazel	B-2
B.2	Caffeine concentration Gazel	B-3
B.3	Nicotinamide concentration Gazel	B-4
D.1	Concentration - discharge relationships	D-2
D.2	Claduègne concentration time-series 1	D-3
D.3	Claduègne concentration time-series 2	D-4
D.4	Claduègne concentration time-series 3	D-5
D.5	Claduègne concentration time-series 4	D-6

List of Tables

2.1	Claduegne soil properties	26
3.1	POCIS locations	39
3.2	Pharmaceutical limits of quantification	42
3.3	Systematically used molecules	43
3.4	PhAC's properties	44
3.5	Veterinary pharmaceutical use	46
4.1	IVM transfer experiments	79
4.2	Simulated rain events	81
5.1	Tracing water sampling sites	126
5.2	ICP calibration parametrization	128
5.3	List of calibrated model parameters	151
5.4	List of retained parameter values	164
5.5	Sensitivity of age results	171

Acronyms

ACN acetonitrile. 111

ANR Agence Nationale de la Recherche. 173

ATC Anatomical Therapeutic Chemical. 29

BCF bioconcentration factor. 61, *Glossary*: BCF

cdf cumulative distribution function. 141, 143

CEC contaminant of emerging concern. 28, 32

CNRS Centre National de la Recherche Scientifique. 9

COVID-19 coronavirus disease. 60

DEM digital elevation model. 10, 23, *Glossary*: DEM

DOC dissolved organic carbon. 76, 109

DOR Doramectin. 96, 111

FBZ Fenbendazole. ii, 45, 47, 51, 53, 54, 172

GABA γ -amino butyric acid. 60, 61, *Glossary*: GABA

HOF hortonian overland flow. 59, 103, 107

IC ion chromatography. 122, 125

ICP inductively coupled plasma - optical emission spectrometry. 122, 125

IM-CRDS induction module cavity ring-down spectroscope. 122

INSU institut national des sciences de l'Univers. 9

IVM Ivermectin. i, ii, 2, 3, 6, 7, 31, 36–38, 42, 43, 45, 52–54, 56, 57, 59–65, 76–78, 96–98, 102, 108, 111–115, 121, 171, 174

. 6, 41

LD limit of detection. 47, 53, 64, 81, 111

LiDAR light detection and ranging. 23, *Glossary*: LiDAR

LOEC lowest observed effect concentration. 42, 61, *Glossary*: LOEC

LQ limit of quantification. 6, 32, 51, 54

MBZ Mebendazole. ii, 45, 47, 54

MED molarity of ethanol droplet. 81, 82, 107

- MIC** minimal inhibitory concentration. 30
- mRTD** master residence time distribution. 147, 156, 161
- mTTD** master transit time distribution. 147, 156, 161
- NSE** Nash-Sutcliffe Efficiency. 149, 151, 155, 162–164
- nwf** new water fraction. 120, 146, 156, 165–168, 170, 174, *Glossary*: nwf
- OF** overland flow. i, ii, 56, 57, 59, 90, 95, 97, 98, 102–105, 107, 109, 112–115, 165, 166, 171
- OHM-CV** Cévennes-Vivarais Mediterranean Hydrometeorological Observatory. 4, 9, 10, 12, 172, 173
- OM** organic matter. 26, 58, 80–82, 84, 86, 105, 107, 109, 113, 114, 173
- OZCAR-RI** French Critical Zone Observatories Research Infrastructure. 10, 173
- pdf** probability density function. 119, 141, 143
- PEC** predicted environmental concentration. 52, *Glossary*: PEC
- PhAC** pharmaceutically active compound. i, 2, 5, 29, 31–33, 35–39, 43, 45, 47, 52, 53, 56, 114, 118, 119, 121, 166, 171
- PNEC** predicted no effect concentration. ii, 39, 42, 43, 52–54, 114, *Glossary*: PNEC
- po** pour-on. 37, 62, *Glossary*: po
- POCIS** polar organic compound integrative sampler. 5, 6, 36, 39, 41, 51, 53, 173
- PP** pharmaceutical product. 2–4, 6, 7, 12, 28–33, 35, 43, 63
- RTD** residence time distribution. 119, 147
- SAFRAN** Système d'Analyse des Renseignements Adaptés à la Nivologie. 16, 161, *Glossary*: SAFRAN
- SARS-CoV-2** Severe Acute Respiratory Syndrome Coronavirus 2. 60
- sc** subcutaneous. 37, 41, 62, *Glossary*: sc
- SMBO** Sequential Model-Based Optimization. 150
- SMX** Sulfamethoxazole. 45, 51
- SOF** saturation excess overland flow. 59, 103
- SPE** solid phase extraction. 41, 47, 76, 98, 111, 112, *Glossary*: SPE
- srb** sustained-release bolus. 62, *Glossary*: srb
- SWR** soil water repellency. i, 58, 59, 81, 82, 103, 104, 106–108, 113, 114, 171, 172, 174
- TMP** Trimethoprim. 45, 47, 51
- TOC** total organic carbon. 80, 81
- TPE** Tree-structured Parzen Estimator approach. 150
- TTD** transit time distribution. i, 4, 119, 120, 146, 147, 156
- WDPT** water drop penetration time. 82
- WWTP** waste water treatment plant. 28, 29, 32–35, 39, 45, 47, 52, 53
- ywf** young water fraction. 120, 146, 156, 165, 167, 168, 170, 174, *Glossary*: ywf

Symbols

- A non-linearity of discharge response to the volume of water inside a reservoir. 139, 161
- CA the contact angle between a solid and a liquid. 57, 58, 82, 84
- CR overland flow coefficient ($\frac{Q_R}{P}$). 90, 95, 106, 107, 112
- $CR_{10 \text{ min}}$ the overland flow coefficient of the first ten minutes of a simulated rain event. 106, 107
- d_{50} the median grain size d_{50} of a soil is the grain diameter at which 50 % of the soils grains are larger and 50 % are smaller. 80
- d_{rep} representative dose of a pharmaceutically active compound in one treatment of one animal in $\left[\frac{\text{mg}}{\text{treatment}}\right]$. 37, 38, 42
- $\Delta\Theta$ the difference between initial and final water content of the soil before and after a simulated rain event. 106
- E_i evaporation from interception reservoir. 138
- E_p potential evapotranspiration, volume or height of water per time. 16, 17, 136–138
- E_u evapotranspiration from unsaturated reservoir. 138, 145, 148
- f_{ev} event water fraction, the fraction of water that origins from the current precipitation event. 106, 107
- f_{treat} average amount of a pharmaceutically active compound administered to each animal of a species per year in $\left[\frac{\text{doses}}{\text{animal}\cdot\text{year}}\right]$. 38, 42
- γ the surface tension between a liquid and a gas. 82
- δ^2H normalized difference of sample deuterium isotope ratio compared to Vienna Standard Mean Ocean Water. 7, 115, 125, 137, 149, 151, 155, 162–164, 167, 172
- H hydraulic head. 58
- h pressure head. 57, 58, 83, 84
- H_w water level. 13
- k silica dissolution constant. 148, 155
- K_d the soil sorption coefficient K_d of a contaminant to a soil is the ratio of adsorbed to aqueous concentration of this contaminant to a particular soil. 62
- K_{fs} field saturated hydraulic conductivity. 83
- K_H hydraulic conductivity. 58, 83–85, 103

- K_{HS} saturated hydraulic conductivity. 58, 83–85, 103, 174
- K_{oc} the organic carbon - water distribution coefficient of a contaminant is its sorption coefficient to soil organic carbon, calculated from K_d and the soils organic carbon content. 62, 113
- K_{ow} the octanol-water partition coefficient (K_{ow}) is the equilibrium liquid concentration ratio between octanol and water and a measure for hydrophobicity (apolarity). 56, 62
- LC_{50} the lethal concentration LC_{50} is the concentration of a contaminant at which an individual of a test population has a 50% chance to die. If given, an exponent defines the period over which this occurs. 60, 61
- m_{used} used mass of a pharmaceutical in g yr^{-1} . 38, 39, 45
- n porosity [volume/volume]. 76, 106
- $n_{animals}$ estimated number of individuals per species held inside the catchment. 38
- $\omega_m(T)$ master SAS function over a period. 147
- $\omega_Q(T, t)$ the SAS function in its initial definition $\omega_Q(T, t)$ describes the unitless age preference in a flux at a time t as a function of age T . 120, 141
- $\omega_Q^*(P_S(T, t), t)$ the SAS function in the form used in this work $\omega_Q^*(P_S(T, t), t)$ describes the unitless age preference in a flux, at a time t expressed as a function of the reservoirs cumulative age distribution $P_S(T, t)$. 141, 145
- P precipitation, height of water per time. 17
- P_e effective precipitation is the part of precipitation that reaches the soil. 137, 138
- $P_Q(T, t)$ cumulative distribution function of $Q(T, t)$. 143
- $p_Q(T, t)$ probability density function of $Q(T, t)$, corresponding to the TTD. 119, 143, 146, 156
- $P_S(T, t)$ cumulative distribution function of $S(T, t)$. 141, 143
- $p_S(T, t)$ probability density function of $S(T, t)$, corresponding to the RTD. 119, 143, 147
- Q discharge, in units of volume or height of water per time. 13, 119, 136, 139, 143, 145–147, 149, 151, 154, 155, 162–164, 167, 172
- Q_D drainage flow. 90, 104, 105, 107, 108
- $Q_{D\text{ev}}$ event water contribution to drainage flow. 90
- $Q_{D\text{e-1}}$ contribution of water from previous event to current event drainage flow. 95
- $Q_{D\text{pre}}$ pre-event water contribution to drainage flow. 90
- $Q_D - Q_{D\text{e-1}}$ contribution to drainage flow of water not issued from the previous event. 95
- Q_s stream flow from the saturated zone. 138, 139, 145, 161
- $Q(T, t)$ absolute age distribution of a flux Q at time t , in water volume or height with one value for each age class. 119, 141–143, 146, 147
- Q_u preferential flow including macropore and overland flow. 138, 139, 145, 161, 166
- Q_{us} recharge from the unsaturated to the saturated zone. 138, 139, 141, 145
- R^2 the coefficient of determination R^2 from Krause et al. (2005). 151
- S S describes a reservoir or the amount of water in it (as a volume or height). 119, 120, 139, 143, 147

- SAS_α 'a' parameter of the betafunction used to define the SAS function. 141, 143, 145, 146, 163, 168
- $SAS_{stretch}$ a factor to define how strong the age preference of flows leaving S_u depends on the amount of water in S_u , in mm. The smaller $SAS_{stretch}$, the stronger the variation of age preference. 145, 163
- S_i interception reservoir. 137, 138, 151
- Si silicon. 7, 124, 148, 149, 162, 167
- $[Si]$ dissolved silica concentration in units of mgSi/L. 115, 131, 132, 136, 147, 148, 151, 154, 155, 162–164, 167, 168, 172
- m_{Si} mass of dissolved silica, treated inside the model in units of mass of silicon per surface area of the catchment part. 148
- S_s saturated zone reservoir. 146, 147, 151, 161
- $S(T, t)$ absolute age distribution of a reservoir S at time t , in water volume or height with one value for each age class. 119, 139–143, 147
- S_u unsaturated zone reservoir. 137–140, 145, 148, 151, 166, 175
- Θ volumetric soil water content (unitless or in percent). 58, 90, 95, 96, 106–108
- Θ_i initial volumetric soil water content (unitless or in percent). 90, 95, 96, 106–108
- T age of a water volume. 119, 139–141, 143
- t a moment in time. 119, 139, 140, 148, 149
- $t_{1/2}$ the half-life $t_{1/2}$ of a compound is the time needed to divide its mass by two. This can be due to degradation, export or a mix of processes. 62
- t_{Ds} the time from the start of a drainage flow. Drainage flow is considered to have started after 0.1 mm (18 mL) were collected. 106–108
- Θ_{max} maximum volumetric water content in the soil over the course of an event. 106, 107
- T_p hydrologically passive part of a reservoir [mm], defined for each flux independently. 139
- ts time step in h. 139, 141–143, 148
- V_{pol} maximum volume of water that could be polluted by the total amount of a pharmaceutically active compound that is used. 39, 43, 45, 52
- W_s the threshold on the amount of water in S_u [mm] below which evapotranspiration is limited by water availability. 138, 139, 149, 161–163

1

Introduction

1.1	General introduction / context	1
1.2	Objectives	5
1.3	Approach, encountered problems and redefined goals	5
1.4	Manuscript organization	7

1.1 General introduction / context

Our current sanitary conditions and life expectancy depend on our well-developed medical system including a large number of drugs that are substantial for the treatment of many diseases. In addition, our food production depends on a number of drugs facilitating the prevention and treatment of bacterial and parasitic infections in productive livestock. In April 2020, the French drug regulatory agency ANSM listed 33186 drugs containing 5314 active substances, of which 16911 (3750 active substances) are currently authorized (ANSM, 2020). The veterinary drug regulatory agency listed 759 authorized active substances in veterinary medicine (ANMV, 2020).

Besides the substantial role drugs play in sustaining our life standard, significant adverse effects can be observed for ecosystems on one hand and for human health on the other hand. Drugs that are made to kill or inhibit pathogenic bacteria and parasites can create resistant populations of target organisms (Ventola, 2015; Roca et al., 2015; Spellberg et al., 2008) or impact beneficial organisms (Lumaret et al., 2007; Halley et al., 1989a).

Most pharmaceutical products (PP) are hardly metabolized and a part of them is excreted. After veterinary use in livestock, this excreted part often ends up on soils, where it is exposed to different fates. The molecules can be degraded by light or microorganisms, adsorbed to soil minerals and organic matter or transferred to other environmental compartments with water flow (Kim et al., 2018; Kümmerer, 2008). Both the parent compound as well as transformation products can be toxic to present organisms. This toxicity can vary over many orders of magnitudes for the same molecule depending on the environmental compartment and present organisms. Veterinary pharmaceutical residues can for example restrain the degradation of contaminated dung by affecting dung degrading insects (Römbke et al., 2010), contribute to spreading of resistances in pathogenic bacteria (Grenni et al., 2018) or kill aquatic organisms (Garric et al., 2007; Halley et al., 1989a). It is difficult to quantify the actual consequences for the receiving ecosystem due to the multitude of used molecules with diverse chemical properties, uncertainties in their environmental behavior, lacking knowledge of their potential interactions and the heterogeneity of environmental systems (Kümmerer, 2008).

The toxicity of Ivermectin (IVM), the molecule which a part of this study focuses on, is very high for aquatic organisms (Garric et al., 2007; Halley et al., 1989a) while no such extreme toxicity is reported for soil organisms. The possibility of a small amount reaching the streams could have much more severe consequences than the continuous input to soils. Many authors have searched different types of pharmaceutically active compounds (PhAC) in streams and rivers in different regions of the globe and detected them at concentrations from less than 1 ng L^{-1} to several hundred $\mu\text{g L}^{-1}$ or more in rare cases (Obimakinde et al., 2017; Charuaud et al., 2019a).

The processes that govern the fate of pharmaceuticals happen at different scales in time and space. Adsorption and degradation take place on the scale of single molecules and may depend on different factors like mineral and organic matter composition, radiation, temperature, redox potential and pH to name a few (Kümmerer, 2008). These factors are variable at different spatial scales within and between soil aggregates, between fields with contrasted soil types and areas on different geology to regions under different climatic conditions. They also vary with time depending on variable temperature and hydric condition and can take from a few minutes or hours to months or years. The transport pathways depend on the flow of water, which itself is determined by different factors on different scales in time and space (Glaser et al., 2019; Blöschl, 2001; Soulsby et al., 2003; Bachmair and Weiler, 2014; Beven and Germann, 2013). In time, water flow can vary from rapid variations during a flood event, over seasonality to long-term changes in climatic conditions. Spatially, on the sub-metric scale, macroporosity may determine dynamic and pathways of flow (Beven and Germann, 1982; Flury et al., 1994; Chen et al., 2021). On the hillslope-scale flow paths and dynamic are determined by the permeability of the soil horizons, bedrock morphology, slope, connectivity of overland flow paths and re-infiltration zones (Beven and Germann, 2013). On the catchment-scale, the importance of preferential flow paths today still remains an important subject of research (Beven and Germann, 2013; Glaser et al., 2019).

In the Mediterranean region, the climate is characterized by a dry summer followed by intense storm events in autumn leading to overland flow and flash floods (Nuissier et al., 2008; Delrieu et al., 2005). While some authors studied the impact of dynamic hydro-meteorology on the environmental transfer of contaminants (Mandaric et al., 2019; Palma et al., 2020; Osorio et al., 2014), much remains

unknown on the extent to which these extreme conditions affect the transfer patterns of veterinary pharmaceutical residues from agricultural soils into streams. In these conditions, flow paths and transit times may completely change within minutes. While rapid overland and subsurface storm flow occur, long-term equilibrium sorption processes and degradation may be of negligible importance for the transfer into streams and the mobility of the studied compounds. Little is still known about the capability of these conditions to load streams with significant amounts of theoretically immobileⁱ compounds and thereby substantially impact river ecosystems.

Experiments on the environmental transfer of PP have been conducted at different scales, starting from batch sorption studies (Krogh et al., 2008a) over saturated soil column experiments (Kay et al., 2005a) to metric scale lysimeters (Kay et al., 2005b; Goss et al., 2010) and 2D soil boxes (Popova et al., 2013; Fernández et al., 2011). Beyond the metric scale (e.g. hillslope and catchment), contaminant transfer experiments under controlled conditions are sparse (e.g. Stoob et al., 2007) due to the high cost and effort as well as the amount of contaminant that would have to be introduced in the environment. At these scales, observation and modeling are more common.

Given the complexity of environmental systems, models are often the best way to understand, quantify and prioritize the different processes, especially at larger scales, where many different processes take place in parallel. Hydrological models exist in different levels of complexity and with different underlying philosophies (Hrachowitz and Clark, 2017). Catchment hydrological models can be spatially distributed, explicitly representing the whole area of a catchment at a high resolution in two or three dimensions (e.g. PARFLOW (Maxwell, 2013; Kollet and Maxwell, 2008), HYDRUS-3D (Šimůnek et al., 2008)) or integrate processes over the whole catchment (lumped, e.g. unit hydrograph (Sherman, 1932), HBV (Bergström, 1992)) or larger conceptual parts of it (semi-distributed, e.g. SWAT (Arnold et al., 1998), TOPMODEL (Beven and Kirkby, 1979), mhM (Samaniego et al., 2010)). Furthermore, hydrological models can represent physical processes inside the system on variable levels of complexity from no representation of any physical processes (e.g. unit hydrograph (Sherman, 1932)) to a full physical representation surface and variably saturated subsurface flow through Richards' equation (e.g. PARFLOW (Maxwell, 2013; Kollet and Maxwell, 2008)). In addition to physical processes of water flow, chemical processes concerning the transport of dissolved and particulate matter can be implemented at different levels of complexity. The existing models form a continuum along these different axes of complexity and the different types of models have different advantages and drawbacks making one or the other type more adapted according to the research goals and available data and process knowledge. Models with high process complexity and a high spatial resolution can reproduce the right results for the right reasons (Kirchner, 2006) with little calibration if correctly parametrized, but require a large amount of precise, spatially distributed data and knowledge of the system and are computationally demanding. Models with lower complexity are more adaptive and less demanding in terms of computational power and data, but rely on calibration of empirical parameters to reproduce observed data. Hrachowitz and Clark (2017) argue that all models are spatially lumped and contain conceptual elements to varying degrees and all models are build on a physically sound basis if they

ⁱ Theoretically immobile refers to the fact that in early environmental risk assessments, hydrophobic compounds like IVM were considered unproblematic for aquatic organisms due to their strong sorption to soil. Nevertheless these compounds are found in environmental waters. See Chapter 4 for more details.

are well implemented. Hrachowitz et al. (2014) highlight the importance of constraining models with expert knowledge.

After an initial focus of hydrological modeling to reproduce total water discharge at a point in a river corresponding to the outlet of a catchment, today an increasing focus is set on the characterization of water in the stream with regards to transit times and flow paths. Various methods have been developed recently to model not only the discharge of water at the outlet but also the transfer of water through the catchment on a spatial and / or temporal dimension. This tracking of water volumes through models allows to quantify transit times through the catchment. Approaches reach from the application of fixed steady-state transit time distributions (TTD) (McGuire and McDonnell, 2006) over age selectivity of fluxes (Rinaldo et al., 2015) to particle tracking in spatially distributed models (Yang et al., 2018). The parameters of these models are calibrated against observed concentrations of a variety of tracers in addition to discharge in order to obtain a realistic representation of water flow through the system. These insights into water flow through environmental systems can help to form and evaluate hypotheses on the transfer of contaminants on a scale where transfer experiments under controlled conditions are less feasible or impossible.

This PhD thesis aims to improve understanding of environmental transfer of veterinary PP after regular application to farm animals. We consider the case of extensive agriculture in a context of highly dynamic hydro-meteorology. These are the conditions found in our study site, the Claduègne catchment and representative of the foothill region located between the Monts d'Ardèche mountains and the Rhône Valley. The Claduègne is a mesoscale (42 km^2) catchment with Mediterranean climate including intense autumn storms regularly causing flash floods. These particular conditions build the base for investigations on the effect of flood events on the transfer of organic contaminants, more specifically veterinary pharmaceuticals issued from extensive cattle breeding from pastures into surface water bodies. The study focuses on understanding the transfer dynamics without explicit quantification of adsorption and degradation. In other words, the effect of these processes that fundamentally impact the transfer are taken into account implicitly but their individual contributions could not be determined.

The Claduègne catchment is part of the Cévennes-Vivarais Mediterranean Hydrometeorological Observatory (OHM-CV), under hydrologic monitoring since 2011 and equipped with automatic stream water samplers. Different recent studies brought insights into hydrological functioning of the catchment (Nord et al., 2017; Uber et al., 2018; Braud et al., 2014), meteorology of the region (Nuissier et al., 2008; Boudevillain et al., 2016) and transfer of sediment through the catchment (Uber, 2020). Furthermore, the presence of the CERMOSEM laboratory on site facilitated contact with local stakeholders. The catchment is at a scale that is large enough to integrate a certain diversity of land uses and processes. At the same time it is small enough to allow data-acquisition through direct contact with the stakeholders, as well as direct diffusion of scientific results and their practical implications to them which may influence their actions toward more sustainable management of the territory.

1.2 Objectives

The global question of this study is what happens to residues of veterinary pharmaceuticals, when they are released into the environment through grazing of treated animals in the specific context of the Claduègne catchment with its extensive cattle breeding and dynamic hydro-meteorology. The environmental compartment of interest of this study are surface water bodies, as they are particularly sensitive to some of the used compounds. Therefore, rather than considering the forward perspective on all possible fates of pharmaceutical residues once mobilized, we follow a backward approach aiming to identify the factors and conditions that allow pharmaceutical residues to reach the surface water bodies. This sets the focus on transfer. Adsorption and degradation impact the amount of dissolved contaminants and are thereby taken into account, however not quantified explicitly.

The question is split into three main sub-questions:

1. Which pharmaceuticals are dominantly used by livestock breeders in the Claduègne catchment, in which seasons and what are the applied quantities?
2. In what quantities and under what conditions is a model PhAC mobilized from contaminated dung and transferred through and over soil at the plot scale?
3. In what conditions and seasons does event water rapidly get discharged out of the system, from plot to catchment scale?

1.3 Approach, encountered problems and redefined goals

This PhD thesis was originally aiming to quantify the transport of veterinary pharmaceuticals from their diffuse sources on pastures into the rivers on the catchment scale. Due to the rural character of the site with few towns and pasture being dominant land use, we chose to focus on animal husbandry and neglect domestic animals. The goal was to link source dynamics (periods of animal treatment and manure application) to periods of high export at the catchment outlet, via consideration of hydro-meteorological conditions, soil hydric conditions and more generally water transfer pathways and transit times throughout the catchment and their temporal evolution.

To begin, we investigated the first question in a semi-quantitative way through interviews with the livestock breeders in the catchment. Initially we planned to link the results of these interviews to analyses in the Claduègne river. We installed polar organic compound integrative samplers (POCIS) at four different seasons in six places in the stream network, representative of different land use practices with the goal to conduct a screening analysis (suspect workflow) trying to identify the different molecules present in the stream water and compare them to the molecules that are used. In addition, during the first year of the PhD, water samples were taken at variable frequency (high frequency during flood events and occasional sampling outside of these events) at the Claduègne's outlet and a subcatchment with the objective to investigate the variation of concentrations of the veterinary pharmaceuticals systematically used in the catchment and link them to treatment periods and hydro-meteorological conditions. Samples were collected and filtered using heat-treated glassware and frozen until analysis. These activities were funded by the Bassin du Rhone Water Agency as part of the PharmaBV project, a collaboration between IGE (Grenoble), INRAe (Lyon) and CERMOSEM,

a rural branch of the UGA in Ardèche region, associated with PACTE laboratory. However, unfortunately none of the molecules identified during the interviews was part of the analytical method at INRAe Lyon. With the available budget we were unable to find any laboratory able to analyze the majority of those molecules in a significant number of samples at low limits of quantification (LQ). Just before the end of the PhD project (during a six month prolongation), Christine Baduel at the IGE laboratory managed to integrate a few of those molecules in an analytical method using high performance liquid chromatography (HPLC) and a tandem mass spectrometer. This finally allowed us to present a few observed concentrations of some of these veterinary pharmaceuticals in the stream water. Unfortunately, the screening analysis of the POCIS could not be realized, due to time lack and travel restrictions caused by the 2020 pandemic (planned analysis in Sweden).

These limitations led us to restrain the initial catchment-scale approach to water transit time modeling and develop an experimental device on a smaller (submetric) scale that allowed us to sample intact soil and conduct transfer experiments under simulated rainfall. We investigated the transfer of a model molecule, IVM which is largely used in livestock breeding in the catchment on intact soils from the catchment. The analytical method to quantify this molecule could be developed in parallel by Marie-Christine Morel and Céline Voiron at the IGE lab. The experiments aim to answer the following five questions:

1. How do the soils' hydrologic responses vary between rain events regarding the temporal dynamic, repartition between overland and subsurface flow and the proportions of event and pre-event water?
2. What soil characteristics and conditions explain these variations?
3. What order of magnitude of dissolved concentrations and quantities of IVM can be mobilized from cow dung by a short intense precipitation and pass through and over the soil without being adsorbed?
4. How do these amounts depend on the two main soil types in the Claduègne catchment?
5. How do the amounts depend on the initial condition of the soil and the period of time between cow dung application and precipitation?

These experiments were conducted on a decimetric scale and cannot directly be interpreted with regards to contaminants reaching the stream. Experiments allowing this kind of interpretation would require to be conducted at the hillslope or small catchment scale, as these scales have features that are not accounted for in the conducted experiments. This however would require larger, more expensive installations and imply the significant drawback of polluting the environment, if a controlled application of pharmaceuticals was conducted. This was not possible within the scope of this PhD research. We decided to use the experiments in order to estimate the potential of mobilization of IVM. As a second step, the question of the risk of transfer of commonly used PP towards surface water bodies was approached via a modeling study of transit times on the scale of the Claduègne catchment. The underlying hypothesis that due to the high sorption coefficients of the commonly used pharmaceuticals, longer transit times would lead to their adsorption to soil and thus periods with short transit times can be interpreted as high-risk periods for pharmaceutical contamination of surface water bodies. The model has a time step of one hour and the focus here are very short transit times below one day. The main questions are:

1. In which conditions and which seasons, are there significant fractions of the discharge in the Claduègne that are less than one day old?
2. How high are these fractions?

In order to build the model, hypotheses about the catchment functioning had to be formed and translated into a hydrological model. Therefore, before treating the questions mentioned above, the following question was evaluated:

3. Can our simplified hypotheses of catchment functioning reproduce discharge and tracer dynamics at the outlet?

1.4 Manuscript organization

After this short introduction, our study site, the Claduègne catchment is described (Chapter 2), by presenting its hydro-meteorology, geology, land use, topography, pedology, as well as the instrumentation in place. In the following (Chapter 3), a general assessment of veterinary pharmaceutical use in the study region is presented, obtained by the means of interviews with farmers. This assessment serves to identify the molecules of systematic use in the catchment. It is accompanied by an introduction on the occurrence and fate of PP in the environment and the presentation of the analysis results of some PP in the Claduègne stream water samples. In the following (Chapter 4) the focus is brought to one specific molecule, IVM). IVM is a common livestock antiparasitic drug with very high invertebrate toxicity (Garric et al., 2007; Halley et al., 1989a). After an introduction of the molecule, its properties and previous studies on its environmental transfer, we present a device that we designed during the PhD project allowing to sample intact soil and conduct transfer studies on it via rainfall simulation. We then present the results of IVM transfer experiments on intact soils from two contrasted origins of our study region. The goal was to understand the magnitude of IVM mobilization from from dung of treated beef on pastures of and how it depends on different factors like the soil and dung initial condition. The chapter includes a detailed characterization of the two soils as well as a published article on the experimental device which was developed during the PhD. Finally, in Chapter 5 a dataset of different tracers on variable frequencies is presented that was obtained in parallel on the scales of the Claduègne catchment and its subcatchment, the Gazel. This dataset was used to conceptualize the catchment functioning and build a semi-distributed conceptual hydrological model of the catchment. The model was calibrated on discharge and two tracers (dissolved silica and δ^2H) and uses storage selection (SAS) functions to model and track water transit times through the catchment. These transit times are interpreted with regards to the risk of transfer of contaminants from pastures into streams. These four chapters are followed by a general conclusion. There is no exhaustive general literature review in the beginning of the manuscript. Instead, each chapter has its own introduction with a summary of existing work on the respective subject.

This manuscript contains two published articles. Hachgenei et al. (2022a) describes the method used in Chapter 4 and is therefore included in the methods section as subsection 4.2.1. Hachgenei et al. (2022b) describes an algorithm to correct the memory effect in stable isotope analysis, developed for this PhD work. In order to avoid interrupting the text with such a specific method, this article is included in Appendix E.

2

Study site: the Claduègne catchment

2.1	Context of the OHM-CV and previous studies	9
2.2	Land use	13
2.3	Hydro-meteorological monitoring	13
2.4	Meteorology	16
2.5	Hydrology	17
2.6	Geology	20
	2.6.1 Coiron basaltic plateau	20
2.7	Topography	23
2.8	Pedology	24

2.1 Context of the OHM-CV and previous studies

The Cévennes-Vivarais Mediterranean Hydrometeorological Observatory (OHM-CV)ⁱ is a French national observation service accredited and financed by the Centre National de la Recherche Scientifique (CNRS) institut national des sciences de l'Univers (INSU) since 2000. It is dedicated to the study of hydrometeorological phenomena, sometimes extreme, affecting the Mediterranean region, in particular intense rainfall, flash floods and associated transport of dissolved and particulate matter.

ⁱ <http://www.ohmcv.osug.fr>

The studied territory (Fig. 2.1) is characterized by various contrasts: topographic (from sea level to more than 1500 masl), climatic (Mediterranean to mountainous), geological (granites, schist, marls, limestones and basalt) and land use (e.g. peri-urban, pastures, scrubs, crops and forests). The OHM-CV is part of the French Critical Zone Observatories Research Infrastructure (OZCAR-RI)ⁱⁱ, which groups observatories of the critical zoneⁱⁱⁱ. The OHM-CV gathers the skills of researchers from various disciplines with the objective of improving knowledge and forecasting capabilities of the above phenomena in a context of strong anthropic pressure and climate change. The objectives of the observatory are (i) to understand how water and dissolved and particulate matter are transferred from the hillslopes to the rivers; (ii) to analyze the evolution of high-impact events in a context of global change; (iii) to improve the understanding of human behavior with regards to these events. The OHM-CV encompasses three different ensembles of sites in the Cévennes-Vivarais region (see Fig. 2.1), representative of different land uses in the Cévennes-Vivarais region: (i) the sites called *Olivier de Serres*, representative of the agricultural land use of the southern Vivarais foothills, (ii) the *Mont Lozère* sites, representing the Cévennes mountain plateau and (iii) the *Valescure* bassin representing the forested areas of the Cévennes. Two complementary observation strategies are implemented by the OHM-CV to monitor relevant hydrological and social variables:

1. A multi-instrument and multi-scale approach ranging from the small catchment (1 km²) to the meso-scale basin (100 km²) on those three ensembles of sites. The variables monitored continuously (typically every 10 minutes or less) concern rainfall, soil moisture, water level and discharge, groundwater level and physico-chemical properties of surface water (temperature, electrical conductivity, turbidity). In addition, the concentration of suspended sediment and major ions are frequently analyzed. Environmental characterization data are also stored (e.g. geology, pedology, soil properties, land use, digital elevation model (DEM), hydrographic network).
2. The realization of hydrological and sociological post-event surveys on extreme phenomena occurring in all Mediterranean regions, by means of physical surveys and interviews with the population shortly after a major event. They allow the collection of information on the highest water levels reached, peak discharges, flood dynamics, perception and knowledge of the risk and the behavior adopted by the population.

The Claduègne The study site of this PhD project is the Claduègne catchment (42 km²) and its sub-catchment called Gazel (3.35 km²) which lie in the French Ardèche department (Fig. 2.2). Together with the Auzon (116 km²), they constitute the *Olivier de Serres* sites of the OHM-CV. The *Olivier de Serres* sites and associated datasets are presented in detail by Nord et al. (2017). The northern, upstream half of the Claduègne catchment lies on the Coiron basaltic plateau and the southern downstream part lies on sedimentary marly limestone bedrock. It ranges in altitude from 205 masl to 838 masl. Principal land uses are pastures, cultivated soils (vine & cereals), small forests, shrubland and villages. It shares significant parts of the five communes Mirabel, Saint-Gineys-en-Coiron, Berzème, Saint-Jean-le-Centenier and Villeneuve-de-Berg. The site is characterized by its low

ⁱⁱ <https://www.ozcar-ri.org/>

ⁱⁱⁱ The critical zone is the zone at the earth's surface in which interactions between atmosphere, geosphere, hydrosphere and biosphere take place and generally spans from the tree canopy to the bedrock

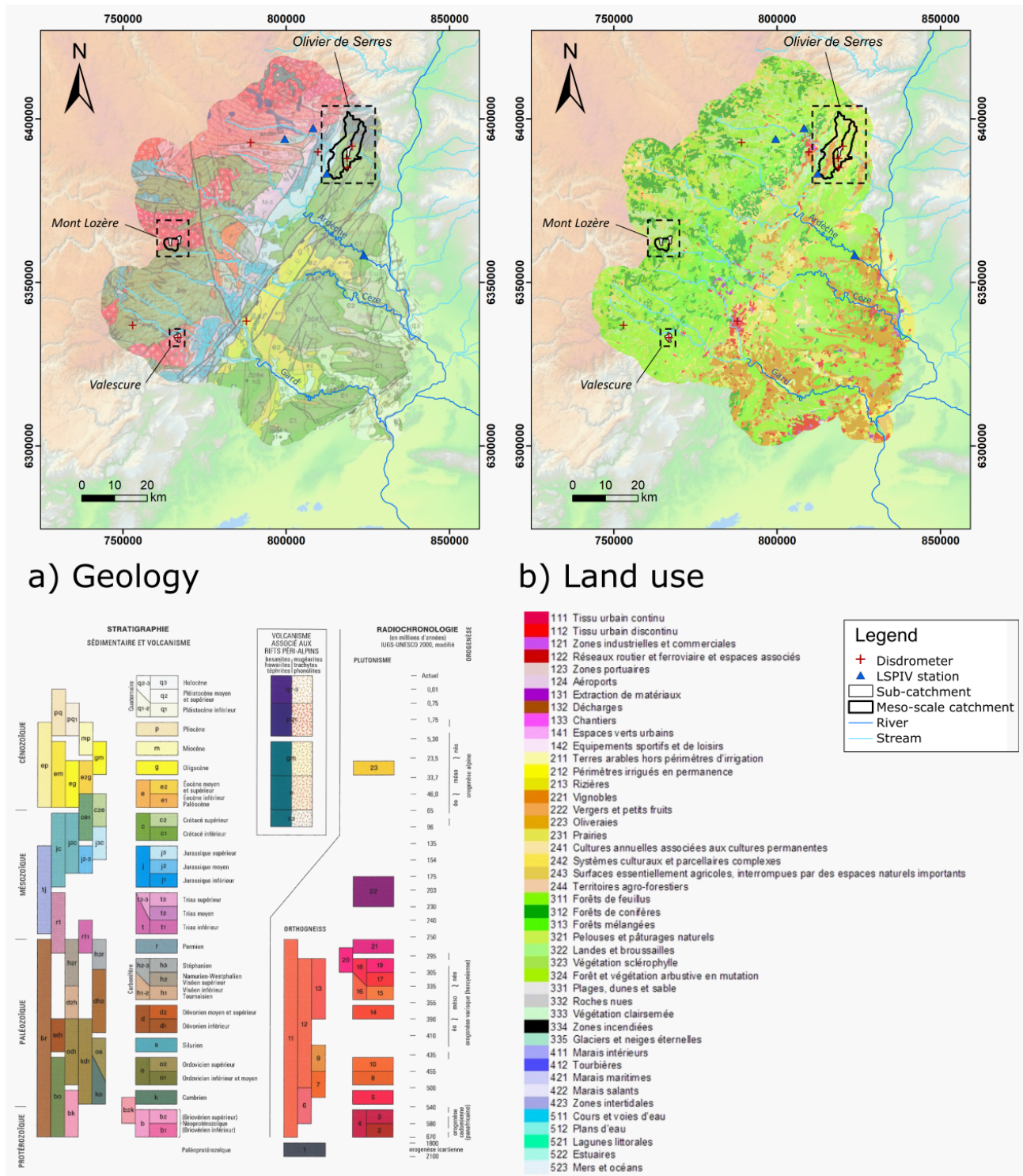


FIGURE 2.1: Sites of the OHM-CV observatory with a) geology and b) land use. Coordinates are in Lambert 93 [m], northing on Y, easting on X. Source: <http://www.ohmcv.osug.fr>.

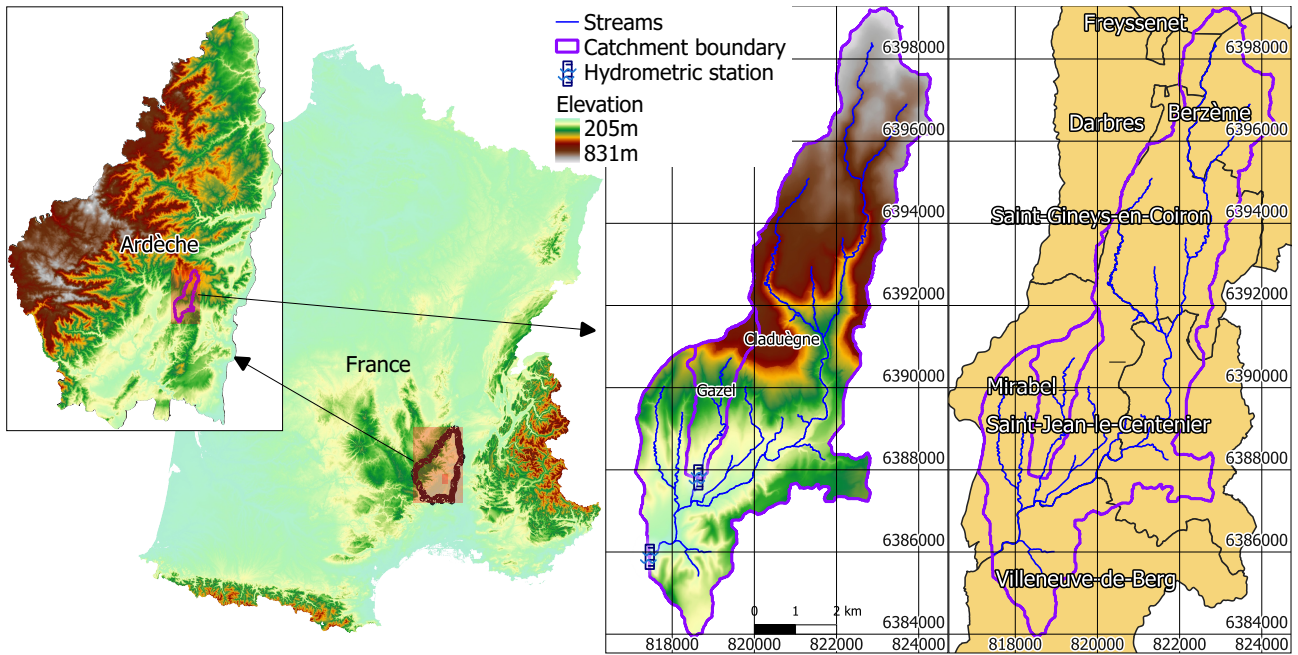


FIGURE 2.2: Location of the study site with elevation, river network and the communes. The elevation colorscale in the legend refers to the catchment map. Coordinates are in Lambert 93 [m], northing on Y, easting on X.

population density (32.6, 8.5, 9.5, 52.0, and 117.9 inhabitant km^{-2} respectively for the communes listed above; calculated from INSEE (2017)), extensive agriculture and natural vegetation. The Claduègne catchment is exposed to Mediterranean climate and is prone to flash floods.

Previous hydrological studies Several projects took place on the *Olivier de Serres* sites focusing on different research questions and there were multiple PhD theses and habilitations linked to the OHM-CV. HyMeX (Ducrocq et al., 2013) and Floodscale (Braud et al., 2014, 2016) focused on flash floods and their generating processes. Studies included characterization of the hydraulic properties of soils of the Claduègne catchment in the field (Braud et al., 2017; Braud and Vandervaere, 2015) and factors governing the catchment's hydrologic response (Uber et al., 2018; Nord et al., 2017) as well as the generation, evolution and characterization of intense precipitation events in this region (Boudevillain et al., 2016, 2011; Wijbrans et al., 2015). Vannier (2015) and Bouyer (2014) used the CVN model, a physically based semi-distributed model trying to reproduce flood events in the Claduègne catchment. The PhD thesis of Magdalena Uber used sediment fingerprinting to characterize the origin of suspended sediments and its evolution throughout and between flood events (Uber, 2020; Uber et al., 2019). The Pharma BV project (Martins et al., 2019) investigated the occurrence of certain pharmaceuticals in the stream network of the Claduègne catchment. This is continued by this PhD thesis as well as the currently running project IDESOC trying to link sources of pharmaceutical products (PP) to the occurrence of PP in the streams.

Olivier de Serres It is worth mentioning that Olivier de Serres who was born in Villeneuve de Berg and managed the farm "Le Pradel" in the heart of the Claduègne catchment is also often entitled the "father of French agriculture" (Vidal, 2019). This title is owed to his book "Le Théâtre d'agriculture

et mesnage des champs", first published in 1600, which was a manual to agriculture, read by generations of farmers. The book instructed farmers on how to organize their farm, plow and fertilize the soils, grow wheat and vine, hold productive livestock, plant vegetables, use water and wood resources and process and conserve food products.

2.2 Land use

The characteristic land use forms in the Claduègne catchment are extensive agriculture and natural vegetation with the principal land cover forms being pastures, cultivated soils, forest, shrubs, vineyards and villages. 57 % of the catchments surface are farmland registered in the *registre parcellaire graphique* (RPG, IGN (2021)). 46 % are pastures, 5.2 % are vineyards, 2.8 % are feed crops and 2.3 % are cereals. There are mainly five different species of livestock that are held inside the catchment: beef, sheep, goats, pork and chicken. Figure 2.3 shows the agricultural land use in the Claduègne catchment from the RPG (IGN, 2021) as well as towns and campgrounds. Areas with no attributed land use Fig. 2.3 are mostly uncultivated shrubland and forests. In the sedimentary part of the catchment there are some badlands that act as sources of suspended sediment (Uber et al., 2019). For some parts of this study, a focus is set on the Gazel subcatchment (3.35 km²), which has a larger part on the sedimentary geology (77 %), but reflects the diversity of land-uses of the Claduègne catchment on a smaller surface.

2.3 Hydro-meteorological monitoring

Hydrometric stations were installed at the outlets of the nested Claduègne and Gazel catchments, in October and April 2011 respectively (Fig. 2.4). They are situated on an abandoned roadbridge and on the bank of a natural river stretch respectively. The equipment is described in detail by Nord et al. (2017). At the Claduègne outlet, water level H_w is measured by the means of a radar mounted to the bridge. One measurement is logged every 10 min by averaging over 30 values obtained in less than 1 min. At the Gazel outlet, H_w is measured every 2 min (average of 15 measurements) using an *OTT PLS* hydrostatic pressure gauge. Water discharge Q is calculated through stage-discharge relationships obtained from intense measurement campaigns from 2012 to 2014 and updated via sporadic measurements thereafter. The applied discharge measurement techniques include artificial tracer dilution, current meters, portable surface velocity radar, acoustic doppler current profiler and large-scale particle image velocimetry. In addition, water temperature and electric conductivity are measured using a Campbell scientific CS547 probe and turbidity is measured using a Visolid IQ 700 turbidity sensor (at the same timestep). Furthermore, automated samplers are installed at the two outlets to take samples of water and suspended sediment at high frequency during flood periods. They are described in Chapter 5.

Precipitation is measured at two locations in and close to the Claduègne catchment at 6 min resolution by the French national meteorological service Météo France. The two stations Berzème-RAD on the Coiron Plateau and Mirabel-SA at Le Pradel in the sedimentary downstream part of the catchment are considered representative for the two geological units of the catchment that are contrasted in altitude and lay along the south-west - north-east axis along which the Cevennes storm events often travel

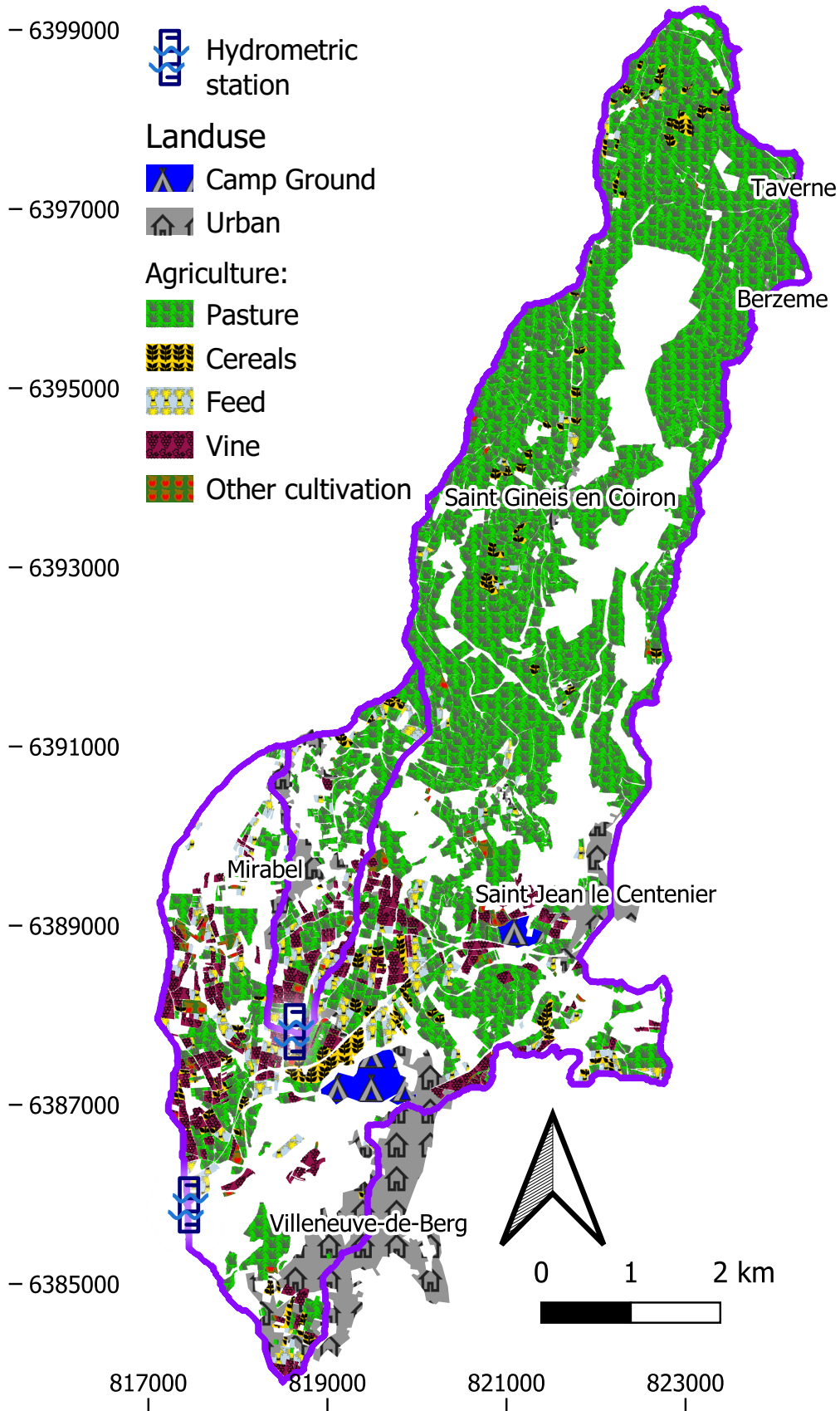


FIGURE 2.3: Land use in the Claduegne catchment. Agriculture is from RPG (IGN, 2021). Coordinates are in Lambert 93 [m], northing on Y, easting on X.

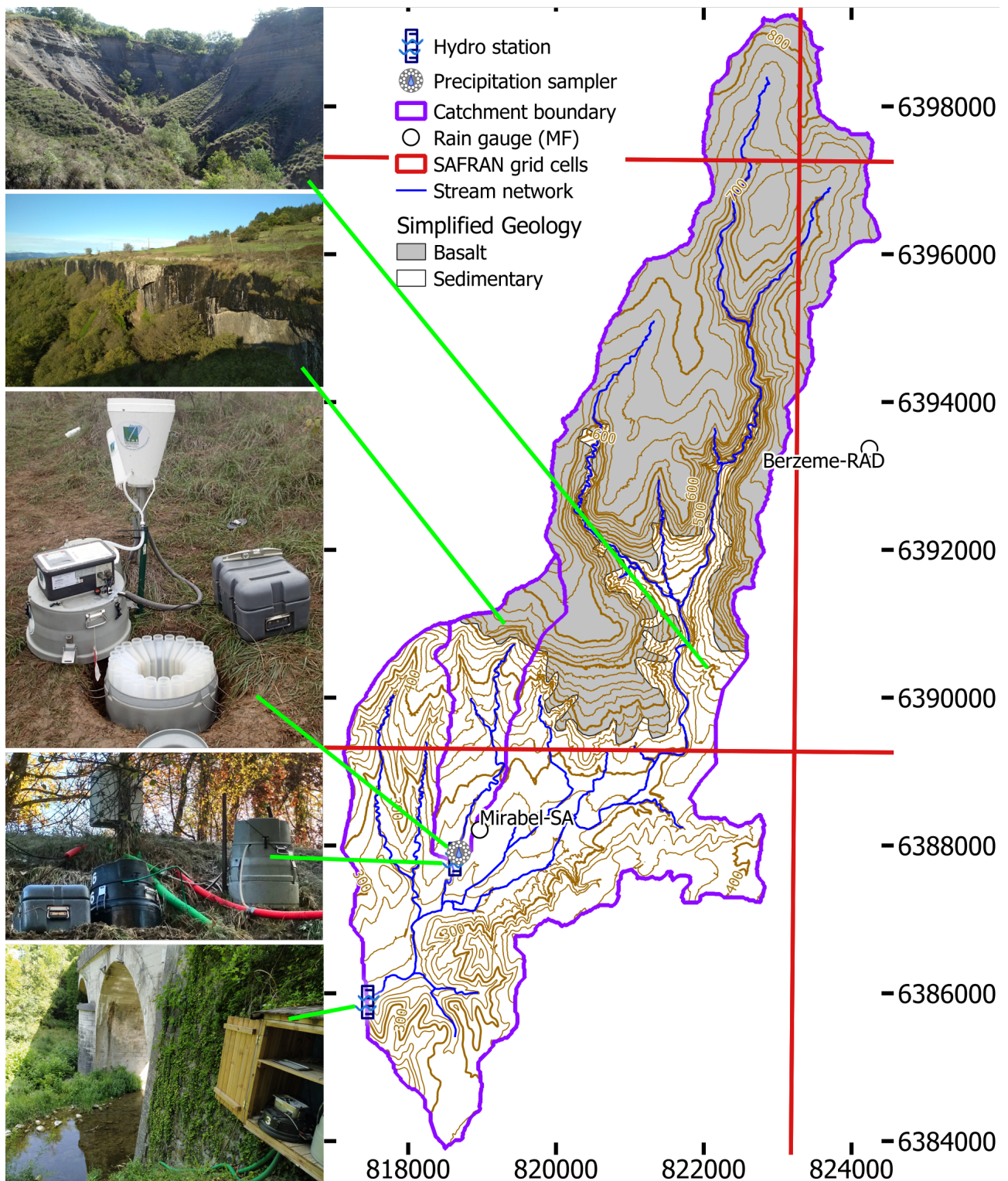


FIGURE 2.4: Measurement sites with continuous / regular observations in the Cladugène catchment. Brown lines are elevation (20 m resolution, bold every 100 m). Coordinates are in Lambert 93. The photos show (from top to bottom): basaltic cliff, sedimentary badland, precipitation sampler, water samplers at the Gazel outlet. Photos: Nico Hachgenei

(Boudevillain et al., 2016). In addition there is a tipping bucket rain gauge to which an automated sampler was connected during this PhD (Fig. 2.4). Precipitation sampling is described in detail in Chapter 5.

Potential evapotranspiration (E_p) is calculated from hourly reanalysis data from the Système d'Analyse des Renseignements Adaptés à la Nivologie (SAFRAN) model (Vidal et al., 2010) (radiation, air temperature, humidity and wind speed) using the formula from Allen et al. (1998) for the period from 01.08.2017 to 01.08.2020. The SAFRAN grid cells are shown in Fig. 2.4. The spatial distribution of these results allows to calculate one value for each of the geological units. This is used for the hydrological model presented in Chapter 5 as well as in order to compare E_p to precipitation for each of the two parts of the catchment. For each of the two geological units, a value is obtained by weighting the values of each grid cell by the proportion of the geological unit covered by this grid cell. The remaining period (beginning of 2017 and end of 2020) is from daily data measured by Météo France observation stations and interpolated to the Berzème and Mirabel station (calculations done by Météo France).

2.4 Meteorology

The Claduègne catchment is subject to a dynamic hydrometeorology and strong seasonality with a dry summer followed by an autumn with frequent intense storm events. Snow rarely occurs. The average annual precipitation height at Le Pradel in the sedimentary foothills is 1030 mm (Huza et al., 2014). See also Fig. 3 in Nord et al. (2017). Being located in the northern part of the Cévennes-Vivarais region, the Claduègne catchment is subject to what Boudevillain et al. (2016) call Cévennes events. These are mesoscale convective systems with an orographic component that regularly appear in autumn in this region (Nuissier et al., 2008; Boudevillain et al., 2011). The spatial distribution of extreme precipitation events is shown in Fig. 2.5. The pattern causing these events can be described as follows (Nuissier et al., 2008):

1. Due to the high temperature of the Mediterranean sea in the end of summer, the lowest part of the troposphere is charged with humidity.
2. A southern circulation on the synoptic scale transfers those moist warm air masses inland, leading to an instability.
3. Convection is triggered and the air mass channelized by the relief of the Cévennes mountains.

This pattern can produce intense and persistent precipitation, primarily affecting the coastal departments Gard, Hérault and Bouches du Rhône, but also reaching up into the Ardèche department including the Claduègne catchment (Nuissier et al., 2008; Boudevillain et al., 2016). This situation regularly provokes flash floods some of which are causing immense destruction and casualties like 2002 in the Gard river (Delrieu et al., 2005) and 2015 in the Brague river (Carrega, 2016). Precipitation amounts can reach 600 mm to 700 mm over 24 h as an example in the 2002 Gard event (Gaume et al., 2004; Nuissier et al., 2008). Generally, the yearly precipitation amount in this region increases with altitude from 500 mm at sea level to 2000 mm at the mountain ridges, while the intermittency of precipitation decreases with altitude and the highest hourly precipitation intensities are observed at

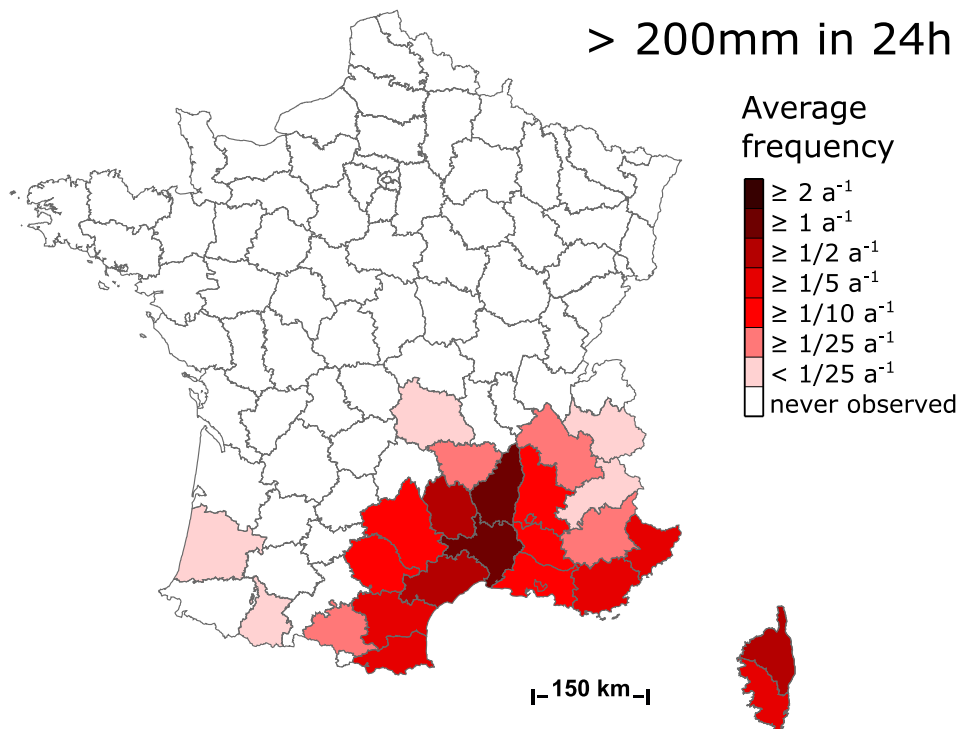


FIGURE 2.5: Spatial distribution of frequency of extreme precipitation events with a total amount $> 200 \text{ mm}$ over 24 h in the period from 1971 to 2020. Source: Météo France (<http://pluiesextremes.meteo.fr>), edition 25/03/2021.

lower altitude (Molinié et al., 2012; Boudevillain et al., 2016). Beuerle (2021) established intensity-duration-frequency curves for the Berzème and Mirabel rain gauges. The 30 min precipitation intensity with a 10 yr return period is 120 mm h^{-1} and 116 mm h^{-1} for Berzème and Mirabel respectively.

Figure 2.6 shows the average monthly precipitation (P) and E_p in the upstream (Berzème) and downstream (Mirabel) part of the catchment. October and November can be identified as the months with highest precipitation volumes. From March to September, E_p is higher than P . The driest months are June, July and August, when E_p is between 3.4 and 3.8 times P . The wettest month is November, where P is 4.1 to 5.3 times E_p (Mirabel and Berzème respectively).

2.5 Hydrology

The time of concentration of the Claduègne and Gazel are 4.5 h and 2.5 h respectively (Hachgenei, 2018). A study of characteristic times at 13 points throughout the stream network showed that the drainage network of the sedimentary part is generally more efficient leading to shorter characteristic times (Hachgenei, 2018). The discharge at the two hydrometric stations has a strong seasonality which follows the seasonality of precipitation and is typical for catchments under Mediterranean climate (Latron et al., 2009). Figure 2.7 shows the distribution of discharge values for each month. The highest extreme values occur in autumn, due too the precipitation pattern presented in Section 2.4. Some high maximum discharge values can also be observed in spring due to convective precipitation events. High average values occur from autumn to spring and lowest average values are observed in

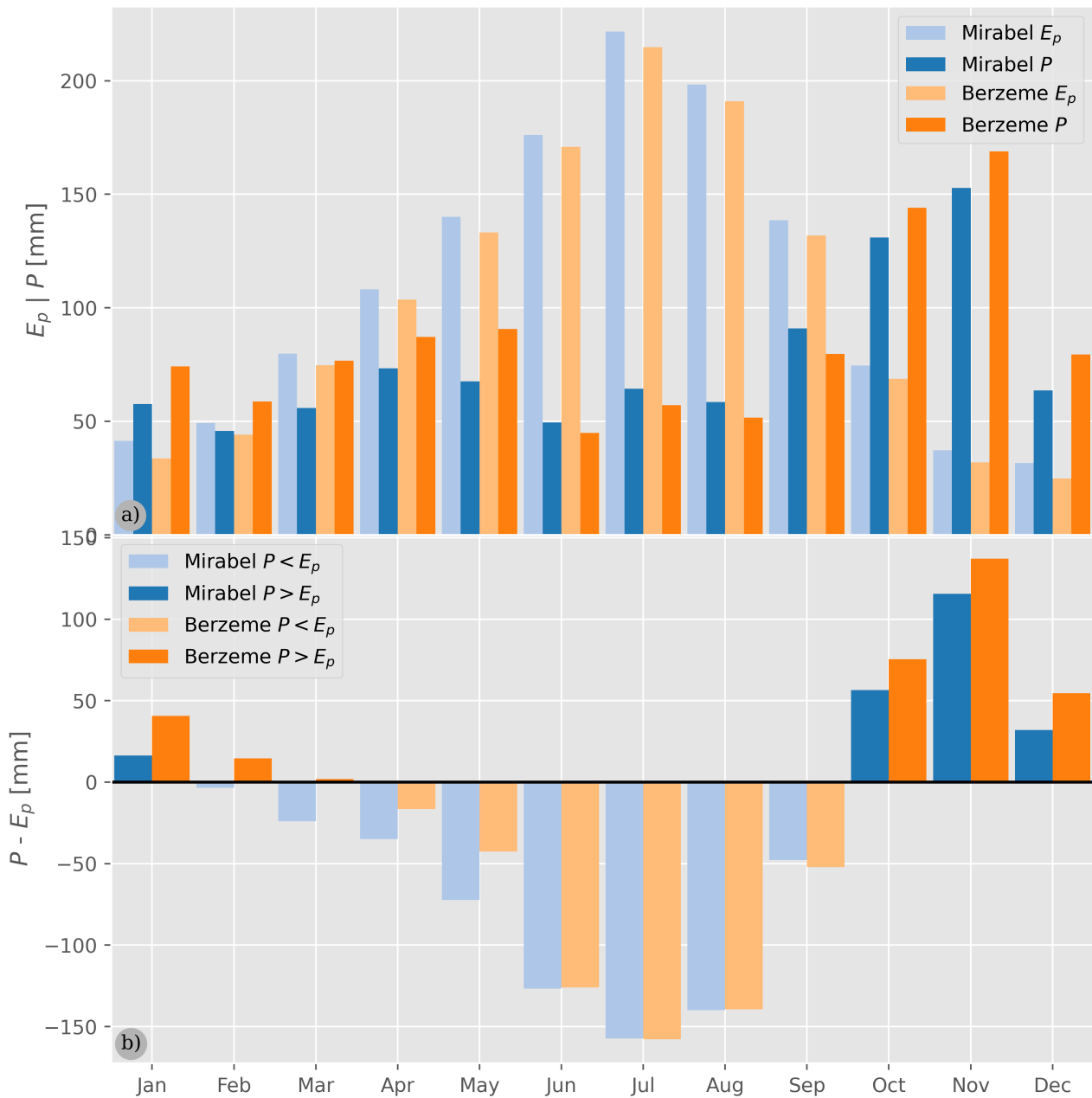


FIGURE 2.6: a) Average monthly precipitation (P) and evapotranspiration (E_p). P : observations from the two Meteo France stations from 2011 to 2020. E_p : predictions from Meteo France for the same stations. b) Difference ($P - E_p$).

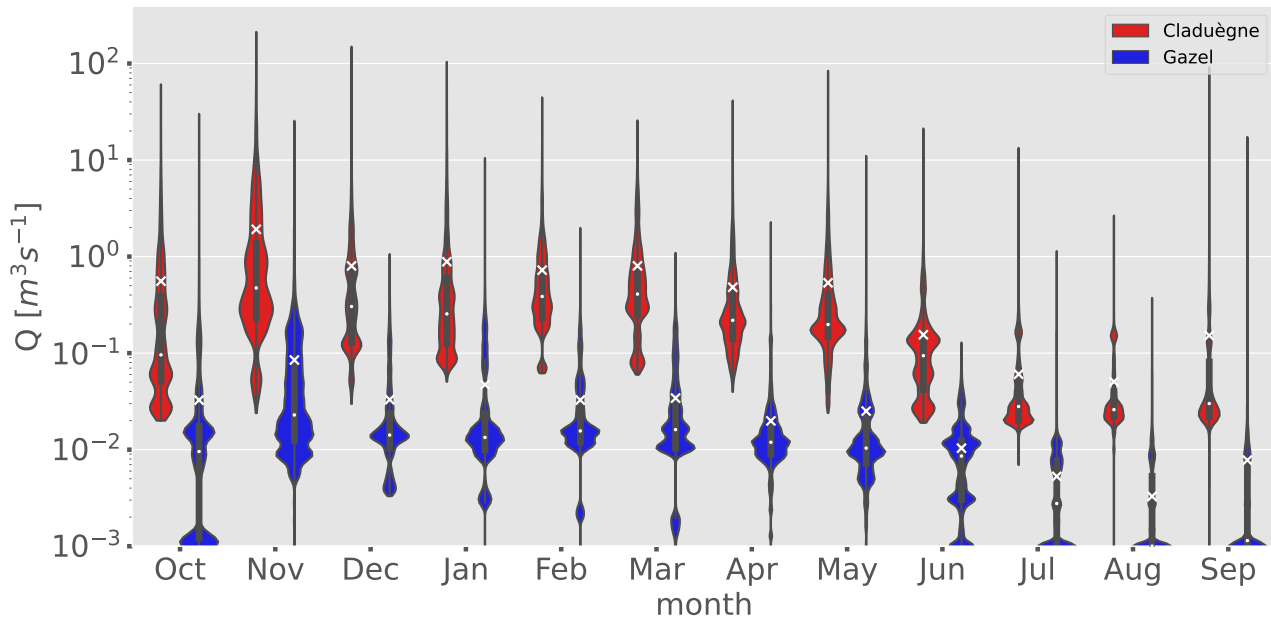


FIGURE 2.7: Distribution of discharge (Q) values at the two hydrometric stations and their seasonal evolution from 2011 to 2020 (Claduègne) and 2011 to 2019 (Gazel). Note the logarithmic scale. No flow is represented by $10^{-3}\text{m}^3\text{s}^{-1}$ (1L s^{-1}). The colored areas represent the kernel density estimation of log-transformed discharge. Interior gray lines and boxes represent range and inter-quartile range of discharge. White points are median and white crosses arithmetic mean of (non-transformed) discharge.

summer. Over the observation period, 1/3 of all water left the catchment during the 1.4% of time with the highest discharge. The Gazel is intermittent, regularly running dry between June and October, while this rarely happens in the Claduègne. Discharge ranged from no flow to $30\text{m}^3\text{s}^{-1}$ in the Gazel and $212\text{m}^3\text{s}^{-1}$ in the Claduègne for the period from 2011 to 2020 (Claduègne) and 2011 to 2019 (Gazel). The largest spread in discharge values occurs in October and November at both stations, as in this period the catchment usually receives large amounts of precipitation on initially very dry soil and therefore jumps from one extreme to the other. This can also be seen in the multi-peak shape of the distributions in Fig. 2.7.

Uber et al. (2018) found initial soil moisture to be a substantial factor determining the hydrologic response of the Claduègne catchment to precipitation. In order to provoke a strong hydrologic response, intense precipitation needs to fall on moist soil (Huza et al., 2014; Uber et al., 2018). This is well illustrated by Fig. 2.8: It shows the response of the two streams to two consecutive rainfall events, separated by about 12 h. The first one is larger (43.2 mm compared to 23.6 mm) and the maximum 6-minute intensity is similar (18mm h^{-1} compared to 20mm h^{-1}). Nevertheless, the first event only generates a slow response of small amplitude while the second event causes an immediate strong reaction of both streams. This can be interpreted as an 'activation' of the catchment by the first event through humidification of the soils, allowing the utilization of more rapid flow paths (e.g. saturated overland flow) through additional precipitation. Vannier (2015) and Bouyer (2014) had limited success trying to reproduce this non-linearity of the hydrologic response using the CVN model,

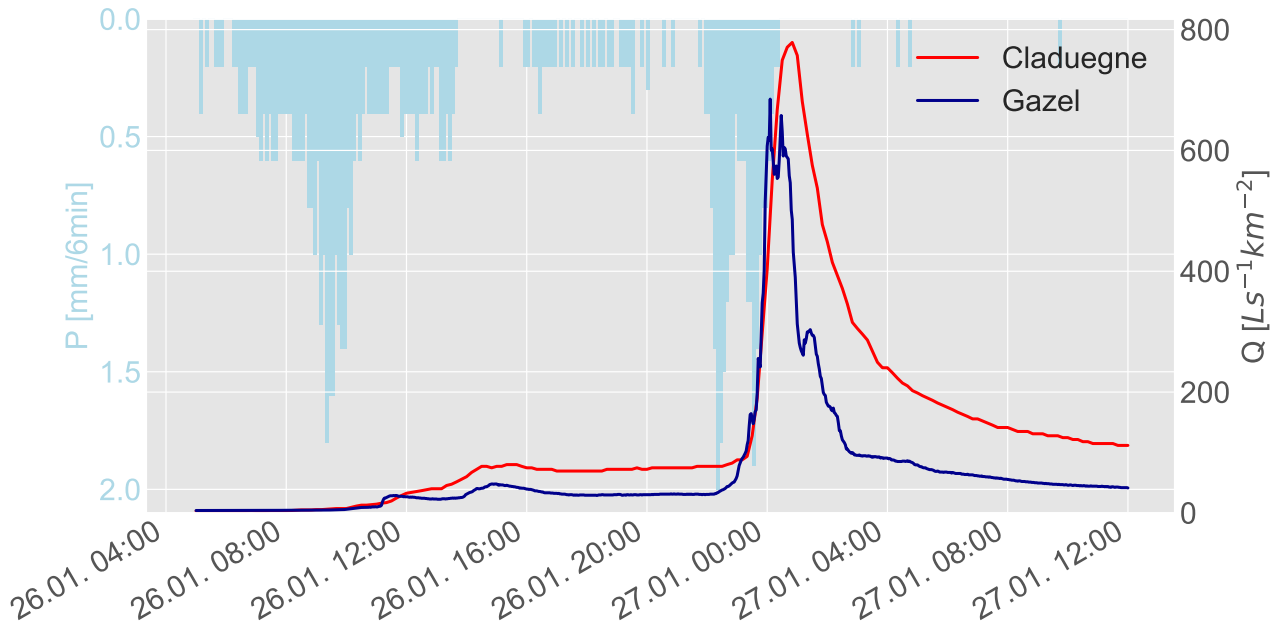


FIGURE 2.8: Example of a flood event in January 2018. Precipitation is from Mirabel station at le Pradel.

a physically based semi-distributed hydrological model. Figure 2.9 shows photos of the Claduègne outlet under normal to low flow and during a flood event in October 2013.

2.6 Geology

Figure 2.10 shows the simplified (a) and detailed (b) geology of the Claduègne catchment. The regions crystalline bedrock was covered by several layers of sediment from early Triassic until early Cretaceous (Grillot, 1971). The last sedimentary layer consists of Valanginian marls that nowadays form the surface geology of the catchment's downstream parts together with some alluvium from the Cenozoic. Several eruptive phases during the end of Miocene and beginning of Pliocene then built the Coiron plateau of basaltic geology. This is where the Claduègne and most of its tributaries have their sources. It forms the upstream 50% of the Claduègne catchment. In the rest of this manuscript, the geology will mostly be reduced to the simplified level depicted in Fig. 2.10 a).

2.6.1 Coiron basaltic plateau

The Coiron was mainly formed in the Pliocene (Blum et al., 2002) and has an alkaline character with a sodic tendency (Frain de La Gaulayrie, 1973). Hydrogeologically it represents a permeable structure on an impermeable (sedimentary) bedrock with a large number of small sources (<1 to a few $L s^{-1}$) at its border. There are three different types of geological structures with a hydrogeological importance (Blum et al., 2002):

1. **basalts from fissural volcanism:** fissured permeability
2. **strombolian volcanism:** low abundance but highly permeable
3. **clay layers:** impermeable



FIGURE 2.9: The Claduègne outlet in early summer condition (left, photo: Nico Hachgenei) and during a flood event (right, photo: Guillaume Nord)

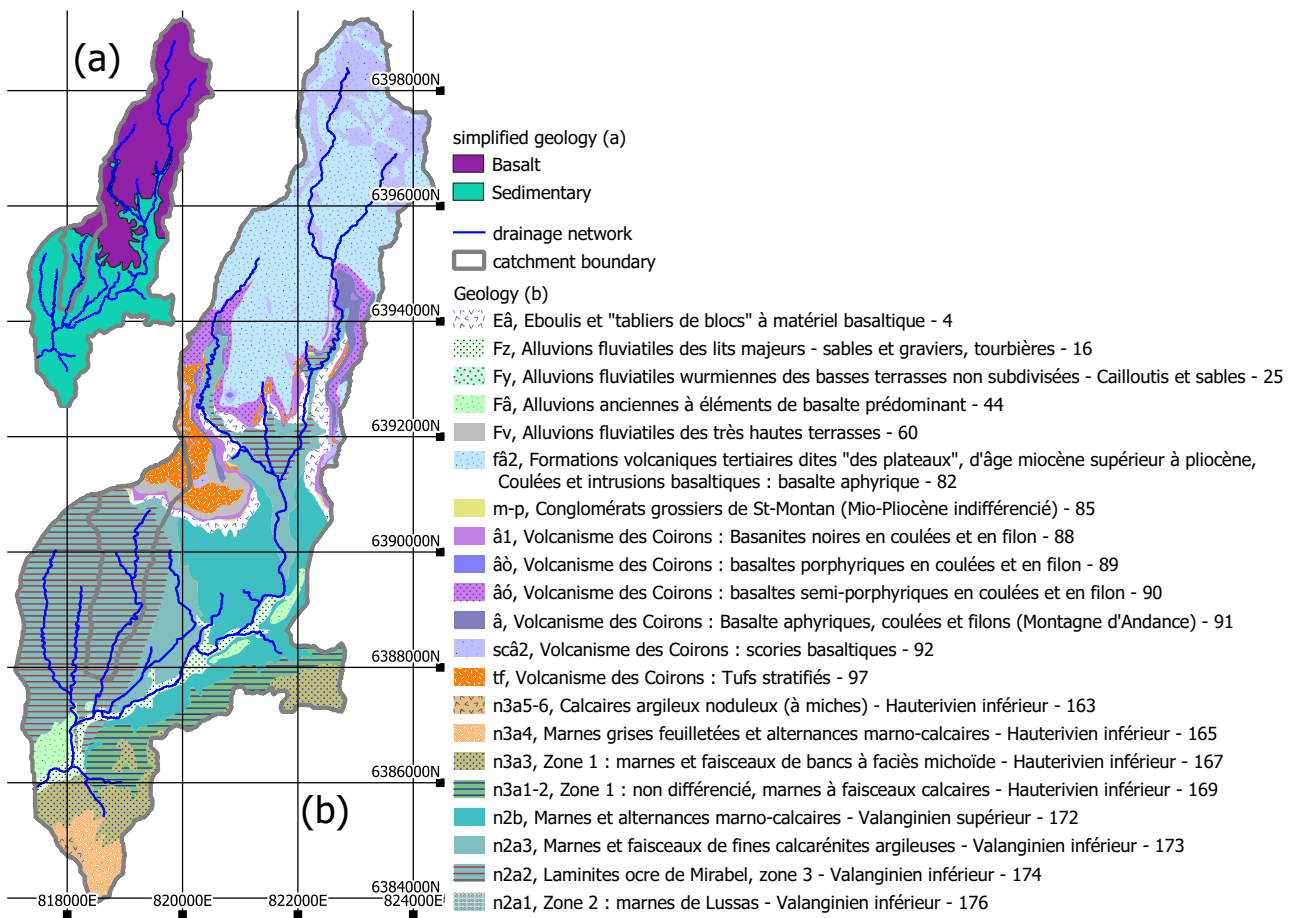


FIGURE 2.10: Geology of the Claduégne catchment (a) simplified, (b) detailed. Coordinates are in Lambert 93 [m] and refer to (b). Source: BRGM carte géologique 1:50000.

These structures cause two main types of sources in the part of the plateau that contributes to the Claduègne catchment (Fig. 2.11):

inter-basaltic sources: due to the impermeable clay layers between two casts

sub-basaltic sources: emerging below the basaltic plateau, either due to the impermeable marly bedrock, or a clayey base-layer

According to Blum et al. (2002), the sources can be considered representative for the plateau's ground water resources. Blum et al. (2002) found oxic conditions in the waters of the entire plateau with a mean redox-potential of 124.5 mV and a mean dissolved oxygen concentration of 8.98 mg L^{-1} . Analyses of water from some of these sources are presented in Chapter 5.

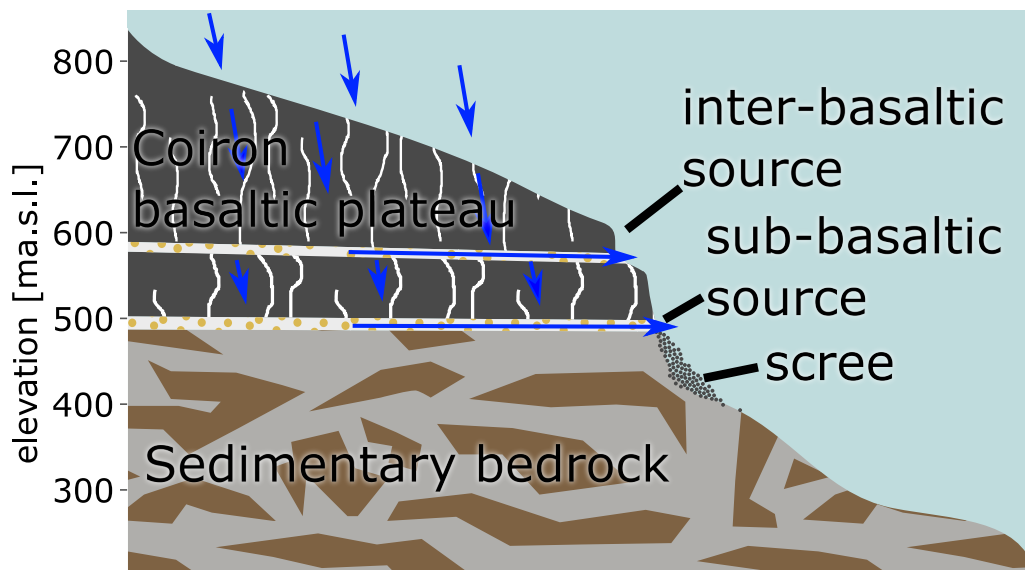


FIGURE 2.11: Simplified conceptual schema of a vertical cut through the catchment geology including the source types in the Coiron basaltic plateau after Blum et al. (2002). The elevation is approximate and the schema is not to scale.

2.7 Topography

Figure 2.12 illustrates the topography of the Claduègne catchment. It is generated from a 1 m resolution DEM, obtained from airborne light detection and ranging (LiDAR) in 2012 (Braud et al., 2014). The Coiron plateau and the sedimentary foothills can be identified as two distinct features on the elevation histogram (Fig. 2.12 a)) at 600 masl to 800 masl and 200 masl to 500 masl respectively. The intermediate elevation levels (500 masl to 600 masl) are occupied by rock cliffs (Fig. 2.4) representing a small part of the catchment's surface and the uppermost part of the foothills (400 masl to 500 masl) is partially covered by screes and talus fans of basaltic material that fell from these cliffs. Figure 2.12 b) relates elevation to slope for the whole Claduègne catchment. On the plateau, a dominance of small slopes about 3° (5 %) can be observed. In the foothills (below 400 masl), low slopes of a few degrees are dominant but going up to 30° on a significant part of the surface. Between 500 masl to 600 masl, slopes reach close to 90° and slopes of 30° are the most abundant. On the screes on an elevation

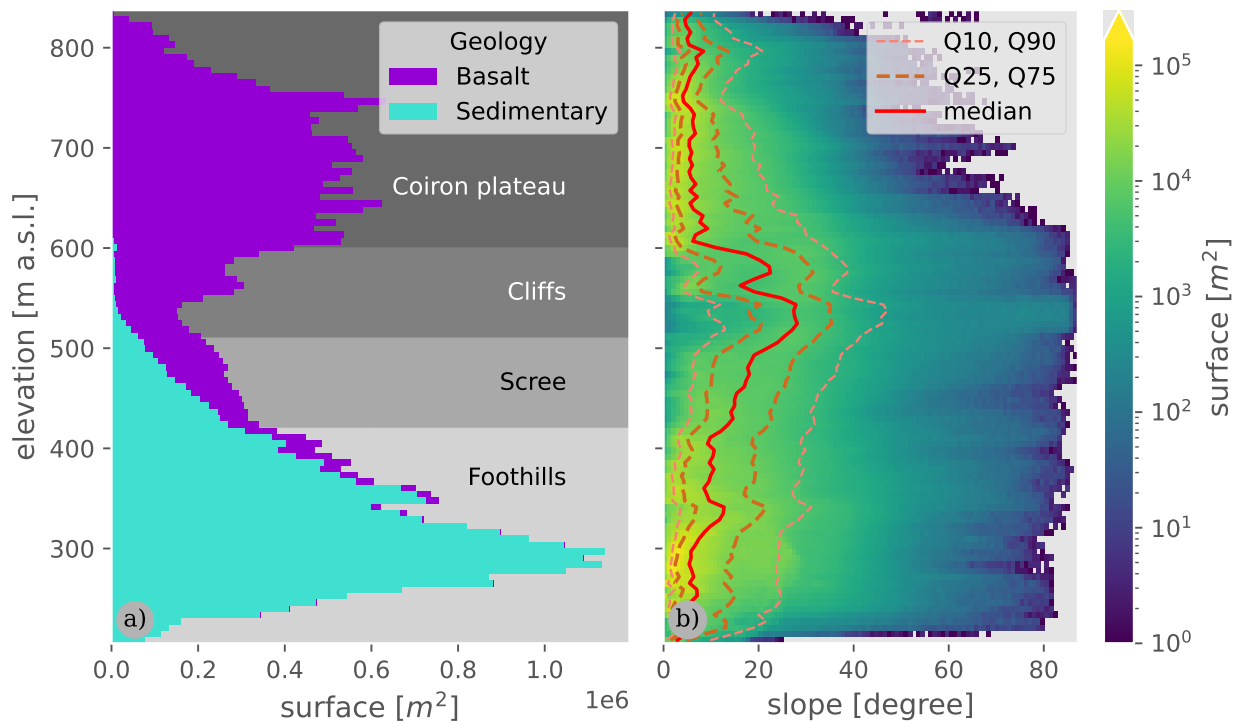


FIGURE 2.12: Topography of the Claduègne catchment: a) elevation histogram, b) evolution of slope distribution with elevation. Note the logarithmic color scale in b).

between 400 masl to 500 masl, slopes from 10° to 30° are dominant. This matches observations in the field: On top of the Coiron plateau, the slopes are very gentle. It is separated from the sedimentary foothills by a steep cliff and scree and talus fans on their foot, covered by a thin layer of soil. Downhill from the cliff, steep ravines are common. The median slope of the basaltic plateau (manually delimited as the part on solid basaltic rock above the main cliff) is 9.7%. The overall median slope of the catchment is 14.3% and in the part on purely sedimentary geology, the median slope is 15.1%. These differences can be explained by the more easily erodible sedimentary material forming the steep ravines in the foothills.

2.8 Pedology

Figure 2.13 shows the pedological map of the Claduegne catchment and the locations of soil samples presented in Table 2.1. Brunisols developed on the majority of the Coiron plateau, with very similar physical and chemical properties (Nord et al., 2017). The dominant grain size classes of the soil matrix are clay to silt with variable rock-load and soil depths of less than 2 m (Nord et al., 2017). The sedimentary part is dominated by calcisols, rendzinas and regosols with soil depths of 20 cm to 70 cm (Nord et al., 2017).

Table 2.1 shows the average and range of a selection of soil properties for the two geological units of the catchment. The soil samples are those shown in Fig. 2.13, grouped by geology. There is a contrast between soils from the two origins: The basaltic soils on the Coiron plateau are richer in

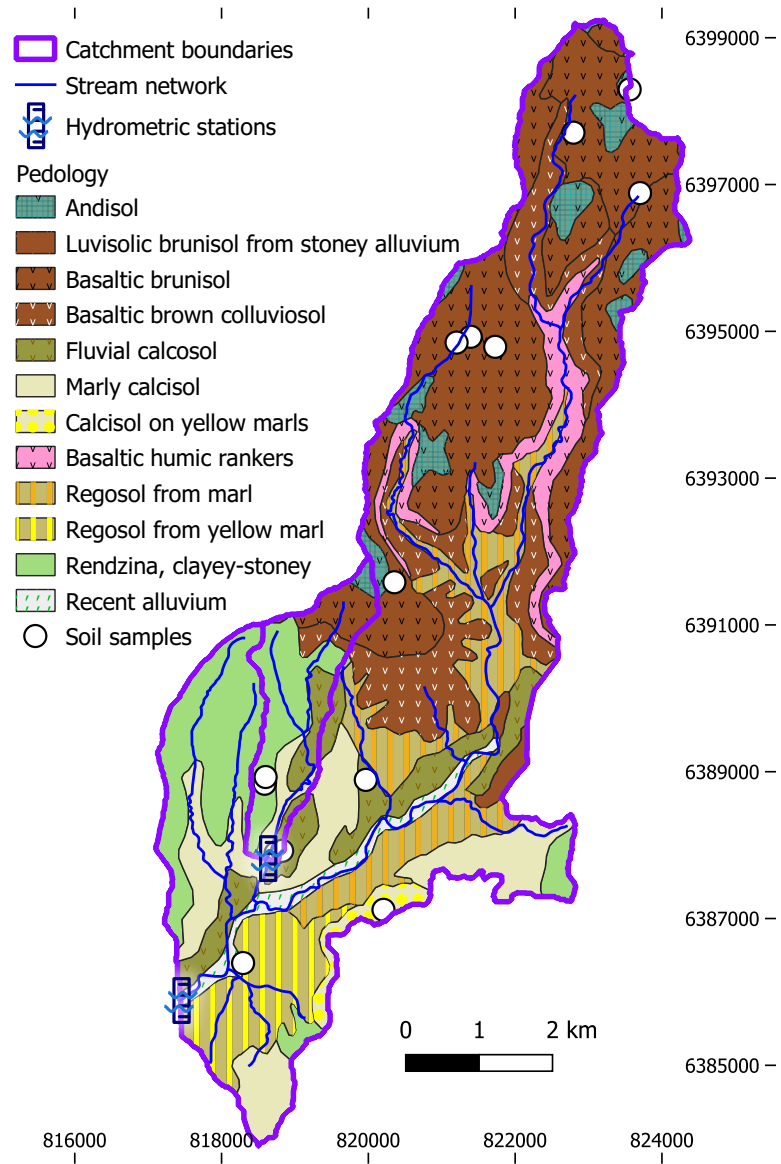


FIGURE 2.13: Pedology of the Claduègne catchment. Source of soil classification: BD-sol, INRA (Robbez-masson et al., 2000)

TABLE 2.1: Properties of soils from the Claduègne catchment from the sampling locations shown in Fig. 2.13 (average and range per geological unit). Xlf is magnetic susceptibility. Minerals and magnetic susceptibility are from Uber et al. (2019). Organic matter (OM) and pH are from the Pharma BV project (Martins et al., 2019).

Parameter	unit	Basalt			Sedimentary		
		mean	min	max	mean	min	max
<i>pH</i>		5.89	5.43	6.34	7.62	7.51	7.71
OM	%	5.36	1.46	13.00	3.34	1.91	5.54
<i>CaCO</i> ₃	g kg ⁻¹	0	0	0	217	56	466
<i>Al</i> ₂ <i>O</i> ₃	g kg ⁻¹	12.6	10.8	14.4	5.1	3.9	7.5
<i>SiO</i> ₂	g kg ⁻¹	25.5	23.2	28.1	43.0	34.4	54.4
<i>P</i> ₂ <i>O</i> ₅	g kg ⁻¹	0.367	0.221	0.546	0.160	0.000	0.298
<i>K</i> ₂ <i>O</i>	g kg ⁻¹	0.553	0.383	0.722	0.868	0.740	0.969
<i>CaO</i>	g kg ⁻¹	2.52	1.16	3.93	10.61	2.54	20.54
<i>TiO</i> ₂	g kg ⁻¹	3.82	3.23	4.16	0.67	0.48	1.23
<i>V</i>	g kg ⁻¹	0.0335	0.0233	0.0456	0.0113	0.0066	0.0173
<i>MnO</i>	g kg ⁻¹	0.1331	0.0948	0.1655	0.0356	0.0102	0.0728
<i>Fe</i> ₂ <i>O</i> ₃	g kg ⁻¹	13.70	11.97	15.10	3.37	2.03	6.56
<i>Ni</i>	g kg ⁻¹	0.0128	0.0069	0.0206	0.0032	0.0023	0.0063
<i>Cu</i>	g kg ⁻¹	0.0089	0.0065	0.0110	0.0063	0.0055	0.0079
<i>Zn</i>	g kg ⁻¹	0.0149	0.0127	0.0179	0.0068	0.0047	0.0097
<i>Rb</i>	g kg ⁻¹	0.0077	0.0056	0.0121	0.0120	0.0096	0.0152
<i>Sr</i>	g kg ⁻¹	0.0321	0.0220	0.0544	0.0418	0.0194	0.0673
Xlf 976 Hz		1606	945	3062	61	11	131

metallic minerals and elements than those in the sedimentary foothills due to their magmatic parent material containing more metals. Accordingly, the magnetic susceptibility^{iv} is much higher on the Coiron plateau than in the sedimentary part. Furthermore, they contain more organic matter (OM), mainly due to the different land use (predominantly pastures and shrubland). The soils from the Coiron contain less *SiO*₂ and they do not contain *CaCO*₃, which makes up to 46.6% of the sedimentary soils. The *pH* is higher in the sedimentary soils due to the *CaCO*₃-rich parent material. Despite the higher *SiO*₂ concentration in the sedimentary soils, stream water concentration values of dissolved silica are consistently larger in the basaltic part (see Chapter 5). This may be explained by differences in the mineralogical form under which *SiO*₂ occurs. Identifying the exact reason for this is beyond the scope of this work.

^{iv} magnetic susceptibility measures how much a material becomes magnetized after application of a magnetic field. It depends on soil minerals and parent material and can be affected by a variety of soil processes (Mullins, 1977)

3

Use of pharmaceuticals in extensive agriculture in the Ardèche region

3.1	Scientific context: Pharmaceuticals in the Environment	28
3.1.1	Sources of pharmaceutical products in the environment	29
3.1.2	Types of pharmaceuticals	29
3.1.2.1	Focus on antibiotics	30
3.1.3	Environmental effects of pharmaceuticals	30
3.1.4	Use of pharmaceuticals in livestock	31
3.1.5	Occurrence of veterinary pharmaceuticals in rivers	32
3.1.6	Occurrence of pharmaceuticals in Mediterranean rivers	32
3.1.6.1	Studies in the Claduègne catchment: Pharma BV	33
3.1.7	Knowledge gap	35
3.1.8	Objectives of this chapter	36
3.2	Methods	36
3.2.1	Interview methodology	36

3.2.2	Water sampling & chemical analysis	39
3.3	Results	42
3.3.1	Use of veterinary pharmaceutical products in the Claduègne catchment	42
3.3.2	Stream concentrations of selected pharmaceuticals	46
3.4	Discussion	52
3.4.1	Use of veterinary pharmaceuticals in the Claduègne catchment	52
3.4.2	Applicability of the results	53
3.4.3	Pharmaceuticals in the streams of the Claduègne Catchment	53
3.4.4	Lessons from the contact with farmers	55

3.1 Scientific context: Pharmaceuticals in the Environment

The European chemicals agency currently lists 106212 existing chemical substances (ECHA, 2022), mostly based on the EINECS inventory (Geiss et al., 1992) besides some additional sources. This large number makes it difficult to estimate all their potential adverse effects on environmental organisms as well as humans.

The European Statistics Agency Eurostat regularly publishes numbers on the production and consumption of hazardous chemicals in the European Union since 2004 (Eurostat, 2021). The overall consumption of chemicals in the European Union has been relatively stable with an decrease of 4.7% in the quantity of hazardous substances from 2004 to 2020 to a total of 230.1 Mt in 2020.

The popular term emerging contaminant, or contaminant of emerging concern (CEC) describes molecules contaminating the environment that have either recently been developed / discovered or that have been used before but have only recently been found to have adverse effects for the environment (Sauvé and Desrosiers, 2014). Many of these molecules are observed in the environment, while no clearly defined toxicity thresholds do yet exist for many of them and they are not analyzed by routine water quality monitoring (Baken et al., 2018).

The groups of chemicals today considered as CEC include persistent organic pollutants, personal care products, human and veterinary pharmaceutical products (PP), endocrine-disrupting chemicals as well as some nanomaterials (Ankley et al., 2008). Many of them are only partially removed from waste water by waste water treatment plants (WWTP) (Kim et al., 2018).

Contaminants are called micropollutants if they are harmful at very low concentrations (ng L^{-1} to $\mu\text{g L}^{-1}$) that can be at or even below the limits of detection of modern analytical methods. This results in difficulties for their detection as well as the understanding of their fate in natural environments. Furthermore, today's WWTP are designed to treat classical macropollutions like nutrients but perform poorly in the removal of emerging and micropollutants (Verlicchi et al., 2010). However, additional

treatment steps are currently implemented in WWTP in several countries aiming to remove micropollutants (Eggen et al., 2014). A large number of PP belong to this group, once emitted into the environment. This PhD-thesis focuses on certain veterinary pharmaceuticals that can be considered micropollutants.

3.1.1 Sources of pharmaceutical products in the environment

Some pharmaceutically active compounds (PhAC), occur in soils naturally. This is the case for many antibiotics (Gothwal and Shashidhar, 2015), as well as avermectines (substances active against a wide range of parasites; Ōmura and Crump (2004)) among others. The majority of PP in the environment however is emitted by human activity. Aus der Beek et al. (2016) did a global review of over 1000 original publications on PP in the environment. They conclude that the occurrence of PP in environmental waters is a subject of global concern, though the density of studies is much higher in developed countries. PP can origin from different sources and enter the environment by different ways. Globally, aus der Beek et al. (2016) identify urban wastewater discharge as the dominant source of PP in the environment. After human use, a portion of the PhAC is excreted into wastewater. Even in developed countries with modern wastewater treatment systems, many PhAC are only partially removed from wastewater. High concentration in wastewater or poor removal efficiency of WWTP can therefore lead to significant amounts getting discharged into the streams and rivers (Kim et al., 2018). Other, locally important sources include manufacturing, hospitals, animal husbandry and aquaculture. While urban wastewater, hospitals and manufacturing represent rather point sources, animal husbandry is often a diffuse source. Treated livestock may excrete the residues of PhAC directly onto the pastures when grazing or they may be applied to crop fields with manure application. Therefore their fate depends on a complex mix of factors including the PhAC's properties (degradability, sorption behavior), properties of the environment (soil properties, temperature and irradiation) as well as hydrometeorological conditions (Kümmerer, 2008).

3.1.2 Types of pharmaceuticals

PP can be classified after their therapeutic category, their pharmacologic class or other properties. The US food and drug administration lists 50 therapeutic categories (FDA, 2018). The world health organization classifies human drugs after the Anatomical Therapeutic Chemical (ATC) classification system into 14 anatomical categories, each of which is sub-classified into therapeutic and then chemical categories (WHO, 2021). Instead of listing all categories, some of the most environmentally relevant therapeutic categories are presented here. Several types of drugs are relevant in human and veterinary medicine: Antimicrobials are drugs against pathogenic microorganisms and include antibiotics, which are used to treat bacterial infections. They include a large variety of different molecules and are heavily used in human and veterinary medicine across the world. Analgetics and anti-inflammatory drugs are used to treat pain and inflammations. Antiparasitics are used to treat parasitic infections. Hormones can be used in livestock to time their birth or in humans, e.g. for contraception. Other common applications of drugs, mainly in human medicine include the cardiovascular system, nervous system, immune system, alimentary tract among others.

3.1.2.1 Focus on antibiotics

A large part of the studies on the fate and effects of PP in the environment focus on antibiotics. This is because they play a crucial role in modern human medicine and their efficiency is threatened by their widespread presence in the environment. Therefore, their role and the effects of their environmental presence are summarized in this section. Antibiotics are drugs that act against pathogenic bacteria. They are very important in human and veterinary medicine, being the only treatment for a large number of diseases, some of which are deadly. *E. Coli* is considered the globally most important pathogen (World Health Organization, 2011). Especially in poor regions, bacterial infections are the most important causes of death. Lower respiratory infections and diarrheal diseases were amongst the top three causes of death worldwide in 2000 and still are in Africa in 2016 (World Health Organization, 2018). The decrease of the importance of bacterial infections is to a large part due to the development and increased access to antibiotics. The global consumption of antibiotics increased by 65 % between 2000 and 2015 (Klein et al., 2018). This increase was small in high-income countries (4 %) and the global increase was driven by low-income countries, narrowing the gap between them.

Bacterial resistance The beneficial effects of antibiotics are threatened by the development of resistances in pathogenic bacteria. Nowadays, antibiotic-resistant bacteria are found in surface and ground waters all over the planet. These resistances can be either natural or acquired (Davies and Davies, 2010; van Hoek et al., 2011). Natural resistances are intrinsic to a species, while acquired resistances are due to a modification of the bacteria's genome. These acquired resistances start to be a serious problem for human medicine, as they reduce the means of treating the corresponding diseases. Several authors talk of an antibiotic resistance crisis (Ventola, 2015; Roca et al., 2015; Spellberg et al., 2008). Acquired resistances can either be obtained by genetic mutation and selective pressure due to the presence of antibiotics in the environment, or by transfer of genetic material between the bacteria. The risk of the spreading of genetic mutations is favored by environmental presence of antibiotics even at low concentrations which can be ng L^{-1} or ng kg^{-1} , which is far below the minimal inhibitory concentration (MIC) that would have a direct acute toxicity (Grenni et al., 2018).

3.1.3 Environmental effects of pharmaceuticals

The adverse effects of presence of antibiotics in environmental systems are not limited to human health. Besides the longterm-effect of development of resistances, antibiotics can also have direct, short-term effects on (beneficial) environmental bacteria (Grenni et al., 2018). The direct effects concern the antibiotic's bacteriostatic and bactericide actions that can harm the microbial communities and thus impact their ecological functioning. Microbial activity is crucial to the functioning of soil ecosystems, as most processes in soil are driven by microorganisms. Most processes in the biogeochemical cycles are performed by bacteria (Hayat et al., 2010). Antibiotics are designed to kill or inhibit bacteria. Thus, antibiotic concentrations above the MIC can affect natural microbial communities, which can have a negative impact on the microbe-driven soil processes. Grenni et al. (2018) (table 3) synthesize various studies on the effects of different antibiotics on the microbial communities in soil and water ecosystems. The observed effects include impacts on nitrogen transformation, methanogenesis, sulfate reduction, nutrient cycling and organic matter degradation (Roose-Amsaleg

and Laverman, 2016). An effect on bacterial DNA has been observed above a concentration of $5.2 \mu\text{g L}^{-1}$ for ciprofloxacin for example (Hartmann et al., 1999). Yan et al. (2011) however did not find any significant impact of three tested antibiotics in environmental concentrations (100 ng L^{-1} and 1000 ng L^{-1}) on the denitrification in soils.

Antiparasitic drugs are made to be effective against invertebrates. Therefore, many of them also have a direct toxic effect on environmental invertebrates, often at very low concentrations (Lumaret et al., 2007; Halley et al., 1989a). The environmental fate and effects of Ivermectin (IVM), a widely used antiparasitic PhAC are elaborated in detail in Chapter 4. Drugs of different categories can have a large variety of impacts in the environment. Residues from veterinary use of the common human and veterinary anti-inflammatory drug Diclofenac have been shown to be the cause of a strong decline of vulture populations in different parts of the world (Prakash et al., 2003; Oaks et al., 2004; Naidoo et al., 2009). Presence of Ethinylestradiol, a synthetic estrogen used for contraception in treated wastewater has been shown to impede fish reproduction (Nash et al., 2004; Purdom et al., 1994). These are two prominent examples of direct adverse effects of a single molecule in environmental concentrations. In the environment, residues of PhAC usually occur as mixtures of a large number of different molecules at variable concentrations. The toxic effects of these different PhAC can add, causing stronger effects than would be expected from individual concentrations (Cleuvers, 2004; Li and Lin, 2015).

3.1.4 Use of pharmaceuticals in livestock

Besides human medicine, drugs are used in food producing animals. These can be ingested by humans through residues in the food products (Dasenaki and Thomaidis, 2015; Pugajeva et al., 2019) or excreted into the environment (Laffont et al., 2001; Kumar et al., 2005). In the beginning of the 1990's, large amounts of antibiotics were used as growth promoters, which is forbidden in many parts of the world nowadays (Dibner and Richards, 2005). Otherwise, antibiotics can be used to treat animals with bacterial infections (curative) or to treat the whole herd to prevent infections (preventive). The use of antimicrobials in food animals is still increasing in some parts of the world (Van Boeckel et al., 2015). China's livestock industry alone was estimated to account for 30% of the worldwide antimicrobial consumption by 2030 (Obimakinde et al., 2017). The use of antibiotics in animal husbandry in the EU has started to decline end of the 20th century (Kummerer, 2003) and continued to decline thereafter (Tiseo et al., 2020). This decline is owed to legal restrictions. Due to their importance in human medicine, the use of antibiotics in food animals has been progressively restricted in many regions of the world (Maron et al., 2013). In France, the Décret no2016-317 (16.03.2016) banned the use of antibiotics in a preventive manner and restricted the use of a number of molecules.

Besides antimicrobial medication, antiparasitic and anti-inflammatory drugs as well as hormones are used in livestock breeding. They will not be detailed much further here, but in all of these categories there are molecules that are excreted into the environment and may have adverse effects. Antiparasitic PP are used to treat and prevent parasite infestations in livestock. As they are made to kill parasites, they are often also toxic to non-target organisms, particularly invertebrates as discussed

before. Anti-inflammatory drugs are used to treat inflammations. Their use in livestock can be expected to be much lower than in human medicine. Hormones have been used as growth promoters in livestock in the past and are still used in order to synchronize the animals' reproductive cycles. They are molecules that the animals naturally produce, but their artificial addition can lead to increased excretion into the environment. Some of those hormones were shown to have adverse effects on wildlife (Ojogoro et al., 2021; Lange et al., 2002).

3.1.5 Occurrence of veterinary pharmaceuticals in rivers

Many studies assess the occurrence of PP in rivers with a focus on human sources, often in urbanized catchments (Lecompte et al., 2016; Moreau-Guigon et al., 2011), identifying the effluent of WWTP as the major source into the environment. Studies that specifically investigate the occurrence of veterinary PP in environmental waters exist but are less abundant. Concerning the occurrence of CEC from diffuse sources in the environment, a larger effort has been put into studies of phytosanitary products (pesticides) (Stravs et al., 2021; Spycher et al., 2018; Kaushik et al., 2008; Ccancapa et al., 2016; Rabiet et al., 2010; Konstantinou et al., 2006; Doong et al., 2002).

Residues of veterinary PP have been observed in natural waters around the globe and even in drinking water after treatment through a water purification plant (Charuaud et al., 2019a; Wei et al., 2011; Zhou et al., 2013; Obimakinde et al., 2017). Most studies however largely focus on antibiotics. Charuaud et al. (2019b) did a review of the use and occurrence of veterinary pharmaceutical residues in environmental and tap water. They considered 38 studies that analyzed 64 different veterinary PhAC. Within those 64 veterinary PhAC, there were only 9 antiparasitic PhAC that have been analyzed in between 11 and 27 samples. In contrast, they identified 52 antibiotics that have been searched in up to 1219 samples. They found 35 veterinary PhAC that had been looked for in the environment in more than 100 samples in these studies (up to 1219), 30 of which (86 %) were antibiotics and none antiparasitic. This indicates a lack of studies looking for antiparasitic PhAC in environmental waters.

Charuaud et al. (2019a) quantified 17 out of 38 searched veterinary PhAC in surface, ground or tap water from sites with intensive livestock breeding in Brittany in northern France. They found the highest concentrations for the antibiotics Sulfadiazine, Florfenicol, Trimethoprim and Oxytetracycline. They also found some antiparasitic drugs at concentrations above their limit of quantification (LQ) of 0.5 ng L^{-1} (Eprinomectin, Ivermectin, Triclabendazole, Levamisole).

3.1.6 Occurrence of pharmaceuticals in Mediterranean rivers

Studies on the fate of PhAC in catchments and rivers under Mediterranean climate are less abundant and no studies focusing on the transfer of veterinary PhAC from their diffuse sources into streams and rivers could be identified. Some studies investigated the occurrence of pharmaceuticals in Mediterranean catchments, characterized by a dynamic hydro-meteorology. Mandaric et al. (2019) analyzed 62 PhAC in a Greek temporary river with a 2418 km^2 catchment under Mediterranean climate that has a natural upstream part and a city and agriculture in the downstream part. They concluded that the main source was a WWTP and dilution from variable flow governed the concentration (meaning

lower concentration in times of higher discharge). Furthermore, they compared the attenuation (reduction of the amount) of PhAC in a segment of the stream in different seasons by comparing input to output. They found mostly increased attenuation at lower flow due to increased transit time. Palma et al. (2020) analyzed 27 PhAC in four Portuguese streams on 12 dates during two years. They also found the highest concentrations during the driest period. Osorio et al. (2014) analyzed 73 PhAC in a Spanish Mediterranean river with a 4957 km² catchment. Again, they generally observed decreased concentrations at higher flow, however the inverse is the case for some molecules, including the two veterinary PhAC they analyzed.

3.1.6.1 Studies in the Claduègne catchment: Pharma BV

Pharma BV (Martins et al., 2019) was a project from 2017 to 2018, funded by the Bassin du Rhône Water Agency in collaboration between the following research institutions: IGE (Grenoble), INRAe (Lyon) and CERMOSEM, a rural branch of PACTE (Grenoble) located within the Claduègne catchment. This project included some first interviews with farmers and veterinarians (Duplus, 2017) as well as some analyses of PhAC in water samples from streams in the Claduègne catchment at variable frequency (high frequency during some flood events at the Claduègne and Gazel outlet). Duplus (2017) investigated the use of PP in the Claduègne catchment. They identified a large number of PhAC and categorized them by their usage by cattle breeders and in the medical institutions (hospital, retirement home). Unfortunately, none of the molecules included in the analytical method used on the water samples during Pharma BV was found to be actually used in livestock breeding inside the catchment. This project illustrated some of the essential difficulties in making the link between the sources of PP in the environment and concentrations found in different environmental compartments. The large diversity of PhAC in use makes it necessary to continuously adapt existing analytical methods. The analytical method applied in Pharma BV included a number of human drugs as well as some pesticides. Accordingly, little was found in samples taken in the upstream parts of the catchment, where no towns are present and the main land use is beef and sheep breeding. Different molecules could be detected at mostly low concentrations in the lower parts of the catchment. The main source of the analyzed molecules was identified to be the town of Villeneuve-de-Berg through its WWTP. I participated in the sampling and interpretation of the results during the first year of my graduate studies, however due to the analytical limitations, I will not describe the method of this project in more detail. Only a summary of the results will be presented in this section.

The measured concentrations are highly variable in time, in particular during high-flow periods. Different patterns of concentration-discharge relationships could be observed during flood events. Part of the molecules have a tendency of decreasing concentration during flood events, indicating dilution. This can easily be explained by a more or less constant source of these molecules (e.g. in human wastewater) that is diluted by the additional rainwater. This corresponds to the results obtained by Mandaric et al. (2019) and Palma et al. (2020), presented above. Other molecules show a strong increase in concentration during flood events or are only present in detectable concentrations during these periods. This indicates a different mechanism: these molecules are most likely present in environmental reservoirs that are hydrologically connected to streams only during flood events. An

example would be pesticides applied to the soil surface and washed out by rapid preferential or over-land flow. For molecules with a good removal efficiency in waste water treatment, such an increase could also take place during activation of an overflow in a WWTP, bypassing part of the treatment. Figure 3.1 shows examples of these two patterns. The molecules showing strongly increased con-

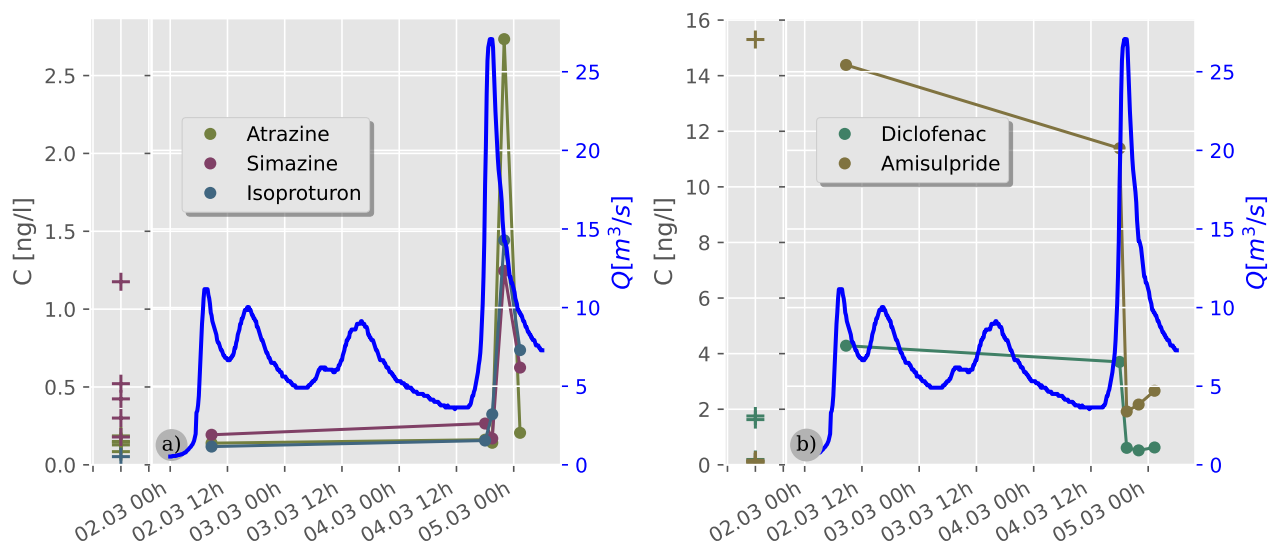


FIGURE 3.1: Evolution of the concentration of three pesticides (a) and two human PhAC (b) at the Claduègne outlet over a flood event in March 2018. Each "+" in the left part of each figure represents a concentration value >LQ detected outside of major flood events.

centrations during or at the end of flood events include the pesticides Isoproturon, which is used in cereals and lavender, as well as Simazine, the use of which was forbidden in France in 2003, Atrazine, the use of which was forbidden in the European Union in 2005 (Fig. 3.1 a)). This may indicate their mobilization from recent and old sources in and on the soil during wet conditions, in places where they are not mobile during dry conditions, assuming these molecules are not used illegally 15 years after their ban. Their concentration remains very low (a few ng L^{-1}) in most samples, but values of Simazine concentration of up to 500 ng L^{-1} have been observed in the Gazel (not shown). Half-lives of Atrazine and Simazine vary from a few days to weeks in aerobic top-soil (Shaner and Henry, 2007; Walker and Thompson, 1977; Comber, 1999) to several years in anaerobic sub-soil (Accinelli et al., 2001; Comber, 1999). These are good examples of molecules that were initially thought to rapidly disappear but finally persist in the environment over longer periods of time. This is in accordance with Riedo et al. (2021) who found residues of Atrazine and other pesticides in organic agricultural soils as a remainder of their previous conventional use.

Most of the analyzed pharmaceuticals appeared at much higher concentrations at the outlet of the Claduègne catchment than at the outlet of the Gazel catchment and other upstream parts of the streams. This can be explained by the fact that the Claduègne receives the treated wastewater from the small town of Villeneuve-de-Berg. Most of the molecules show a dilution tendency during flood events in the Claduègne river (see the two examples in Fig. 3.1 b)), but slight increases in concentration of some of these molecules can be observed during flood events at the Gazel outlet. While no

in-depth investigations were performed, one hypothesis to explain this increase during flood events was bypassing of the non-collective wastewater treatment systems of Mirabel via an overflow mechanism during flood events. Examples of this contrasting trend between the Gazel and Claduègne streams are Amisulpride, a schizophrenia treatment, Metformin, a treatment for diabetes, Oxazepam, an anxiety and sleep disorder treatment as well as Propranolol, a beta blocker. An increasing trend during flood events in both catchments, with higher concentrations in the Gazel subcatchment was found for Paracetamol, a pain killer for humans that is authorized to be used for pork as well. There is a pork breeder in the Gazel subcatchment, who however refused to give information on treatment practices, and other pork breeders in the region did not use Paracetamol.

3.1.7 Knowledge gap

As we can see, a lot of research has been done on the development of antibiotic resistances and the conditions that favor this development. The presence of antibiotic resistances can be reduced by restriction of the use of antibiotics, as happened recently in France for example. However, the scientific community cannot claim to fully understand the fate of the large number of PP with very variable properties in natural environments, as those systems are very complex with a high spatial heterogeneity and high temporal dynamic. This is particularly true when talking about diffuse agricultural sources and the hydrodynamic of catchments under Mediterranean conditions.

The sorption coefficients of PhAC in soils can be highly variable for the same molecule in different soils as well as between different molecules. This variability is controlled by the molecule's hydrophobicity and the soil's organic carbon content, as well as other factors such as the soil's clay content and pH for some molecules (Kümmerer, 2008). These soil properties are heterogeneous on a large range of spatial scales. This complexity makes it very difficult to understand and predict environmental transfer and therefore understand the risks associated with the use of these molecules. Further knowledge gaps mentioned by Kümmerer (2008) concern, among others, information on the amounts of veterinary medicines used, the development of analytical methods to measure them in the environment, understanding of the environmental release routes and the transfer of PhAC through food chains. While these points have experienced development since then, they are still actively researched subjects.

Different national and international organizations monitor the consumption of PP on global and national scale. However, if we want to understand the fate of those molecules in different environmental systems, processes on much smaller scales are of crucial importance. If we want to understand the transfer dynamics on the scale of a catchment, a first important step is to identify the used molecules, quantify the used amounts and understand the temporal dynamics of their application. This chapter aims to provide an insight on these aspects in the Claduègne catchment.

The results of Pharma BV gave some first insights in possible dynamics of contaminant concentrations in the Claduegne and Gazel streams. The investigated PhAC were found mainly downstream of the WWTP. This raised the question which PhAC were used in livestock breeding, the dominant land use in the upstream parts of the catchment. The first interviews by Duplus (2017) led us to talk

to more farmers for each species of animal inside the catchment in order to identify all molecules that are used in a systematic manner and estimate the amounts used.

3.1.8 Objectives of this chapter

In this chapter we try and respond to the first question of this PhD. The aim was to identify all PhAC that are used in livestock breeding in the Claduègne catchment in a systematic manner, i.e. regular (at least annual) treatment of a significant portion of the herd (at least 30 %). For this purpose, we decided to conduct interviews with local farmers. Furthermore, for these molecules, we aimed to determine the treatment periods, applied doses and localization of the animals. In addition, grab samples of stream water were taken in order to quantify the range and evolution of stream concentrations of these molecules under variable hydrological conditions. The aim was to evaluate the effect of flood events on the stream water concentration of these molecules.

The interviews were accompanied by the installation of polar organic compound integrative samplers (POCIS) in six places throughout the catchment over two weeks during four hydro-meteorologically contrasted periods. The POCIS were designated for screening analysis, aiming to identify the molecules that could be found in surface water downstream of different land uses in different times of the year.

In addition to the identification of the contaminants originating from livestock breeding in the Claduègne catchment, the interviews served to choose a model molecule of high use in the context of our study site and with chemical properties similar to other used molecules. This molecule, IVM was then used for smaller scale transfer studies in the following (see Chapter 4).

3.2 Methods

This section presents the interview methodology as well as the procedure of sample collection, preparation and analysis.

3.2.1 Interview methodology

The platform of territorial development *CERMOSEM*, a rural branch of the PACTE (Grenoble) is located within the Claduègne catchment. Colleagues on site provided us with contact informations of local livestock breeders and we asked each interviewed farmer to provide us with additional contacts. This way, in total 33 livestock breeders of different species located within the study site could be identified and have been contacted from autumn 2018 to summer 2019. 13 of them agreed on participating in semi-structured interviews. We interviewed 7 beef, 2 pork, 1 goat, 1 sheep and 2 chicken breeders on their practices. This is at least one breeder of each farm animal species present inside the catchment. The total number of farmers per species with activity inside the catchment is unknown. In addition, we obtained three complete treatment calendars (1 goat and 2 beef breeders). The fields belonging to these farmers are depicted in Fig. 3.2. We followed a guideline prepared in advance without limiting neither time nor subject of the interviews to a strict question-response scheme. Our questions aimed to identify the drugs used systematically within the catchment (at least 30 % of the herd once a year). We were interested to know the treatment periods and frequencies as well

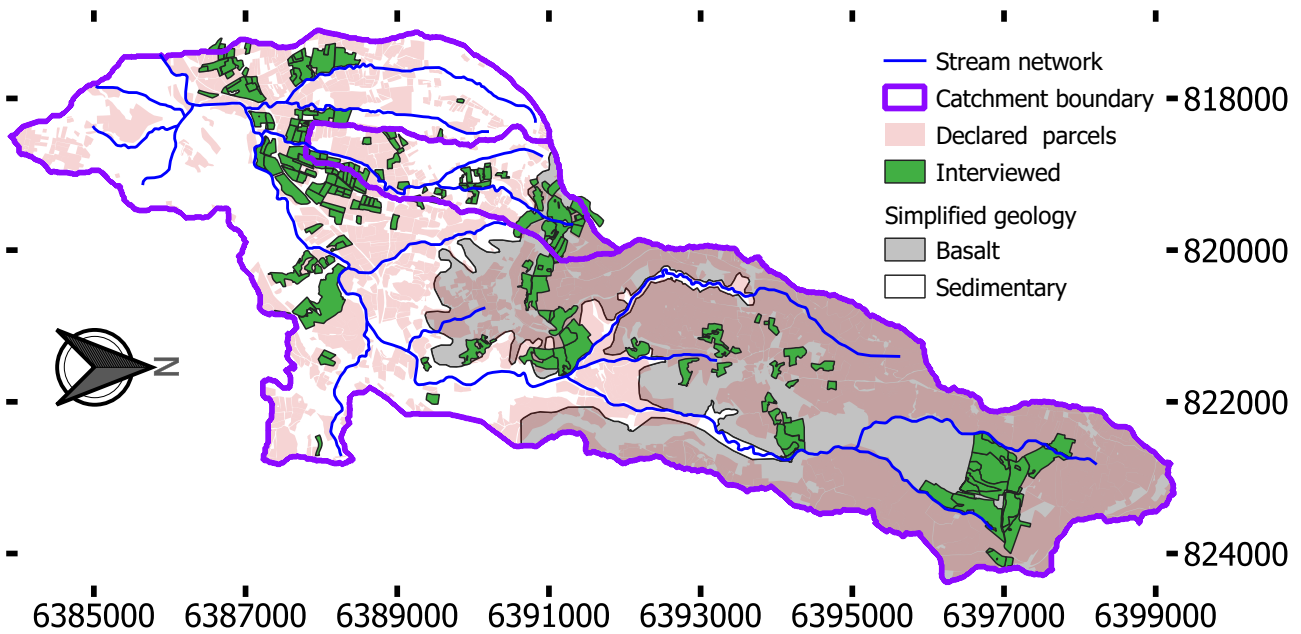


FIGURE 3.2: Map of agriculturally used surfaces from RPG (IGN, 2021) highlighting those, the managers of which were interviewed. Coordinates are in Lambert 93 [m].

as applied doses. We also asked about the localization of each farmer's parcels and other relevant practices (grazing periods, dung application, interchanging of molecules between the years, other agricultural practices). Finally, the interviews were also used to obtain contact details of additional farmers in the area. The interview guideline is provided in the appendix (Fig. A.1).

Some effort was made in order to try and transform the farmers' responses during the interview into quantitative information, however the resulting quantities of PhAC have a high uncertainty. For each drug that occurred in the treatment calendars or was mentioned in the interview, the PhAC and their concentrations in the drug as well as typical doses and the number of administrations (for drugs requiring multiple administrations for one treatment) were obtained from the official register of authorized veterinary drugs in France (Agence nationale du médicament vétérinaire (ANMV), 2015). This yielded a list of 62 drugs used in the catchment, containing 89 PhAC and their respective dosesⁱ. These data were synthesized to obtain a representative dose d_{rep} as mass of PhAC per treatment (of one animal) in $\frac{\text{mg}}{\text{treatment}}$. Where the dose was given per kg of body weight of the treated animal, it was multiplied with the estimated weight at time of treatment of this species in the treated age, obtained from European Medicines Agency (2019). For PhAC administered to one species via different drugs, if there was one dominant formulation, this formulation's dose was retained as representative dose. In cases where different formulations were commonly used, an average dose was approximated. As an example, for IVM, topical application (pour-on, po) preparations with a higher dose of $500 \frac{\text{mg}}{\text{treatment}}$ were only used for heifers, whereas the majority of the herd was treated with subcutaneous (sc) injection of $200 \frac{\text{mg}}{\text{treatment}}$, which is why the sc-dose was used as d_{rep} . Due to the different formulations in use with different doses, d_{rep} should be interpreted as an order of magnitude and not as a totally representative precise quantitative information.

ⁱ this table can be found here: <https://cloud.univ-grenoble-alpes.fr/index.php/s/GG2wiA49xd28g6d>

Then for each PhAC, a factor f_{treat} was calculated from the interviews representing the treated fraction of all individuals of a certain species within the Claduègne catchment times the number of treatments per year. It is estimated as

$$f_{\text{treat}} = f_{\text{herd}} \cdot n_{\text{treat}} \quad (3.1)$$

, where f_{herd} is the fraction of the herd treated with one treatment, n_{treat} is the number of treatments per year. The unit of f_{treat} is $\frac{\text{doses}}{\text{animal} \cdot \text{year}}$. Practically, due to the semi-quantitative character of the information retrieved from the interviews, f_{treat} was estimated instead of being calculated mathematically. To give a practical example: All beef breeders applied one curative anti-parasitic treatment per year, except one who only used curative treatment but only has a few individuals under particular circumstances and is not considered representative. Of the remaining six, the two smaller farms use Deltamethrin, one larger farm changes between drugs containing IVM and Deltamethrin between the years and the remaining three, rather large farms mainly use IVM. IVM preparations containing Chlorsulon were named a little more often than IVM mono-preparations. This led us to assign the values 0.7, 0.5 and 0.3 respectively for f_{treat} of the molecules IVM, Chlorsulon and Deltamethrin. Again, due to the small sample size (1 - 7 farmers per species) and the semi-quantitative character of the interviews, f_{treat} should be considered as an order of magnitude rather than a precise factor. For each molecule used in a systematic manner, a classification as *preventive* or *large-scale curative* was assigned according to the practices identified by the farmers.

The farmers mostly gave semi-quantitative information like "I treat all the cows once per year, either with drug A or with drug B, sometimes in spring, sometimes in autumn". In addition, three farmers provided complete calendars of all treatments over the last years. We compared these three treatment calendars to the information given orally as a verification of the latter. Furthermore, the extensive treatment calendar of the goat farm was translated into a time series of mass of PhAC use for the period from 2015 to 2018.

Josse (2021) did a new series of interviews with a total of 28 farmers in the Claduègne catchment who are exploiting 40% of the declared agricultural surface of the Claduègne catchment. For estimates of the total number of animals per species inside the catchment, their numbers are used as they interviewed more farmers. For all species except chicken, the information obtained from the farmers was the number of mothers, because this is the most stable number throughout the year. These numbers were multiplied with a factor two to obtain the total number of animals given in the results section, which includes young animals and males. In order to obtain an estimation of the total number of animals in the catchment n_{animals} we divided this number by 0.4 to account for the 60% of the agricultural surface in the Claduègne catchment managed by farmers that have not been interviewed. This was not done for goats, because we know that there are no other goat breeders in the catchment. The annually used mass of PhAC m_{used} inside the Claduègne catchment was then estimated (as an order of magnitude) as

$$m_{\text{used}} = n_{\text{animals}} \cdot f_{\text{treat}} \cdot d_{\text{rep}} \quad (3.2)$$

Due to the very variable toxicity of the different molecules, the mass itself is not a good estimate of the polluting potential of a PhAC. In order to obtain a comparable estimate of the toxic potential of the

used amount of PhAC, m_{used} was divided by the predicted no effect concentration (PNEC).

$$V_{pol} = \frac{m_{used}}{PNEC} \quad (3.3)$$

This gives a volume of water V_{pol} which if we dissolved all the annually used PhAC in it, would be at the PNEC. In other words, it is the maximum amount of water that could theoretically be polluted by the mass of PhAC used annually. This number (V_{pol}) can not be interpreted with regards to environmental effects of the PhAC, because it does not take into account metabolism in the animal, environmental transfer, degradation, adsorption or temporal dynamics and spatial distribution of the sources. It is no more than a toxicity-weighted quantification of annual application.

3.2.2 Water sampling & chemical analysis

POCIS had been placed in different locations throughout the Claduègne catchment over four hydrologically contrasted periods for a duration of two weeks each time. They were installed at the Claduegne outlet (CLA) and the locations shown in Fig. 3.3 that focus on the Gazel sub-catchment. An overview of all sampling points is given in Table 3.1. This focus on parts within the Gazel sub-

TABLE 3.1: Overview of locations where polar organic compound integrative samplers (POCIS) were installed.

Name	dominant land use	surface km ²	mean alt. masl	min alt. masl	max alt. masl	contains
CLA	mixed	42	478	205	838	all
GAZ	mixed	3.4	408	242	685	MI1-MI5
MI1	beef	0.23	613	550	685	-
MI2	beef, urban, vine	0.69	433	335	602	-
MI3	pork, beef, urban, vine	2.2	463	304	685	MI1, MI2, MI5
MI4	vine	0.19	290	252	330	-
MI5	pork, beef	1.1	516	350	685	MI1

catchment provides points with small drained areas with more homogeneous land use that remain representative of the different types of land use in the Claduègne catchment. This helps to distinguish different sources of PhAC. The land uses of the different drained areas are as follows: MI1 is purely beef cattle, MI5 additionally includes pork, MI2 includes part of Mirabel village including the phyto-WWTP that treats waste water from the old village center and some vineyards, MI3 contains MI2 and MI5 and the Gazel encompasses in addition some goats. MI4 is dominated by vineyards. The distribution of animal species in Fig. 3.3 is shown to explain the choice of sampling locations. Being a result of this chapter it will be presented in more detail for the whole Claduègne catchment in subsection 3.3.1 and Fig. 3.4.

Grab samples of stream water of approximately 300 mL had been taken manually in the same locations. In addition, some water samples were taken at higher frequencies during two flood events by Teledyne ISCO 3700 automated samplers at the Gazel and Claduègne outlet. These samples served to quantify the concentration ranges and dynamics of different PhAC in the streams. All water samples were taken using glass bottles washed with a professional washing machine (*Miele professional*

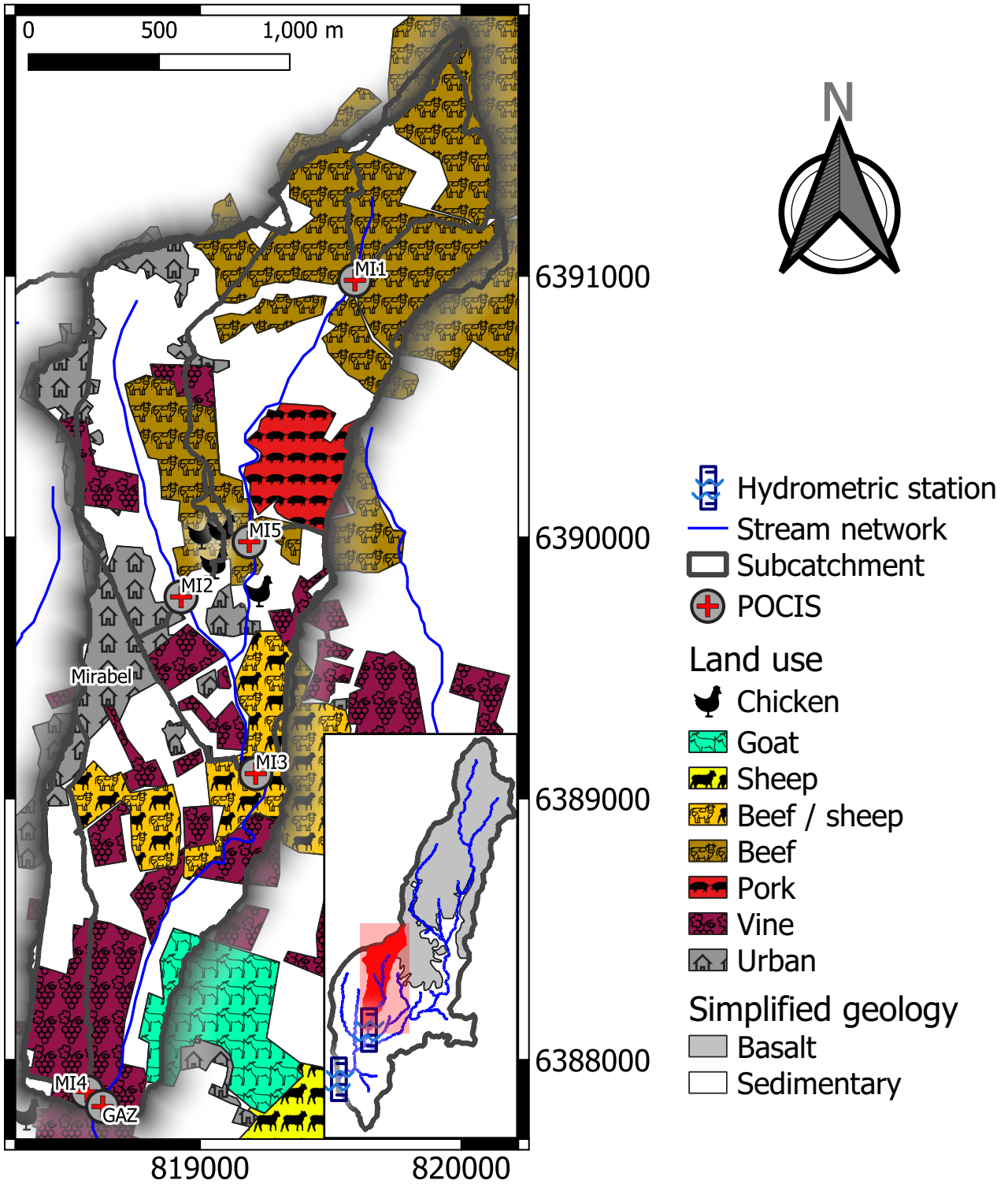


FIGURE 3.3: Locations in the Gazel subcatchment where POCIS were installed and respective subcatchments of each location with land use practices. Coordinates are in Lambert 93.

G 7883) and then heat treated at 500 °C for 3 h. The samples were filtered within 48 h max. after sampling in the stream. We used a DURAN vacuum filtering apparatus with 0.7 µm glass microfiber filters. The filtering apparatus and filters were also heat treated at 500 °C before each set of samples and rinsed with purified water between samples of the same batch (e.g. one flood event). The samples were then frozen at –20 °C until analysis.

A part of the water samples and POCIS have been analyzed for three of the most used veterinary pharmaceuticals (Fenbendazole, Ivermectin and Mebendazole), in addition to a list of different molecules of various use (see subsection 3.3.2). Before analysis, the samples were thawed slowly at 4 °C over two days. For those samples that were not completely thawed, thawing was finished by placing the bottles in a basin with running cold water. Through the process of freezing the samples, some residues had precipitated, presumably organic residues given the optical appearance, making a second filtration necessary. For the second filtration, larger filters (1.6 µm) were used. The filtered samples were concentrated using solid phase extraction (SPE) with Oasis HLB 6cc cartridges with 200 mg of sorbent. They were conditioned using 2×3 mL of methanol and 2×3 mL of water. After drying the cartridges, the samples were eluted using 2×3 mL of methanol into 15 mL polypropylene tubes. They were evaporated at 32 °C under nitrogen flux to a remaining volume of 150 µL. At a remaining volume of 1 mL they were vortexed in order to recover potential residues on the tube walls before continuing the evaporation. Then, 350 µL of water were added to a total volume of 500 µL. They were then frozen until analysis and analyzed within one week. The POCIS were opened and the sorbent was transferred into cartridges and eluted using 2×3 mL of methanol followed by 2×3 mL of acetonitrile. The following procedure was the same as for the extracted water samples.

Samples were analyzed using high performance liquid chromatography (HPLC) (Shimadzu Corp., Kyoto Japan) coupled to a tandem mass spectrometer (QTrap 5500 AB-Sciex, Concord, Ontario, Ca). The analytical method by Christine Baduel has not yet been published but will be in Caracciolo et al.. Briefly, MilliQ water and acetonitrile with 0.1 % formic acid each were used as mobile phases A and B respectively. A linear gradient ranged from 10 % B to 40 % B over 5 min, then from 40 % B to 100 % B over 5 min and then remained at 100 % B for 4 min. In the end it returned to the initial conditions in 0.1 min, followed by 3 min of equilibration. The flow rate was 0.5 mL min⁻¹, the column oven was held at 40 °C. An injection volume of 6 µL was used. The ion source parameters were optimized to the following final conditions: ion spray voltage: 4500 V; temperature: 600 °C; curtain gas: 30 L min⁻¹ and ion source gas at 60 psi. High purity nitrogen was used as nebulizer gas, curtain gas and collision gas. The mass spectrometer was operated in positive electrospray ionisation mode and used scheduled multiple reaction monitoring. Seven calibration standards were prepared at concentrations of 0.5, 1, 2.5, 5, 10, 50, and 100 ppb. Calibration was performed using a 1/*x*-weighted linear regression. Reported values are corrected for recovery of internal standards (using mass-labeled standards of 15 pharmaceuticals). Instrumental limits of detection (LD) and LQ were set respectively to three and ten times the standard deviation of the concentration of the lowest standard with a signal to noise ratio greater than 10 after eight injections. Table 3.2 lists the method detection limits, in ng mL⁻¹ of the concentrated extract as well as recalculated to ng L⁻¹ of the original samples before SPE, using the average concentration factor.

TABLE 3.2: Limits of quantification (LQ) of the analyzed pharmaceutically active compounds (PhAC) in the analyzed extract (concentrated solution after solid phase extraction and evaporation), and the average in the initial matrix (liquid water samples and POCIS).

molecule	extract ng mL ⁻¹	liquid ng L ⁻¹	POCIS ng g ⁻¹
Atenolol	0.20	0.41	0.43
Bisoprolol	0.08	0.16	0.17
Caffeine	1.50	3.07	3.24
Carbamazepine	0.50	1.02	1.08
Cetirizine	0.30	0.61	0.65
Diclofenac	0.08	0.16	0.17
Fenbendazole	0.08	0.16	0.17
Irbesartan	0.30	0.61	0.65
Iopromide	0.50	1.02	1.08
Ivermectine	1.00	2.05	2.16
Lidocaine	0.10	0.20	0.22
Metformin	0.50	1.02	1.08
Mebendazole	0.10	0.20	0.22
Nicotinamide	0.30	0.61	0.65
Sulfamethoxazole	0.30	0.61	0.65
Trimethoprim	0.20	0.41	0.43
Telmisartan	0.20	0.41	0.43

3.3 Results

3.3.1 Use of veterinary pharmaceutical products in the Claduègne catchment

One main outcome from the interviews that is coherent between the different breeders is the generally very minor application of antibiotics in the extensive farming context of the Claduègne catchment. The only species still relatively systematically treated with antibiotics is goats (large-scale curative, approximately 50 % of the herd treated per year). For all other species, the use of antibiotics remains curative on a single case consideration with usually less than 5 % of the animals treated per year. This is also the case for anti-inflammatory drugs. The other coherent outcome is that in contrast to antibiotics, antiparasite drugs are used in a systematic way for all species, in most cases with at least one preventive treatment of all individuals per year. They are used against parasitic worms, ticks and lice for example. With these interviews we were able to identify the most common systematically used molecules in the Claduègne catchment. A synthesis of the 14 molecules retained as systematically used is provided in Table 3.3. Besides the listed drugs, hormones were used in order to synchronize the reproduction cycles in some species. The way of administration was not inquired systematically and different ways existed in some cases for the same molecule. The practiced ways of administration included sc injection, oral administration and topical application. Goats are outside from March to June and from October to November and treated mainly in winter. While some farmers keep their cows outside all year round (in the lower parts of the catchment in winter), most keep them inside in winter. The exact grazing periods are variable. Often the cows are brought inside when the autumn

TABLE 3.3: List of veterinary pharmaceuticals systematically used in the catchment. Pharmaceutical classes: **AP**: antiparasitic, **AB**: antibiotic. Meaning of the comments: **P**: preventive use, **C**: (large scale) curative use, **IC**: interchanging molecules between the years, **MP_{IVM}**: contained in mixed preparations of IVM

Animal	Class	Molecule	f_{treat} treatments animal-year	d_{rep} mg treatment	Season	Comment
Beef	AP	Ivermectin	0.7	200	Mar-Apr	P, IC
	AP	Clorsulon	0.5	1300	Mar-Apr	MP _{IVM}
	AP	Deltamethrin	0.3	500	Mar-Apr	P, IC
Pork	AP	Fenbendazole	3.5	1200	Apr / whole year	P
Goat	AB	Benzylpenicillin	1	2000	Nov, Jan-Mar	C
	AB	Dihydrostreptomycin	1	2000	Nov, Jan-Mar	C
	AB	Nafcillin	0.5	100	Nov	C
	AP	Praziquantel	0.5	280	Nov	C
	AP	Oxfendazole	1	750	Dec	P
	AP	Eprinomectin	0.3	37	Spring	P
	AP	Ivermectin	0.3	20	Autumn	P
Chicken	AP	Levamisole	10	80	whole year	P
Sheep	AP	Moxidectin	0.5	15		P
	AP	Mebendazole	1.5	1125	Jun-Jul (+ Autumn)	P
	AP	Closantel	1.5	750	Jun-Jul (+ Autumn)	P

thunderstorms start. They are treated either in march just before being let outside or in autumn. Sheep are treated in summer and autumn. Most farmers keep their sheep outside all year while moving them to higher altitude on the Coiron plateau in summer. Others keep them inside during the hottest months (June - September). Chicken and pork are treated the whole year with no dominant period. For chicken this is because their life span is only 80 d. This corresponds to about ten cycles per year per building as the chicken are outside half of their lifetime in accordance to the rules of "Label Rouge", a French food quality label which most of the chicken breeders in the catchment have. The obtained treatment periods are in accordance between the interviews carried out in this PhD and by Josse (2021), even though slight differences exist with regards to the exact months. The application period of manure from the periods the animals were kept inside are variable. The period stated by the most farmers is autumn, while all seasons were named as periods of manure application by the different farmers.

The molecules' octanol-water distribution coefficients (with respective sources) and estimated PNECs from Richard (2011) are presented in Table 3.4 for the molecules for which the value was found in literature. PNECs are calculated from the experimentally determined lowest observed effect concentration (LOEC) for the most sensitive investigated organism and a safety factor. Given the high differences in sensitivity between different species, they come with a high uncertainty of multiple orders of magnitude. For the example of IVM, Richard (2011) report the lowest aquatic PNECs to be $0.000025 \text{ ng L}^{-1}$ while Liebig et al. (2010) report 0.0057 ng L^{-1} . It should also be noted that a molecule's $\log(K_{OW})$ is of limited predictive power for the molecule's sorption behavior if protonation or deprotonation occurs at environmental pH values, which is the case for Fenbendazole, Levamisole

TABLE 3.4: Hydrophobicity and aquatic predicted no effect concentration (PNEC) of the molecules systematically used in the catchment. The PNEC are obtained from Richard (2011). For the octanol water partition coefficient $\log(K_{OW})$, experimental values were preferred over calculated values, where available. Column E/C indicates experimental (E) vs. calculated (C) $\log(K_{OW})$ values.

molecule	$\log(K_{OW})$	source	E/C	PNEC water $\mu\text{g/l}$
Ivermectin	3.22	Halley et al. (1989b)	E	0.000 000 025
Clorsulon	1.09	Grabowski et al. (2010)	C	356
Deltamethrin	5.43	Mestres and Mestres (1992)	E	
Fenbendazole	3.93	Mottier et al. (2003)	E	0.000 08
Benzylpenicillin	1.83	Hansch et al. (1995)	E	
Dihydrostreptomycin	-9.05	Grabowski et al. (2010)	C	
Nafcillin	3.30	Montoya-Rodríguez et al. (2020)	C	
Praziquantel	2.42	Grabowski et al. (2010)	C	5.23
Oxfendazole	2.03	Mottier et al. (2003)	E	0.52
Eprinomectin	5.40	Krogh et al. (2008b)	E	0.000 45
Levamisole	2.87	Grabowski et al. (2010)	C	32
Moxidectin	4.77	Krogh et al. (2008b)	E	0.000 03
Mebendazole	3.73	Mottier et al. (2003)	E	0.036
Closantel	8.11	Horvat et al. (2012)	C	32

and Mebendazole. We present for each molecule the lowest aquatic PNEC that has been found in Richard (2011). This represents the maximum tolerable aquatic concentration in water bodies which should lead to no adverse effects. The PNEC varies over ten orders of magnitude from 25 fg L^{-1} (IVM) to $356 \text{ }\mu\text{g L}^{-1}$ (Clorsulon).

The estimates of the total number of animals per species are 2255 beef, 240 pork, 452 goats, 138750 chicken and 9895 sheep. The number of pork is likely to be underestimated, because the largest pork breeder did not agree on interviews. The number of chicken may be overestimated, as the owners of the majority of buildings identified on the orthophoto has responded to the interviews, so the number may have been over-corrected. Table 3.5 shows the estimated mass of PhAC used in the catchment per year for the identified molecules, as well as the volume of water V_{pol} that could potentially be polluted by this mass. V_{pol} spans 10 orders of magnitude due to the differences in PNEC, indicating that for this kind of calculation no high precision for the amount of PhAC is needed and an order of magnitude is sufficient.

Figure 3.4 shows livestock and human activity in the Claduègne catchment with regards to potential sources of PP. As basic reference for the identification of agriculturally used areas we used the registre parcellaire graphique from 2019 (IGN, 2019), which contains all surfaces that are declared for agricultural use. The map is created from information of different levels of precision: Part of it are the exact parcels that farmers pointed out to us during the interviews, either operated by themselves, or by colleagues of them. The rest are interfered from more general information given during the interviews, as well as manual identification through field observation and orthophotos. The main conclusions on the spatial extent of different agricultural practices are as follows: Beef are mostly grazing on the Coiron plateau, except for those that are kept outside in winter. Sheep are partially

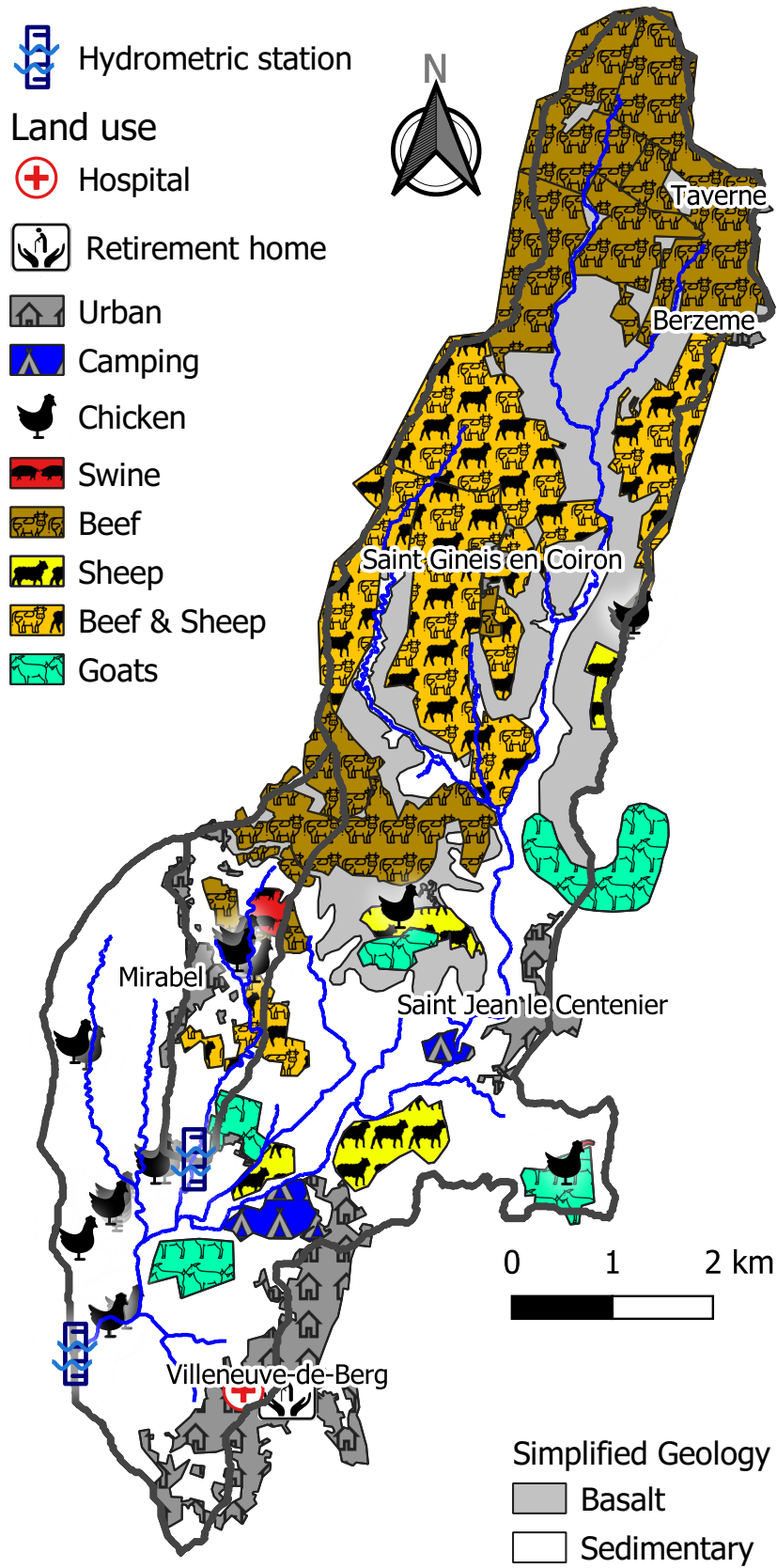


FIGURE 3.4: Livestock and human activities in the Claduègne catchment.

TABLE 3.5: Estimated annual use m_{used} of pharmaceutically active compounds (PhAC) by cattle breeders in the Claduègne catchment. This is a rough estimate and numbers are expected to be very variable between the years. V_{pol} is the volume of water that could be contaminated by the amount of PhAC used. It is no estimation of actual environmental contamination.

Molecule	m_{used} g yr ⁻¹	V_{pol} m ³
Ivermectin	348	13 923 880 000
Clorsulon	1466	4.1
Deltamethrin	338	
Fenbendazole	1008	12 600 000
Benzylpenicillin	904	
Dihydrostreptomycin	904	
Nafcillin	22.6	
Praziquantel	63.3	12.1
Oxfendazole	339	652
Eprinomectin	5.0	11 149
Levamisole	111 000	3469
Moxidectin	74.2	2 473 750
Mebendazole	16 698	463 828
Closantel	11 132	348

held in both parts of the catchment. In winter they are moved to the parcels on the Coiron plateau that are occupied by beef in summer. In general the Coiron is rural with little anthropogenic impact except the extensive beef and sheep breeding. The land use in the sedimentary part is more diverse with some goats, pork, and a large surface of vineyards, as well as two main small towns and two relatively large campgrounds. The larger campground has its own WWTP, as well as Villeneuve-de-Berg, the town in the southernmost part of the catchment. Mirabel, the town within the Gazel subcatchment has non-collective wastewater treatment systems and a small phyto-WWTP. Chicken are held in and around buildings, which is why they are marked as points rather than areas. Each building holds about 4000 chicken at a time.

3.3.2 Stream concentrations of selected pharmaceuticals

Figure 3.5 shows the detection frequencies of the analyzed PhAC in the Claduègne catchment. The three PhAC systematically used in veterinary medicine are highlighted in red and the corresponding results framed in black. IVM has not been detected in any of the samples. Fenbendazole (FBZ), the dominant antiparasitic PhAC used by pork breeders in the catchment, was detected in most of the samples from the Gazel subcatchment and in only one sample from the Claduègne catchment. Mebendazole (MBZ), the dominant sheep antiparasitic was detected in some samples from both, as well as in the two samples from the two Gazel subcatchments MI2 and MI5, but not in the MI1 subcatchment. In a large part of the samples from Claduègne and Gazel, MBZ could not be quantified due to an analytical interference with another (unidentified) molecule. Two antibiotics that are authorized in veterinary medicine (Sulfamethoxazole (SMX) and Trimethoprim (TMP)), were detected occasionally in the Gazel (7/21 and 6/21 samples respectively) and rarely in the Claduègne (1/8 and

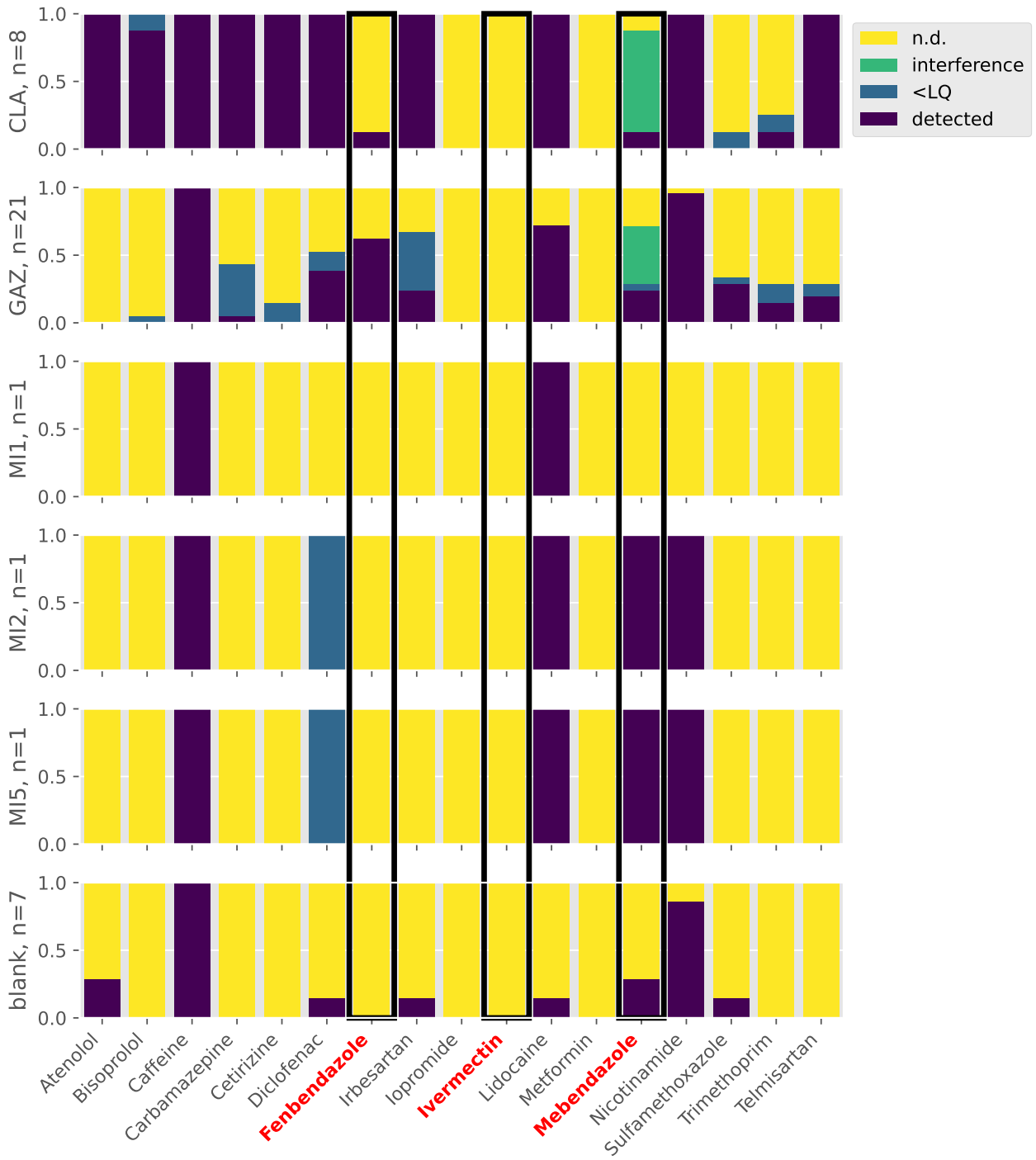


FIGURE 3.5: Detection frequencies (as a fraction of the number of samples) of selected pharmaceuticals in the stream water of the Claduègne catchment at five locations with the respective number of samples (n). The three pharmaceuticals systematically used in veterinary medicine are highlighted. Mebendazole interfered with an unidentified molecule in part of the samples.

2/8 samples respectively). During the interviews, TMP was identified as occasionally used to treat sick goats, while none of the farmers declared to use SMX. Caffeine was detected in all of the samples in all locations, Nicotinamide (used in different drugs and cosmetics) and Lidocaine (an anesthetic) were detected in most samples from most locations. Caffeine and Nicotinamide were also detected in most of the blanks at low concentrations. Most of the human drugs were uniquely or dominantly detected at the Claduègne outlet, which is downstream of the WWTP of Villeneuve-de-Berg, including wastewater from the town, a hospital and a retirement home as well as the WWTP of a large campground. The molecules include drugs for the heart and vascular system (Atenolol, Bisoprolol, Irbesartan and Telmisartan), an anti-inflammatory drug (Diclofenac), an anti-epileptic (Carbamazepine) and an antihistaminic drug (Cetirizine).

Figure 3.6 shows the evolution of the concentration of MBZ, a systematically used sheep antiparasitic PhAC at the Gazel outlet. The highest concentrations were observed during the two peaks of the autumn flood event depicted in Fig. 3.6 b). In the sample in October before the major autumn flood, no FBZ was detected.

Figure 3.7 shows the evolution of the concentration of FBZ, the systematically used pork antiparasitic PhAC at the Gazel outlet. Like MBZ, FBZ could not be detected in the October sample, but peaked in concentration during both peaks of the autumn flood at about 5 ng L^{-1} as well as the summer flood in June 2020 at a concentration reaching 28.4 ng L^{-1} in the end of the flood event. The Gazel station is downstream of the major pork farm in the catchment.

Figure 3.8 shows the evolution of the concentration of TMP at the Gazel outlet. While in most samples the concentration is below the LD, during the first discharge peak of the autumn flood event in Fig. 3.8 b) it rises to just below the LQ and during the second peak it rises to a quantifiable concentration. During the spring flood depicted in Fig. 3.8 c), no TMP could be detected. This same behavior was observed for SMX (Fig. B.1). At the Gazel, Caffeine and Nicotinamide show the same trend of highest concentrations during flood events, but were detected in more samples (Figs. B.2 and B.3).

At the outlet of the Claduègne catchment the temporal evolution of concentrations is more difficult to interpret, due to the limited number of samples that survived the freezing process (8) and their location in the flood events. All eight valid samples were close to flood peaks, so the evolution of concentration during the flood events cannot be compared to before and after. In general, the concentrations of many of the human-use drugs at the Claduègne outlet tend to be higher than the concentrations of the five veterinary molecules (three of systematic use) in both catchments. The highest concentration of all 18 molecules in all 32 samples (580 ng L^{-1}) was observed for Cetirizine at the Claduègne, while the highest concentration of a veterinary molecule was observed for FBZ at the Gazel outlet (28.4 ng L^{-1}).

Although the initially planned screening analysis of the POCIS could not be done, four POCIS were analyzed using the same method as for the liquid samples. Figure 3.9 shows the concentrations on those POCIS in four locations within the Gazel subcatchment over two weeks in June 2019 during low flow and the concentrations detected on a blank sample. The POCIS from the Gazel was not analyzed because the outlet fell dry during the period the POCIS were in place. Diclofenac, Caffeine and Nicotinamide were detected above blank values in all four sites. The concentration of Diclofenac

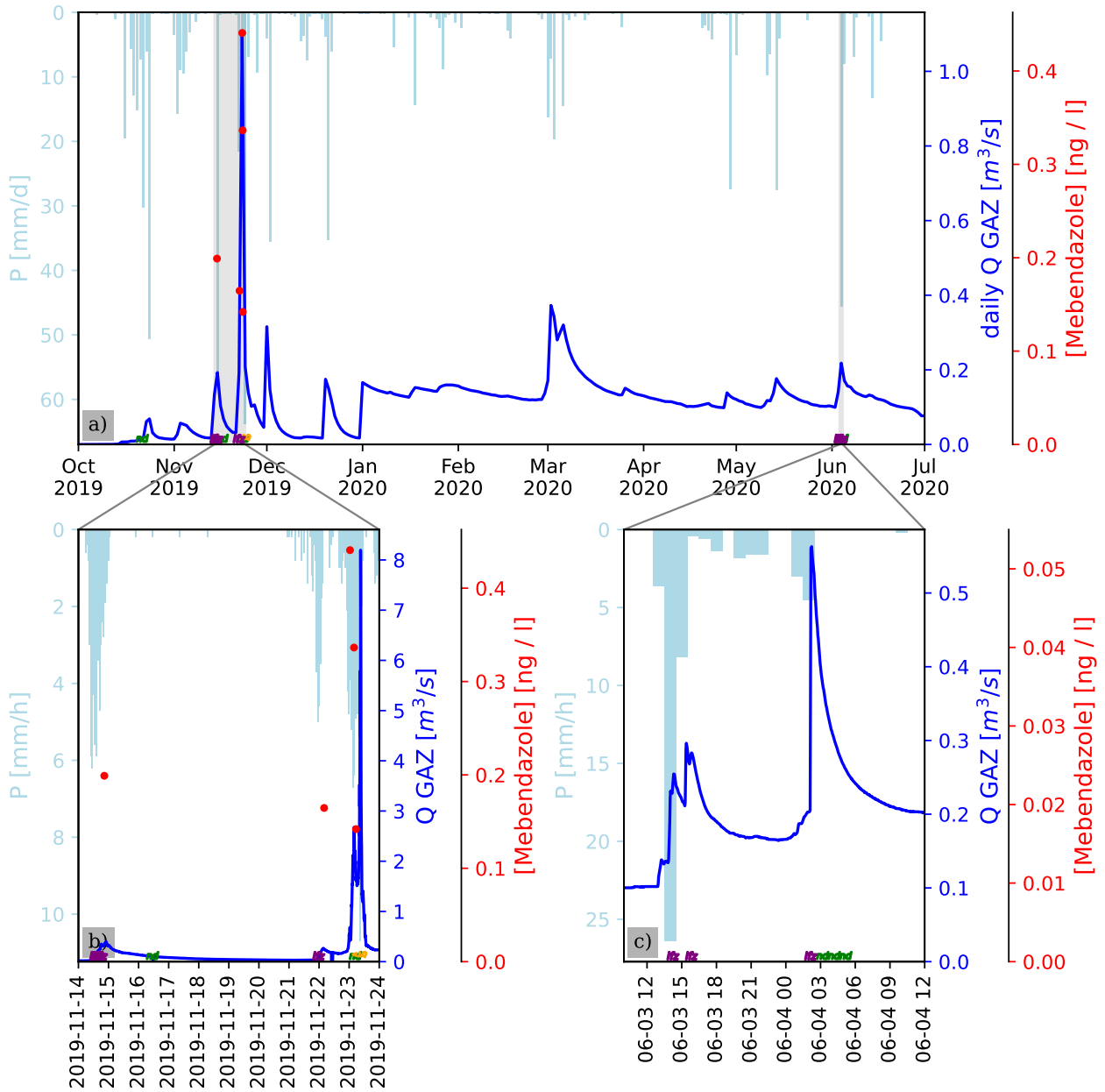


FIGURE 3.6: Temporal evolution of the concentration of Mebendazole in grab samples from the Gazel outlet together with discharge (Q) and precipitation (P). Green 'nd' symbols at the bottom indicate samples without detectable concentration. Orange '< LQ' labels at the bottom of the plot indicate detection of a concentration below the limit of quantification (LQ). Purple 'ifz' labels indicate samples for which an analytical interference made the correct quantification impossible. The discharge after 01.01.2020 has not been corrected and only serves to illustrate the rough evolution.

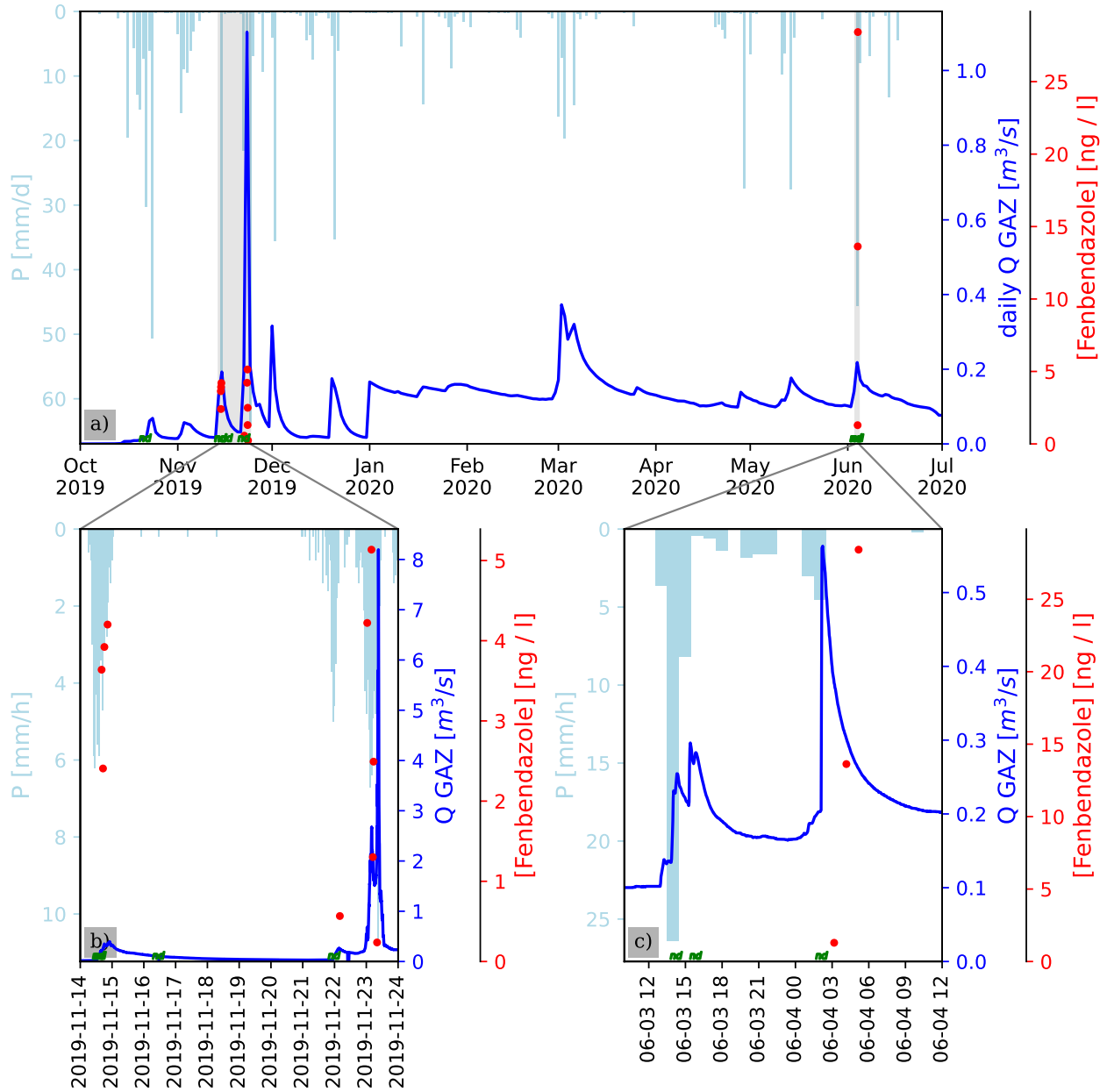


FIGURE 3.7: Temporal evolution of the concentration of Fenbendazole in grab samples from the Gazel outlet together with discharge (Q) and precipitation (P). Green 'nd' symbols at the bottom indicate samples without detectable concentration. Orange '< LQ' labels at the bottom of the plot indicate detection of a concentration below the limit of quantification (LQ). The discharge after 01.01.2020 has not been corrected and only serves to illustrate the rough evolution.

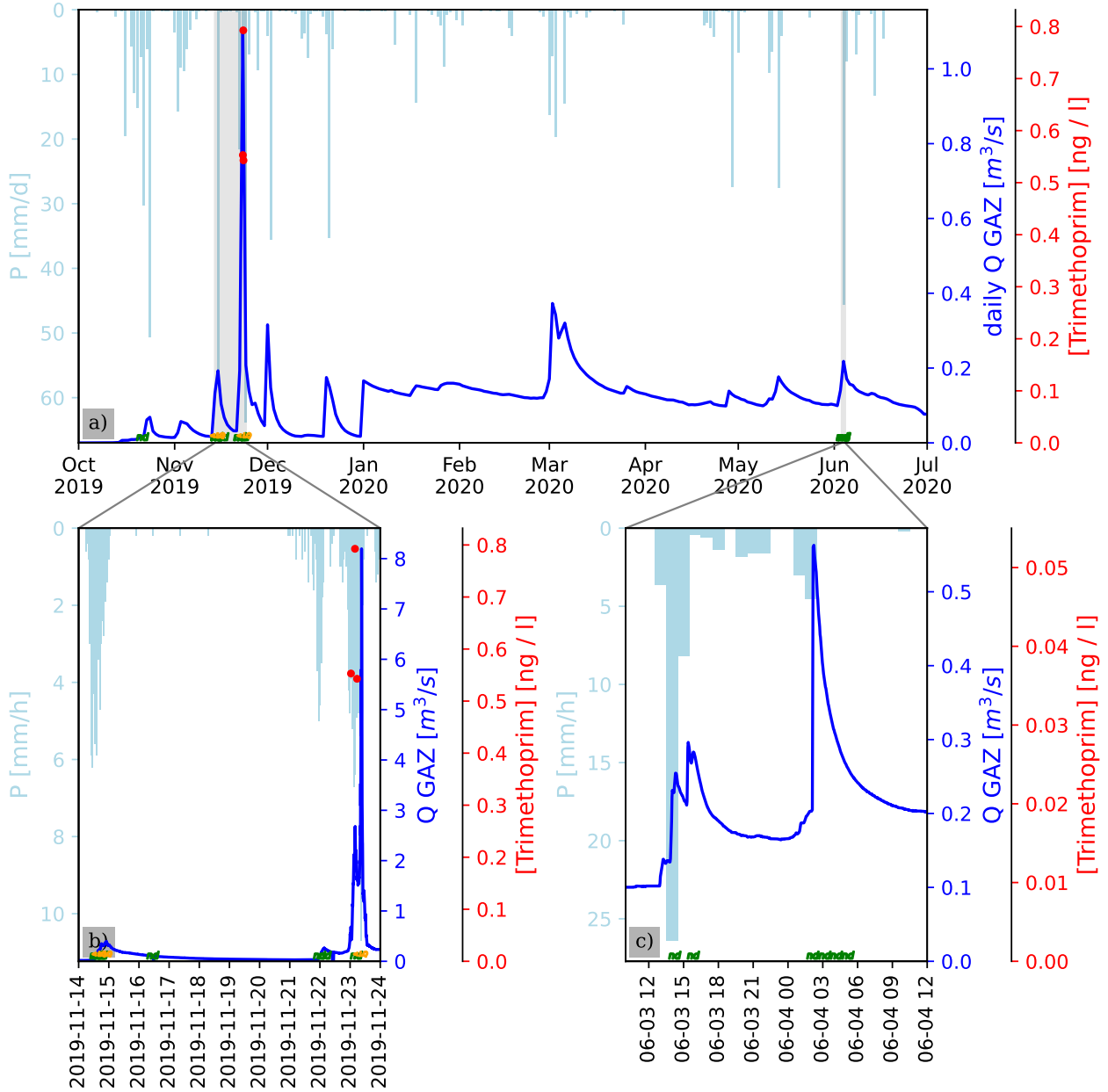


FIGURE 3.8: Temporal evolution of the concentration of Trimethoprim in grab samples from the Gazel outlet together with discharge (Q) and precipitation (P). Green 'nd' symbols at the bottom indicate samples without detectable concentration. Orange '< LQ' labels at the bottom of the plot indicate detection of a concentration below the limit of quantification (LQ). The discharge after 01.01.2020 has not been corrected and only serves to illustrate the rough evolution.

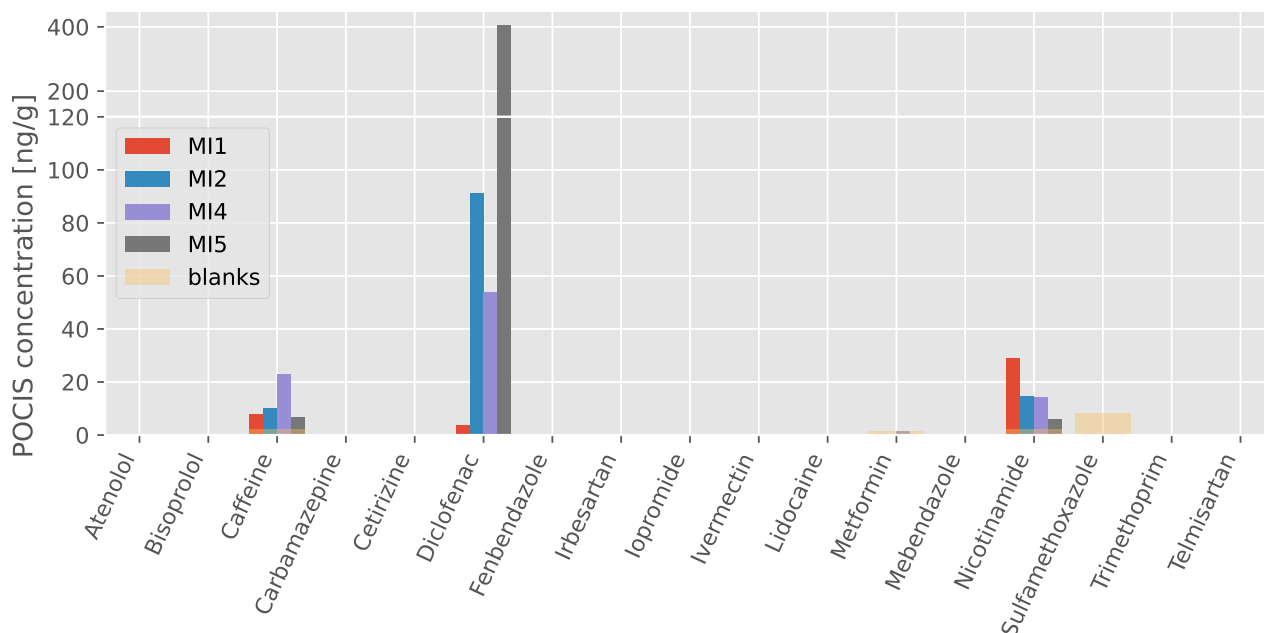


FIGURE 3.9: Concentrations analyzed on POCIS located in 4 locations in the stream network for two weeks in June 2019. Note the break in the scale of the y-axis.

was low at the upstream point MI1 and highest in MI5 downstream of the pork farm. Intermediate concentrations were found at MI2 which receives water from the phyto-WWTP of Mirabel and MI4 which includes a small part of the newly constructed areas of the town of Mirabel.

3.4 Discussion

3.4.1 Use of veterinary pharmaceuticals in the Claduègne catchment

The interviews revealed the high importance of antiparasitic pharmaceuticals and the rather low importance of antibiotics in the context of our study site. It should be noted that for an estimation of the relative importance of a pharmaceutical, the number of treatments is likely to be more meaningful than the applied mass, because a smaller dose often signifies higher efficiency. Nevertheless, the applied mass is of importance for estimations of environmental transfer and comparison to river fluxes. For a more precise estimation of the environmental impact of one molecule for one environmental compartment, predicted environmental concentrations (PEC) need to be estimated for this compartment and compared to PNECs. The prediction of the concentration in an environmental compartment is complex and subject to large uncertainties. The PEC depends on the amount of the molecule used and its timing and frequency, the chemical properties of the molecule, chemical and physical properties of the medium (e.g. soil) governing the molecules mobility as well as the persistence of the molecule with regards to different degradation mechanisms. Furthermore it depends on hydrometeorology at the period of application of the molecule, as water is usually the principal vector of transport.

V_{pol} can not directly be understood as an estimation of the risk, as the transfer and degradation of these molecules are strongly variable. On one hand, only a small portion of the used PhAC will ever reach the stream due to metabolism in the treated animal as well as degradation and immobilization along the transfer path. On the other hand, transfer is very variable, so a large part of the total released amount may reach the streams in a small portion of time, leading to much higher concentrations than would be expected from only using an average transfer. Table 3.5 shows that the amount of IVM used annually may pollute up to $1.4 \times 10^{10} \text{ m}^3$ of water. As an order of magnitude, the average annual runoff volume of the Claduègne river is $1.9 \times 10^7 \text{ m}^3$. In other words, if 1‰ of the applied quantity reaches the stream, equally distributed over the whole year, this would be at the threshold of acceptable concentrations. As the amounts reaching the stream can be expected to be highly variable, an average annual export of 1‰ would already lead to unacceptable stream concentrations over part of the year.

3.4.2 Applicability of the results

In spite of the analytical limitations, largely constraining the realization of the initial goals, these interviews led to important information on agricultural practices in the study region. One of the main outcomes from these interviews is the rare use of antibiotics in contrast to significant use of antiparasitic drugs. Comparing this to the large dominance of antibiotics in the molecules searched in environmental waters highlights the under representation of these compounds in studies of environmental occurrence and fate of emerging contaminants. An effort to include these molecules more systematically in analytical methods is needed.

More concretely, the interviews guided the reorientation of the PhD-studies. For the transfer study developed from the end of the first year on (see Chapter 4), the interviews determined the model PhAC: IVM. It is the dominantly used PhAC in cattle breeding and cattle is the dominant livestock in the catchment. Furthermore, it has a chemical property that is characteristic of most of the used antiparasitic PhAC, which is hydrophobicity. This property is expected to fundamentally influence the soil transfer. In addition it is the molecule for which Richard (2011) obtained the lowest PNEC. More detail on its mode of action, toxicity and chemical properties are given in the introduction of Chapter 4. At the time this decision was made, we were not yet able to analyze this molecule at the IGE laboratory, however, Marie-Christine Morel and Céline Voiron developed the analytical method in parallel to the PhD with the assistance of Jeewan Babu Rijal and in exchange with Jean-Francois Sutra and Anne Lespine from InTheRes, Toulouse.

3.4.3 Pharmaceuticals in the streams of the Claduègne Catchment

A clear difference can be seen between PhAC for human use that are dominantly found at the outlet of the Claduègne catchment and can be expected to be introduced into the streams by the WWTP and PhAC of veterinary use that are mostly observed at the Gazel outlet. In between the two stations, these molecules may either be photo- or biodegraded, adsorbed to sediment or diluted at the confluence to a concentration below the LD.

Regarding the evolution of the concentration of veterinary PhAC, all of them seem to be either exclusively present during flood events (at detectable concentrations) or present in higher concentrations during flood events than before and after. As they are expected to enter the stream mainly from animal dung on soil as diffuse source, this behavior suggests that they can only be mobilized and leach into streams during strong rain events causing overland flow or other preferential flow. If this preferential flow is connected all the way to the stream, large amounts of these molecule could reach the streams. This hypothesis of the need for a high discharge in order to transport the veterinary PhAC into the streams is supported by the fact that none of the veterinary PhAC is detected on the POCIS that were installed in four points of the Gazel catchment over a low flow period. We did not translate the concentrations on the POCIS into stream water concentrations because the conversion depends on many factors (flow velocity, variability of concentrations, molecule sorption coefficients) and is never 100% quantitative, but in general POCIS are more sensitive to low concentrations than grab water samples. This suggests that these molecules are not present during low flow.

The observed concentrations of FBZ (Fig. 3.7) are all well above the PNEC of 0.08 ng L^{-1} (Richard, 2011). The peak concentration during the flood event in June 2020 at 28.4 ng L^{-1} (Fig. 3.7 c)) is 355 times the PNEC for fish acute toxicity (Richard, 2011). In order to quantify the risk from these concentration peaks for different species, more detail on the toxic effect of different durations of exposure as well as further analyses to determine the duration over which these high concentrations persist are needed. The subsequent samples we have during this flood event have a rising trend, and the highest concentration was observed in the last sample, so the evolution of the concentration thereafter is unclear. The autumn flood event (Fig. 3.7 b)) suggests that concentrations in the range of a few ng L^{-1} can persist for hours to days over flood periods. These results suggest that the treatment of pork with FBZ in the Gazel catchment may present a serious risk for aquatic life.

Concerning the non-detection of IVM there may be several reasons. It may not have been present in the water at detectable concentrations during the two flood events that were sampled. This may be because it had not entered the waterways, or because it had been adsorbed to sediment or degraded between entry of the waterways and sampling ('between' on a temporal and / or spatial scale). Furthermore, it may have been degraded during the transport or storage of the samples, or, as a strongly hydrophobic molecule it may have been mostly adsorbed to the particulate matter that was filtered out of the samples before freezing. The remainder may have adsorbed to the particulate organic matter that reformed during freezing and was filtered out afterwards. So not detecting it mainly means that it is uncertain if there was IVM at a detectable concentration in the stream water in the time of sampling. Taking into account the rapid photodegradation of IVM (see Chapter 4), it may also be advisable to take more samples on the Coiron plateau in order to be closer to the cow pastures. Now the analytical method is established, it would be advisable to take some additional samples and analyze them rapidly after sampling without a need to store them in frozen form. It would also be interesting to spike some of the samples with an internal standard of marked IVM at the moment of sampling, in order to quantify the loss between sampling and analysis. These processes are likely to also have influenced the detected molecules FBZ and MBZ, suggesting that the actual stream concentration at the moment of sampling might have been higher. An additional

problem in the interpretation of 'negative' results (non-detection) of IVM is its extremely high aquatic toxicity with a PNEC ($0.000\ 025\ \text{ng L}^{-1}$) well below the LQ of $2\ \text{ng L}^{-1}$ (factor 10^5).

The observed concentrations of MBZ are below the PNEC from Richard (2011) of $36\ \text{ng L}^{-1}$. As discussed for IVM above, this is not a proof that the stream concentrations at the moment of sampling actually were as low. A particularity of treatment of porcs with FBZ is that several treatments are applied throughout the year as opposed to one antiparasitic treatment per year in spring or autumn for sheep and beef and in winter for goats. There is a possibility that with the two analyzed flood events, the treatment periods for sheep and beef were missed and therefore concentrations may be higher in other parts of the year.

3.4.4 Lessons from the contact with farmers

The interviews showed that in the eye of many of the farmers, the scientific world builds the base of restrictions and bureaucracy against them with the goal of environmental protection, but without sufficiently proposing alternatives for them. Accordingly, a large part of the farmers regarded us with suspicion. The contact would have been much more difficult without the local contacts at CERMOSEM.

4

Soil transfer study

The methodology of this chapter was developed specifically for this PhD study and was published in Vadose Zone Journal (Hachgenei et al., 2022a). The article is included in the methods section of this chapter (subsection 4.2.1), complemented by some additional methodological specifications.

4.1	Introduction	58
4.1.1	Flow of water through soil: basic concepts	59
4.1.2	Ivermectin	61
4.1.2.1	History & use	61
4.1.2.2	Mode of action	62
4.1.2.3	Environmental fate and effects	62
4.1.3	Knowledge gaps	67
4.2	Methods	67
4.2.1	Device to simulate contaminant transfer through intact soil (VZJ, 2022)	67
4.2.2	Additional methodological specifications	78

4.2.3	Soil sampling locations and experiments	78
4.2.4	Soil characterization	80
4.2.4.1	Grain size distribution	82
4.2.4.2	Soil organic carbon	82
4.2.4.3	Soil water repellency	83
4.2.4.4	Hydraulic conductivity	85
4.2.4.5	Structure: tomography	87
4.3	Results	92
4.3.1	Hydrological functioning	92
4.3.2	Ivermectin transfer	98
4.4	Discussion	105
4.4.1	Hydrological functioning	105
4.4.1.1	Solute transfer	111
4.4.2	Ivermectin transfer	113
4.4.2.1	Quantification problems and potential reasons	113
4.4.2.2	Factors controlling the transfer of Ivermectin	113
4.5	Conclusion	116
4.6	Link to the catchment scale	117

4.1 Introduction

As elaborated in Section 1.3, due to the availability of analytical methods a focus was set to one single molecule and the scale was changed from catchment to plot scale with artificial input of the investigated molecule. We focused on Ivermectin (IVM), a pharmaceutically active compound (PhAC) which is largely used in the catchment and which has an extremely low lethal concentration for aquatic organisms (see below for details). It has a high K_{ow} , similar to some of the other antiparasitic PhAC used in the study site (Table 3.4). This hydrophobicity is expected to govern its transfer through strong soil adsorption coefficients. We chose to investigate the mobility of IVM over the surface of and through intact soils from the study site on a submetric spatial scale and intra- and inter-event temporal scale after application in the form of contaminated cow dung. The goal was to understand the factors governing the transfer of water and dissolved IVM through and over soil for two contrasted types of soil from the study site. In order to accomplish this, we needed a device and protocol to sample intact soil monoliths and subject them to simulated rainfall, while measuring both shallow leaching and overland flow (OF) discharges on a high temporal resolution, sampling them and minimizing the

risk of chemical interactions with the device itself. As we could not identify any well documented devices fulfilling these criteria, we decided to develop one. The main questions were:

1. How do the soils' hydrologic responses vary between rain events regarding the temporal dynamic, repartition between overland and subsurface flow and the proportions of event and pre-event water?
2. What soil characteristics and conditions explain these variations?
3. What order of magnitude of dissolved concentrations and quantities of IVM can be mobilized from cow dung by a short intense precipitation and pass through and over the soil without being adsorbed?
4. How do these amounts depend on the two main soil types in the Claduègne catchment?
5. How do the amounts depend on the initial condition of the soil and the period of time between cow dung application and precipitation?

In order to answer these questions, fresh, untreated cow dung was contaminated with IVM at a concentration that can be found in the excretions of treated cattle. It was applied to intact soil monoliths extracted from two pastures on the two geological units of the catchment in the form of a reshaped cow pat and precipitation was simulated. An understanding of the hydrological processes inside the soil and factors governing the flow of water is an essential prerequisite for understanding the transfer of IVM through the soil. Therefore, the hydrological condition of the soil and the transfer of water through it were monitored by quantifying water fluxes, soil water content and event water fractions and their evolution at high frequency. IVM concentration was measured from samples of both water fluxes (drainage and OF), collected at high frequency. As mentioned in Chapter 1, bio- and photodegradation as well as adsorption and desorption are not assessed explicitly in this study. They are expected to take place, but could not be assessed analytically. The focus is set on the quantities and concentrations that can be mobilized and pass through and over soil without being retained. The factors that were varied between the different experiments were the soil type, initial soil moisture and the period of time between dung application and precipitation. In addition the evolution over successive rain events was studied.

4.1.1 Flow of water through soil: basic concepts

Soil is a porous medium that can be decomposed into two main compartments or three phases: The solid, consisting of more and less reactive mineral and organic material and the pores, filled with liquid (water), gas (air) or a mixture of both. The solid phase can have variable properties and one of crucial importance concerning the flow of water through the soil is the wettability or water repellency. This property can be quantified over the solid-liquid contact angle CA , where a $CA < 90^\circ$ indicates wettability and a $CA > 90^\circ$ indicates water repellency. The further CA is from 90° , the higher the degree of water repellency or wettability (Roy and McGill, 2002).

In most cases, soil is considered to be wettable ($CA < 90^\circ$). In this case, pores would attract water through capillarity as long as the soil is unsaturated. The tension created by the force of this attraction is expressed in units of water height as pressure head h , which is negative in the case of a tension and positive in case of pressure from a water column above. The smallest unsaturated pores exert

the strongest capillary force, and therefore determine h and become saturated first with the arrival of water. Pores filled completely with water would not exert any more capillary force. h can be linked to the radius r_0 of the smallest pores that are currently unsaturated and therefore governing h via Jurin's law (Jurin, 1718):

$$r_0 = \frac{2 \cdot \gamma_w \cdot \cos CA}{\rho \cdot g \cdot h} \quad (4.1)$$

where γ_w is the surface tension of water (0.0728 N m^{-1} at $20 \text{ }^\circ\text{C}$), ρ is the mass density of water (998 kg m^{-3} at $20 \text{ }^\circ\text{C}$), g is gravitational acceleration (9.81 m s^{-2}). CA is the contact angle between water and soil solid.

An important parameter governing the flow of water through porous media is the hydraulic head H , which is defined as the sum of pressure head h and elevation head z .

$$H = h + z \quad (4.2)$$

The flow of water through a porous medium follows the hydraulic gradient ∇H that is the ratio of difference in hydraulic head ΔH to distance L as

$$\nabla H = \frac{\Delta H}{L} \quad (4.3)$$

The flow rate expressed as specific discharge q in units of length per time depends on the soil's hydraulic conductivity K_H (in units of length per time), as described by Darcy's law (Darcy, 1856):

$$q = -K_H \cdot \nabla H \quad (4.4)$$

In an unsaturated soil, K_H increases with the soil's water content Θ . It can be expressed as a function of h as $K_H(h)$. $h = 0$ corresponds to saturation and $K_H(h = 0) = K_{HS}$ is the soil's saturated hydraulic conductivity.

Under these conditions, flow through unsaturated soil will pass through the smallest pores as they exert the strongest capillary force if unsaturated and therefore saturate first. The closer the soil is to saturated condition, the larger will be the pores that contribute to the flow of water until at saturation all connected pores will contribute to the flow of water. This process would lead to a higher proportion of rapid preferential flow through macropores with increasing wetness. This behavior was observed via tracer experiments by different authors (Beven and Germann, 1982; Jaynes et al., 2001; Kung et al., 2000).

In some cases, under dry conditions, soil or parts of it can be water repellent, mostly due to a high content of natural organic matter (OM) (Täumer et al., 2005; Haas et al., 2018) sometimes linked to the presence of specific plant species (Doerr et al., 2000). In this case, $CA > 90^\circ$ and the capillarity is inverted (corresponding to a change of sign in Jurin's law). Therefore, the smallest pores would be the most repulsive. Soil water repellency (SWR) caused by natural OM is normally reversible with moistening of the soil. In the presence of water, the amphiphilic molecules causing the SWR reorient themselves and the soil becomes hydrophilic (Doerr et al., 2000). In this case of water repellent soil, water would mostly flow through the largest macropores advancing rapidly through the soil while

bypassing the majority of the soil volume, as long as the soil is relatively dry. On moist soil, water repellency would be lifted and water would pass through a larger portion of the pore volume and therefore advance less rapidly. This is the inverse of what was described above for hydrophilic soil. Hardie et al. (2011) could illustrate this behavior via dye tracers that advanced further and through more preferential paths on dry soil than on wet soil.

Besides water flow through soil, water can flow over soil. Overland flow (OF) can be divided into two types: (i) saturation excess overland flow (SOF) occurs on saturated soil where excess precipitation water cannot infiltrate due to this saturation and water ponds and runs of along the surface (Freeze, 1974). (ii) Infiltration excess overland flow or hortonian overland flow (HOF) occurs when the precipitation intensity exceeds the soil's infiltration capacity (Horton, 1933). This happens on unsaturated soils and is not necessarily linked to the soil's water content. The soil's infiltration capacity can however temporarily be impacted by SWR which can cause HOF.

4.1.2 Ivermectin

In contrast to antibiotics for which the use has been strongly restricted in France since 2016 (see above), antiparasitic medicaments are largely used in beef and sheep farming, either in a preventive manner or for treating the whole herd. One of the most commonly used parasiticides by the farmers on our study site is Ivermectin. In the following paragraphs, this molecule is described in terms of its history, use, mode of action, chemical properties and environmental fate and toxicity.

4.1.2.1 History & use

In the early 1970s, a research team around Satoshi Ōmura collected the soil microorganism *Streptomyces avermectinius* from a Japanese soil. It was discovered to produce a mixture of eight avermectines during its fermentation process, which were found responsible for a strong antiparasitic activity of *S. avermectinius* (Fig. 4.1). A research team around William Campbell identified the aver-

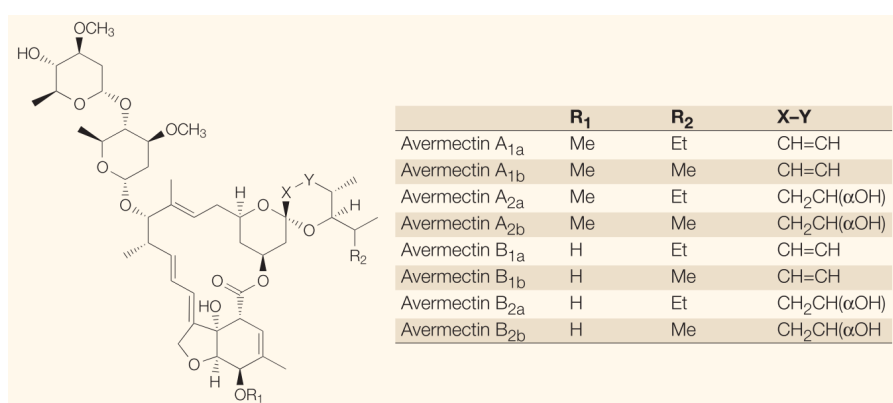


FIGURE 4.1: Structure of the eight avermectines produced by *Streptomyces avermectinius*. Source: Ōmura and Crump (2004)

mectines B_{1a} and B_{1b} to have the highest activity. They synthetically modified them (reduction of the C₂₂-C₂₃ double-bond) to enhance activity and safety. Their semi-synthetic mixture of 80% B_{1a} and

20% *B_{1b}* got the commercial name Ivermectin (Ōmura and Crump, 2004). IVM was introduced commercially as a veterinary broad-spectrum antiparasitic drug in 1981 and is effective against a high number of parasites and 25 times more potent than all currently available anthelmintics (Ōmura and Crump, 2004). It is also highly effective against a wide range of insect and acarine pests (Jackson, 1989). IVM was approved for human use by the French government in 1987. It now plays an important role in human medicine in the treatment of onchocerciasis (also called river blindness, a public health problem in Sub-Saharan Africa caused by the parasite *Onchocerca volvulus*) and lymphatic filariasis (also known as Elephantiasis, a disfiguring disease affecting people in tropical and subtropical regions caused by the filarial worms *Wuchereria bancrofti*, *Brugia malayi* or *B. timori*). Crump and Ōmura (2011) entitle it a 'wonder drug' for saving billions of lives of poor and disadvantaged people in the tropical regions. Due to its widespread use in animals, some parasites developed IVM resistance (Wolstenholme et al., 2004). Despite its use as monotherapy of onchocerciasis, no resistance in *Onchocerca volvulus* has yet been found, however Lustigman and McCarter (2007) indicate a potential for a development of such resistances. In 2015, Satoshi Ōmura and William Campbell earned half a share of the Nobel Prize in Physiology or Medicine 'for their discoveries concerning a novel therapy against infections caused by roundworm parasites' (Nobel Media AB, 2015). Recently, IVM has also been tested against Severe Acute Respiratory Syndrome Coronavirus 2 (SARS-CoV-2), the virus causing a global pandemic since the beginning of 2020 and some activity against SARS-CoV-2 has been found (Popp et al., 2021). IVM is currently used in the treatment of coronavirus disease (COVID-19) in some countries in South America (Heimfarth et al., 2020) and even preventive use is studied (Behera et al., 2021).

4.1.2.2 Mode of action

Today, IVM is known to act on several pentameric ligand-gated ion channels. Its biological target is the glutamate-gated chloride channel receptor that is abundant in the muscular and neuronal cells of nematodes and arthropods, but does not exist in vertebrates. IVM irreversibly activates a chloride inflow through those channels, that silences nerve and muscle activity (Wolstenholme and Rogers, 2005). It has been shown to also activate or modulate the anion-permeable glycine and γ -amino butyric acid (GABA) type A receptors, that also exists in vertebrates (Estrada-Mondragon and Lynch, 2015). However, in mammals these channels are part of the central nervous system and thus protected by the blood-brain barrier. Here, the P-glycoprotein efficiently restricts IVM's penetration into the brain, for which reason IVM has a high safety-margin in mammals (Geyer et al., 2009).

4.1.2.3 Environmental fate and effects

Environmental toxicity While IVM is relatively safe for mammals, many other organisms are sensitive to its action. Adverse effects of environmental IVM concentrations have been studied and observed for different species. Many studies show negative effects on coprophagous insects. Lumaret et al. (2007) found an LC_{50} of IVM in the dung of cows treated with a topical application for the dung-feeding beetle *Aphodius Constans* of $470 \mu\text{g kg}^{-1}$ to $692 \mu\text{g kg}^{-1}$ dry dung. Hempel et al. (2006) found an LC_{50} after 21 days for the larvae of *Aphodius Constans* of $880 \mu\text{g kg}^{-1}$ to $980 \mu\text{g kg}^{-1}$ dry dung. Jochmann and Blanckenhorn (2016) tested the effect of a low concentration of $6.6 \mu\text{g kg}^{-1}$

on natural insect communities on 24 swiss farms. They found a significantly increased mortality for 1/3 of the 32 investigated *Diptera* and *Hymenoptera* species. They found stronger effects on small Hymenoptera taxa (62 %) and large dipteran predators (38 %) than on primary coprophagous dung consumers (23 %). Verdú et al. (2015) showed inhibition of the locomotor and olfactory systems of *Scarabaeus cicatricosus*, a key dung beetle species of the Mediterranean region by low doses of IVM. They showed a significant impact on the beetles antenna response to Trimethylamine and Ammonia exposition when exposed to dung containing IVM at a concentration as low as $1 \mu\text{g kg}^{-1}$ fresh weight and a significantly lower foreleg muscle force at an IVM concentration of $3 \mu\text{g kg}^{-1}$. The time the beetle needed to detect and arrive at a food source was significantly increased and the time to ataxia (coordination troubles) and death was drastically decreased by the lowest used concentration of $1 \mu\text{g kg}^{-1}$. They explain the observed effects by IVMs action on glutamate- and GABA-gated chloride-channels of sensory neurons as well as muscle cells. Römbke et al. (2010) observe reduced degradation of dung pats of IVM-treated cattle over 86 days, compared to those of untreated cattle. Verdú et al. (2018) found that the treatment of beef cattle with IVM lead to reduced dung degradation and relocation on the short term and accumulation of dung on the soil leading to changes in some soil functionality (higher mineralization rates of C and N) on the long term.

IVM is particularly toxic to aquatic organisms, in especially for crustaceans. The acute toxicity for *Daphnia Magna* is between $LC_{50}^{48h} = 1.7 \text{ ng L}^{-1}$ to 25 ng L^{-1} (Garric et al. (2007) and Halley et al. (1989a) respectively). Garric et al. (2007) found long-term inhibition of *Daphnia Magna* reproduction and growth at the lowest observed effect concentration (LOEC) = 1 pg L^{-1} . The toxicity for the alga *Pseudokirchneriella subcapitata* was much lower with an estimated LC_{50} of $4000 \mu\text{g L}^{-1}$. Sanderson et al. (2007) studied acute (1 d to 10 d), chronic (10 d to 97 d) and long-term (97 d to 265 d) toxicity of IVM in aquatic outdoor mesocosms. They also found acute and chronic impacts on several aquatic species at the lowest tested concentration of a few ng L^{-1} . Long-term effects concerned mainly sediment-active species, as water concentration of IVM rapidly decreased due to sorption to sediment. The toxicity of IVM for fish is lower, with LC_{50}^{96h} of $3 \mu\text{g L}^{-1}$ for rainbow trout *Salmo gairdneri* and $4.8 \mu\text{g L}^{-1}$ for bluegill sunfish *Lepomis macrochirus* (Halley et al., 1989a). A similar LC_{50}^{96h} of $17 \mu\text{g L}^{-1}$ was found by Kilmartin et al. (1996) for rainbow trout *Oncorhynchus mykiss*. Davies et al. (1997) determined the LC_{50}^{96h} for blue mussel *Mytilus Edulis* to be 70 ng L^{-1} .

The hydrophobic characteristics of IVM let suspect a potential for bioconcentration. The bioconcentration of Avermectin B1a in bluegill sunfish was studied in 1996 by van den Heuvel et al. (1996) at an aquatic concentration of $0.1 \mu\text{g L}^{-1}$. They found an equilibrium bioconcentration factor (BCF) of 56 L kg^{-1} (whole fish vs. water concentration) reached after 10 d to 14 d. They also found an half-life of 3.3 d after replacing the water with clean control water. They conclude a low risk for biomagnification. Römbke et al. (2018) did similar experiments of bioconcentration in zebrafish using two different aqueous concentrations of $0.01 \mu\text{g L}^{-1}$ and $0.1 \mu\text{g L}^{-1}$. They observed BCF of 101 L kg^{-1} and 113 L kg^{-1} respectively. During depuration phase, the concentration bisected in 0.7 d and 1.5 d and decreased by 95 % in 3 d and 6.5 d respectively. Concerning mussels, a BCF of 750 L kg^{-1} was found by Davies et al. (1997) for *Mytilus Edulis* with a depuration half-life of 22 d.

Excretion by treated animals Different IVM excretion rates by treated cattle were found in different studies, but they generally agree about the fact that no matter the way of admission the majority of the applied dose is excreted via the feces in form of the unchanged parent compound. Slight differences in total excretion percentage and strong differences in the temporal dynamic of excretion can be observed between the different ways of administration.

Today, two ways of IVM-administration are current in France. The subcutaneous (sc) injection of $200 \mu\text{g kg}^{-1}$ body weight and topical application (pour-on, po) of $500 \mu\text{g kg}^{-1}$ body weight. A third way of admission, the sustained-release bolus (srb) has been forbidden in France in 2003 (Ministere de la sante et de la protection sociale, 2004).

For sc injection, excretion rates in feces range from 62 % to 98 % (Chiu et al., 1990; Jackson, 1989). For po administration, Laffont et al. (2001) found an excretion rate of 70 %, however this rate has decreased to 6.6 % when cattle are prevented from licking themselves and each other. Alvinerie et al. (1998) found 80 % to 90 % of the quantity applied to cattle via a srb being excreted over the following 4 months. González Canga et al. (2009) generally state an excretion of >90 % via feces and ≈ 2 % via urine, similar to an excretion of 1.5 % via urine found by Chiu et al. (1990). Differences between those studies might partially be explained by different quantification limits and dung monitoring periods of the different studies. Wratten and Forbes (1996) found 40 % to 75 % of excreted avermectins to be the parent compound and the remainder being less active polar metabolites. According to Cook et al. (1996) the concentrations of IVM in the dung of grain-fed cattle are five-fold higher than those of pasture-fed cattle. However, they explain this effect by the higher mass of dung excreted by pasture-feeding cattle and not by a difference in total excreted IVM.

The temporal dynamic of the excretion strongly depends on the form of application. While using a po formulation, most of the excretion takes places over the five days after application. Using a sc injection, the peak concentration is lower, but IVM is excreted over a longer time (Sommer et al., 1992; Herd et al., 1996). Herd et al. (1996) measured a concentration peak of 17.1 mg kg^{-1} and 1.38 mg kg^{-1} dry dung for the po and sc application respectively (median of 4 animals). This corresponds to 2.7 mg kg^{-1} and 0.22 mg kg^{-1} fresh dung. The difference between the two ways of administration was less pronounced in the earlier study by Sommer et al. (1992). According to Laffont et al. (2001), elimination of the po formulation is much slower when cattle are prevented from licking, explaining potential differences in the excretion dynamics found for po formulations by different authors. Laffont et al. (2003) estimate via pharmacokinetic modeling that in licking cattle 58 % to 87 % of the applied IVM enters the animal via the oral way and only 10 % was absorbed percutaneously. Of the ingested IVM, about 72 % transited directly into the feces. The srb resulted in much higher excretion over a long period of time (several months), which is the reason for its interdiction.

Ivermectin chemical properties, sorption and degradation IVM is a hydrophobic molecule with $\log(K_{ow}) = 3.2$ and $\log(K_{oc}) = 4.1 - 4.2$ (Bloom and Matheson, 1993; Halley et al., 1989a). The K_d ranges from 57 L kg^{-1} to 396 L kg^{-1} as tested for three different European soils by Krogh et al. (2008a). It has a persistence of $t_{1/2} = 7 \text{ d}$ to 217 d in soils under aerobic conditions (Boxall et al., 2004; Halley et al., 1993; Krogh et al., 2009) and ($t_{1/2} < 45 \text{ d}$) in dung (Sommer et al., 1992). In an outdoors aquatic mesocosm study, Sanderson et al. (2007) found no decrease of concentration in

aquatic sediment over their whole study period of 265 d. Thus it is potentially very persistent in the environment (Kümmerer, 2008; Krogh et al., 2009). On the other hand, it is rapidly isomerized by UV-radiation (Campbell, 1989), leading to a very short theoretical half-life in surface waters. Boxall et al. (2004) found a $t_{1/2}$ below 0.5 h. Sanderson et al. (2007) found an aquatic half-life of 3 d to 5 d including degradation and sorption to sediment. After studying the dissipation kinetics of IVM on three natural and one artificial soil, Krogh et al. (2009) conclude, that dissipation of IVM from soil is governed by sorption, which is determined by the soils pH and cation exchange capacity. Furthermore, dissipation was positively related to temperature and under anaerobic conditions no significant dissipation was observed.

Transfer from feces and through soil Di Guardo et al. (2004) conducted some basic equilibrium modeling for certain pharmaceutical products (PP) based on their physical chemical properties, in order to identify the environmental compartments of importance. They identified soils and sediment to be the most important compartments for IVM. In their model, if added to soils, IVM is never transferred into the water and sediments but stocked and degraded in the soils due to its strong sorption coefficient. If added directly to waterways, most of it is sedimented and either degraded or buried in the sediment. However, Raich-Montiu et al. (2008) detected $0.8 \mu\text{g L}^{-1}$ IVM in the unfiltered leachate of heifer dung. This indicates that IVM can be transferred with water, presumably to a large part adsorbed on suspended matter. Rath et al. (2016) conducted leaching experiments of IVM in packed soil columns of 35 cm height and 4 cm inner diameter with a sandy and a clayey soil. After application of 200 mm of artificial rain, in the clayey soil, 74.7% of the IVM stayed in the top 6 cm of the soil. In the sandy soil, the largest part (over 40%) was in a depth between 6 cm to 12 cm. This indicates a retardation in the transfer of IVM through adsorption, which is stronger on the clay soil.

Popova et al. (2013) studied the transfer of IVM from feces placed on soil. They used six wooden boxes (0.3 m wide, 1.2 m long and 0.2 m deep) filled with repacked soil of two contrasted types and a drainage layer of molded glass beads on the bottom. They planted the boxes with grass and let it grow for three month. Then they cut the grass, placed the soil at a slope of 7%, saturated the soil with water and applied 1 kg cow dung (80% humidity) spiked with 200 μg each IVM, chlortetracycline and oxytetracycline to the top of the boxes in form of a traversing stripe. Then they irrigated the boxes via run-on with 82 mm over 30 min 3 times with breaks of one week between the irrigation events. They recovered surface runoff and leachate. Two out of three boxes per soil type produced surface runoff. After the three events they obtained about 1% of the applied 200 μg of IVM, the majority of it via surface runoff. The concentrations were similar in surface runoff and leachate, however one event generated an average of 16 L of surface runoff vs. 5.7 L of leachate. The highest concentrations they observed in filtered runoff and leachate were below $0.5 \mu\text{g L}^{-1}$.

Later they studied the concentration of the same molecules in the surface runoff from a spiked and run-on-irrigated pasture in the field with a slope of 2% to 4% (Bair et al., 2017). They applied the products with and without manure on a strip perpendicular to the slope, irrigated uphill over 60 min and collected the runoff downhill. Again, they found little mobility of IVM with concentrations in filtered runoff not exceeding $0.556 \mu\text{g L}^{-1}$ and the proportion of IVM exported being less than one percent. The extractable concentrations in the manure and soil below ranged from $54 \mu\text{g kg}^{-1}$ to $118 \mu\text{g kg}^{-1}$

and $1 \mu\text{g kg}^{-1}$ to $14 \mu\text{g kg}^{-1}$. They let the plots dry for 2 weeks, which reduced the moisture content in the dung by over 86%. Another irrigation event after this drying period only exported 17% of the amount of pharmaceuticals exported during the first irrigation.

Wohde et al. (2016) conducted a long-term study on IVM dissipation from dung into the soil of pastures in Canada, France, Switzerland and the Netherlands over 13 months. They found IVM dissipation from dung depending strongly on the dung's humidity. On the Dutch site, where the dung stayed humid, over 98% of the initial IVM dissipated within 6 months. On the French site, the dissipation kinetics were similar for the first 2 months but then the dung dried out between the third and fifth month, so that hardly any dissipation occurred after the fifth month and after 13 months in the field, up to 48% of the initial IVM content was recovered. During the whole experiment, they found no evidence for relevant transformation products, which they explain by their probably higher mobility. They found concentrations of IVM in the top 5 cm of soil below the dung pats being highest 3 months after treatment in more humid regions and 9 months after the treatment in the drier region (Montpellier, France). In Montpellier, they still detected up to $3 \mu\text{g kg}^{-1}$ dry soil after 13 months, indicating a potential for long-term accumulation.

Mesa et al. (2017) conducted a study of the fate and toxicity of IVM in microcosms containing 1250 mL of water, artificial sediment and 20 g of dung spiked with IVM at different concentration levels as well as three species of aquatic invertebrates. They analyzed concentrations in water, sediment and organisms 7 and 17 days after the beginning. The aquatic concentration remained below the limit of detection (LD) of 0.5 ng g^{-1} while the concentration in the sediment increased with time. With regards to toxicity, they found an initial dung concentration between 22 ng g^{-1} and 50 ng g^{-1} (wet) to lead to a mortality of 50% for the zooplankton *Ceriodaphnia dubia* and the amphipod *Hyalella*, at an unknown aquatic concentration (<LD). Mesa et al. (2020) studied the evolution of the concentration of IVM in different compartments (sediment, water and different organisms) in a wetland, the surroundings of which were grazed by treated cows. They found concentrations to increase in sediment and aquatic fauna after treatment of the cattle.

Environmental risk Because of IVM's very high acute toxicity to invertebrates, a first environmental risk assessment (ERA) was conducted as early as 1986 (Liebig et al., 2010). Early ERAs (Bloom and Matheson, 1993) did not expect a significant environmental impact of IVM use. They mention the high toxicity to aquatic organisms, but consider the risk for the aquatic compartment to be very low, due to the dilution, strong sorption to sediment and photodegradation. Liebig et al. (2010) conducted a large environmental risk assessment predicting environmental concentrations in different compartments (surface water, sediment, soil and dung) and evaluating them against predicted no effect concentrations of different species of each compartment. They conclude that there is an unacceptable risk of IVM use for daphnids and dung organisms. IVM is one of the few veterinary pharmaceuticals of which the found environmental concentration levels exceed not only long-term but also acute toxicity for a range of non-target organisms (Bártíková et al., 2016; Mesa et al., 2020; Lumaret et al., 2007; Sanderson et al., 2007; Garric et al., 2007).

4.1.3 Knowledge gaps

The above studies can be summarized by saying that IVM has a low mobility in the environment, which is increased in humid conditions. While in simplified theoretical models, IVM would be adsorbed and degraded in soils, laboratory experiments show that it does leach through soil at low concentrations (Popova et al., 2013; Rath et al., 2016) and field studies show its occurrence in environmental waters and aquatic sediment (Charuaud, 2018; Charuaud et al., 2019a; Mesa et al., 2020; Sanderson et al., 2007). Furthermore, IVM tends to persist in dung and soil under dry conditions. The strong adsorption of IVM suggests, that the difference between predictions from reactive transport modeling and experiments on soil might be due to the heterogeneity of real-world water flow through and over soil including bypassing flow reducing the molecule's adsorption to soil.

None of the above studies investigated the transfer of IVM through and over intact soil and their intra-event dynamics. Furthermore, the effect of soil condition (e.g. initial soil moisture) on the transfer of IVM through and over soil has not been studied. In order to better understand the risk of IVM contamination of surface water bodies by grazing of treated cows and manure application to fields, it seems to be crucial to account for the structure of natural soil as well as the spatiotemporal dynamics of water flux through and over soil. This is of particular importance in the context of Mediterranean hydro-meteorology with a very high dynamic.

4.2 Methods

4.2.1 Device to simulate contaminant transfer through intact soil (VZJ, 2022)

We developed a soil sampling device and protocol for this part of the PhD, a full description of which has been published as Technical Note in Vadose Zone Journal (Hachgenei et al., 2022a). It is included hereafter. The supplemental material containing further illustrations is included in Appendix C. This article includes a description of the soil sampling device, the sampling strategy, the rainfall simulator, the experimental protocol, the measured and calculated variables and the performed chemical analysis. One IVM transfer experiment was included as a technical validation of the device, but no interpretation was done. Additional chemical analyses that were performed are described after the article, as well as some further methodological specifications that are of importance for the conducted transfer experiments. This is followed by a description of all conducted experiments and a detailed characterization of the used soils. The results of the experiments are presented and discussed with regards to hydrological functioning and transfer of IVM thereafter.

TECHNICAL NOTES

A device to simulate contaminant transfer and surface and subsurface flow through intact soil monoliths

Nico Hachgenei¹  | Guillaume Nord¹  | Lorenzo Spadini¹ | Henri Mora¹ | François Courvoisier¹ | Jean-François Sutra² | Jean-Pierre Vandervaere¹  | Cédric Legouët¹ | Marie-Christine Morel^{1,3} | Jean Martins¹  | Anne Lespine²  | Celine Duwig¹ 

¹IGE, Univ. Grenoble Alpes, CNRS, IRD, Grenoble INP, Grenoble 38000, France

²INTHERES, INRAE, ENVT, Univ. de Toulouse, Cedex 3, Toulouse 31076, France

³le CNAM, Laboratoire d'analyses chimiques et bio analyses, Cedex 3, Paris, France

Correspondence

Céline Duwig, IGE, CNRS, IRD, Univ. Grenoble Alpes, Grenoble INP, Grenoble, 38000, France.

Email: celine.duwig@ird.fr

Assigned to Associate Editor Vilim Filipović.

Funding information

Agence Nationale de la Recherche, Grant/Award Number: #ANR-10-LABX-56; Institut National des Sciences de l'Univers, Centre National de la Recherche Scientifique, Grant/Award Numbers: SNO SIC ANO-1, Zone critique et eau continentale/OHMCV

Abstract

Many contaminants of agricultural origin are released into rural environments, particularly at the soil surface. Their fate has been extensively investigated in repacked soils, but only few studies have addressed their transport in structurally preserved natural soils. Much remains unknown about their fate and transfer within and between environmental compartments, while the susceptibility of these compartments to the contaminants adverse effects can vary considerably. The lack of studies regarding surface and subsurface transfer of contaminants through intact soil compared with studies on repacked soil led us to propose a device and protocol for sampling intact soil monoliths (60 × 30 × 22 cm³, length, width, depth [LWD]) without heavy machinery. This is achieved by a modular design with removable top and bottom lid and a protocol of cutting the soil and replacing the affected bottom soil with a drainage layer of glass beads. The device allows the application of artificial rainfall events with simultaneous highly resolved quantification of infiltration excess overland flow and drainage discharge. It is designed to facilitate the collection of samples for physical, biological, and chemical analyses that fulfill cleanliness standards for organic contaminant analysis at trace levels using only poorly reactive stainless steel and glass materials. Testing of the device was performed by measuring the transfer of the antiparasitic drug ivermectin (IVM) through and over a silt-loam pasture soil. This test case illustrates how the device can be used to gain valuable information on the transfer of trace organic contaminants through topsoils.

Abbreviations: CR, overland flow coefficient; D_m , mean diameter; IVM, ivermectin/22,23-Dihydroovermectin B₁; LWD, length, width, depth; PI, precipitation intensity; Q_D , drainage discharge; Q_R , overland flow discharge.

This is an open access article under the terms of the [Creative Commons Attribution](https://creativecommons.org/licenses/by/4.0/) License, which permits use, distribution and reproduction in any medium, provided the original work is properly cited.

© 2021 The Authors. *Vadose Zone Journal* published by Wiley Periodicals LLC on behalf of Soil Science Society of America

1 | INTRODUCTION

Soils are exposed to a large number of contaminants of different types (e.g., pharmaceuticals [Obimakinde et al., 2017], pesticides [Hedlund et al., 2020], pathogenic bacteria [Bicudo & Goyal, 2003; Chen et al., 2021] and microplastics [Nizzetto et al., 2016]). These compounds are often applied directly or indirectly to soil surfaces in a variety of ways. From there, they can be transported to other environmental compartments. Some of these contaminants have adverse effects on different environmental compartments such as soil, surface water, and groundwater (Boxall, 2017; Schäfer et al., 2007). The environmental risk of a compound can be evaluated by comparing predicted no-effect concentrations to predicted environmental concentrations (e.g., Liebig et al., 2010; Stuer-Lauridsen et al., 2000). The latter are often obtained via numerical modeling, using simplified assumptions for water flow.

Various studies emphasize the importance of soil structure, which determines the configuration of the soil pore system and thereby controls movement of water and contaminants through soil as well as surface–subsurface flow repartition (Bachmair et al., 2009; Chen et al., 2021; Duwig et al., 2019; Flury et al., 1994; Martín et al., 2017). Flury et al. (1994) studied flow patterns in 14 soils, in the field and concluded that bypass flow is stronger in structured soils, which therefore present an elevated risk for contaminant leaching. Bachmair et al. (2009) studied vertical and horizontal patterns of water infiltration into five different soils and identified different soil features being responsible for the observed patterns in the different soils, including the pore structure, surface microtopography, surface cover, water repellency as well as topsoil matrix characteristics such as bulk density and organic matter content. Natural root systems, micro and macrofauna as well as drying cracks in clayey soils greatly affect the soil porous system (Milleret et al., 2009). The soil surface structure (microtopography and crusts) also essentially affects flow repartition between surface and subsurface (Carmi & Berliner, 2008; Govers et al., 2000). Furthermore, surface microtopography may affect the contact surface and contact time between soil and water as it determines hydraulic roughness and more or less concentrated overland flow paths (Darboux et al., 2002; Govers et al., 2000; Hairsine et al., 1992). Repacked soil does not mimic the internal and surface structure of natural soil and therefore fails to reproduce natural flow patterns that would occur in situ (Boyle et al., 1989; Franzluebbbers, 2002). Repacked soil favors matrix flow compared with preferential flow (Guo & Chorover, 2006) leading to reduced contaminant transfer and decreased saturated hydraulic conductivity (Chen et al., 2021; Sadeghi et al., 2000). This generally hinders infiltration and increases overland flow, which is known to be an important vector of contaminants (Sarmah et al., 2006). The difference between repacked and intact soil is expected to be

Core Ideas

- A device for collecting intact soil and subjecting it to artificial rainfall was developed.
- The setup allows for high resolution measurement and sampling of drainage and overland flow.
- It is designed for clean sampling permitting analysis of various contaminants at trace levels.
- We present an experiment to test the device on transfer of ivermectin from cow dung.

particularly effective for intense storm events that result in a high proportion of rapid preferential flow and overland flow. Therefore, in order to better evaluate the risk of contaminant transfer through and over soils, it seems crucial to study transfer through and over intact soil that includes native vegetation with well-developed root channels, biopores, and other features of the natural soil structure as described above.

Different techniques for the sampling of intact soil exist. Sampling techniques can be coarsely classified into two categories, either a sampling frame is forced into the soil (Feyereisen & Folmar, 2009), or the surrounding soil is removed and the soil sample is then surrounded by a support structure and the sides are sealed with substances like concrete or resins (Benecke et al., 1976; Buchter et al., 1984; Krogmann, 1986). The first one has the advantage of being relatively simple, but is not adapted for soils containing stones, as forcing on these stones destroys the structure of the soil. Furthermore, this technique depends on heavy machinery in order to push the frame into the soil and is therefore limited to well accessible sampling locations. The second technique is more adapted for a large variety of soils; however, the use of resin or concrete should be avoided in experiments on the transfer of organic contaminants at trace levels. These compounds require the use of inert material that does not interact with the studied compounds and allows cleaning with organic solvents or heat treatment of the parts that are reused.

There are different approaches to studying contaminant transfer through soils using dynamic experiments under controlled conditions. Three types of approaches have been commonly used in other studies: (a) Soil columns (Archundia et al., 2019; Kay et al., 2005b; Rath et al., 2016) are often small and inexpensive, allowing the study of basic chemical and physical processes underlying contaminant transfer through the soil matrix under controlled conditions and generating reproducible results. However, the applicability of their results to environmental systems is limited because they do not account for some important soil properties and processes: structure (soils are often repacked), vegetation cover, overland flow, erosion and transport of particles. (b) Lysimeters (Goss

et al., 2010; Kay et al., 2005a) are an excellent tool for in-situ studies of long-term vertical transfer through intact soil and the potential for leaching of contaminants into groundwater. However, they are often complex and expensive pieces of equipment and installations, making them less convenient for testing specific factors on multiple soils and for investigations on the scale of a few simulated intense rainfall events. Furthermore, they are often not designed for quantification and sampling of overland flow. (c) 2D-Soil boxes have been used by some authors to study the transfer of pharmaceuticals, by drainage and overland flow (Fernández et al., 2011; Popova et al., 2013). However, the only well documented design allowing the use of intact soil for surface and subsurface transfer studies of organic contaminants that the authors could find uses heavy machinery to push the sampling frame into the soil (Feyereisen & Folmar, 2009). This restricts them to accessible sampling locations and stone-free soils. Therefore, we state the need of an experimental device and protocol to study pollutant transfer through and over a wide range of intact soils under simulated rainfall in controlled conditions. This device should allow to test the effect of different factors such as rainfall intensity, initial soil moisture, slope and soil type on the transfer of contaminants, while using all stainless-steel equipment and capturing the intra-event dynamics of water and pollutant fluxes at a high temporal resolution.

We developed a hand maneuverable system that allows to sample a $60 \times 30 \times 22 \text{ cm}^3$ (length, width, depth [LWD]) intact soil cuboid in the field. The sampling device fits in a rainfall simulator and allows high-frequency measurement and sampling of drainage and overland flow. The system is entirely designed in stainless steel, to minimize chemical interactions with the studied organic molecules. The use of intact soil allows for a realistic soil response and the ex-situ rainfall simulation allows for controlled conditions and monitoring of all fluxes while avoiding contaminating the study site. This device can provide insight into the hydrological behavior of natural topsoils under different conditions and forcing as well as the transfer of different types of contaminants (trace organic molecules such as pharmaceuticals and pesticides, bacteria and viruses, particles such as microplastics, metallic trace elements).

This paper presents the sampling strategy, the experimental setup, the limitations of the system, and potential applications. A technical validation experiment was conducted by studying the transfer of ivermectin (IVM), a common livestock antiparasitic drug, from artificially contaminated cow dung on an agricultural soil.

2 | MATERIALS AND METHODS

2.1 | General design of the experimental device

2.1.1 | The rainfall simulator

The rainfall simulator consists of a support for the soil box, a rainfall simulator frame for the sprinkler, a booster (pump with pressurized water reservoir), one or several water reservoirs, a rain collector frame surrounding the upper edge of the soil box and a transparent PVC chimney (Figure 1). The soil box support has an adjustable slope ($0\text{--}18^\circ$ [$0\text{--}32.7\%$], 8° in this work). The height-adjustable aluminum rainfall simulator frame (total height 114 cm) accommodates a sprinkler nozzle, a battery or mains operated motor that rotates the nozzle continuously at 65 rpm, a pressure gauge, and spigots. We have tested different full cone sprinkler nozzles of the Lechler 490 series generating intensities ranging from 50 mm h^{-1} (490.488.30) to 100 mm h^{-1} (490.608.30). The nozzles are easily exchangeable to adjust the rainfall intensity. They generally generate fine drops with little kinetic energy. This choice of finer raindrops was made in order to better preserve the soil structure from one experiment to the next. This allows comparing the soils reaction in different conditions (e.g., wet vs. dry) on a soil that had been formed by natural rainfall in the field although it limits soil erosion that would be expected with such intense precipitation (see Discussion section for more detail).

The booster (Mac Allister 900W) generates a pressure fluctuating between 1.4 and 2.8 bar. It is connected to a pressure regulator to minimize variations in output pressure. The booster is fed by 100-L water reservoirs, in which water tracers can be applied. The rain collector frame covers 1.5 cm of the soil's edges and collects all the rainwater falling onto these edges and outside the soil surface by means of the PVC chimney. The excess rainwater is returned to the reservoir. During the rainfall simulation, a short PVC hose is connected to each of the two outlets of the soil box (drainage and overland flow) to conduct the flow to glass containers placed on scales. In our test, we used a Denver Instrument S-2002 (2 kg max, $d = 0.01 \text{ g}$) for overland flow and a Precia Molen X201-B (30 kg max, $d = 1 \text{ g}$) for drainage. The scales are connected to a PC that records mass values at 1 Hz. There are no depressions in the flow path between soil and sample collection that could accumulate water and hinder flow continuity. This ensures the samples to contain both the liquid fraction and the suspended matter.

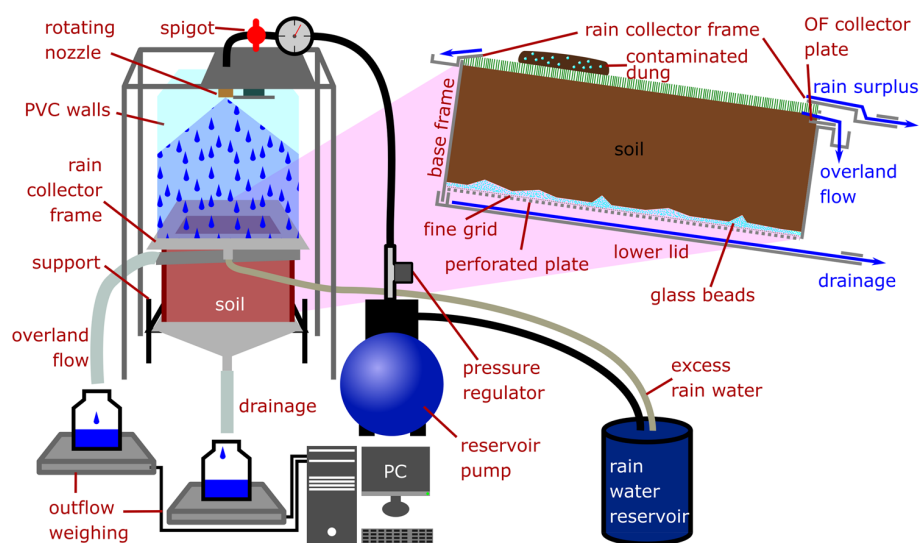


FIGURE 1 Schematic illustration of the rainfall simulation setup and a 2D longitudinal cut through the sampling box

2.1.2 | The sampling box

The sampling box is illustrated in Figure 1. It is made entirely of stainless steel in order to minimize chemical interactions with the studied organic molecules and allow cleaning with an organic solvent (acetonitrile) or thermal treatment. Blueprints and photos are provided in Supplemental Figures S1–S3. It consists of a $60 \times 30 \times 25 \text{ cm}^3$ (LWD) base frame and removable bottom and top lids. The base frame includes a horizontally mounted removable 0.7-mm wire grid with 2-mm gaps, supported by a 3-mm thick perforated plate with 5-mm square holes, mounted 22 cm from the top of the frame. The perforated plate is supported by a mount welded to the bottom lid. On the downhill side, the top 3 cm of the base frame is perforated with 5-mm square holes to allow overland flow to pass through. A gap below the perforated portion allows for the insertion of a $3 \times 296 \times 90 \text{ mm}^3$ overland flow collector plate into the soil 3 cm from the surface of the box. An inclined U-shaped profile with an outlet (2-cm pipe) on the side is welded to this side of the base frame allowing for the collection of overland flow. The bottom lid is designed to collect the drainage flow. Its downhill end converges to a 2-cm pipe for water collection. The top lid is only used during soil sampling. Both lids are attached to the base frame with stainless steel toggle latches (RS PRO).

2.2 | Procedure for sampling intact soil in the field

The soil sampling protocol is designed to preserve the soil structure. Sampling should be done under intermediate to dry conditions, in order to avoid sampling very soft to liquid

muddy soil, which would lose its structure. Under very dry conditions, the soil should be slightly moistened with purified water to soften it and ensure sufficient cohesion during cutting. The required water content depends on the soil type. In practice, gradual moistening of an area close to the sampling location can help determine the right amount of moistening that provides cohesion without making the soil muddy. The soil sample should be selected in a representative location (vegetation, land use, slope, part of the hillslope). The original slope should correspond approximately to the slope that will be used in the experiment. The sample should have a relatively even surface. The following sampling procedure is divided into 12 numbered steps, a selection of which is shown in Supplemental Figure S4. The positional terms used are depicted in Supplemental Figure S1. (1) The sampling frame is placed at the selected sampling location, oriented with the outlet pointing down the slope. (2) A trench approximately 35-to-40-cm deep, 1.5-m long and 1-m wide is excavated on one side of the selected sample location for easy access to the soil from the side. A narrower trench is dug on the other three sides while leaving 5–10 cm of intact soil on each side of the sample to protect it.

The frame is gradually lowered around the sample by repeating the following four steps (3–6) a few centimeters each time until the soil surface is aligned with the top edge of the sampling case (not extending beyond the frame's upper edge and not being more than 15 mm below it): (3) The soil is carefully cut to fit the case. (4) Small rocks protruding from the side are removed and the holes are filled with wet, compacted original soil. If a hole is too large (more than a few centimeters of diameter), changing the sampling location should be considered. (5) The sidewalls are covered with bentonite clay to seal them before (6) sliding the case along the walls

(perpendicularly to the soil surface). (7) The cutting of the bottom of the soil starts by making a set of horizontal bores below the bottom of the soil from the side using a battery powered drill with a rock drill bit. Then (8) 6 mm (35-mm wide) steel blades are carefully hammered into the bores, one by one, next to each other, from the side, to support the soil. (9) The top of the soil sample is covered with a lid attached to the base frame. Two steel bars are slid under the blades in longitudinal orientation (perpendicularly to the blades). Two other steel bars are placed on top of the sample and screwed to the bottom bars with four 32-cm long M10 threaded rods. This step serves to firmly hold the sample. (10) The sample is lifted by hand (three people) and turned upside down by slowly rolling it over the edge of the hole. With the sample held firmly in the frame, disturbance should be minimal when turning the sample slowly. After removing the steel bars, (11) the bottom 3 cm of soil that was potentially affected by the steel blades is removed. To ensure a uniform surface of the bottom of the soil and to distribute the soil's weight, (12) a thin layer (<1 cm) of 4-mm glass spheres is added before closing with the grid, the perforated plate and the lid firmly clipped onto the bottom soil. The sample is then turned upright for transport to the laboratory. Prior to the rainfall simulation experiments, the overland flow collector plate is entered horizontally into the upper soil on the downhill side of the box (1-cm deep, 3 cm below the frames upper edge; see Figure 1). Finally, the upper edges of the soil are sealed with a mixture of field soil matrix and water. This sealing as well as the rain collector frame covering the boundaries are used to prevent infiltration through potential gaps along the sidewalls. We could not apply petroleum jelly as used by other authors (e.g., Williams et al., 2020) because of potential chemical interferences with the studied contaminants. However, in addition to the measures described above, flow along gaps between the sidewalls and the soil should be limited as long as the soil is in unsaturated condition. Vegetation is cut to a level below the rain collector frame.

2.3 | Rainfall simulation experiment

2.3.1 | Measured variables

Artificial rainfall is applied at the selected intensity and duration. In the test case section, we present two nozzles that allow to obtain intensities of 50 and 100 mm h⁻¹. Drainage and overland flow are collected in separate, pre-weighed sample containers placed on two scales. The mass values are transmitted to a PC via a serial port at 1 Hz and stored together with the time in a “.csv” file. Because of the flow monitoring via mass values, special care must be taken when changing the sampling containers: First, the hose is moved to the new container. After waiting 3 s, the old container is removed and the

new one is placed on the scale. The times of moving the hose and placing the new container are noted, as well as the ID of each pre-weighed container. The mass values during the container change are removed from the mass time series. The soil is weighed with the box before and after the rainfall simulation experiment. The difference gives the change in soil water storage (ΔS_{TOT}).

2.3.2 | Calculated variables

The mass values of the empty containers are systematically subtracted from the mass time series and after each container change, the previous mass is added to all subsequent timesteps by a python program. This provides a cumulative time series for each water outflow (drainage and overland flow), assuming that all mass recovered is water and has a density of 1 g ml⁻¹. The water volume can be converted to water height by dividing it by the soil surface (30 × 60 cm²). The values at the last timestep of these series are the total outflow volume of the drainage (VD_{TOT}) and overland flow (VR_{TOT}). The instantaneous water discharges of drainage $Q_D(t)$ and overland flow $Q_R(t)$ at each time t are obtained by dividing the volume difference by time difference between two consecutive measurements. Weighing is continued for several hours after the end of rain application (until dripping stops) to capture all outflow water.

The total soil water content at the beginning (V_{sw0}) and end (V_{swf}) of each experiment is obtained by subtracting the weight of the whole soil dried at 105 °C until stabilization (approximately 10 d) after the rainfall simulation experiments are completed and the mass of the empty box from the total mass.

The total precipitation volume (VP_{TOT}) is calculated by closing the water mass balance as follows:

$$VP_{TOT} = VD_{TOT} + VR_{TOT} + \Delta S_{TOT} \quad (1)$$

The precipitation intensity $PI(t)$ is set to (VP_{TOT}/T) for the duration of the rainfall simulation and 0 otherwise, assuming constant intensity. T is the rainfall duration.

If a tracer (e.g., bromide, deuterium oxide) is used, the event water fraction (i.e., fraction of flow from current rain event) can be calculated through a two end member mixing model. Assuming a known concentration c_s in the soil water prior to the experiment (e.g., $c_s = 0$ if no tracer has been added previously), a known concentration c_p in the tracer-enriched artificial rainwater, and a measured drainage concentration C_D , we can decompose Q_D by applying the water mass conservation hypothesis:

$$Q_D = Q_{D_{ev}} + Q_{D_{pre}} \quad (2)$$

and the tracer mass conservation hypothesis:

$$Q_D \times c_D = Q_{Dev} \times c_p + Q_{Dpre} \times c_s \quad (3)$$

where Q_{Dev} is the discharge of water from the current rain event in the drainage and Q_{Dpre} is the discharge of pre-event water in the drainage (water that was stored in the soil before the rain event). By substituting Equation 2 into Equation 3, we can then determine

$$Q_{Dev} = Q_D \times \frac{(c_D - c_s)}{(c_p - c_s)} \quad (4)$$

where $(c_D - c_s) / (c_p - c_s)$ represents the event water fraction f_{ev} .

The overland flow coefficient CR for a whole event (i.e., the period between the start of precipitation to end of outflow) and at a time t during the event CR(t) are calculated as cumulative overland flow volume (of the whole event or up to t , respectively) divided by the cumulative precipitation volume (of the whole event or up to t , respectively).

2.4 | Technical validation

2.4.1 | Homogeneity and stability of simulated precipitation

The spatial homogeneity of the simulated rainfall was experimentally validated by placing 105 cylindrical plastic containers with a diameter of 4 cm and a height of 5.8 cm inside the empty sampling case, aligning the plastic containers and the base frame at the top edge. Rain was then simulated for approximately 20 min and the water height in each container was measured. Temporal variability and overall intensity were verified by simulating rain on an empty sampling device and continuously measuring the discharge. We proceeded like this for various full cone sprinkler nozzles of the Lechler 490 series generating intensities ranging from 50 mm h⁻¹ (490.488.30) to 100 mm h⁻¹ (490.608.30).

2.4.2 | Contaminant transfer test

The device was tested on a colluvial brown calcareous pasture soil with silt-loam texture from Le Pradel, 07170 Mirabel in France (44.58206° N, 4.49998° E, WGS84). The site is part of the OHMCV observatory and is presented in Nord et al. (2017). Fresh cow dung (80% humidity, cows not treated with avermectins) was contaminated with IVM (veterinary oral solution ORAMEC) to a final concentration of 3 mg kg⁻¹ fresh weight, corresponding to the highest observed concentration in dung after pour-on treatment (Herd et al., 1996).

The contaminated cow dung was homogenized and shaped by hand into a circular cake, 20 cm in diameter. It was placed with its edges 30 cm from the downhill edge, 10 cm from the uphill edge and 5 cm from both sides of the sampling device (Supplemental Figure S5). Artificial rain (distilled water with 130 mg L⁻¹ bromide tracer for the calculation of event water fractions) was applied for 1 h at an intensity of 92 mm h⁻¹, corresponding to a rainfall event with a return period of 10–20 yr for this region (Beuerle, 2021). The same intensity over half an hour corresponds to return period of about 5 yr. The length of the simulated rainfall event allows following the evolution of water and contaminant fluxes, while the event can still be used to approximate the water and contaminant transfer during a shorter more frequent event by analyzing the beginning of the event. The experiment was conducted on semi-dry soil ($\theta_0 = 22\%$). Sampling and measurement were stopped 4 h after the start of the simulated rainfall. In total we collected 14 drainage samples and 9 overland flow samples. For the drainage samples, the collection interval varied from 2.5 min at the beginning of the experiment over 6 min during most of the simulation to 2 h for the last sample. For overland flow, the collection interval was 6 min at the beginning of the simulation and 8 min at the end.

2.5 | Water sampling and chemical analysis

Samples were collected in glass bottles (Schott Duran 500 ml), which were washed using a professional washing machine (Miele professional G 7883) and then heated to 500 °C for 3 h (Nabertherm L 9/11/B170 oven) before use to ensure analytical level cleanliness. Immediately after collection, the bulk water samples were split for different analyzes. In this test, the following analyses were carried out: major anions, dissolved organic carbon (not presented) and IVM. The coefficient of variation and limit of quantification determined for the IVM analyzes were <5% and 1 ng L⁻¹, respectively. More details on the chemical analysis, which is specific to our test experiment, can be found in the Supplemental Material file.

3 | RESULTS AND DISCUSSION OF THE TECHNICAL VALIDATION

3.1 | Rainfall simulation

3.1.1 | Homogeneity and stability

Here we present results obtained with the Lechler 490.680.30 sprinkler nozzle mounted 67 cm above the soil surface (center), which is the configuration used in the presented test. The coefficient of variation of rain intensity was 8% over the 78 spatially distributed samples that were not covered by the

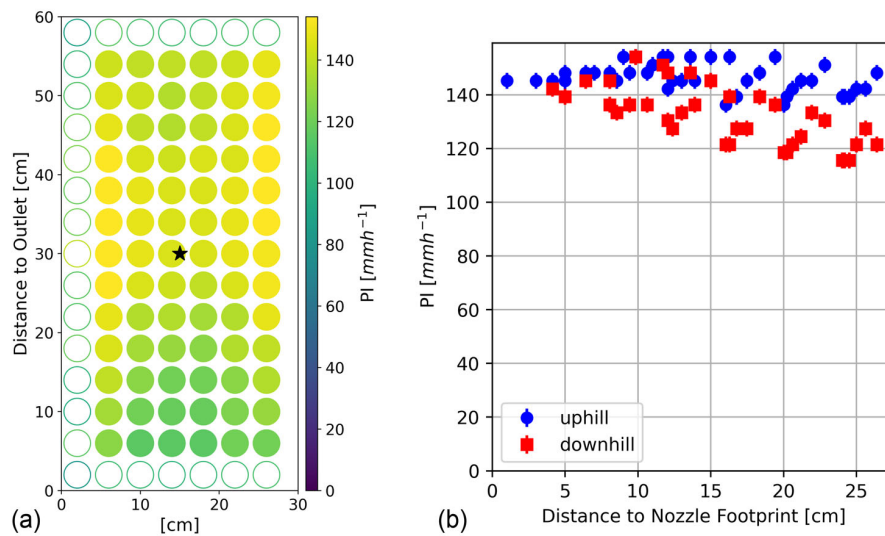


FIGURE 2 Validation of spatial homogeneity of rainfall. (a) Spatial distribution of rainfall intensity across the box given in color gradients and plotted at cm-coordinates of the box; $y = 0$ represents the outlet (bottom side of the box). The black star indicates the nozzle location. Empty markers represent containers partially covered by the border and not considered in the data analysis. (b) Rain intensity measured in plastic containers as a function of box-surface parallel distance to the nozzle footprint. Blue circles represent the locations uphill and red squares the locations downhill of the nozzle footprint. Error bars indicate the uncertainty of the water height measurement

border. The spatial distribution is shown in Figure 2. As expected, the 8° slope resulted in a slight decrease in intensity toward the bottom of the slope, where raindrop trajectory and dispersion are highest. Regarding temporal stability, the system produced small periodic variations in rain intensity of 10% with a period of 2.5–3 min due to pumping cycles with a constant average throughout the artificial rain event. With the Lechler 490.488.30 sprinkler nozzle, the coefficient of variation in rain intensity was 7% over the spatially distributed samples and the periodic variations due to pumping cycles were 10% with a period of 3–3.5 min.

3.1.2 | Limitations of the rainfall simulation protocol

The two sprinkler nozzles used Lechler 490.488.30 and 490.680.30 generate fine droplets (mean diameter $[D_m] = 0.69$ and 0.75 mm, respectively) with low kinetic energy ($E_{kin} = 1.48$ J m⁻² mm⁻¹ and 2.76 J m⁻² mm⁻¹, respectively). For comparison, we analyzed disdrometric rainfall data from the nearby La Souche meteorological station from July 2012 to March 2020 (OHMCV, 2012). For rainfall intensities between 50 and 100 mm h⁻¹, the average D_m was 1.05 mm (0.41–1.94) and the average E_{kin} was 63.4 J m⁻² mm⁻¹ (16.1–208.7). This shows that the simulated rain has less kinetic energy and slightly smaller drops than the observed average for similar precipitation intensities. While D_m is within the range of observed values,

the kinetic energy is much lower. The size distributions of simulated raindrops measured with an *OTT Parsivel2* disdrometer are illustrated in Supplemental Figure S6.

The choice to generate fine droplets with low kinetic energy was made with the intention of preserving soil structure over several rainfall simulation experiments so that transfer through initially wet vs. dry soil could be compared for the same state of the soil surface. The soil surface itself being formed by natural precipitation and other processes in the field, which a rainfall simulator could most likely not perfectly imitate. Furthermore, the goal was to assess contaminant transfer in the dissolved phase rather than to study soil erosion processes. This has the drawback of not generating realistic erosion thus underestimating transfer of soil particles and sorbed contaminants. If this were the focus, a different nozzle could be used and mounted at higher distance from the soil surface to higher kinetic energy and larger drop size, as for example in Humphry et al. (2002).

Monitoring water discharge via the outflow mass has the advantage of being non-contact and independent of the receiver, which facilitates analytical level cleanliness and avoids stagnating zones that could trap water and sediment. It allows relatively precise measurement (depending on the scale's precision) and simple automated processing. However, it requires a particular rigor when changing the sampling containers. Assuming an average mass uncertainty of 2 g at each container change, we obtain a cumulated uncertainty of 30 ml (0.17 mm) over the whole event, which represents 0.2% of the total rainfall (92 mm).

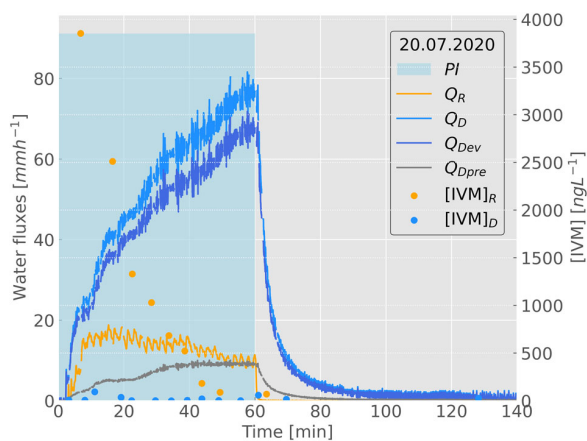


FIGURE 3 Dots represent ivermectin concentration ([IVM]) in drainage (blue, subscript D) and overland flow (orange, subscript R) during the rainfall simulation experiment, lines represent corresponding water discharges (same color). The drainage discharge is divided into event water (dark blue) and pre-event water (gray) using the bromide tracer concentrations. For illustration purposes, a sliding average of 15 triangularly weighted values is applied to the water discharges to smooth them

The calculation of soil water content by subtracting dry mass assumes that there is no significant change in soil dry mass during the experiments. For solid matter fluxes with water, this can be verified and corrected by drying or filtering the outflows and determining their dry mass. For plant growth and organic matter decomposition, this is considered negligible over a few days. For longer experiments, this adds uncertainty to the absolute water content. The evolution of water content and the magnitude of water content change (ΔS_{TOT}) are not affected. The uncertainty of weighing the entire soil box was 100 g, which corresponds to an uncertainty in the absolute volumetric water content of 2.8% (0.56 mm). It should be kept in mind that in the current setup (seepage face as lower boundary condition), the device is designed to study infiltration excess overland flow and leaching.

3.2 | Application of the experimental device to transfer of IVM

3.2.1 | Water and IVM fluxes

The event CR for the contaminant transfer test experiment was 13.5%, while $Q_R(t)$ is slightly decreasing over the course of the event (from 17 mm h⁻¹ after 15 min to 10 mm h⁻¹ after 60 min; Figure 3). The $Q_D(t)$ increases throughout the event reaching 75 mm h⁻¹ after 60 min. The event water fraction in the drainage was relatively constant throughout the experiment (87%). The IVM concentration values are generally higher (69–3,854 ng L⁻¹) in overland flow with highest

values in the beginning of the event and decreasing with time, while they are lower (0.5–94 ng L⁻¹) and much more irregular with multiple peaks in drainage. Overall, during the event, 174 ng IVM (0.058‰ of applied quantity) were exported via drainage, while 2,974 ng (0.99‰) were exported via overland flow. As this experiment was deployed to test the device, potential environmental implications are not discussed in this article and will be part of another study.

3.2.2 | Applicability of the experimental setup

The test confirmed the design of the box in terms of the feasibility of intact soil sampling and the overall setup for contaminant transfer experiments. The setup allows experiments to be conducted under controlled conditions (rain duration and intensity, initial soil condition, temperature, contaminant input) on intact field soil at a scale that preserves soil structure and especially macropores acting as preferential flow paths (drying cracks, earthworm galleries, root channels). Using the box for both sampling and rainfall experiments without the need to transfer the soil facilitates handling and increases experimental reliability. All mass balance components can be measured or calculated and water discharges as well as contaminant and tracer concentrations can be measured at very high (seconds) and high (minutes) intra-event frequency, respectively. Working with intact soils potentially limits the reproducibility of results due to sample heterogeneity and the large number of influencing factors, but nonetheless represents a more realistic approach to mimic real environmental systems and parameters. This is crucial for a better estimation of environmental risks by a more accurate, although less precise, prediction of environmental concentration.

This protocol can be adapted to different scientific questions. A wide range of rain intensities and durations can be selected by using different nozzles. The rain simulator could also be adapted to produce larger drops with higher kinetic energy if erosion is to be studied.

The presented device has the potential to contribute to a more realistic estimation of the transfer of environmental contaminants through and over the topsoil and thereby improve the environmental concentrations predicted in environmental risk assessments. Further application of this device is underway and we are open to collaborations willing to use it.

ACKNOWLEDGMENTS

We acknowledge the work of many engineers at the Institut des Géosciences de l'Environnement (IGE) of Grenoble for the construction of the devices (Service Technique) and for the chemical analysis (Plateau Air-O-Sol, with the funding of some of the equipment by the Labex OSUG@2020 - ANR10 LABX56). Bernard Mercier (IGE) is thanked for having developed a program for serial communication with the

scales. Christine Baduel (IGE) is thanked for her expertise in setting up the SPE protocol at IGE. Céline Voiron (IGE) is thanked for her analytical support. The Domaine Olivier de Serres (Ardèche, France) is thanked for giving access to the study site and allowing soil sampling. The HyDRIMZ team is thanked for many fruitful discussions. The OHMCV SNO observatory of the INSU of CNRS is part of OZCAR Research infrastructure (<https://www.ozcar-ri.org>) that is supported by the French Ministry of Research Institutions and Universities.

AUTHOR CONTRIBUTIONS

Nico Hachgenei: Conceptualization, data curation, formal analysis, investigation, methodology, project administration, software, supervision, validation, visualization, writing - original draft. Guillaume Nord: Conceptualization, funding acquisition, investigation, methodology, resources, supervision, writing - review & editing. Lorenzo Spadini: Conceptualization, investigation, methodology, resources, supervision, writing - review & editing. Henri Mora: Investigation, methodology, resources. François Courvoisier: Formal analysis, investigation, software. Jean-François Sutra: Formal analysis, investigation. Jean-Pierre Vandervaere: Conceptualization, methodology, resources, writing - review & editing. Cédric Legoût: Conceptualization, writing - review & editing. Marie-Christine Morel: Conceptualization, validation, writing - review & editing. Jean Martins: Conceptualization, writing - review & editing. Anne Lespine: Data curation, writing - review & editing. Céline Duwig: Conceptualization, funding acquisition, investigation, methodology, resources, supervision, writing - review & editing.

CONFLICT OF INTEREST

The authors declare no conflict of interest.

ORCID

Nico Hachgenei  <https://orcid.org/0000-0002-0490-2103>

Guillaume Nord  <https://orcid.org/0000-0001-5541-9368>

Jean-Pierre Vandervaere  <https://orcid.org/0000-0002-9620-0589>

Jean Martins  <https://orcid.org/0000-0003-0314-1311>

Anne Lespine  <https://orcid.org/0000-0001-8153-8555>

Celine Duwig  <https://orcid.org/0000-0003-1505-8996>

REFERENCES

- Archundia, D., Duwig, C., Spadini, L., Morel, M. C., Prado, B., Perez, M. P., Orsag, V., & Martins, J. M. F. (2019). Assessment of the sulfamethoxazole mobility in natural soils and of the risk of contamination of water resources at the catchment scale. *Environment International*, 130(February), 104905. <https://doi.org/10.1016/j.envint.2019.104905>
- Bachmair, S., Weiler, M., & Nützmann, G. (2009). Controls of land use and soil structure on water movement: Lessons for pollutant transfer through the unsaturated zone. *Journal of Hydrology*, 369(3–4), 241–252. <https://doi.org/10.1016/j.jhydrol.2009.02.031>
- Benecke, P., Beese, F., & van der Ploeg, R. R. (1976). Bodenhydrologische Methoden zur Untersuchung ungestörter, skelettreicher Böden. *Zeitschrift Für Pflanzenernährung Und Bodenkunde*, 139(3), 361–371. <https://doi.org/10.1002/jpln.19761390311>
- Beuerle, A. (2021). *Implémentation d'un modèle conceptuel distribué pour simuler l'effet de la variabilité spatiale de la pluie sur les transferts de surface*. ENSE3, G-INP Université Grenoble Alpes.
- Bicudo, J. R., & Goyal, S. M. (2003). Pathogens and manure management systems: A review. *Environmental Technology (United Kingdom)*, 24(1), 115–130. <https://doi.org/10.1080/09593330330309385542>
- Boxall, A. B. A. (2017). Contamination from the agricultural use of growth promoters and medicines. In *Encyclopedia of the Anthropocene* (Volume 5, pp. 257–262). Elsevier Inc. <https://doi.org/10.1016/B978-0-12-809665-9.09900-6>
- Boyle, M., Frankenberger, W. T., & Stolzy, L. H. (1989). The influence of organic matter on soil aggregation and water infiltration. *Journal of Production Agriculture*, 2(4), 290–299. <https://doi.org/10.2134/jpa1989.0290>
- Buchter, B., Leuenberger, J., Wierenga, P. J., & Richard, F. (1984). Preparation of large core samples from stony soils. *Soil Science Society of America Journal*, 48(6), 1460–1462. <https://doi.org/10.2136/sssaj1984.03615995004800060053x>
- Carmi, G., & Berliner, P. (2008). The effect of soil crust on the generation of runoff on small plots in an arid environment. *Catena*, 74(1), 37–42. <https://doi.org/10.1016/j.catena.2008.02.002>
- Chen, J., Yang, L., Chen, X., Ripp, S., Radosevich, M., & Zhuang, J. (2021). Bacterial mobility facilitated by soil depth and intact structure. *Soil and Tillage Research*, 209, 104911. <https://doi.org/10.1016/j.still.2020.104911>
- Darboux, F., Davy, P., Gascuel-Oudou, C., & Huang, C. (2002). Evolution of soil surface roughness and flowpath connectivity in overland flow experiments. *Catena*, 46(2–3), 125–139. [https://doi.org/10.1016/S0341-8162\(01\)00162-X](https://doi.org/10.1016/S0341-8162(01)00162-X)
- Duwig, C., Prado, B., Tinet, A.-J., Delmas, P., Dal Ferro, N., Vandervaere, J. P., Denis, H., Charrier, P., Gastelum Strozzi, A., & Morari, F. (2019). Impacts of land use on hydrodynamic properties and pore architecture of volcanic soils from the Mexican Highlands. *Soil Research*, 57(6), 629. <https://doi.org/10.1071/SR18271>
- Fernández, C., Porcel, M. A., Alonso, A., Andrés, M. S., & Tarazona, J. V. (2011). Semifield assessment of the runoff potential and environmental risk of the parasiticide drug ivermectin under Mediterranean conditions. *Environmental Science and Pollution Research*, 18(7), 1194–1201. <https://doi.org/10.1007/s11356-011-0474-8>
- Feyereisen, G. W., & Folmar, G. J. (2009). Development of a laboratory-scale lysimeter system to simultaneously study runoff and leaching dynamics. *Transactions of the ASABE*, 52(5), 1585–1591.
- Flury, M., Flühler, H., Jury, W. A., & Leuenberger, J. (1994). Susceptibility of soils to preferential flow of water: A field study. *Water Resources Research*, 30(7), 1945–1954. <https://doi.org/10.1029/94WR00871>
- Franzuebbers, A. (2002). Water infiltration and soil structure related to organic matter and its stratification with depth. *Soil and Tillage Research*, 66(2), 197–205. [https://doi.org/10.1016/S0167-1987\(02\)00027-2](https://doi.org/10.1016/S0167-1987(02)00027-2)
- Goss, M. J., Ehlers, W., & Unc, A. (2010). The role of lysimeters in the development of our understanding of processes in the vadose zone relevant to contamination of groundwater aquifers. *Physics and Chemistry of the Earth*, 35(15–18), 913–926. <https://doi.org/10.1016/j.pce.2010.06.004>

- Govers, G., Takken, I., & Helming, K. (2000). Soil roughness and overland flow. *Agronomie*, 20(2), 131–146. <https://doi.org/10.1051/agro:2000114>
- Guo, M., & Chorover, J. (2006). Leachate migration from spent mushroom substrate through intact and repacked subsurface soil columns. *Waste Management*, 26(2), 133–140. <https://doi.org/10.1016/j.wasman.2004.12.024>
- Hairsine, P., Moran, C., & Rose, C. (1992). Recent developments regarding the influence of soil surface characteristics on overland flow and erosion. *Soil Research*, 30(3), 249. <https://doi.org/10.1071/SR9920249>
- Hedlund, J., Longo, S. B., & York, R. (2020). Agriculture, Pesticide Use, and Economic Development: A Global Examination (1990–2014). *Rural Sociology*, 85(2), 519–544. <https://doi.org/10.1111/ruso.12303>
- Herd, R. P., Sams, R. A., & Ashcraft, S. M. (1996). Persistence of ivermectin in plasma and faeces following treatment of cows with ivermectin sustained-release, pour-on or injectable formulations. *International Journal for Parasitology*, 26(10), 1087–1093. [https://doi.org/10.1016/S0020-7519\(96\)80007-5](https://doi.org/10.1016/S0020-7519(96)80007-5)
- Humphry, J. B., Daniel, T. C., Edwards, D. R., & Sharpley, A. N. (2002). A portable rainfall simulator for plot – Scale runoff studies. *Applied Engineering in Agriculture*, 18, 199–204. <https://doi.org/10.13031/2013.7789>
- Kay, P., Blackwell, P. A., & Boxall, A. B. A. (2005a). A lysimeter experiment to investigate the leaching of veterinary antibiotics through a clay soil and comparison with field data. *Environmental Pollution*, 134(2), 333–341. <https://doi.org/10.1016/j.envpol.2004.07.021>
- Kay, P., Blackwell, P. A., & Boxall, A. B. A. (2005b). Column studies to investigate the fate of veterinary antibiotics in clay soils following slurry application to agricultural land. *Chemosphere*, 60(4), 497–507. <https://doi.org/10.1016/j.chemosphere.2005.01.028>
- Krogmann, H. (1986). Ungestörte Bodensäulen: Eine Methode zur Herstellung, Berechnung und Installation im Labor. *Zeitschrift Für Pflanzenernährung Und Bodenkunde*, 149(3), 271–276. <https://doi.org/10.1002/jpln.19861490304>
- Liebig, M., Fernandez, Á. A., Blübaum-Gronau, E., Boxall, A., Brinke, M., Carbonell, G., Egeler, H., Fenner, K., Fernandez, C., Fink, G., Garric, J., Halling-Sørensen, B., Knacker, T., Krogh, K. A., Küster, A., Löffler D., Cots, M. Á. P., Pope, L., Prasse, C., ..., Duisy, K. (2010). Environmental risk assessment of ivermectin: A case study. *Integrated Environmental Assessment and Management*, 6(SUPPL. (1)), 567–587. <https://doi.org/10.1002/ieam.96>
- Martín M. Á., Martínez F. S. J., Perfect E., Lado M., Pachepsky Y. (2017) Soil structure and function in a changing world: Characterization and scaling. *Geoderma*, 287, 1–3. <https://doi.org/10.1016/j.geoderma.2016.08.015>
- Milleret, R., Le Bayon, R. C., Lamy, F., Gobat, J. M., & Boivin, P. (2009). Impact of roots, mycorrhizas and earthworms on soil physical properties as assessed by shrinkage analysis. *Journal of Hydrology*, 373(3–4), 499–507. <https://doi.org/10.1016/j.jhydrol.2009.05.013>
- Nizzetto, L., Futter, M., & Langaas, S. (2016). Are agricultural soils dumps for microplastics of urban origin? *Environmental Science and Technology*, 50(20), 10777–10779. <https://doi.org/10.1021/acs.est.6b04140>
- Nord, G., Boudevillain, B., Berne, A., Branger, F., Braud, I., Dramais, G., Gérard, S., Le Coz, J., Legoût, C., Molinié, G., Van Baelen, J., Vandervaere, J. P., Andrieu, J., Aubert, C., Calianno, M., Delrieu, G., Grazioli, J., Hachani, S., Horner, I., ..., Wijbrans, A. (2017). A high space-time resolution dataset linking meteorological forcing and hydro-sedimentary response in a mesoscale Mediterranean catchment (Auzon) of the Ardèche region, France. *Earth System Science Data*, 9(1), 221–249. <https://doi.org/10.5194/essd-9-221-2017>
- Obimakinde, S., Fatoki, O., Opeolu, B., & Olatunji, O. (2017). Veterinary pharmaceuticals in aqueous systems and associated effects: An update. *Environmental Science and Pollution Research*, 24(4), 3274–3297. <https://doi.org/10.1007/s11356-016-7757-z>
- Observatoire Hydro-météorologique Méditerranéen Cévennes-Vivarais (OHMCV). (2012). *DSD network, La Souche*. Centre national de la recherche scientifique, Observatoire des sciences de l'Univers de Grenoble, Observatoire de Recherche Méditerranéen de l'Environnement. <https://doi.org/10.17178/OHMCV.DSD.SOU.12-16.1>
- Popova, I. E., Bair, D. A., Tate, K. W., & Parikh, S. J. (2013). Sorption, leaching, and surface runoff of beef cattle veterinary pharmaceuticals under simulated irrigated pasture conditions. *Journal of Environmental Quality*, 42(4), 1167–1175. <https://doi.org/10.2134/jeq2013.01.0012>
- Rath, S., Pereira, L. A., Bosco, S. M. D., Maniero, M. G., Fostier, A. H., & Guimarães, J. R. (2016). Fate of ivermectin in the terrestrial and aquatic environment: Mobility, degradation, and toxicity towards *Daphnia similis*. *Environmental Science and Pollution Research*, 23(6), 5654–5666. <https://doi.org/10.1007/s11356-015-5787-6>
- Sadeghi, A. M., Isensee, A. R., & Shirmohammadi, A. (2000). Influence of soil texture and tillage on herbicide transport. *Chemosphere*, 41(9), 1327–1332. [https://doi.org/10.1016/S0045-6535\(00\)00028-X](https://doi.org/10.1016/S0045-6535(00)00028-X)
- Sarmah, A. K., Meyer, M. T., & Boxall, A. B. A. (2006). A global perspective on the use, sales, exposure pathways, occurrence, fate and effects of veterinary antibiotics (VAs) in the environment. *Chemosphere*, 65(5), 725–759. <https://doi.org/10.1016/j.chemosphere.2006.03.026>
- Schäfer, R. B., Caquet, T., Siimes, K., Mueller, R., Lagadic, L., & Liess, M. (2007). Effects of pesticides on community structure and ecosystem functions in agricultural streams of three biogeographical regions in Europe. *Science of the Total Environment*, 382(2–3), 272–285. <https://doi.org/10.1016/j.scitotenv.2007.04.040>
- Stuer-Lauridsen, F., Birkved, M., Hansen, L. P., Holten Lützhøft, H. C., & Halling-Sørensen, B. (2000). Environmental risk assessment of human pharmaceuticals in Denmark after normal therapeutic use. *Chemosphere*, 40(7), 783–793. [https://doi.org/10.1016/S0045-6535\(99\)00453-1](https://doi.org/10.1016/S0045-6535(99)00453-1)
- Williams, M. R., Coronel, O., McAfee, S. J., & Sanders, L. L. (2020). Preferential flow of surface-applied solutes: Effect of lysimeter design and initial soil water content. *Vadose Zone Journal*, 19(1), 1–15. <https://doi.org/10.1002/vzj2.20052>

SUPPORTING INFORMATION

Additional supporting information may be found in the online version of the article at the publisher's website.

How to cite this article: Hachgenei, N., Nord, G., Spadini, L., Mora, H., Courvoisier, F., Sutra, J.-F., Vandervaere, J.-P., Legoût, C., Morel, M.-C., Martins, J., Lespine, A., & Duwig, C. (2022). A device to simulate contaminant transfer and surface and subsurface flow through intact soil monoliths. *Vadose Zone Journal*, 21, e20184. <https://doi.org/10.1002/vzj2.20184>

4.2.2 Additional methodological specifications

In addition to the analyses described in the article and supplemental material, subsamples of each water sample were collected systematically for the quantification of dissolved organic carbon (DOC) in 55 mL polypropylene centrifuge tubes (Roth SA, France). They were centrifuged for 15 min and filtered at 0.45 μm with *Sartorius Minisart NML* cellulose acetate filters. DOC concentrations were analyzed at ISTERre institute (Grenoble, France) using a *TOC Shimadzu VCSN* carbon analyzer. Blank DOC samples contained mostly below 1 mg L^{-1} but in some cases up to 5 mg L^{-1} were detected. Therefore, low DOC concentrations should be considered with care. The source of this pollution might be the organic material of the filters or the polypropylene tubes used for sampling. The solid phase extraction (SPE) and chemical analysis are described briefly in the article's supplemental material (Appendix C). The sample preparation and SPE were performed at the IGE lab. The SPE protocol was based on a protocol provided by INTHERES laboratory, Toulouse, France and adapted for this study. The quantification of IVM from the events 1C, 2C, 1D and 2D (see below) was performed at INTHERES laboratory, Toulouse, France after the method described by Lifschitz et al. (2000) and in the above article. For all following samples, a new method has been developed at the IGE and validated by an inter-comparison with the INTHERES laboratory (Rijal, 2020; Rijal et al., 2021). Before the IVM transfer experiments, a soil and dung blank was generated by applying an untreated cow pat to soil E (see below) and simulating a precipitation event. The cow pat was removed directly after this blank experiment before conducting the transfer experiments. A bulk water sample from this event was analyzed and no IVM was detected, confirming its absence in detectable concentrations on these soils and in the unspiked dung. The choice to artificially spike the dung of untreated cows instead of using the dung of treated cows was made in order to (i) avoid the risk of affecting the IVM by freezing of the dung for storage and (ii) be able to have the same, reproducible initial condition of the dung in the beginning of each experiment.

As mentioned in the article, water samples were collected over a few minutes each and usually there was a break of several minutes between two samples. Continuous solute fluxes (IVM, COD, anions) were calculated by applying the analyzed values to the respective sampling period and performing a linear interpolation between them, like described for event water fractions in the article. The soils' porosities n were estimated from bulk density ρ_b assuming an average particle density ρ_p of 2.65 g cm^{-3} .

4.2.3 Soil sampling locations and experiments

We sampled pasture soils in three different locations in the Claduègne catchment, two on sedimentary and one on basaltic geology (Fig. 4.2). On sedimentary geology, the focus is on Pradel 2 (Fig. 4.2). The locations were chosen to represent typical pastures of each of the two geological units in order to compare them in terms of transfer dynamics of water, solutes and IVM. In the following, the term experiment refers to a series of simulated precipitation events on one soil or cow pat. The term precipitation event refers to the hour over which precipitation was simulated and the term event includes a precipitation event and the generated fluxes until the end of monitoring and sampling. We conducted experiments of successive simulated precipitation events on 6 soils from these three locations, called B, C, D, E, I and J, to each of which a contaminated cow pat was applied before

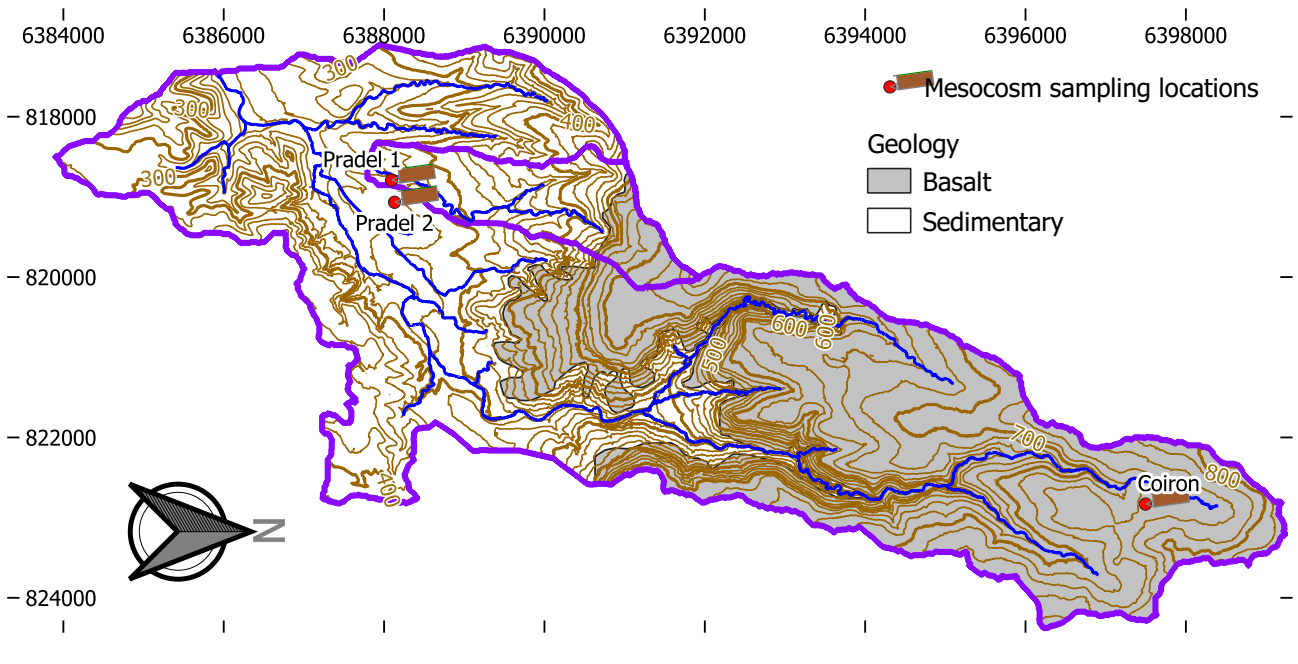


FIGURE 4.2: Map of mesocosm sampling locations: Pradel 1: soils A & B, Pradel 2: soils C, D & E, Coiron: soils I & J. Coordinates are in Lambert 93 in m. Elevation contour lines are every 20 m and every 100 m in bold.

event one. All soils were subjected to two consecutive precipitation events of a duration of 1 h and an intensity of about 90 mm h^{-1} , spaced by two days. In addition we conducted three experiments with the same sequence of precipitation events simulated on cow dung placed on a metal grid in the same location in the soil box, but without soil (F, G, H). These experiments served as a reference of IVM release from cow dung that could be compared to the concentrations leaving the soil. The difference between those three experiments was dung aging. The dung was spiked and exposed to ambient air at room temperature for one and six weeks for the dungs F and H respectively, whereas dung G was subjected to the first precipitation event shortly after spiking it. The goal was to identify and quantify the effect of dung aging on mobilization of IVM. Table 4.1 lists all IVM-transfer experiments. All exper-

TABLE 4.1: List of the experiments conducted to study the transfer of IVM through and over soil. Dung age describes the time between spiking of fresh cow dung and first simulated precipitation. ρ_b is bulk density and n calculated porosity. Θ_i is the initial volumetric water content at the first simulated precipitation. "ev" is the number of events during which the IVM concentration was monitored.

ID	Type	Soil origin	Geology	$\rho_b [\text{g cm}^{-3}]$	n	Dung age	Θ_i	ev
B	Soil + dung	Pradel 1	sedimentary	1.36	49%	1 hour	19.6%	2+0
C	Soil + dung	Pradel 2	sedimentary	1.47	45%	1 hour	21.6%	2+1
D	Soil + dung	Pradel 2	sedimentary	1.47	45%	1 week	19.8%	2+0
E	Soil + dung	Pradel 2	sedimentary	1.38	48%	1 hour	18.7%	2+0
F	Dung only	-	-	-	-	1 week	-	2+0
G	Dung only	-	-	-	-	1 hour	-	2+0
H	Dung only	-	-	-	-	6 weeks	-	2+0
I	Soil + dung	Coiron	basalt	1.3	51%	1 hour	31.2%	2+2
J	Soil + dung	Coiron	basalt	1.23	54%	1 hour	45.6%	2+1

iments were conducted at a slope of 8° (15%). Each of them received the standard sequence of two precipitation events after application of contaminated cow dung. Some of them received additional events before dung application in order to modify the initial conditions and generate blank samples, or after the standard rain sequence for a longer monitoring or supplementary investigations. The factors that changed between the different experiments are the soil type, the initial water content before the first event and the time between contamination of fresh cow dung and start of the first event.

The first two soils (A and B) were sampled on fluvial calcosol in the sedimentary part of the catchment (Pradel 1) just before the COVID-19 lockdown, and therefore had to be put on hold for a long period during lab closure. They were stored outside but may have been altered by the storage. Therefore, soil A was only used for testing and is not included here. Only soil B was used for an IVM transfer experiment but with limited confidence on the results being representative of field conditions. By the time we could return to their sampling location, it had been freshly tilled. Therefore we had to choose another sampling location (Pradel 2), still on fluvial calcosol in the sedimentary part of the catchment. We sampled three soils (C, D and E) at this new sampling location. Soil C and E were used as replicated experiments under the same conditions, with a first precipitation event immediately after applying the spiked cow dung. Soil D was left in a greenhouse for one week between cow dung application and first precipitation event in order to study the effect of drying of cow dung on the soil on the mobilization of IVM. In addition, we sampled two basaltic brunisol soils on the Coiron plateau (Coiron, soils I and J). Both received the first event immediately after application of freshly spiked dung. Soil I served to compare the two locations. Soil J received a first precipitation event before application of the cow dung and followed the same protocol thereafter. Unfortunately the time and analytical limitations neither allowed to simulate additional events with lower precipitation intensity, which was initially planned, nor to replicate all experiments.

Table 4.2 lists all relevant simulated precipitation events that were conducted. It includes events with and without sampling for IVM and tracer concentrations. Event number 1 is defined as the first event after spiked cow dung is applied to the soil. The first precipitation event on soil J was before application of cow dung and is therefore called 0J. The three higher precipitation intensities (3C, 5C, 4I & 3J) were not intended. The pressure of the reservoir pump had not changed, the reason might have been corrosion of the sprinkler nozzle due to a longer break before each of them and insufficient cleaning of the nozzle, leading to a more concentrated jet and a therefore increased precipitation intensity. Figure 4.3 summarizes all relevant events on a temporal dimension.

4.2.4 Soil characterization

We conducted several experiments and analyses in order to characterize the soils from the two geologically contrasted parts of the catchment, the Coiron basaltic plateau and the sedimentary downstream part. The majority of these experiments and analyses (grain size distribution, organic carbon, $CaCO_3$, nitrogen, hydrophobicity tests and X-ray tomography) were performed on soils from the mesocosms after their destruction. The analyzed samples included one mixed sample of soil A, two samples of soils C, D and E (upper and lower half) and vertical profiles of soils B, I and J (five depths). Infiltration experiments were conducted in the field at the two main sampling sites.

TABLE 4.2: List of all relevant simulated rain events with soil type, initial soil moisture, rain intensity (I) and whether bromide tracer was used (KBr).

ID	Soil origin	Geology	Θ_i	KBr	I [mm/h]
1B	Pradel 1	Sedimentary	19.6 %		87
2B	Pradel 1	Sedimentary	40.2 %	X	82
1C	Pradel 2	Sedimentary	21.6 %	X	91
2C	Pradel 2	Sedimentary	30.7 %		88
3C	Pradel 2	Sedimentary	17.1 %		130
4C	Pradel 2	Sedimentary	20.5 %		94
5C	Pradel 2	Sedimentary	29.3 %		117
1D	Pradel 2	Sedimentary	19.8 %		88
2D	Pradel 2	Sedimentary	30.1 %	X	84
1E	Pradel 2	Sedimentary	18.7 %		79
2E	Pradel 2	Sedimentary	28.2 %	X	76
1I	Coiron	Basalt	31.2 %		91
2I	Coiron	Basalt	34.6 %	X	90
3I	Coiron	Basalt	42.2 %		82
4I	Coiron	Basalt	35.1 %		117
0J	Coiron	Basalt	34.5 %		86
1J	Coiron	Basalt	45.6 %	X	93
2J	Coiron	Basalt	47.3 %		91
3J	Coiron	Basalt	33.4 %		122

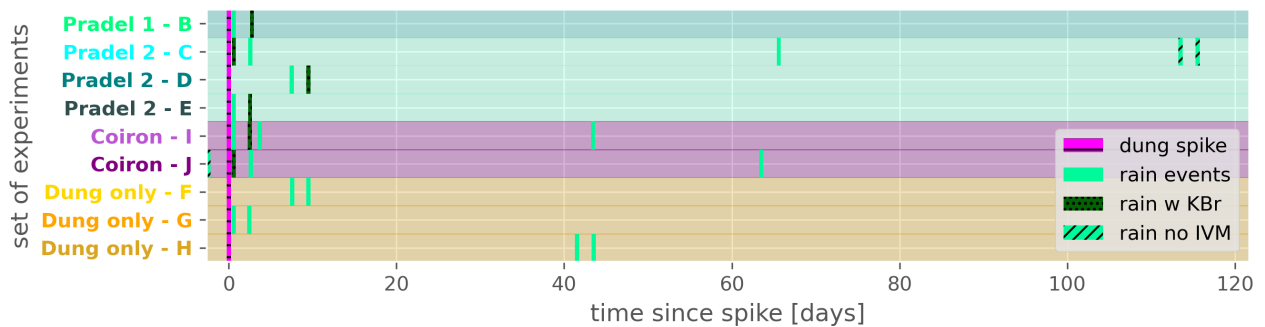


FIGURE 4.3: Timeline of relevant events as time since spike of fresh cow dung. The background color corresponds to soil origin / dung without soil and the label color per soil will be used throughout this chapter when comparing different experiments. "rain no IVM" are rain events without monitoring of the IVM concentration in the outflux.

4.2.4.1 Grain size distribution

The grain size distribution of each soil sample was analyzed using a Fritsch Analysette 22 NanoTec laser granulometer coupled with a Fritsch wet dispersion unit. Before analysis the samples were sieved at 1.6 mm. Figure 4.4 shows the results classed by sampling site. The three sampling sites

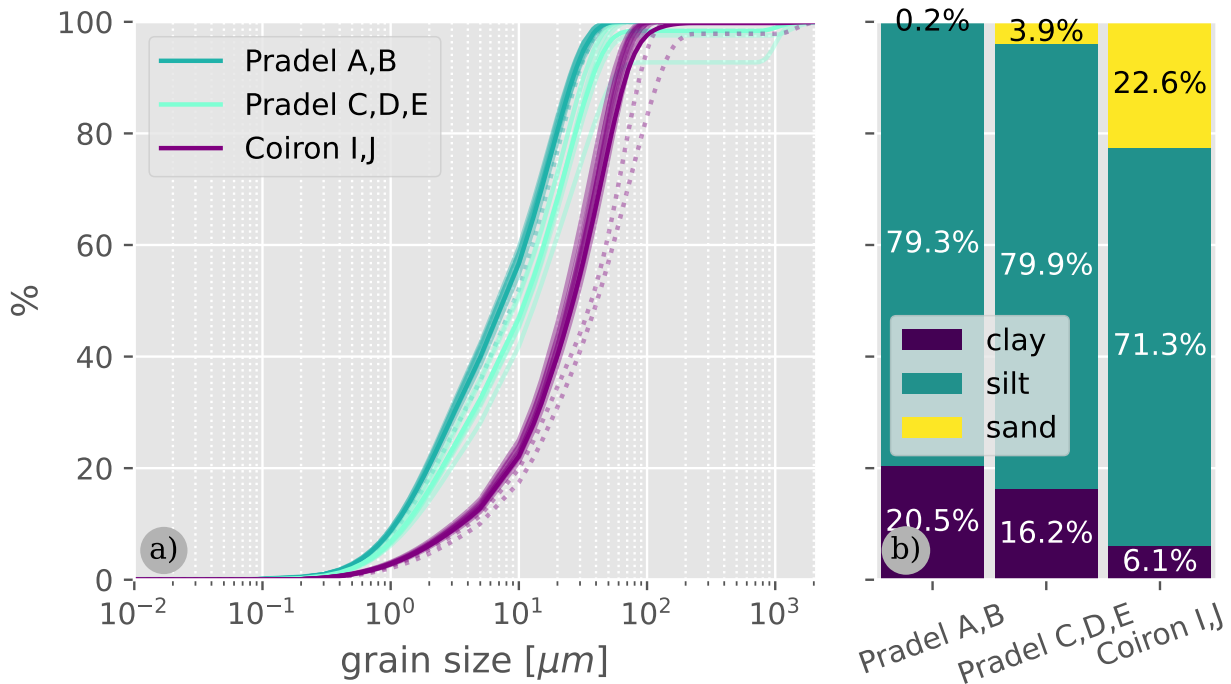


FIGURE 4.4: a) Cumulative grain size distribution of the different soil samples used in the transfer experiments. Overlapping transparent lines are individual soil samples, dashed lines are samples from the soil surface, opaque lines are the mean of all soils from one location. b) Size classes of the soils (from mean grain size distributions).

differ significantly, while the intra-site variability is lower. The difference between the two geologies is larger than the difference between the two sampling locations in the sedimentary part of the catchment. The soils from basaltic geology have larger grains with 78% of the grains larger than $10\ \mu\text{m}$, whereas for the sedimentary soils this number is 43% and 53% for the sampling locations Pradel 1 (A, B) and Pradel 2 (C, D, E) respectively. The grains were larger at the surface samples of the three vertical profiles (marked with a dashed line in Fig. 4.4 a). The median grain size d_{50} (Fig. 4.5 d) is also larger for the basaltic soils than for the sedimentary soils and decreases with depth.

4.2.4.2 Soil organic carbon

The soil samples as mentioned before had been analyzed for their content of CaCO_3 , total carbon, organic carbon, OM and nitrogen by the *Laboratoire d'Analyses des Sols d'Arras* laboratory (INRAe). The variation with depth of a selection of those parameters as well as the median grain size is presented in Fig. 4.5. OM content is much higher in the basaltic soils than in the sedimentary soils (4.9% to 15% versus 0.9% to 5.8% of dry mass) and decreasing with depth. This corresponds to a total organic carbon (TOC) of 2.8% to 8.6% and 0.5% to 3.3% respectively. The difference between

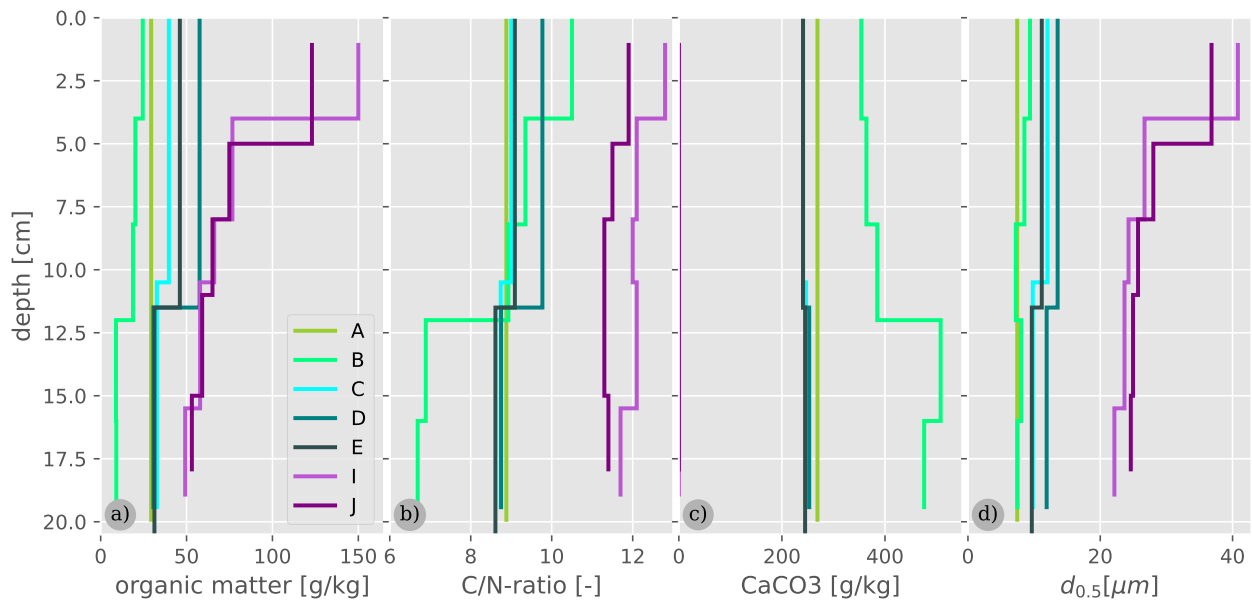


FIGURE 4.5: Evolution with depth of soil organic matter (OM), C/N-ratio, $CaCO_3$ and median grain size of the soils from the mesocosm experiments. Soils from the sedimentary area are represented in shades of turquoise and soils from the Coiron basaltic plateau are represented in shades of purple.

the two soil origins might be explained by stabilization of OM through the formation of metal-humus complexes (Inoue and Higashi, 1988) in the basaltic soils that are richer in metals (see Chapter 2). Torn et al. (1997) showed that minerals from non-crystalline volcanic parent material stabilized soil OM leading to a higher OM content in these soils. The gradient with depth can be associated with the generation of OM at the soil surface. Basaltic soils also have higher C/N-ratio (11.3 to 12.8 versus 6.7 to 10.5) which again is decreasing with depth. Soil C/N-ratio is known to increase with elevation (Zhang et al., 2016). Furthermore, differences in vegetation (more mosses on the Coiron plateau) might explain this difference. Generally these C/N-ratios can be considered low, as they are below all of the natural soils presented by Aitkenhead and McDowell (2000). The Pradel soils are more intensely grazed than the Coiron soils, which could also explain part of this difference, as grazing animals would represent an additional nitrogen source. The basaltic soils all contain less than 0.1% $CaCO_3$ (LD), while the sedimentary soils contain 24.1% to 50.8% $CaCO_3$. The only sedimentary soil where a vertical profile was sampled shows a higher $CaCO_3$ -content in deeper parts.

4.2.4.3 Soil water repellency

Fu et al. (2021) showed a link between SWR and TOC with threshold behavior: Soils with a TOC below 2% were mostly wettable and soils with a TOC above 4% tended to be water repellent. The measured TOC ranged from 0.5% to 3.3% (1.7% in average) for the Pradel soils and from 2.8% to 8.6% (4.5% in average) for the Coiron soils (all depths together). This suggests that water repellency is likely to occur on the Coiron soils while being less likely on the Pradel soils. We applied the molarity of ethanol droplet (MED) test (Doerr, 1998; King, 1981; Roy and McGill, 2002) in order to

quantify the soil samples' SWR or hydrophobicity in dry state. The method estimates the solid-water contact angle CA of dry soil for $CA > 90^\circ$. Soil will only wetten at a CA below 90° . A CA above 90° is what defines water repellency. The method is applied to dry soil as SWR diminishes with increasing water content. Method and theory are described in detail in Roy and McGill (2002). Briefly, the MED test is based on the fact that decreasing the liquid-gas surface tension γ of a liquid will decrease CA . We decrease γ by mixing water with ethanol at different molarity. The resulting corrected liquid-gas surface tension γ_c is calculated from the molarity of ethanol x as

$$\gamma_c = 61.05 - 14.75 \cdot \ln(x + 0.5) \quad (4.5)$$

CA of water for this soil can then be calculated as

$$\cos CA = \left(\frac{\gamma_c}{\gamma_w} \right)^{\frac{1}{2}} - 1 \quad (4.6)$$

where γ_w is the surface tension of water.

We adapted the protocol from Roy and McGill (2002) as follows:

1. Soil samples were dried at 50°C until their mass was stable (up to 10 d). Then they were left to cool down to room temperature during 24 h.
2. Aggregates were crushed and gravel and particulate OM >2 mm were sieved out.
3. The samples were left to air dry again at room temperature for 24 h.
4. Solutions of 0 M to 6 M of ethanol in water were prepared at steps of 0.2 M.
5. Samples were transferred into aluminum dishes into a layer of about 1 cm thickness and tapped onto the tabletop to level them. We made five replicates of each sample.
6. The first solution (0 M) was dripped onto the soil surface with a droplet diameter of about 5 mm.
7. If the droplet started entering the soil within 10 s of application, the molarity of the last solution was retained and the experiment stopped for this replica. Otherwise step 6 was repeated with the next higher concentration of ethanol. The retained value for one soil was the molarity at which the last replicate showed water entry within 10 s. Equations (4.5) and (4.6) were then used to translate the molarity x into CA .

The test was applied to all of the soil samples described before. We only observed a $CA > 90^\circ$ for the surface (top 5 cm) soil samples of I (93.9°) and J (95.2°). In all other samples, water entry started within 10 s. In addition to the degree of soil water repellency estimated by the MED test, we quantified the persistence of soil water repellency by measuring the time until complete entry of the water drop (water drop penetration time (WDPT), Watson and Letey (1970)) at six replicates for the surface samples of I and J. We obtained $\text{WDPT}(I) = (33.6 \pm 4.3) \text{ s}$ and $\text{WDPT}(J) = (40.0 \pm 6.9) \text{ s}$ (average \pm standard deviation). We found that the Coiron soils are water-repellent at their surface for a short period of time, while no water repellency could be determined at greater depth or for any of the Pradel soils. We expected to observe a higher degree of SWR in the Coiron soils due to their high OM content and also due to observations during rainfall simulation experiments that are shown in the results section.

Others authors do not use the start of drop entry within 10 s as a threshold to determine the contact angle, as proposed by Roy and McGill (2002) but complete infiltration within 10 s (e.g. Leelamanie et al. (2008)) which would lead to higher estimated contact angles as infiltration can take several seconds. Furthermore, we thoroughly crushed the soil aggregates using a mortar and pestle, while Roy and McGill (2002) tell to do "gentle aggregate crushing", without further specifying the method. This crushing might have removed the hydrophobic coating of the soil aggregates leading to less water repellency than observed in reality.

4.2.4.4 Hydraulic conductivity

We used tension disc infiltrometers in order to estimate the soil's hydraulic conductivity $K_H(h)$ at pressure head h . At each of the two main sampling sites (Coiron and Pradel 2), we conducted six infiltration experiments at four negative pressure heads $h = -10, -5, -2.5,$ and -1 cm. Grass was cut and a layer of fine sand ($150 \mu\text{m}$) applied to form an even contact surface. To obtain the effective h at the soil surface, the thickness of this contact layer was added to the h inside the infiltrometer. The infiltrometers had a disc radius R of 10 cm. We use the equations and procedure described by Reynolds and Elrick (1991) to obtain $K_H(h)$. Briefly, they use Wooding's solution for infiltration from a shallow pond (Wooding, 1968) and apply it to the tension disk infiltrometer. They show that when fitting a linear relation between $\ln(q_0(h))$ and h for two adjacent value pairs of stabilized water flux $q_0(h)$ and hydrostatic pressure head h , the slope α and intercept β can be used to estimate the field saturated hydraulic conductivity K_{fs} as

$$K_{fs} = \frac{\exp(\beta)}{\frac{4}{\pi \cdot R \cdot \alpha} + 1} \quad (4.7)$$

The actual hydraulic conductivity $K_H(h)$ corresponding to the average of the two adjacent pressure heads h_m can be obtained from the relation

$$K_H(h_m) = K_{fs} \cdot \exp(\alpha \cdot h_m) \quad (4.8)$$

The $K_H(h)$ of the lowest and highest h can be estimated by using α and K_{fs} of the corresponding closest pair of values. K_{fs} is not an accurate estimation of the saturated hydraulic conductivity K_{HS} . In order to obtain K_{HS} , an exponential relation can be fitted between all calculated $K_H(h)$ and h . If the relation between $\ln(K_H(h))$ and h is not linear, only the values of h closest to 0 should be used to estimate K_{HS} , as they are closest to saturated condition.

For the Pradel 2 sampling site in the sedimentary part of the catchment, we observed two distinct exponential $K_H(h)$ relations with a break at h about -5 cm. Two linear equations are fitted to the relation $\ln(K_H(h))$ versus h for $h < -5$ and $h > -5$ respectively, for each experiment and for all experiments together. K_{HS} is calculated as the intercept of this relation for $h > -5$. We obtain $K_{HS} = 233 \text{ mm h}^{-1}$ for the overall fit and individual fits range from 103 mm h^{-1} to 471 mm h^{-1} . Figure 4.6 shows the measured q_0 and calculated K_H as a function of h on a logarithmic scale. The break in the relation between $K_H(h)$ and h is visible and the fitted exponential functions are shown.

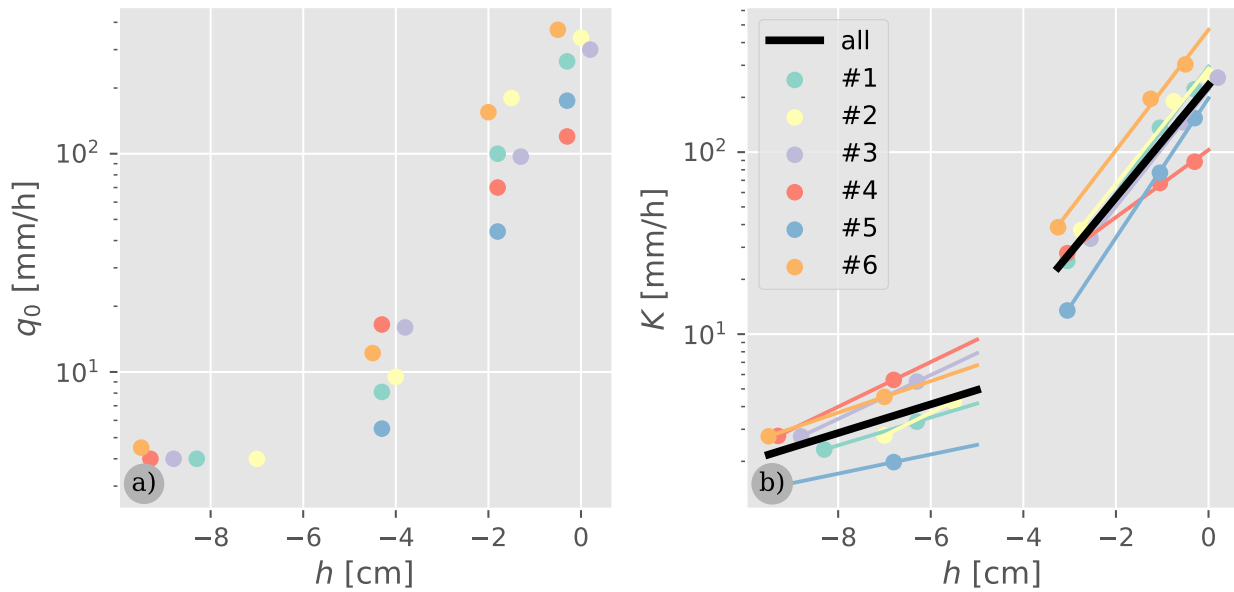


FIGURE 4.6: Results of the 6 tension disc infiltrometer experiments conducted at Le Pradel. a) shows the stabilized infiltration flux q_0 at each applied pressure head h . b) shows the calculated hydraulic conductivity K at each h and the two fitted exponential relationships. Note the logarithmic y-scales.

On the Coiron plateau, the observed K_H were much lower for the most negative h . For the higher h values, the fluxes did not stabilize but steadily increased. Therefore, values of K_{HS} close to $h = 0$ are lacking and K_{HS} could not be determined. Fig. 4.7 shows the measured q_0 and calculated $K_H(h)$ as a function of h . We fitted an exponential relationship between $K_H(h)$ and h , however it is not valid for higher h or moist soil. When using it anyways, estimates of K_{HS} range from 2 mm h^{-1} to 40 mm h^{-1} but are underestimated due to the missing values for h close to 0. At low h , $K_H(h)$ is lower on the Coiron than at le Pradel with $K_H(h = -7 \text{ cm})$ of 1.1 mm h^{-1} (0.4 to 3.5 mm h^{-1}) on the Coiron and 3.4 mm h^{-1} (2 to 5 mm h^{-1}) at le Pradel.

The non-stabilization of infiltration fluxes observed on the soils from the Coiron plateau indicates soil water repellency and the pressure head at which infiltration fluxes start to fail to stabilize corresponds to the pressure head needed to start and moisten the OM and thereby lift the water repellency. For the six infiltration experiments, this happens between $h = -2 \text{ cm}$ and $h = -1 \text{ cm}$. Jurin's law, allows to translate h from capillary suction into a pore radius r_0 . However it requires a water-solid contact angle CA . This parameter is problematic, as it is heterogeneous inside a soil and variable with soil materials and also varies with time (during wetting). It can not easily be measured, so no actual real value can be used. Some authors use a contact angle of zero to obtain an "equivalent" pore radius of a perfectly wetting fluid. This value however is much larger than a realistic pore radius. In order to avoid confusion, we decided to not translate the information from the experiments into pore sizes.

After the infiltration tests, the surface layers of the soils were dug up. From an optical aspect, the Pradel soils were homogeneously moistened. For the Coiron soils, strong heterogeneity of soil moistening could be observed. None of the samples was homogeneously moistened. Fingers of moist soil

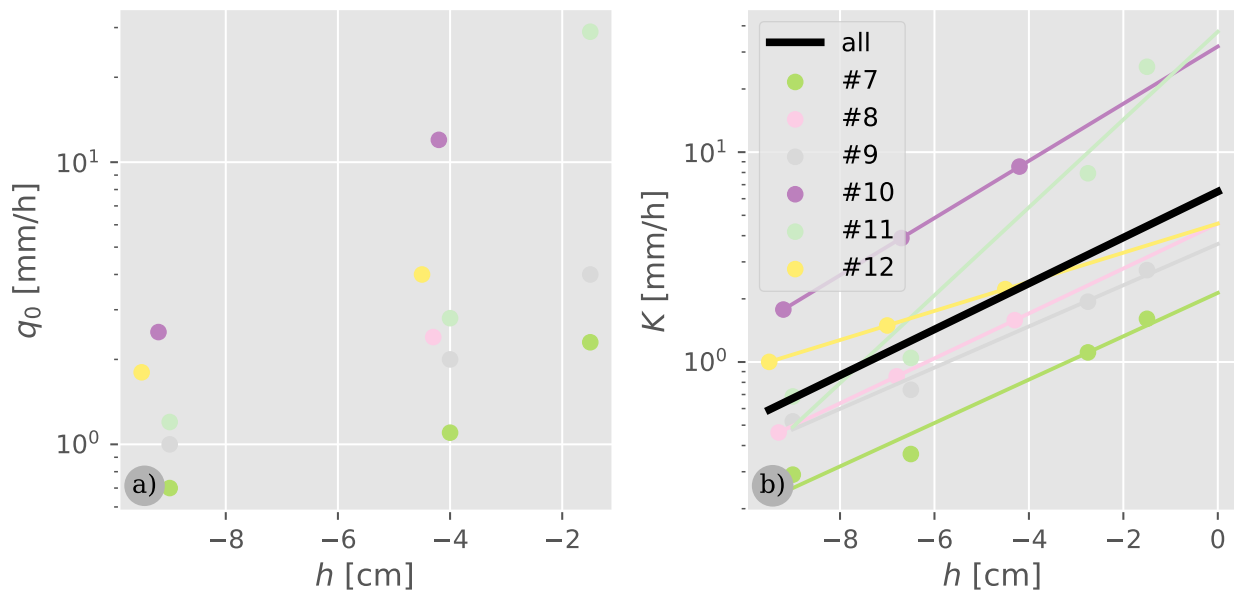


FIGURE 4.7: Results of the 6 tension disc infiltrometer experiments conducted on the Coiron plateau. a) shows the stabilized infiltration flux q_0 at each applied pressure head h . b) shows the calculated hydraulic conductivity K at each h and a fitted exponential relationship. Note the logarithmic y-scales.

were reaching down occupying different proportions of the soil underneath the infiltrometers. This indicates that only part of the soil was infiltrating and explains why the infiltration fluxes did not stabilize as a progressively increasing part of the soil was moistening.

Braud and Vandervaere (2015) did a infiltration study in the Claduègne catchment in 2012 using mini disk infiltrimeters and Beerkan infiltration tests on a number of different soils throughout the catchment. Values of K_{HS} from the Beerkan infiltration test were mostly between 100 mm h^{-1} and 1000 mm h^{-1} for the basaltic soils (ranging from 20 mm h^{-1} to $10\,000 \text{ mm h}^{-1}$) and mostly above 1000 mm h^{-1} on the sedimentary limestone soils (ranging from 20 mm h^{-1} to $20\,000 \text{ mm h}^{-1}$). The results for K_{HS} they obtained from the mini-disk infiltrimeters were globally two orders of magnitude smaller. The results from this study are situated between the two methods and agree about the lower K_H in soils on the basaltic geology.

4.2.4.5 Structure: tomography

We extracted two soil columns with a diameter of 10 cm and a length of 19 cm from the two soil samples from the Coiron plateau (I and J) after the end of the experiments. The soil columns were extracted at 10 cm from the left and right edge of the box and 20 cm from the downhill edge of the box, ranging from the soil surface to a depth of 19 cm. These soil columns were scanned twice using an RX solutions EasyTom XL Ultra tomograph at 3SR laboratory (Grenoble). One first scan in dry condition followed by a second scan two days after having received a simulated rainfall of about 90 mm over one hour. The tomograph used a Tungsten X-ray source at a voltage of 150 kV and a current of $200 \mu\text{A}$. Each image acquisition sequence consisted of 1792 projections of 1456×1840 pixels. The

3D reconstruction stage was based on a cone-beam algorithm (RX Solutions). It resulted in 3D 16 bit gray-scale images of $1424 \times 1424 \times 1649$ voxels with a voxel size of $70.2 \mu\text{m}$ before post-treatment. The images were treated using Fiji (ImageJ) (Schindelin et al., 2012). We extracted a $1649 \times 800 \times 800$ voxels core cuboid ($11.6 \times 5.6 \times 5.6 \text{ cm}^3$) only containing soil. After a contrast stretch we used the Trainable Weka Segmentation (Arganda-Carreras et al., 2017) to segment the images into three classes: soil matrix, macropores and rocks. Briefly, the Weka is an artificial intelligence that classifies pixels into categories as a function of different parameters including the value of the pixel itself, values of surrounding pixels and contrast to neighboring pixels among others. In our case, the Weka was parameterized to do the classification based on the grayscale values of the original image, blurred images (Gaussian blur), a hessian matrix (the images local curvature) and the difference between Gaussian blurred images and anisotropic diffusion filtered images (reduced noise while preserving edges). An individual Weka was trained for each of the four scans by manually selecting samples of each of the three classes (soil matrix, macropores and rocks) from three slices at the top, center and bottom of the soil cuboid. Separately training one Weka per image stack was necessary as optical properties of the materials may have changed by wetting between the analyses. Furthermore, we cannot expect the exact same intensity of a same voxel between two analyses, as the X-ray sensor is calibrated between analyses. An exact comparison of the classes between dry and wet state of the soil was therefore not possible. Macro particulate OM (e.g. roots) had very little X-ray absorbance and was thus classified as macropore. This led to some uncertainty in the classification close to the surface of the soil, where OM was abundant and classified partially as pores, partially as soil according to its X-ray absorbance.

The images reveal some insights into the macropore structure of the soils ($>140 \mu\text{m}$ being the width of two voxels). Fig. 4.8 shows one slice of the X-ray scan of soil I in dry condition (a) as well a 3D representation of macropores and rocks at this location (b). We can observe earthworm galleries traversing the soil with a diameter of about 2.5 mm in the form of curved channels. Some of these channels lead to larger holes in the lower parts of the soil, that correspond to places where the earthworms retract themselves in a knot-shaped structure in order to minimize their surface to prevent themselves from drying out. There are also smaller pore networks of a few hundred μm in thickness. A 3D-view reveals their structure to be mainly curved planes and fractures rather than channels. Some larger holes can also be found with diameters up to 3 cm . These occur mainly close to the soil surface, with the exception of one large hole on the bottom of the sample I. These larger holes are probably filled with light OM that is barely visible on the X-ray scans. Rocks are most abundant and largest towards the bottom of the soil column. Some strongly absorbing grains can be identified throughout the soil column.

Figure 4.9 shows the proportions of the three identified segments, macropores, soil matrix and rocks throughout the soil column of the two samples in their two states (dry and wet). We can observe the macropore abundance to be the highest close to the surface and decrease with depth. However, this result can partially be explained by a higher fraction of OM at the surface that is classified as pores due to its very low X-ray absorbance. Both soils have a very distinct rocky horizon in the bottom starting at about 8 cm and 10 cm below the top of the image respectively. Furthermore, both soils have a few rocks close to the surface, which is also visible on the images. For the reasons

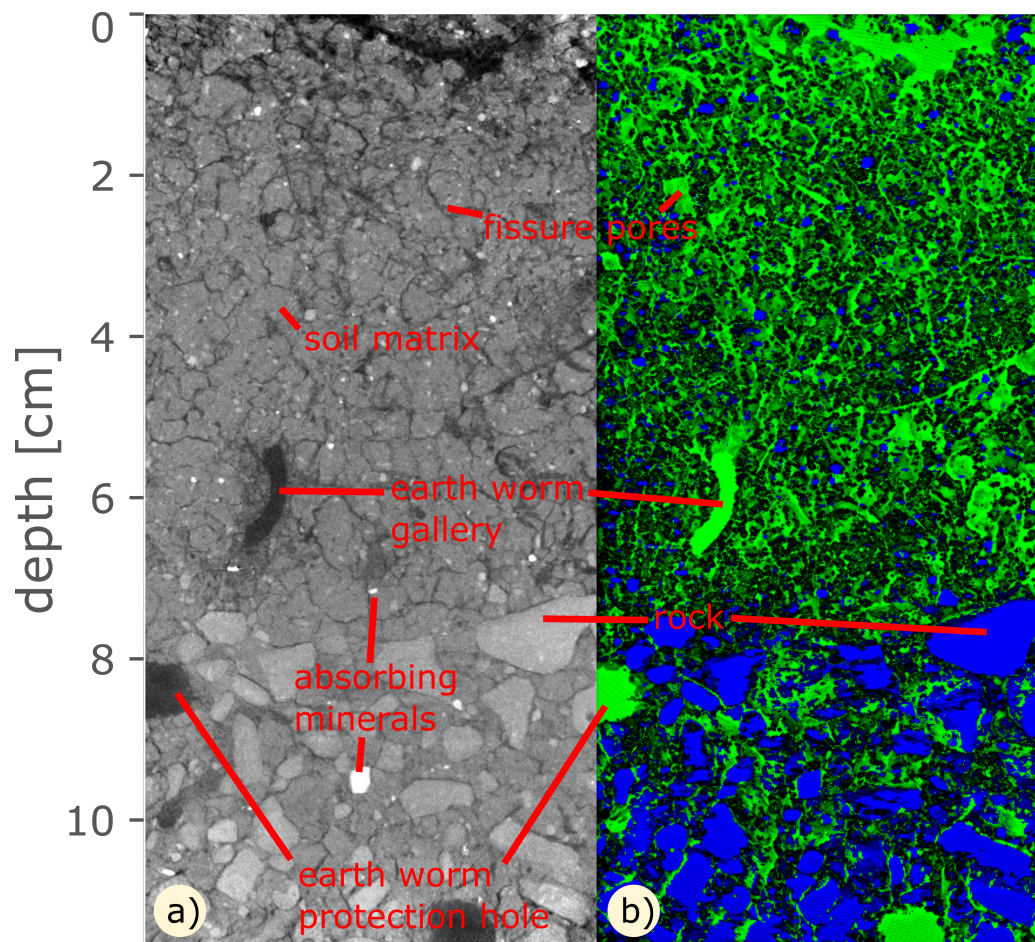


FIGURE 4.8: Images generated from the X-ray tomography of soil I in dry condition. a) shows one slice of the scan, with highest absorbance in white and lowest absorbance in black. b) shows a 3D illustration of the classification with porespace in green, rocks in blue and soil invisible.

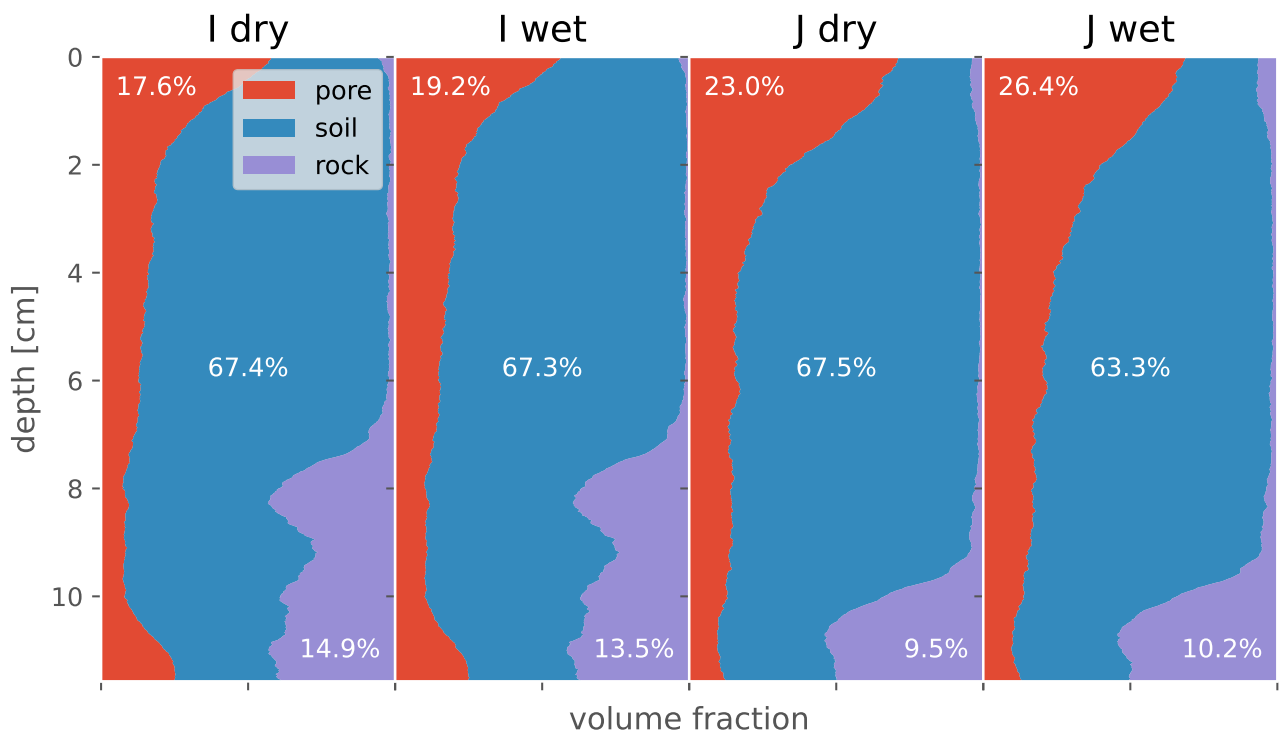


FIGURE 4.9: Evolution of the volumetric fraction of macropores, soil matrix and rocks with depth in the two soil samples in two conditions. Depth 0 is the top of the image, which is about 1 to 2 cm below the soil surface. The written percentages in the figure correspond to the overall fraction of the whole cuboid.

discussed above, the percentages cannot directly be compared between the two states (dry and wet). We consider the few percent of difference to be within the uncertainty bounds of the segmentation algorithm.

In addition, pore size distributions were quantified using BoneJ Trabecular thickness (Doube et al., 2010). Briefly, this tool fits the largest possible sphere into the spaces classified as pore and assigns its diameter to all included voxels. This allows to estimate the pore size distributions at each depth. Figure 4.10 shows the overall pore size distributions of soils I and J in dry condition and their evolution with depth. We can observe the dominance of pores of a few hundred μm throughout most of the soil

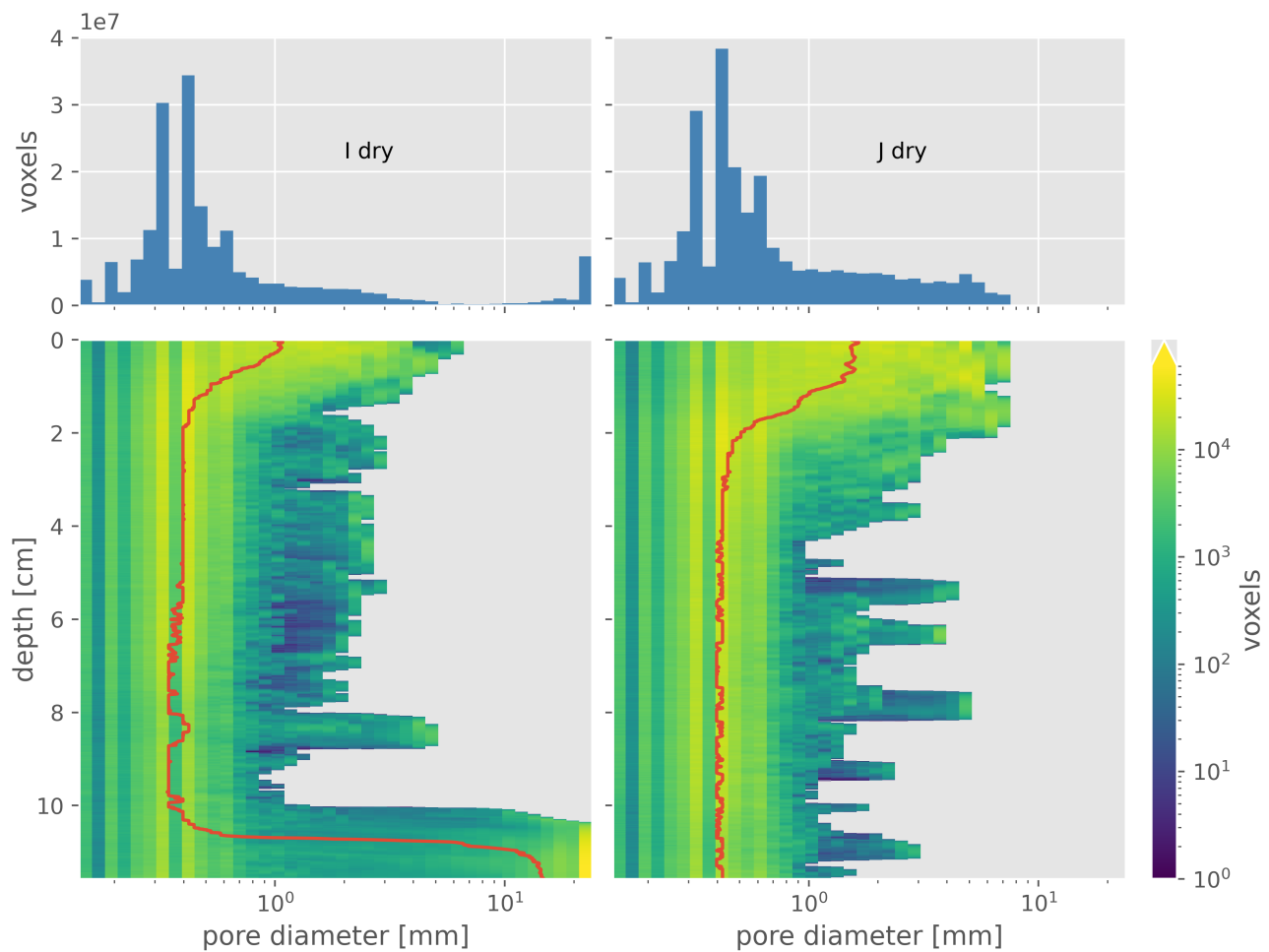


FIGURE 4.10: Overall pore size distributions of the two soil samples in dry state and their evolution with depth. Note that both, the color-bar (number of voxels per class) and the x-axis (pore diameter classes) are on logarithmic scale. The red lines are median pore diameters.

column and in both soils representing the fissure-shaped macro-pores that can be seen in the images (Fig. 4.8). Within these, there seems to be a bi-modal distribution with one peak around $300\ \mu\text{m}$ and another peak around 400 to $500\ \mu\text{m}$. When using a larger number of small size binsⁱ, regularly spaced spikes can be observed that are artifacts of the voxel size of $70.2\ \mu\text{m}$. The separation of these two peaks however is larger and visible with varying bin sizes. This suggests, that these two distinct

ⁱ a bin is a class in a histogram

feature sizes exist in reality. The greater abundance of larger pores close to the surface is also clearly visible. Earthworm galleries correspond to the pores of about 2 mm in size that are present in a large part of soil I, but less in soil J. In soil I we can also identify the hole at a depth of about 8 cm that is also shown in Fig. 4.8, dug by an earth worm to protect it from drying out. Figure 4.10 shows a large hole that is present in the bottom of soil I, the origin of which could not be identified. The histogram was limited to a maximum pore size of 24 mm.

4.3 Results

4.3.1 Hydrological functioning

Figures 4.11 and 4.13 show the time series of simulated precipitation as well as measured drainage and OF during consecutive events on the soils from Pradel 2 and Coiron respectively. As described in the article (subsection 4.2.1; Hachgenei et al. (2022a)), bromide is injected during one rain event on each soil in order to distinguish the water from this rain event from all water previously present in the soil or applied during following events. Figures 4.12 and 4.14 show the evolution of soil water content during those events. We can observe that OF rarely occurs on the soils from Pradel 2, except for the first event on soil C and the very beginning of some of the other events (Fig. 4.13). There is continuous OF during all events on the soils from Coiron except the first event on soil J, where OF stops rapidly (Fig. 4.11). Overland flow coefficients CR on the Coiron soils are generally about 15 %.

Regarding the Coiron soils, different behavior can be observed under subsequent precipitation events with regards to overall flow dynamic, repartition between drainage and OF as well as proportions of event and pre-event water in drainage flow (Fig. 4.11). The first simulated precipitation on soil J (0J) took place a few days after sampling and 2 weeks after the last natural rain in the field. Initial volumetric water content (Θ_i , Fig. 4.12) is 34.5 %. We can observe a small initial spike in OF which quickly stops (Fig. 4.11). Thereafter, drainage flow continuously increases until reaching the intensity of simulated precipitation towards the end of the precipitation event. During the following precipitation event (1J, 3 days later, $\Theta_i = 45.6\%$), there is a relatively continuous OF coefficient CR of approximately 15 % of the precipitation intensity, slightly decreasing toward the end of the precipitation event. The drainage flow starts faster and at a higher rate than during the first event. The pre-event water contribution to drainage flow $Q_{D\ pre}$ is continuously decreasing from $\frac{2}{3}$ of Q_D in the beginning to $\frac{1}{3}$ in the end of the precipitation event. The event water contribution follows the inverse trend. In soil I, the soil had three additional weeks in the lab before the first simulated precipitation, allowing it to dry. The global Θ_i of the first event (1I) was 31.2 % (Fig. 4.12), however one could expect that the surface soil was dryer than deeper layers. Over the first event, Θ barely increased and there was a continuous CR about 70 %. Most of the remaining precipitation left the soil through Q_D and Θ only increased slightly. In the beginning of the second precipitation event (2I), Θ_i was approximately 34.6 %. In contrast to 1J, where the CR was relatively constant at approximately 15 %, in 2I the CR is above 30 % in the beginning, then decreases over the first 20 min to about 15 % and remains stable thereafter (Fig. 4.11). Drainage slowly and steadily increases to approximately 80 % toward the end of the precipitation event. The event water contribution to drainage flow $Q_{D\ ev}$ is close to 100 % of Q_D during the first 20 min. Thereafter, a significant contribution of pre-event water ($Q_{D\ pre}$) starts. This is

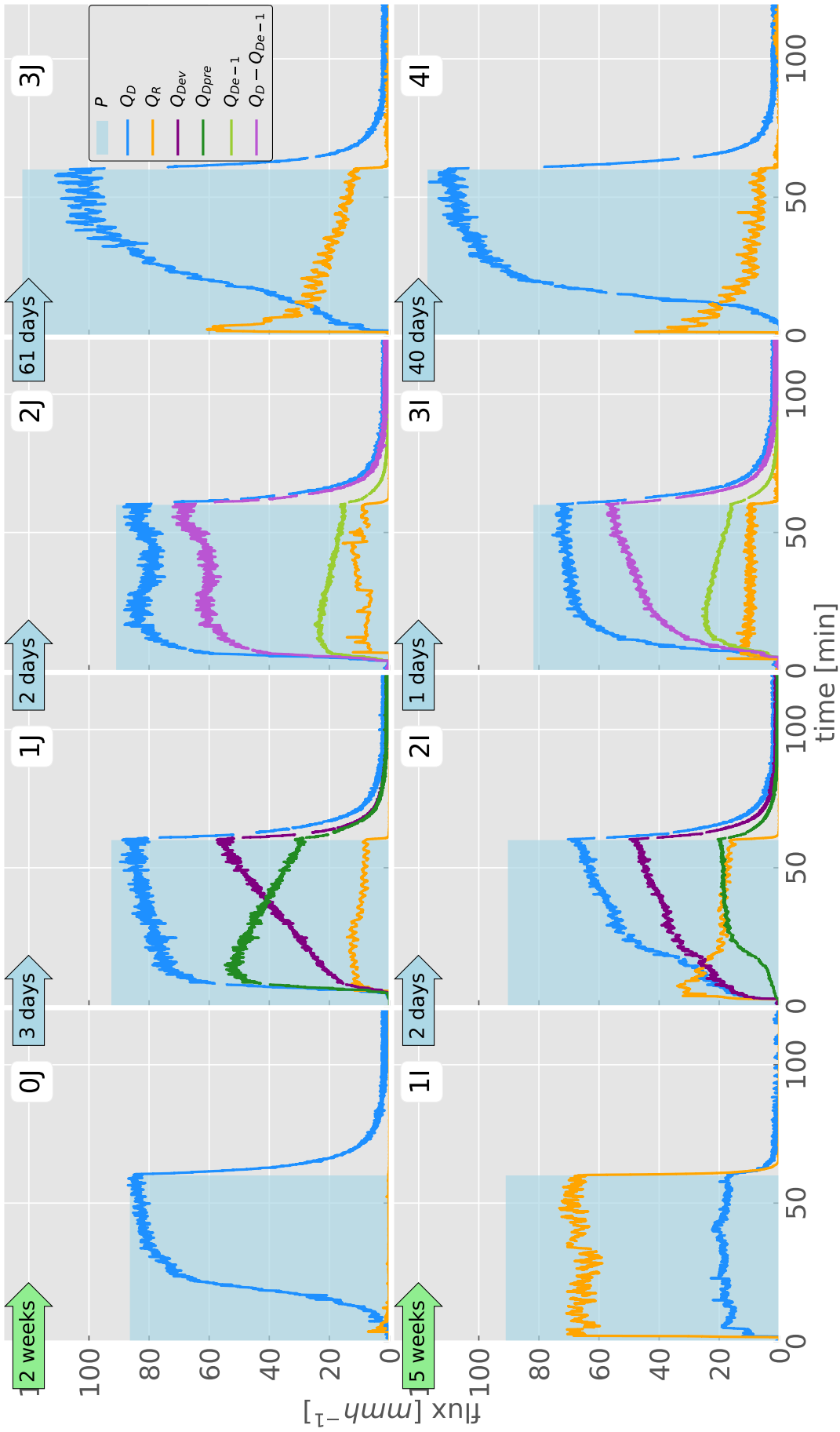


FIGURE 4.11: Time series of simulated precipitation intensity (P), drainage (Q_D) and overland flow (Q_R) of the four events on the two soils from Coiron (I & J)). Drainage flow is separated in event ($Q_{D_{ev}}$) and pre-event water ($Q_{D_{pre}}$) for the events with bromide tracer in the simulated precipitation. Drainage flow is separated in water from the previous event ($Q_{D_{e-1}}$) and any other water ($Q_D - Q_{D_{e-1}}$, mostly event water) for the events following the bromide tracer application. Arrow-shaped labels indicate the time since the last rainfall. Green background indicates last rain was natural, blue means simulated.

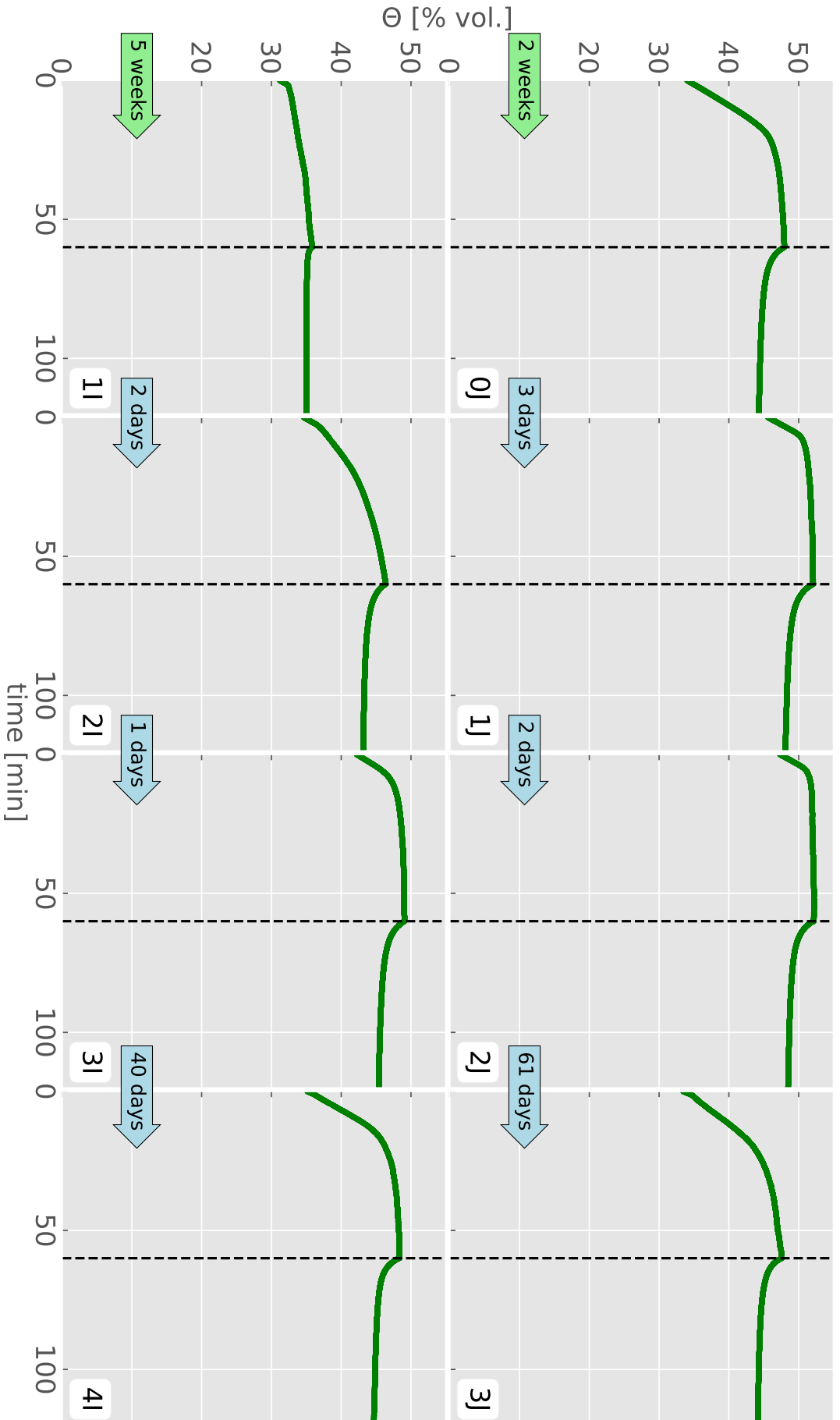


FIGURE 4.12: Time series of volumetric water content of the four events on the two soils from Coiron (I & J). Arrow-shaped labels indicate the time since the last rainfall. Green background indicates last rain was natural, blue means simulated.

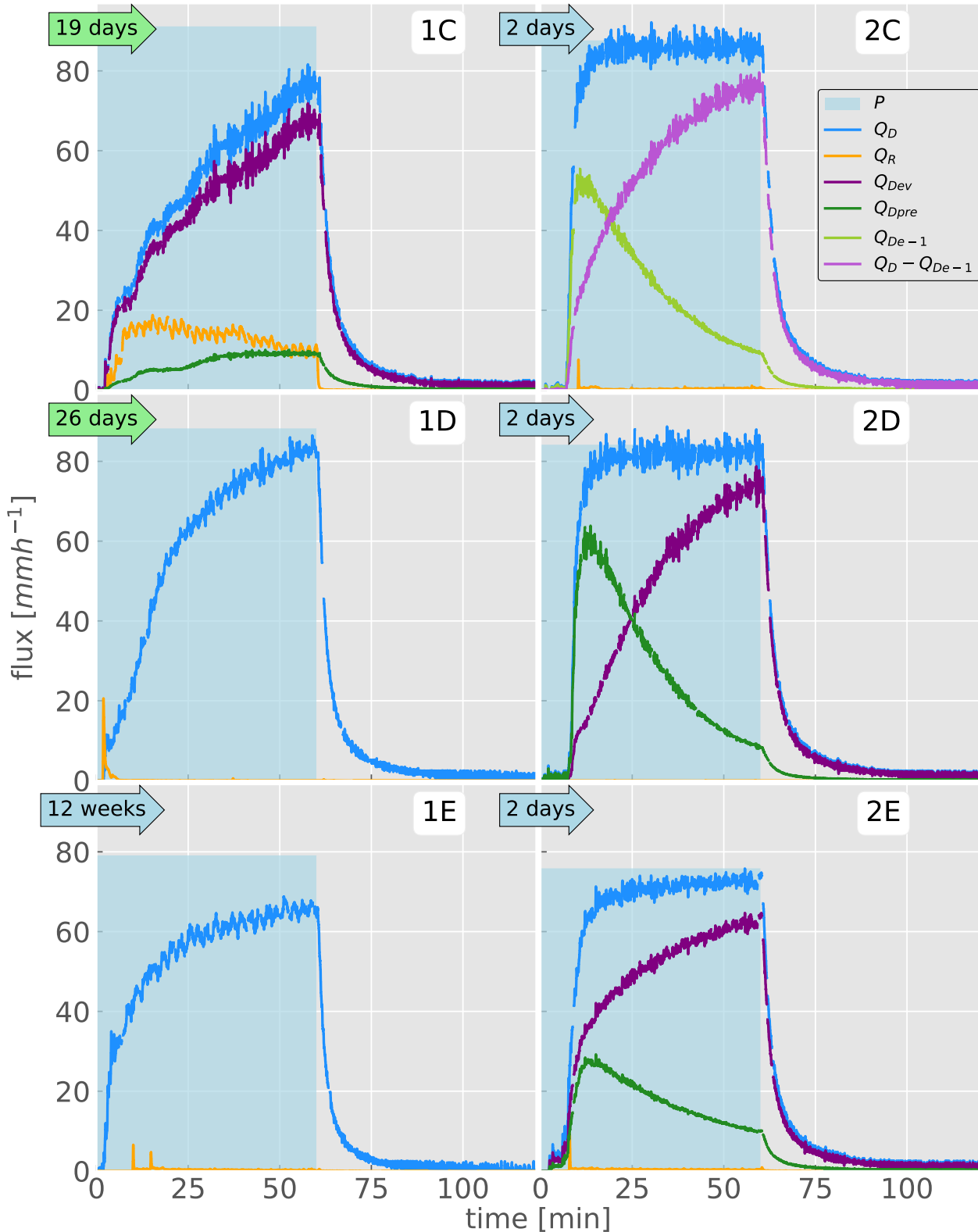


FIGURE 4.13: Time series of simulated precipitation intensity (P), drainage (Q_D) and overland flow (Q_R) of the first two events on the three soils from Pradel 2 (C, D & E). Drainage flow is separated in event ($Q_{D\text{ev}}$) and pre-event water ($Q_{D\text{pre}}$) for the events with bromide tracer in the simulated precipitation. Drainage flow is separated in water from the previous event ($Q_{D\text{e-1}}$) and any other water ($Q_D - Q_{D\text{e-1}}$, mostly event water) for the events following the bromide tracer application. Arrow-shaped labels indicate the time since the last rainfall. Green background indicates last rain was natural, blue means simulated.

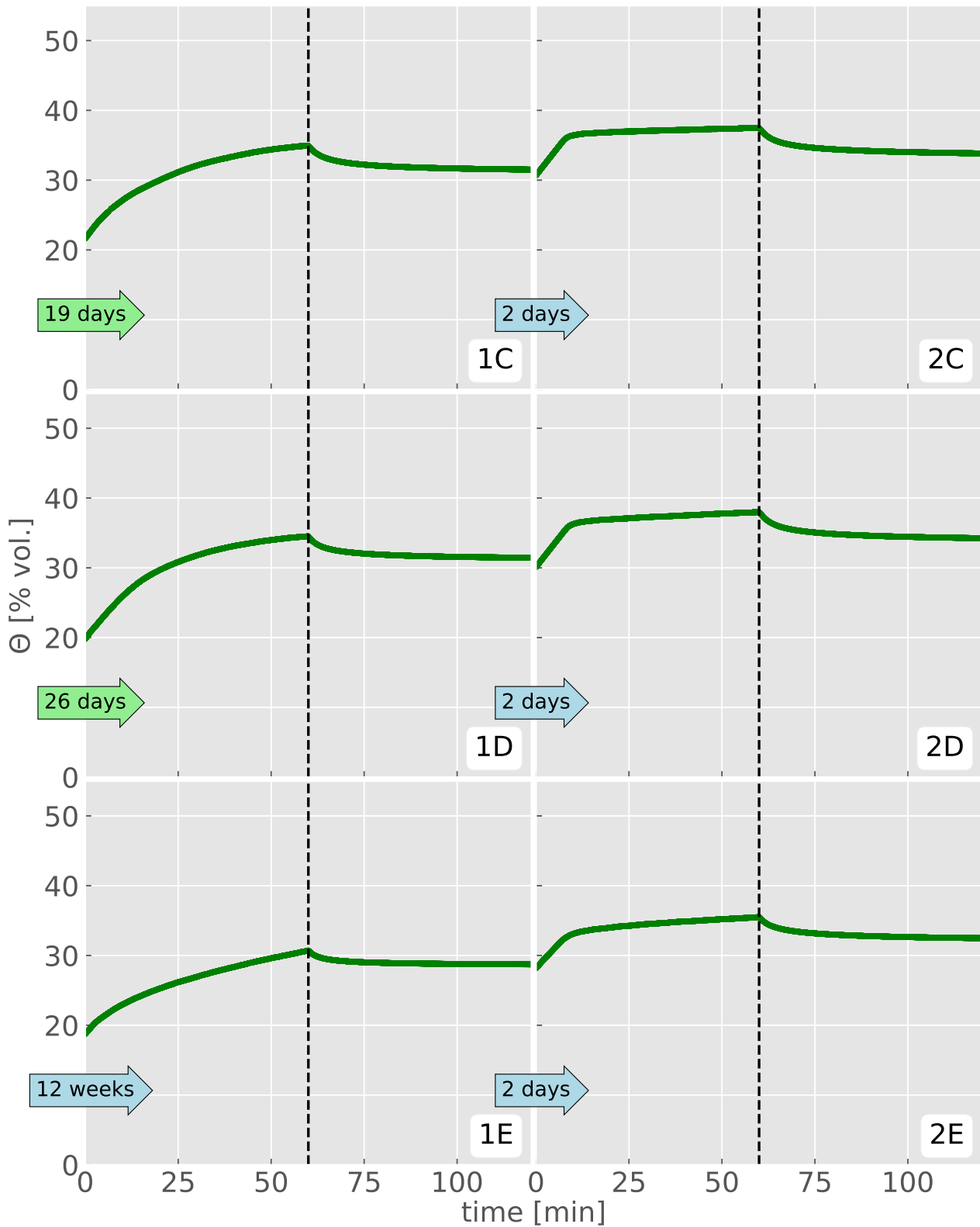


FIGURE 4.14: Time series of volumetric water content of the first two events on the three soils from Pradel 2 (C, D & E). Arrow-shaped labels indicate the time since the last rainfall. Green background indicates last rain was natural, blue means simulated.

the inverse of what was observed in J (event 1J) on more moist soil. The following event on each of the two soils (2J & 3I) is relatively similar to 1J in dynamic and flux repartition. They took place on an Θ_i of 47.3 % and 42.2 % respectively. During these two events the bromide tracer does not allow to distinguish event and pre-event water, as it was added in the previous event. However it can distinguish the water originating from the previous event ($Q_{D\ e-1}$), which would represent the majority of the pre-event water for this event from all remaining water ($Q_D - Q_{D\ e-1}$), which would be mainly constituted of event water, but presumably includes a portion of older water as well. During the last event on each of the two Coiron soils (3J and 4I), the intensity of precipitation was unintendedly higher than during the other precipitation events. Despite this difference, the trend during the last event on each soil (3J and 4I) resembles that observed in 2I and described above. The Θ_i was 33.4 % and 35.1 % for 3J and 4I respectively (Fig. 4.12) after 61 d and 40 d without precipitation. Overland flow starts rapidly on both soils with a CR of over 40 % and then decreases toward the end of the precipitation event. It can be observed that during the events 3J, 1I, 2I and 4I both drainage and OF start rapidly, while in events 0J, 1J, 2J and 3I, both fluxes start significantly later. In Fig. 4.12 three different moistening patterns can be observed. Event 1I shows a particular case with very little moistening despite the low water content. Events 0J, 3J, 2I and 4I show a gradual increase of Θ over a large part of the precipitation event. During events 1J, 2J and 3I, which are the events with the highest Θ_i , the value of Θ rapidly reaches a plateau and remains stable thereafter until the end of the precipitation event.

Regarding the soils from Pradel 2 (Figs. 4.13 and 4.14), all of them start on relatively dry soil after 19 d, 26 d, and 84 d without precipitation for soils C, D & E respectively, at a Θ_i of 21.6 %, 19.8 %, and 18.7 % respectively (Fig. 4.14). Soil E had a particularly long period of 12 weeks without precipitation before event 1E. The Θ_i values of the second event on soil C, D and E (two days after the first one) were 30.7 %, 30.1 %, and 28.2 % respectively (Fig. 4.14). Bromide tracer was injected through precipitation during the first event on soil C and during the second event on soil D and E. On all three soils, flow starts later on the second event on more moist soil than on the first event on drier soil (Fig. 4.13). There is generally less OF than on the soils from Coiron. Event 1C is the only one with significant OF. Events 2C, 1D, 1E & 2E have a short spike in OF in the beginning of the event and produce no more OF thereafter. Event 2D did not produce OF. Concerning the event water contributions to drainage flow, a strong difference can be seen between dry soil (1C) and moist soil (2D and 2E): On dry soil (1C), drainage flow mainly consists of event water (80 %) from the beginning on. This proportion remains constant throughout the precipitation event indicating that older water from the soil matrix is progressively mobilized throughout the precipitation event. On moist soil, this behavior is different. Like observed for the Coiron soils, in the beginning of the precipitation event older water is pushed out of the soil and then progressively replaced by event water. On soil E the event water fraction in drainage during the second event is higher from the beginning than on soil D. The soil moistening patterns of all three Pradel 2 soils (Fig. 4.14) are very similar: During the first event, the soil is generally gradually moistening throughout the whole precipitation event, whereas during the second event, rapid moistening takes place over the first ten minutes and only little change happens thereafter.

Figure 4.15 shows the temporal evolution of Θ during the fourth and fifth event on soil C. For these events, two *Decagon 5TE* sensors measuring volumetric water content Θ using the dielectric constant

as well as electric conductivity and temperature where installed at depths of 0 cm to 5 cm and 5 cm to 10 cm, called S_0 and S_5 in the following. The measured Θ at these two depths are compared

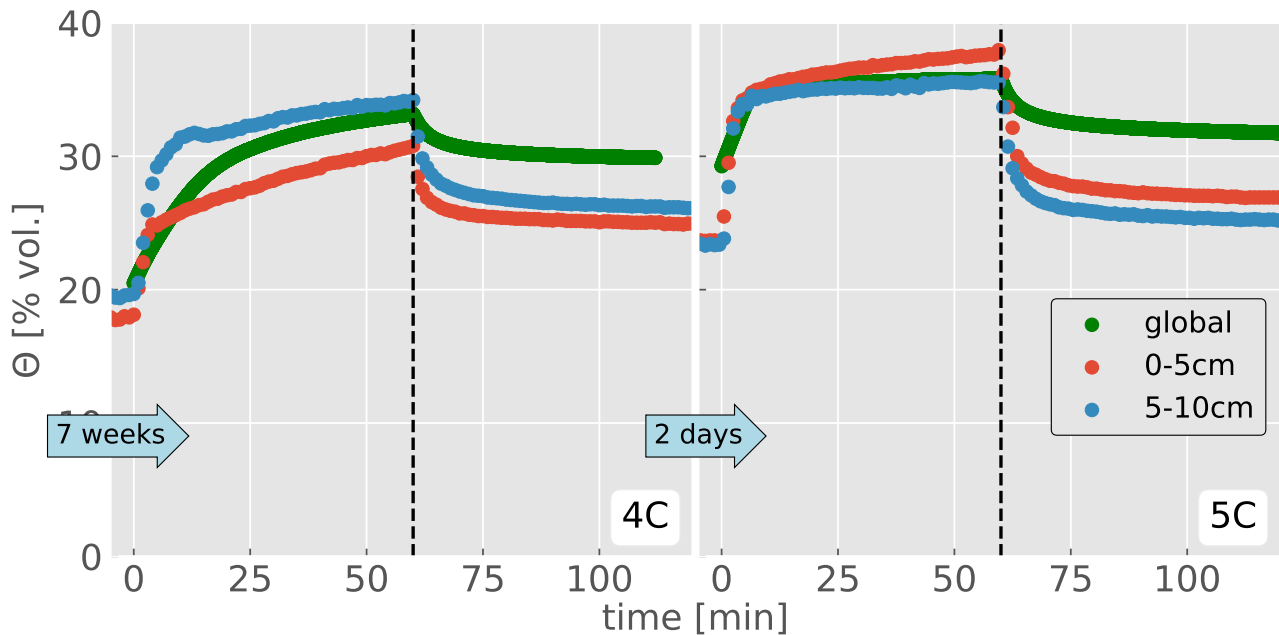


FIGURE 4.15: Time series of volumetric water content of the fourth and fifth event on soil C from mass balance calculation (green) and soil sensors installed at a depth between 0 cm and 5 cm (red) and 5 cm and 10 cm (blue). Arrow-shaped labels indicate the time since the last rainfall.

to global Θ from mass balance calculation in Fig. 4.15. The two ways of estimating Θ give similar results. Event 4C was on initially relatively dry soil ($\Theta_i=20.5\%$). During the event, the global Θ rises to 33% and drops to 30% an hour after the end of rainfall. The sensors start at a similar value of Θ_i but rise more rapidly than the global Θ from mass balance. The deeper sensor S_5 raises to a similar value as the global Θ , while S_0 remains lower. Both sensors indicate a lower value of Θ in the end than the mass balance calculation. This remains that way in the beginning of event 5C (24% for the sensors vs. 29.3% from mass balance), however both rise rapidly to approximately 35% during rainfall simulation, which is the same value as obtained from mass balance calculation. The more rapid reaction of the sensors in the beginning might be explained by preferential flow paths created during installation of the sensors. The lower Θ measured by the sensors as compared to mass balance in moist condition after the end of precipitation might be explained by their location in the upper half of the soil.

4.3.2 Ivermectin transfer

There were some problems in the quantification of IVM that could not yet be unambiguously identified at the time of writing. This leads to increased uncertainty in the concentrations and fluxes of IVM presented hereafter. These problems are detailed in the discussion section. The shown concentrations should be seen as an order of magnitude rather than precise values. Briefly, the recovery of the internal standard Doramectin (DOR) was low and variable. This is assumed to be an actual problem of

recovery of IVM, so samples were still corrected using the recovery of the internal standard. Samples where the internal standard was not detected are not shown when presenting concentrations and the values were replaced with values of the last valid sample or the next valid sample if no valid sample existed previously in order to calculate cumulative export. This concerns the first half of drainage samples from 2I and 2B and the last samples from 2G. All OF samples from 2J and all drainage samples from 3J could not be quantified. For cumulative export estimations their values are set to zero.

Figure 4.16 shows the cumulative export of IVM as a function of cumulative discharge for each of the two water fluxes and the sum of both. Concerning the experiments without soil (G, F, H), the

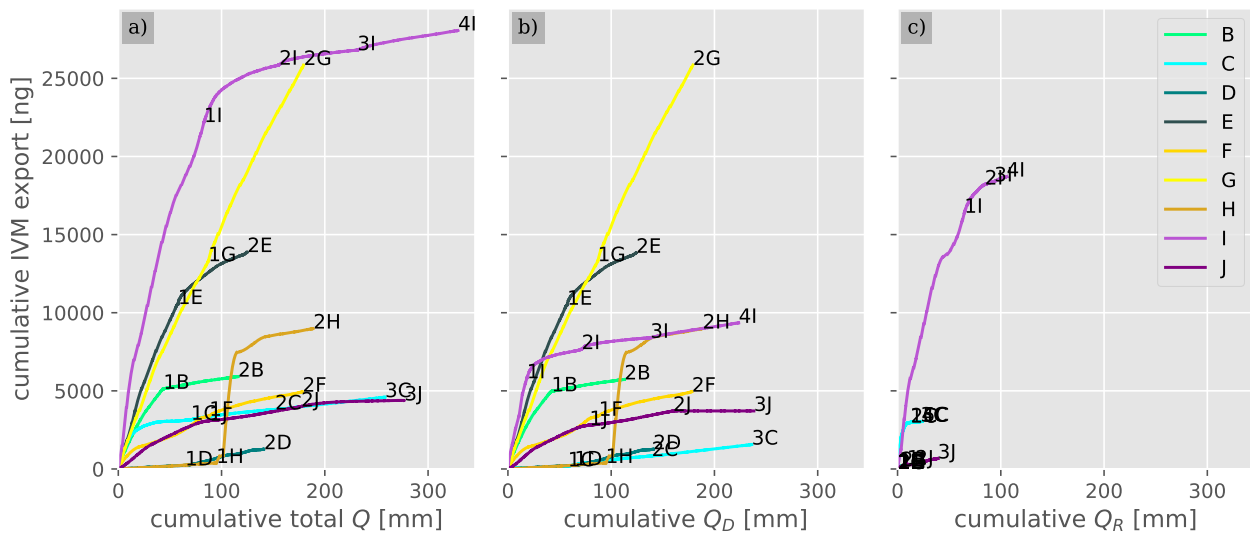


FIGURE 4.16: Cumulative IVM outflux versus cumulative discharge for both fluxes combined (a), drainage (b) and overland flow (c).

highest amount of IVM is exported when freshly spiked dung is subjected to precipitation (G). The cumulated export over two consecutive events is 25.9 μg corresponding to 8.6% of the applied dose. The export rate remains similar throughout both events, suggesting that a similar export could be expected for following events. For the cow dung that had aged for 1 week (F), the overall export is significantly lower (4.9 μg), of which 3.4 μg (69%) were exported over the first event. For the dung that aged over 6 weeks, export during the first event is limited (0.384 μg). During the second event, some high concentrations are observed leading to an overall export of 9.0 μg . In soil C, the export of IVM is highest in the beginning of the first precipitation event, dominated by export through OF, which made 2.975 μg of the exported 3.148 μg (95%). The following two events had comparatively low export of IVM, which was dominated by drainage flow. In total, over the three events, 4.6 μg of IVM were exported. Soil D, where almost no OF took place, has a much lower overall export, but very similar drainage export as soil C. The difference caused by the aging of dung on soil D of 1 week is difficult to evaluate due to the different hydrological behavior. Soils E and B showed significantly higher export of IVM through drainage flow and the total exported masses were 13.9 μg and 5.9 μg respectively over the two events.

Regarding the soils from the Coiron, the overall export shown in Fig. 4.16 is underestimated for events 2J and 3J due to the analytical problems mentioned above. The export from the first two events on soil J is similar to the export from the first two events from soil C, even without OF from event 2J. In contrast to experiment C, on soil J the export was dominated by drainage flow. Experiment I had the highest export of IVM of all experiments. The export of event 1I was 22.2 μg , 1.7 times that of event 1G from cow dung without soil. After two events, the export from soil I was 25.9 μg , exactly as much as from experiment G after two events.

The export from most soils is decreasing over the consecutive events. The only exception is the export through drainage from experiments C and D which is higher during the second than during the first event.

In the following, the evolution of concentrations throughout individual events is presented. Figure 4.17 shows the concentration evolutions from the three experiments on cow dung of different age. Concentration values are plotted at the mid-time of each sampling period. The rain on fresh cow dung (G) leads to continuous high concentrations of IVM about 1000 ng L^{-1} . During each of the two events there is a slightly decreasing trend throughout the event. The dung that has aged for one week (F) shows much lower concentrations that are only high in the beginning of the event (754 ng L^{-1}) and decrease rapidly over the first 15 min to about 100 ng L^{-1} . The second event starts with 260 ng L^{-1} and decreases to about 100 ng L^{-1} thereafter. The dung that had aged over six weeks produces the lowest concentrations during the first event, between 20 ng L^{-1} and 30 ng L^{-1} . The second event produces very high and very variable concentrations up to 4600 ng L^{-1} for one sample after ten minutes. There was one modification of the sample preparation protocol for this particular event: As no particles were visible in samples from this event, the samples had not been centrifuged before the SPE.

Figure 4.18 shows the evolution of IVM concentrations from two of the Pradel 2 soils, C and D. The highest concentrations were observed in OF from the first event on soil C (1C) being 3855 ng L^{-1} in the first sample and decreasing monotonously to 69 ng L^{-1} in the last sample. The concentrations in drainage were lowest during the first event but variable. They were below 10 ng L^{-1} for most of the samples with a few peaks of up to 100 ng L^{-1} . During the second event, the drainage concentrations were higher and less variable, decreasing from 120 ng L^{-1} in the beginning to 40 ng L^{-1} in the end. The single OF sample from this event has a concentration of about 70 ng L^{-1} . During the third event, concentrations in OF and drainage varied between 20 ng L^{-1} and 60 ng L^{-1} in the beginning of the event. The samples from the end of the event could not be quantified because the internal standard was not detectable. On soil D, no significant overland flow took place. The only overland flow sample was from the first event and had a concentration of 6.5 ng L^{-1} . During the first event, concentration values in drainage were constant at about 20 ng L^{-1} . During the second event, concentration values in drainage rose from 40 ng L^{-1} in the beginning to 140 ng L^{-1} in the middle of the precipitation and then decreased to 20 ng L^{-1} toward the end.

Figure 4.19 shows the evolution of IVM concentrations from the two Coiron soils. As mentioned before, the drainage samples of the second half of event 2J as well as event 3J and the overland flow samples of event 2J could not be quantified because the internal standard was not detectable. In event 3I, only one total OF sample was taken. For those samples that could be analyzed, the OF

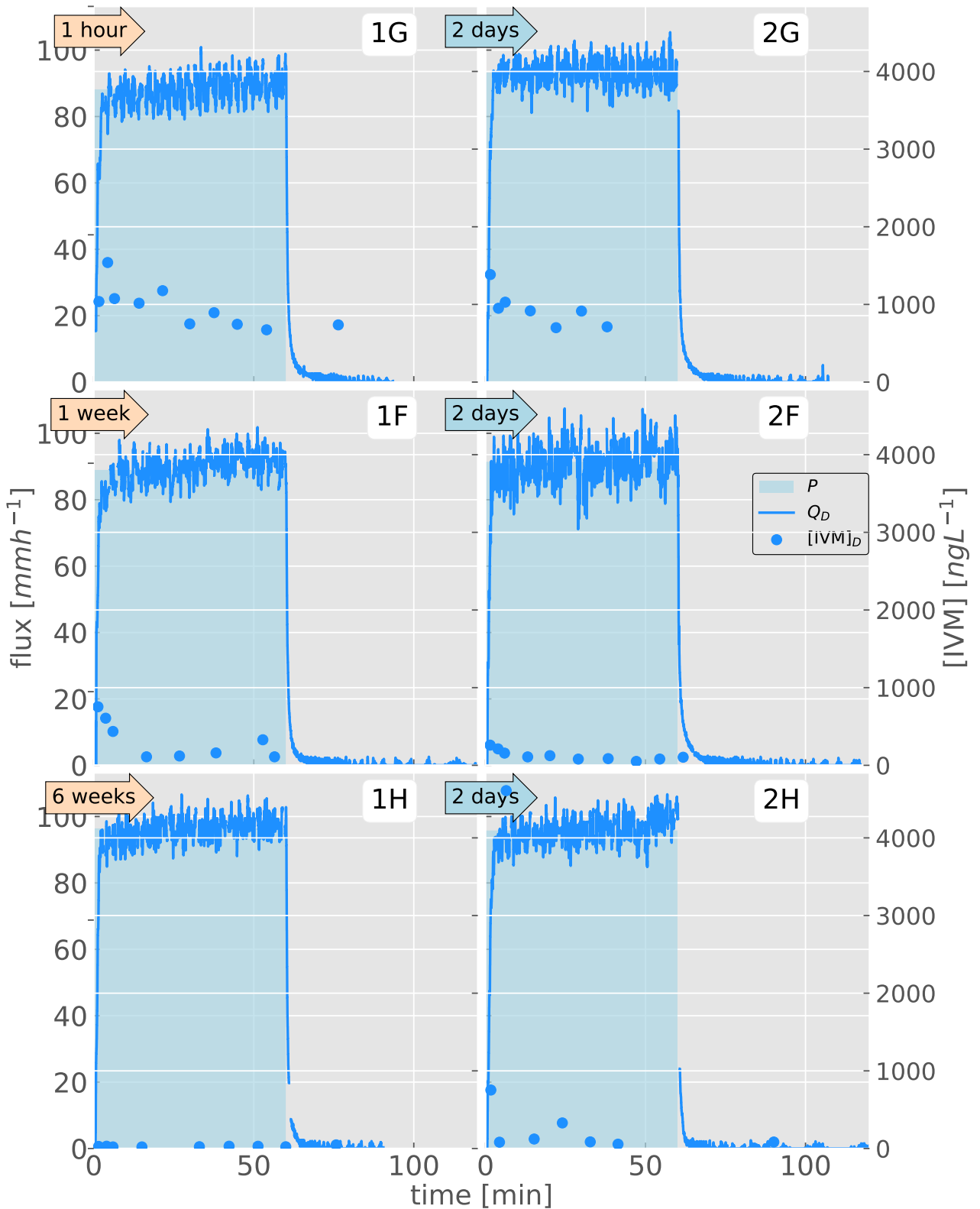


FIGURE 4.17: Time series of outflow and IVM concentrations from the three experiments on cow dung. Brown arrow-shaped labels indicate the aging time of the dung after contamination and blue arrow-shaped labels indicate the time between the two rain events.

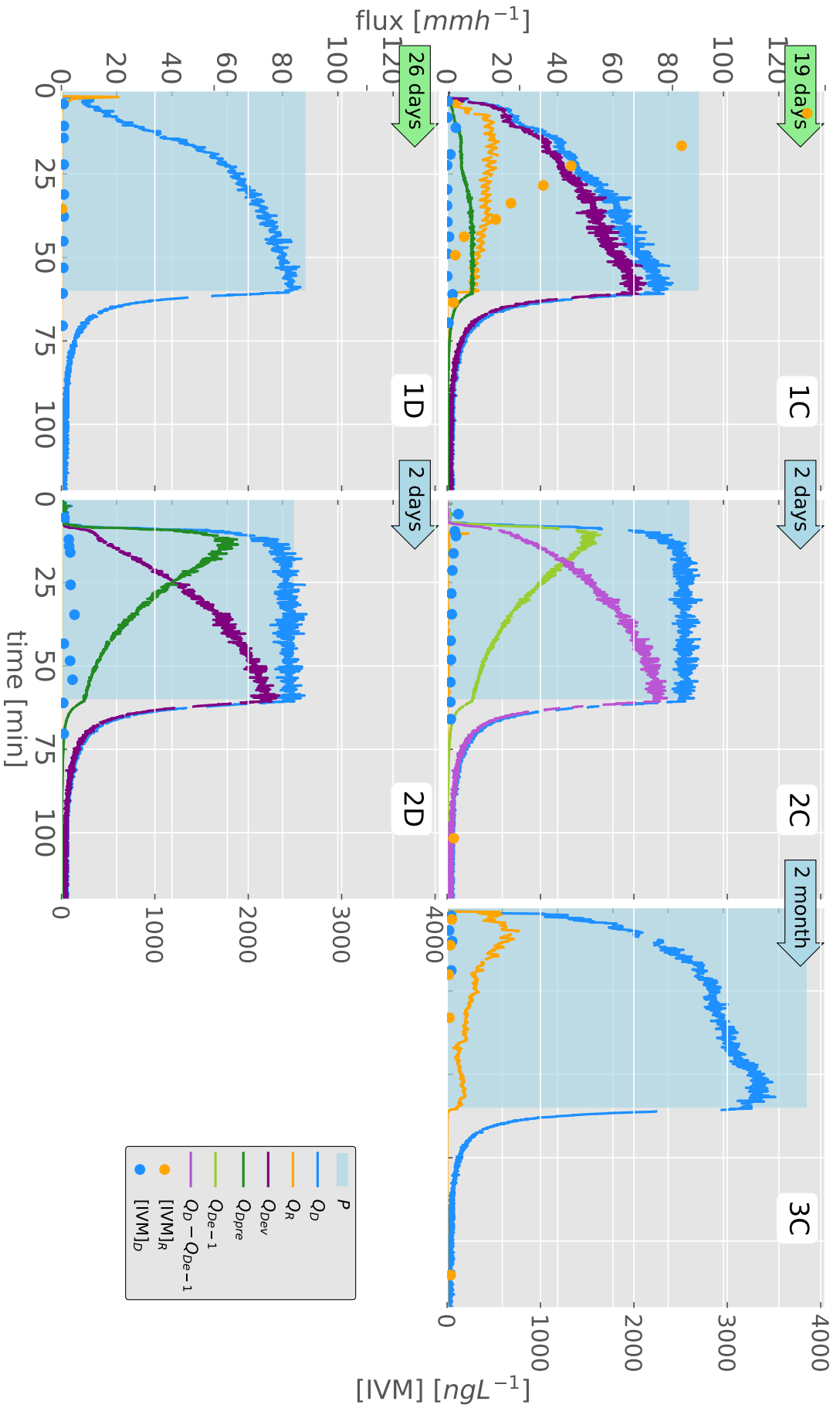


FIGURE 4.18: Time series of outflow and IVM concentrations from experiments C & D on Pradel 2 soils. Arrow-shaped labels indicate the time since the last rainfall. Green background indicates last rain was natural, blue means simulated.

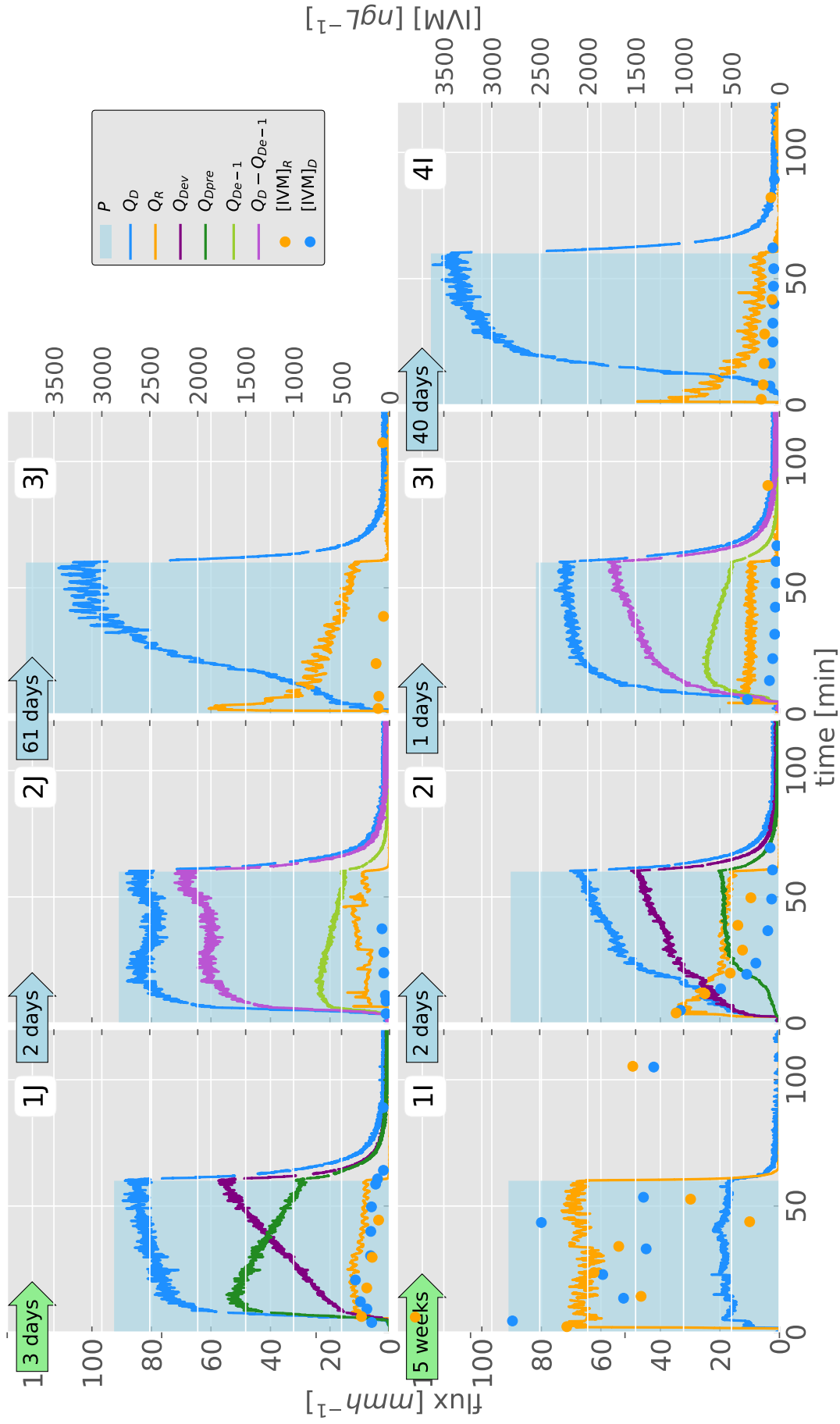


FIGURE 4.19: Time series of outflow and IVM concentrations from the two experiments on Coiron soils (I & J). Arrow-shaped labels indicate the time since the last rainfall. Green background indicates last rain was natural, blue means simulated.

and drainage samples had similar ranges of concentration values, which is in contrast to experiments C and D. The highest concentration values were observed in OF and drainage samples from event 1I. They were variable but remained high until the end of the event. Event 2I started with high concentrations ($>1000 \text{ ng L}^{-1}$ in drainage and OF) which progressively decreased to 72 ng L^{-1} and 298 ng L^{-1} for drainage and OF toward the end of the event. On the Coiron soils, the drainage concentrations are higher and reach their maximum faster than in Pradel 2 soils. On the Coiron soils, they are generally higher during the the first event than during the following events.

Figure 4.20 shows the evolution of IVM concentrations from soils E and B from Pradel 2 and 1 respectively. As mentioned above, both soils were subject to an elongated indoors waiting period

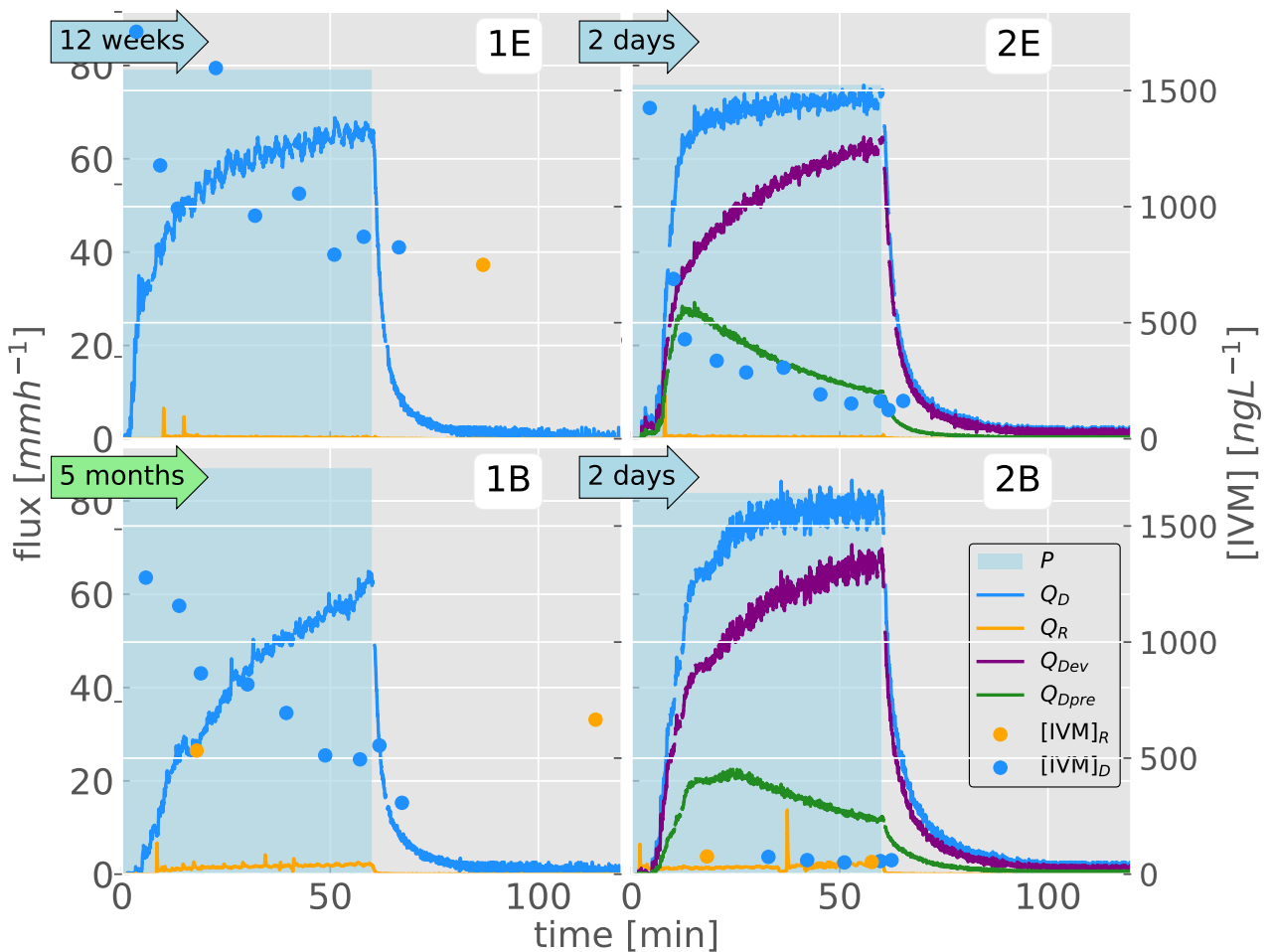


FIGURE 4.20: Time series of outflow and IVM concentrations from experiments E & B on soils from Pradel 2 and 1. Arrow-shaped labels indicate the time since the last rainfall. Green background indicates last rain was natural, blue means simulated.

before the start of the transfer experiments. The drainage samples from the first half of event 2B could not be quantified. On both soils, little overland flow occurred and the measured concentrations in drainage are highest in the beginning of the first event and decrease thereafter. The highest IVM-concentration was 1753 ng L^{-1} in the first drainage sample from event 1E.

4.4 Discussion

4.4.1 Hydrological functioning

Globally, the Coiron soils produce more OF than the Pradel 2 soils. This is in accordance with the higher observed hydraulic conductivity K_H of the Pradel 2 soils as compared to the Coiron soils. All estimated values of K_{HS} for the soil at the Pradel 2 sampling location were above the simulated precipitation intensity, except for the unintendedly high intensity of events 3C and 5C which fell into the range of estimated K_{HS} values (Fig. 4.6). Even though no robust estimate of K_{HS} could be obtained for the Coiron soils, the results of the infiltration tests suggest that it is significantly lower than on the Pradel 2 soils and therefore may well be below the simulated precipitation intensity (Fig. 4.7). The stronger overland flow on soils from the Coiron matches field observations, where strong, large-scale OF has been observed on the Coiron (Fig. 4.21). All OF during the experiments was HOF, due



FIGURE 4.21: Observations of overland flow on the Coiron plateau during a rain event on the 23.10.2013. Photos: Guillaume Nord

to the seepage face lower boundary condition of the experimental setup not allowing for SOF. The occurrence of OF in these experiments is therefore governed by K_H . The results suggest that HOF may occur on the Coiron plateau during intense precipitation.

Between the subsequent events on the same soil and between different soils, the OF proportion was very variable. Nevertheless some patterns can be observed for soils from both locations: Overland flow is higher in the beginning of the precipitation events than in the end and it is mostly higher on dry soils than on moist soils. Furthermore, dry soils react faster than moist soils, also regarding drainage flow. The event water proportion in drainage flow tends to be lower in the beginning and increasing on moist soil whereas it is high from the beginning on dry soil, sometimes even with a decreasing tendency. These patterns can be explained by SWR. Figure 4.22 illustrates some hypotheses on the mechanisms responsible for this behavior. While this schematic illustration is a simplified representation of two extremes, in reality, a mix of both would occur with a progressive transition between them. These are hypotheses based on the observations from the experiments, but they could not be proven. In dry condition (Fig. 4.22 a, referred to as condition a in the following), the soil matrix (brown area) is mostly water repellent and only little infiltration into the soil matrix occurs.

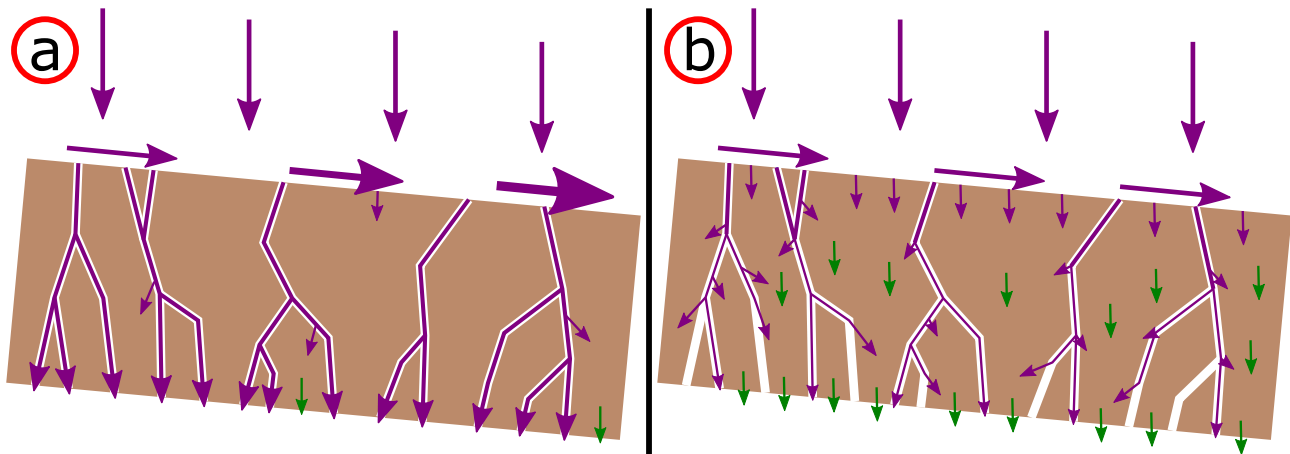


FIGURE 4.22: Illustrative schema of the effect of soil water repellency on the flow of water through and over soil. The brown area represents the soil matrix, while the white area illustrates macropores and arrows indicate flow of water, purple represents event water and green represents pre-event water.

Water can still flow through the macropores, from where infiltration into the soil matrix remains limited. It therefore rapidly bypasses the soil matrix and leaves the soil as drainage flow. Furthermore, the limited infiltration into the soil at its surface leads to increased OF.

Condition a would occur in the beginning of a precipitation event on dry soil and can be transformed to condition b with progressive moistening of the soil leading to a decrease in SWR or persist throughout a precipitation event in heavy cases (11), where moistening of the soil is insufficient to lift SWR. Typical examples of the macropores responsible for the bypassing flow are the earthworm galleries traversing the soil column as well as the network of fissure-shaped macropores that could both be observed in the X-ray tomography. The X-ray tomography showed that there is a significant portion of macropores throughout the soil column with the lowest portion in the rocky layer in the bottom of the soil about 5% to 10%.

Condition b (Fig. 4.22 b) occurs either during an event on initially moist soil or when the soil is sufficiently moistened during an event to lift SWR. In condition b, the soil is not water repellent. The negative pressure head in the soil leads to infiltration of water into the soil matrix progressively filling smaller and then larger pores with water. Macropores do not have sufficient suction to fill with water until the soil is close to saturation. Saturation will first occur locally at the bottom of the soil after the hydraulic head throughout the soil is high enough to cause a pressure head of atmospheric pressure at the bottom of the soil. Then drainage flow starts. This condition has several effects on flow behavior: The increased overall infiltration into the soil leads to less OF as compared to condition a. Even though, there is more infiltration into the soil, condition b would also lead to a retarded beginning of drainage flow as compared to condition a. Furthermore, with condition b, Q_D would be determined by the increase of pressure head due to the arrival of new water at the surface, but old water present in the soil would leave it first due to its location at the bottom of the soil. In other words, in condition b, Q_D is determined by pressure wave propagation through the soil, pushing out old water (celerity

or piston flow effect), while under condition a, Q_D would be the direct arrival of new water traversing the soil.

The presented hypotheses are in accordance with dye distribution patterns observed by Hardie et al. (2011). They showed that under dry antecedent conditions, water infiltrated deeply into soils through preferential flow paths while bypassing large parts of the soil. Under wet antecedent conditions they observed a more homogeneous infiltration front advancing less deeply into the soil. They also explain the preferential flow by hydrophobicity and shrinkage cracks. Performing short rainfall simulation experiments on dry and moist soil from the two sampling locations using a dye tracer could help verifying these hypotheses for the soils from the Claduègne catchment. In addition this kind of experiment could help to confirm the absence of preferential flow between the soil and the sidewalls of the sampling frame, which could act as artificial macropores.

Examples for condition a are event 1I as well as the beginning of events 2I, 3J, 4I, 1C and 1D (see Figs. 4.11 and 4.13). This effect seems to be stronger on the Coiron soils, which matches the observed water repellency in the surface layers of soils I and J (subsection 4.2.4). Furthermore, the Coiron soils contain more OM than the Pradel soils (Fig. 4.5) and OM is usually the cause of water repellency in soils (Täumer et al., 2005; Haas et al., 2018). Condition b can be observed for example in events 2C, 2D, 2E, 1J, 2J, 3I and towards the end of most other events. A good example to illustrate the contrast between the two conditions are the events 1J and 2I (Fig. 4.11). While 1J starts with moist soil corresponding to condition b, 2I starts on dry soil corresponding to condition a. In 1J, the drainage flow takes twice as long to start and consists mainly of old water, while in 2I the drainage flow starts rapidly and almost exclusively consists of event water. The initial OF of 2I is over twice that of 1J. During the first 20 min to 30 min, the condition in 2I evolves from a to b with progressive moistening of the soil. In this time the OF decreases and old water starts to be mobilized from the soil matrix and out of the soil. The soils' water content evolution (Fig. 4.12) also supports this hypothesis: Over event 2I, the soil is progressively moistened while water is already flowing out of the soil, whereas in event 1J, the soil is first rapidly moistened to a threshold and flow starts thereafter keeping the soil water content relatively constant. This threshold would correspond to a pressure head 0 at the bottom of the soil.

While the two conditions presented in Fig. 4.22 work well to explain the main patterns observed during the rainfall simulation experiments, there are some special cases that cannot be explained by them. The missing OF in event 0J, while OF steadily occurs during all following events is difficult to explain. To explain the particularly strong OF during event 1I an additional hypothesis is needed. The dry condition of the soil, the high OF coefficient and the rapid start of drainage flow match condition a. However, the constant and exceptionally high OF of approximately 70% of the precipitation intensity has neither been observed on any other soil nor during any other event on this soil. The most probable hypothesis is that the strong water repellency at the soil surface in the beginning of the event leads to a continuous layer of water above the soil surface. This water would hinder the air contained in the pores of the soil from escaping through the surface, trapping it inside the soil. This would in turn block water from entering the soil. This mechanism was observed by other authors (Wang et al., 1998).

Up to 60 descriptive parameters were calculated for each event, describing the hydrologic response to rainfall as well soil condition and water and solute transfer, depending on the performed analyses. All calculated parameters are listed for each event under <https://cloud.univ-grenoble-alpes.fr/index.php/s/6QySdTSH7YEbxxg> and defined under <https://cloud.univ-grenoble-alpes.fr/index.php/s/TD35FFSTLpfREgn>. Figure 4.23 shows how a selection of these parameters depend on the initial water content Θ_i . Figure 4.23 a) shows how the difference between initial and final Θ , $\Delta\Theta$, depends

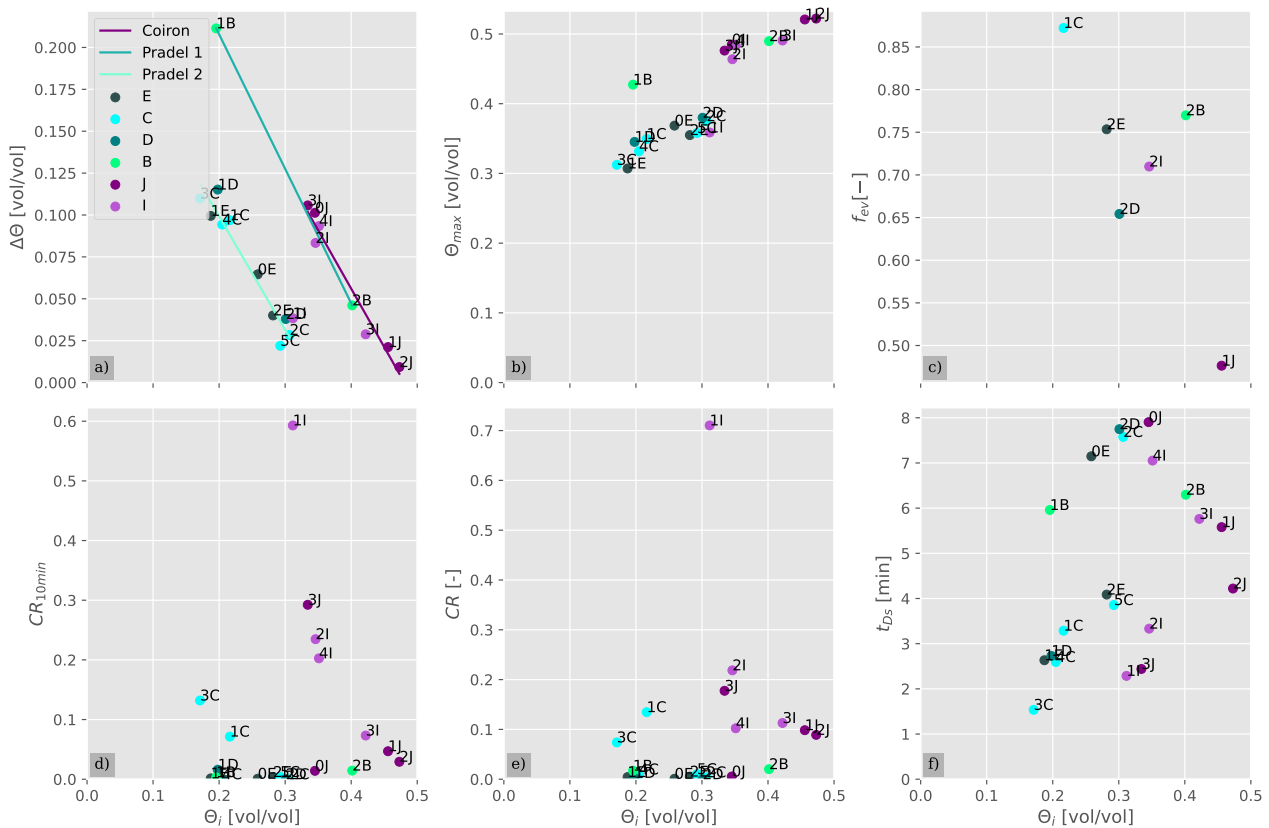


FIGURE 4.23: Dependence of different parameters characterizing the hydrologic reaction of the soils on initial soil water content Θ_i . $\Delta\Theta$ is change in soil water content; Θ_{max} is the event's maximum soil water content; f_{ev} is the overall event water fraction in drainage flow; CR and $CR_{10\min}$ are the overland flow coefficient of the event and during the first 10 min of an event respectively and t_{Ds} is the time until the start of drainage flow. Lines in a) are linear regressions for the three sampling locations.

on initial soil water content Θ_i . For the soils from each origin there is a linear relation, where $\Delta\Theta$ decreases with Θ_i . The only exception from this relation is event 1I, which was not well moistening, potentially due to a mix of SWR and air entrapment as discussed above. A linear regression was performed for soils from each of the three sampling locations. Event 1I was excluded due to its limited infiltration. A similar slope was found for the three soil origins: -0.70 , -0.68 and -0.80 for Coiron, Pradel 2 and Pradel 1 (based on two points only) respectively. However, the intercept is higher for Pradel 1 and Coiron than for Pradel 2. This corresponds to the higher porosity n in Coiron and Pradel 1 than in Pradel 2 (Table 4.1). Making the assumption of a continued linear relation, one could estimate the Θ_i at which no more additional water would remain in the soil, even after a strong rain event

like the one simulated as the intercept with the x-axis. This is 0.48, 0.35 and 0.46 for Coiron, Pradel 2 and Pradel 1 respectively. As we stopped the measurements after about 3 h, this number is expected to be slightly above the field capacity, which has not been quantified. The maximum water content reached during an event Θ_{max} is positively correlated with Θ_i (Fig. 4.23 b)). This means that one precipitation event is not sufficient to moisten the soil to the maximum even if there is a continuous flow of water leaving the soil. This can also be seen in the individual time series of Θ (Figs. 4.12 and 4.14). The overall event water fraction f_{ev} is negatively correlated with Θ_i (Fig. 4.23 c)). This was to be expected as less pre-event water is available in an initially dry soil. With regards to the f_{ev} , the main outcome of these experiments is their evolution during a rainfall event which is discussed earlier.

Figure 4.23 d) shows the relation between OF coefficient of the first 10 min of each event ($CR_{10\ min}$) and Θ_i . On the Pradel soils OF was rare, but the two events with a significant quantity of OF had a low initial soil moisture ($\Theta_i < 0.22$). On the Coiron soils, a clear relation of decreasing $CR_{10\ min}$ with increasing Θ_i can be observed, however not linear. There seems to be a bend in the relation at a Θ_i of 0.35. The only exception from this relation was event 0J which had exceptionally little OF that could not be explained. This figure illustrates the pattern that was observed from looking at the events one-by-one: More OF occurs on dry soil than on wet soil. This fits the conceptualization of soil behavior during wet and dry conditions illustrated in Fig. 4.22: SWR on dry soil reduces the soils infiltration capacity and thereby leads to stronger HOF. For the overall event OF coefficient CR (Fig. 4.23 e)), this relation is less clear because on initially water repellent soils, the water repellency often decreases and so does the CR . This concerns soils with $\Theta_i < 0.35$.

Figure 4.23 f) summarizes the relation between Θ_i and t_{Ds} . t_{Ds} is the time from the start of precipitation to the start of drainage, which is defined as a cumulated volume of 0.1 mm (18 mL). For the Pradel 2 soils there is a relatively clear relation with a more rapid start of drainage flow on drier soil. Here, in addition to SWR, drying cracks can be expected to explain this behavior. The Pradel soils have a higher clay content (Fig. 4.4), and are known to form cracks due to retraction of clay minerals when drying. This creates larger macropores that can rapidly channel water through the soil without much infiltration into the matrix (Hardie et al., 2011). As the lower OM content and the MED test suggest a lower SWR in the Pradel soils, these drying cracks are expected to be the dominant mechanism governing the relation between Θ_i and t_{Ds} .

For the Coiron soils, this relation is less clear. In those events with the lowest Θ_i (1I, 2I and 3J), drainage starts the quickest, however the two events with intermediate Θ_i (0J and 4I) take the longest time until start of drainage flow. This might indicate an intermediate condition at the threshold of SWR at $\Theta_i = 0.35$: the soil is just sufficiently moist to not be water repellent and allow the water to infiltrate well into the matrix, but also sufficiently dry to infiltrate larger amounts of water until the pressure head approaches zero at the bottom of the soil and drainage flow starts. The Θ_i at which this occurs corresponds to the location of the bend in Fig. 4.23 d). Conceptually, this value could be understood as a the water content below which SWR occurs down to lower layers of the soil. This theory of a threshold behavior in SWR could be worth evaluating in future experiments. It is supported by the shapes of the drainage flow curves in Fig. 4.11: For the events with a slow start of drainage ($t_{Ds} > 4\ min$, Fig. 4.23 f), events 0J, 1J, 2J, 3I and 4I), Q_D has a relatively "rectangular" shape with a

quick rise to relatively flat plateau fitting the assumption of condition b of drainage flow starting only once the bottom of the soil is saturated and thereby entering into a steady state. For the events with a rapid start of drainage flow and initially dry condition ($t_{Ds} < 4$ min, Fig. 4.23 f), events 3J and 2I, event 1I is an exception), the shape of Q_D is more "triangular" with a long rise. This indicates the transition from condition a to condition b with progressive moistening of the soil while drainage flow already takes place despite the soil being far from saturation. With these two counteracting factors in mind (SWR with a threshold behavior and the saturation deficit which is progressive), the rapid response of the three soils 1I, 2I and 3J due to their water repellency seems as logical as the negative relation between Θ_i and t_{Ds} for the five remaining events on Coiron soils due to decreasing saturation deficit (Fig. 4.23 f)).

Looking at the evolution of Θ during the second event on the Pradel 2 soils (Fig. 4.14), each of the three soils reaches a point about 15 min into the event after which Θ stops increasing significantly and the outflow is close to the intensity of precipitation. This corresponds to a Θ of about 37 % for soils C and D and about 34 % for soil E. This matches the range of threshold values of Θ_i at which Uber et al. (2018) observed a strong hydrologic response at the scale of the Gazel and Claduègne catchments. Our experiments indicate that at this range of Θ values, the soil cannot hold any additional water even though it is below saturation. Added water will directly push out water at the bottom of the soil through celerity. This explains the runoff coefficients of up to 1 observed by Uber et al. (2018) at a Θ_i of about 37 %. On the Coiron soils, the Θ value at which the soil cannot take any more water is higher: 49 % to 52 % for soil I and J respectively. Accordingly, we would expect this threshold observed at about 35 % on the sedimentary soils by Uber et al. (2018) to be much higher on the basaltic soils. Performing similar investigations in the basaltic part of the catchment could verify this and observations of a strong hydrologic response in the basaltic soils at significantly lower Θ could indicate an importance of SWR on a larger scale.

When comparing these values of Θ to the porosity calculated from bulk density (Table 4.1), a difference between soils C and D versus soil E can be observed. While soils C and D have a lower porosity (both 45 % versus 48 % for soil E), their Θ at which no additional water can be held in the soil is higher (both about 37 % versus 34 % for soil E). This indicates a remainder of 8 % for soils C and D versus 13 % for soil E that are not filled with water during such a strong precipitation event. This volume may be interpreted as very large pores that cannot hold the water against gravity. Therefore the difference indicates additional large macropores in soil E as compared to soils C and D. Soil E was kept on hold at the laboratory over a much longer period than soils C and D before the first event. Accordingly, these additional macropores may represent drying cracks that occurred over this period. The same applies to soil B. While these drying cracks are likely to be caused under artificial conditions (the sampled soil resting indoors), drying cracks do also occur naturally in the field and are regularly observed on soil in the sedimentary part of the catchment after extended dry period. We decided to interpret the experimental results from these soils only with regards to the potential effect of drying cracks on the transfer of water and solutes IVM. The hypothesis of larger drying cracks in soil E as compared to soils C and D is also supported by the fact that the event water proportion of the second event on soil E (2E, moist soil) in drainage flux starts at a much higher value than on soil D (event 2D, see Fig. 4.13). Figure 4.13 also shows that drainage starts rapidly with a small flux in event 2E,

as opposed to events 2C and 2D. The same relatively rapid start of drainage flow can be observed in experiment 5C despite its rather high Θ_i (Fig. 4.23 f)). By the time event 5C was simulated on soil C, the soil had experienced multiple precipitation events and subsequent drying cycles in the laboratory which might have led to additional drying cracks.

4.4.1.1 Solute transfer

Figure 4.24 shows the cumulative export of different solutes versus cumulative discharge for each of the two fluxes and their sum. Y-axes are shared in each row and x-axes are shared for all subplots to facilitate the interpretation with regards to both total fluxes and relation between solute export and water outflow regardless the very different total volumes of the two fluxes. The figure starts with the first event after cow dung application. The slope corresponds to the concentration. Chloride export is lowest from dung without soil, while dung aging did not impact the amount of exported chloride. The Coiron soils export intermediate amounts of chloride. The soils from Pradel 2 export the most chloride but with a decreasing trend. With chloride being a well soluble tracer with little reactivity, the different sources in the system can be added together to obtain the overall export. This indicates that the Pradel 2 soils initially contain the highest amounts of chloride that are washed out by precipitation over the successive events. The Coiron soils seem to initially contain less chloride. The addition of chloride from soil plus dung leads to a progressive increase in chloride export.

All soils from Pradel 2 show a continuous high export of nitrate that does not change over the events, while this export is lower for soil B from Pradel 1. The Coiron soils export almost no nitrate until the third event after dung application. The dung without soil does not export any nitrate. The nitrate is almost exclusively exported via drainage flow. The form under which nitrogen is present in the environment is governed by redox conditions. The amines from cow dung are only oxidized into nitrate in an oxidative environment (Marschner and Rengel, 2007). The cow dung is expected to be a very reduced environment explaining the absence of nitrate. This explains why no nitrate is observed in experiments F, G and H. In the Coiron soils, little nitrogen is present originally (Fig. 4.5) and it is expected to be fixated inside the soils OM. Some of the nitrogen entering it from dung during the rainfall simulation events is oxidized into nitrate during the longer period before the events 4I and 3J, leading to the export thereafter. The Pradel 2 soils already contain nitrate from the beginning on that leaves the soil through drainage flow. Phosphate is exported in high quantities through both fluxes, for those events producing OF. The export is highest on the first event after a longer period without precipitation (all events labeled one, except 1J plus events 4I, 3J and 3C, refer to Figs. 4.11 and 4.13). It should be noted that only orthophosphate is analyzed, whereas the majority of the stock is expected to be organic phosphate (Marschner and Rengel, 2007). The large difference between the first and second event may be explained by microbial consumption of orthophosphate over the two days between the events. After a longer period, re-dissolution might lead to a new export of orthophosphate, however these are only hypotheses the verification of which is beyond the scope of this work. DOC export is relatively similar over the different events, but slightly higher for the Pradel 2 soils than for the Coiron soils. This may seem counter-intuitive with regards to the higher content of OM in the Coiron soils, but may be explained by stronger stabilization of OM in these soils as

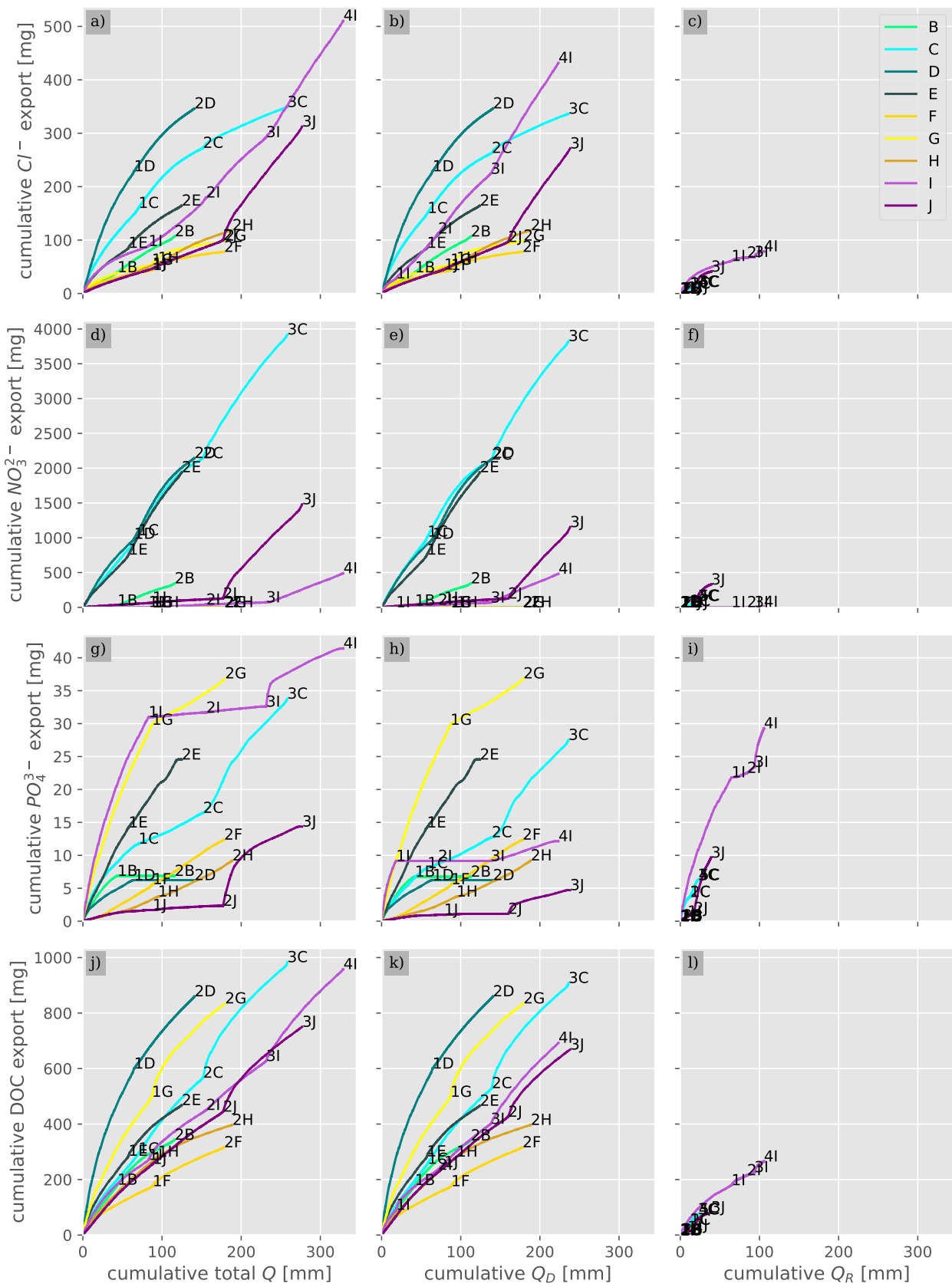


FIGURE 4.24: Cumulative flux of different solutes versus cumulative discharge for both fluxes combined (a, d, g, j), drainage (b, e, h, k) and overland flow (c, f, i, l).

explained in subsection 4.2.4. For the dung there is a significant difference between the fresh dung that has a high DOC export and the two aged dungs that have a lower DOC export.

4.4.2 Ivermectin transfer

4.4.2.1 Quantification problems and potential reasons

The measured concentrations of the internal standard DOR were very variable with some samples below the LD. Those samples also had very low concentrations of IVM, often below the LD, which would not be expected when looking at previous and following samples. Therefore it is assumed that those low recoveries are not just linked to a problem with the internal standard itself but with an actual low recovery of both molecules (DOR and IVM) from the samples. A few samples also had a recovery of DOR greater than 100%. Investigations are currently underway in order to understand these points. Due to the complex chain of sample preparation including SPE and derivatization, many sources of error are possible. Concerning the low and variable recovery of DOR and IVM, this is likely to be linked to the SPE and potentially to an incomplete elution of IVM. This assumption is based on a test where after elution of the cartridge with 3 mL of acetonitrile (ACN), a second elution of the cartridge was performed with the same amount of ACN. This was done for two samples. The first sample had a good recovery of DOR at the first elution and hardly anything was found after the second elution. For the second sample, the recovery during the first elution was much worse and in the second elution, almost the same quantity of DOR and IVM were found in the extract. Unfortunately, we received the results of this test and almost all samples after all experiments were finished, so no adaptations of the method were possible. As this whole study was developed as a reorientation of the PhD after the first year and the analytical method was developed in parallel, the limited time did not allow to wait for completion of the analytical protocol and extensive testing of the sample preparation protocol before conducting the experiments. A first series of samples had been sent to INTHERES laboratory, Toulouse for analysis in order to validate the sample preparation. The results arrived midtime through the experiments. They revealed recoveries of DOR below 70% for a significant part of the samples. However, due to the restrained time frame and the delay of the analyses, we had to accept these low recoveries and keep the experimental protocol unchanged. It was only a posteriori with the completion of the remaining analyses that the full extent of the problem became perceptible, with very low recoveries for many of the samples. Concerning the recovery of DOR greater than 100%, further work is in progress in order to find the source of this DOR-contamination, but could not be concluded yet. Potential sources include a possible contamination of the medicament used to spike the cow dung (Oramec) or a contamination of the cow dung itself with DOR. However, the latter should not be the case as the farmer stated not to use DOR. For consistency, even samples with a recovery of DOR greater than 100% were treated the same way as all other samples and corrected using this DOR concentration.

4.4.2.2 Factors controlling the transfer of Ivermectin

Event G shows that over the course of two successive events, about 1% of the quantity of IVM initially contained in cow dung can be mobilized in form of dissolved IVM, and the trend in Fig. 4.16 suggests that further export would follow on further precipitation events. With regards to the effect of aging

of contaminated cow dung, the results of experiment F suggest that as little as one week of drying at room temperature without solar radiation can substantially decrease the mobility of IVM, as it cut the overall export by a factor five. In event 1H after 6 weeks of dung ageing the cow pat had a very dry occurrence and the export of IVM was negligible, indicating an immobilization of IVM by cowpat drying. On the other hand, during the second rain, large concentrations of IVM were observed, indicating that this immobilization through drying can be reversed through moistening of the cow pat. This matches observations by Wohde et al. (2016), where in wet conditions IVM dissipated more rapidly from cow dung than in dry conditions, where it persisted at high concentrations for more than 1 yr. It is difficult to explain that the export from 2H is twice that of events 1F and 2F. This could theoretically be due to a pollution in the sample preparation and analysis chain. On the other hand, no IVM was detected in any of the blank samples. As noted before, there was one modification of the sample preparation protocol for this particular event: As no particles were visible in samples from this event, the samples had not been centrifuged before the SPE. Even though no particles were visible in the samples, IVM might have been adsorbed to some kind of invisibly small particulate matter, that would have been excluded by centrifugation.

In most cases, the presence of soils reduces the concentration in drainage flow and thereby export of IVM significantly. While strong OF in the beginning of an event (1C, 1I) leads to high export, the export through drainage is limited and delayed on soils C and D. The filtering effect of soils through sorption seems to be particularly strong for the Pradel 2 soils C and D. The highest observed drainage concentration (140 ng L^{-1}) is less than 4% of the highest observed overland flow concentration (3854 ng L^{-1}). Furthermore, a retardation of the export of IVM through drainage can be observed regardless the rapid transfer of event water: The concentration in drainage is generally higher in the second than in the first event (Fig. 4.18). The short concentration peaks in drainage during event 1C may indicate the arrival of small amounts of preferential flow through some preferential flow paths that are marked by little interaction between soil and water. The significantly higher concentration in OF from the beginning of event 1C (Fig. 4.18) as compared to the fresh dung without soil (1G, Fig. 4.17) may be explained by the OF flowing around the dung and mobilizing more IVM than the precipitation alone can mobilize without soil. This effect is even stronger in event 1I with very strong overland flow leading to an overall export that is 1.7 times as high as from fresh dung without soil (Fig. 4.16). As a general contrast, the Coiron soils show much higher concentrations in drainage flow than soils C and D (Figs. 4.18 and 4.19). This may be explained by the hydrophobicity of these soils leading to strong fingering flow as observed after the field infiltration experiments. This would signify stronger bypassing of the matrix through macropores which would lead to less interaction between water and the solid phase of the soil and therefore less sorption. Due to the strong overland flow and hydrophobicity of these soils, preferential flow along the walls acting as artificial macropores cannot be excluded with certainty. However, several measures are in place to avoid this. The boundaries were sealed with compacted soil reaching higher than the soil sample itself and protected from precipitation through covering the outer 1.5 cm (see the article, Hachgenei et al. (2022a)). Therefore, the only probable risk would be exfiltration of water from the soil toward the boundaries, which could take place to some extent, but is not expected to represent a substantial part of the flow of water and contaminants. Furthermore, the X-ray tomography confirmed the presence of connected natural macropores in the soil that can explain rapid preferential flow.

An interesting observation from event 1J on initially moist soil are the low concentration values of IVM in OF (Fig. 4.19) as compared to event 1C (Fig. 4.18) even though the CR was very similar. The concentration of IVM in OF of event 1J is even lower than that of event 2I, which had already exported a large quantity of IVM through a previous event. A plausible explanation in accordance with the hypotheses on the hydrological functioning of the soil (Fig. 4.22) would be that the moist soil allows more infiltration of water from OF along the way. Therefore, the OF would mainly consist of water from the lower part of the slope whereas a large part of the water from the higher part of the slope that passed the cow dung would have infiltrated on the way. This would also explain why the concentration in OF of event 1C decreases so drastically toward the end of the precipitation event when water repellency is lifted and overland flow decreases, while in event 1I during which the soil remains dry, the concentrations remain in the same order of magnitude and also in event 1J, the concentration values decrease less throughout the event. Another potential explanation could be rapid adsorption of IVM along the flowpath, even from OF, which would be stronger on humid, not water repellent soil due to increased contact between soil and water.

Concerning soils E and B (Fig. 4.20), the suspected drying cracks in these soils (see above) led to a much higher IVM concentration in drainage as compared to the other soils from the sedimentary area (C and D). This is likely to be caused by increased rapid preferential flow through those drying cracks (as indicated by the high event water fractions during the second event from the beginning on (Fig. 4.20 as compared to soil and D in Fig. 4.18)) limiting contact time and surface between water and soil and thereby retention of IVM on the soil.

The higher export through drainage flow and the higher overland flow coefficients on the Coiron soils strongly suggest an increased mobility of IVM through these soils and therefore an increased risk of contamination of water ways on the basaltic plateau as compared to the sedimentary part of the catchment. Overall, the results suggest that the occurrence of OF is a determining factor for the mobility of IVM and SWR increases both the risk of the formation of OF as well as the risk of transfer of IVM through the soil via subsurface storm flow and over the soil via OF. It could be shown that the occurrence of overland flow leads not only to a higher transfer of IVM but also increases the mobilization of IVM out of the cow pat. The results also suggest that initially moist soils may reduce the mobility of IVM, even in OF, potentially through increased water-soil contact and reinfiltration, at least in the case of water repellent soils like those from the basaltic part of the Claduègne catchment.

A parameter that is expected to be very important, but could not be studied due to the time-consuming and work-intensive analytical method is transport with particulate matter. With its $\log K_{oc}$ of about 4, IVM should be 10000 times more concentrated sorbed to OM than dissolved. The suspended matter content was estimated for some of the events by collecting and weighing all water from each of the two fluxes, decantation and drying of the remains. The overall suspended sediment load was between 0.1 g L^{-1} to 1 g L^{-1} for both fluxes with an average of 0.29 g L^{-1} to 0.19 g L^{-1} for drainage and OF respectively. The OM fraction of this suspended matter was not quantified but is expected to be high from an optical aspect. Using an estimated OM fraction on the suspended sediment of $1/3$, the load of IVM transported can be expected to be about the same order of magnitude as the dissolved fraction. The observations from event 2H (Fig. 4.17), where particularly high and variable concentrations were observed when the samples had not been centrifuged suggest that this transport

pathway might be of higher importance than expected from the above estimations. A reason for a potential over-proportional importance of particulate transfer of IVM could be an insufficient time to obtain an equilibrium between highly concentrated particles from dung and the rain water. As this observation only concerns a few samples, this remains a hypothesis.

The decision to use fine raindrops to preserve the natural soil structure (see the article, Hachgenei et al. (2022a)), comes with the drawback of being less representative of natural rain during such intense events and more specifically creating less erosion of the soil and presumably the cow dung as well. While this decision was important to be able to compare soils from one event to another, the mechanical impact of larger raindrops with higher kinetic energy could have contributed to the disintegration of cow dung increasing IVM mobilization.

An aspect that is beyond the scope of this study and was entirely put aside, but might be of importance on the long-term is accumulation of veterinary PhAC in soils with potential future remobilization. The quantities of IVM inside the soils and their evolution after the experiments (persistence vs. degradation) were not quantified. As explained above, the experiments focused on the event-scale transfer dynamics and integrated effect of factors influencing the exported mass and dissolved concentration of IVM without explicitly quantifying the individual physical and chemical processes (adsorption-desorption and different degradation mechanisms).

4.5 Conclusion

Large differences in the hydrologic response could be observed between the different events. In general, more OF occurred on the soils from the basaltic part of the catchment, which was linked to lower hydraulic conductivity and higher content of OM leading to water repellency. On the same soil type, dry conditions generally led to more OF, more rapid drainage flow and a higher proportion of event water in drainage flow from the beginning of the event on. This can be explained by water repellency in dry conditions favoring preferential flow versus negative pressure head in wettable soil under moist conditions requiring saturation at the bottom of the soil in order for drainage flow to start. In addition to water repellency, the formation of drying cracks on the more clayey Pradel soils might explain a more rapid drainage response under drier conditions.

We could show that up to 1% of IVM contained in cow dung can be mobilized by two subsequent intense storm events. The highest concentration values (up to 3855 ng L^{-1}) were observed in OF in the beginning of rain events. OF concentrations were lower on initially moist soil (1J) than on initially dry soil (1C, 1I, 2I). Drainage concentrations were lower than OF concentrations in the Pradel soils C and D ($<150 \text{ ng L}^{-1}$), but the experiments on soils B and E suggest that higher drainage concentrations can be expected after an extended dry period through the formation of drying cracks. On Coiron soils the difference between drainage and OF was much smaller. In general, the risk of IVM mobilization is higher on the basaltic soils, mainly due to the higher OF. On this scale, the mobilization of IVM is higher under dry conditions. Higher initial soil moisture reduced the values of IVM concentration in drainage and OF from the Coiron soils, presumably through removed SWR leading to higher contact between soil and water and thereby increased adsorption of IVM to the soil. A transfer of this result to a larger scale however seems critical, as on the hillslope scale, drier conditions could also lead to

higher re-infiltration than wet conditions and a much smaller portion of the OF reaching the stream. The same is the case with regards to the higher drainage concentrations under dry conditions, as these experiments do not allow conclusions on the larger scale connectivity of preferential flow under these conditions. Globally, the occurrence of large-scale connected overland flow on the Coiron plateau can be confirmed by field observations (Fig. 4.21).

Aging of cow dung of as little as one week substantially reduced the mobilization of IVM but re-mobilization through an elongated moist period cannot be excluded. All measured concentrations are far above aquatic predicted no effect concentration (PNEC) for IVM (up to 8 orders of magnitude) but they do not represent expected stream concentrations, as the effect of hillslope scale hydrological and chemical processes can not be predicted from these experiments. Re-infiltration of OF leading to sorption of IVM could strongly reduce the amounts of IVM reaching streams. On the other hand, run-on from higher parts of the hillslope may also increase the mobilization of IVM on lower parts of the slope, according to the observation that export of IVM was higher from dung on soil with strong OF than it was from dung without soil. The results suggest, that by far the highest short-term risk of export of IVM toward surface water bodies is through OF, but export through subsurface storm flow could also occur in smaller quantities. If this is likely to occur in the field during intense precipitation on dry soil like observed on the sub-metric scale cannot be concluded from these experiments.

4.6 Link to the catchment scale

The conditions that led to the strongest OF and the highest drainage IVM concentrations during the above experiments on the sub-metric scale (intense precipitation on dry soil) do not lead to major flood events at the scale of the Claduègne catchment. As found by Uber et al. (2018) and discussed in Chapter 2, the strongest hydrological response is caused by intense precipitation on a wet catchment. It should however be noted, that the simulated precipitation event of about 90 mm h^{-1} over one hour corresponds to a rare event with a return period of 10 yr to 20 yr (Beuerle, 2021). In other words, a similar event at the catchment scale would represent very wet conditions. While the most unexpected and therefore most highlighted result of this chapter is the strong effect of initial soil moisture on the transfer of water and IVM through and over soil, this should not cloud the fact that we simulate a major precipitation event that would certainly cause a major flood event at the scale of the Claduègne catchment. With regards to concrete applicability to the Claduègne catchment and similar sites under Mediterranean climate, the major outcome is that very large amounts of IVM may be mobilized from cow dung on soil during intense precipitation events.

The increased preferential flow through dry soil that may be water repellent or present drying cracks is interesting from a research perspective. However, the connectivity of this kind of flow through dry soil along the hillslope and through the catchment is expected to be limited. Concerning drainage flow, these conditions are expected to lead to deeper infiltration of event water and contaminants, but an increasing water content with depth reducing SWR and drying cracks would be expected to buffer this effect on a larger spatial scale. OF generated by SWR might in many cases infiltrate into the soil in another location along the hillslope that is less water repellent and only small parts of it may actually reach the streams. Lemnitz et al. (2008) show a decrease in runoff coefficients from

water repellent soil with increasing scale from plot to hillslope which they link to observed spatial heterogeneity of SWR.

In order to understand the continuity of flow of event water toward the streams and the outlet of the catchment, in the following chapter, a geo-chemical and a meteorological water tracer ($[Si]$ & δ^2H) are used to quantify the evolution of transit time distributions at the Claduègne outlet over time through different hydro-meteorological conditions via a conceptual numerical model. This allows to verify if during major flood events, a significant fraction of the streamflow consists of event water which would have a high chance of containing contaminants mobilized during the event. As the dominant mechanism of flood generation on the catchment scale is intense precipitation on wet soil, the model will focus on reproducing this mechanism.

5

Solute transfer and water age tracking in the Claduègne catchment

5.1	Introduction	120
5.1.1	Transit time tracing in hydrology	120
5.1.2	Goals of transit time tracing within the PhD	122
5.2	Methods	124
5.2.1	Dataset description	124
5.2.1.1	Tracer choice and sampling strategy	124
5.2.1.2	Water analysis	127
5.2.1.3	Synthesis of results / data	129
5.2.2	The model	137
5.2.2.1	Forcing and calibration data	139
5.2.2.2	Model structure	139
5.2.2.3	Age of water	141
5.2.2.4	Tracers	149

5.2.2.5	Model calibration	151
5.2.2.6	Initial conditions	153
5.3	Results	153
5.3.1	Model fit	153
5.3.1.1	Goodness of fit interdependence	158
5.3.2	Transit times	158
5.4	Discussion	164
5.4.1	Calibrated parameters	164
5.4.1.1	Implications on catchment functioning	167
5.4.2	Discussion and implications of the modeled transit time distributions	168
5.4.3	Constraints, limitations and possible improvements	169
5.4.4	SAS functions and reactive transport	171
5.5	Conclusion	172

5.1 Introduction

This chapter presents a hydro-geochemical dataset used to gain insights into water transfer through the Claduègne catchment. A semi-distributed hydrological model with age tracking functionality was developed in order to estimate transit time distributions. The model does not represent the transfer of pharmaceutically active compounds (PhAC), but the resulting transit time distribution can be interpreted in terms of risk of transport of PhAC into the stream.

5.1.1 Transit time tracing in hydrology

The temporal dimension is a crucial part of understanding water and mass transfer throughout a catchment. In classical hydrological modeling, eg. for flood and drought forecasting, the variable of interest is the discharge of water passing through the catchment outlet at each moment, called runoff discharge. These classical hydrological models focus on water transfer and are calibrated on water quantities only, such as discharge and ground water levels. In the real-world the runoff discharge is often controlled by celerity (pressure wave propagation) instead of mass transfer (Hrachowitz et al., 2016). This means that an increased runoff caused by a rain event does not necessarily consist of rain water that had just fallen but may consist of older water pushed out by the arriving new water. Therefore, these classical models may be very wrong with regards to the actual transfer times of the water from rainfall to streamflow, even if they correctly reproduce the observed discharge. In order to well understand the transfer of water and contaminants throughout the catchment, the actual transfer of mass of water and solutes needs to be understood.

Over the last 15 years, with increasing accessibility of analytical methods and computational power, transit time modeling has become an important subject in hydrology. Different tracers have been used to track the age of water. Observations of environmental tracers allow to extract the mass transfer of water from precipitation-discharge relationships and disentangle it from celerity (Sprenger et al., 2019).

Transit times can be defined in the form of transit time distributions (TTD), representing the proportion of water experiencing each transit time. TTD can be noted in a forward or backward way, which would be equal in a steady-state system but differ significantly in a catchment with unsteady fluxes (Rinaldo et al., 2015). The forward notation represents the distribution of time the water from one rain event would stay in the catchment until leaving it. The backward notation represents the proportions of time a volume of water leaving the catchment in one moment took to transit it. Both forward and backward notations can be of interest (Botter et al., 2011; Benettin et al., 2015). The forward notation is of interest when investigating the fate of water and/or contaminants injected into the system at a certain time, while the backward TTD characterizes the water in the stream and corresponds to "analyzing" the history of a water sample taken in the stream at a certain moment. The compartment of interest of this study are the streams as they are particularly sensitive to many of the investigated PhAC. Therefore, in the following the backward notation of TTD is used. The backward TTD of the flow leaving a catchment corresponds to the water's age distribution in this flow Q , where $Q(T, t)$ is the absolute age distribution in units of water height or volume per time and $p_Q(T, t)$ is its unitless probability density function (pdf) at time t , with T being the age. T equals zero at the time when a volume of water entered the system in form of effective precipitation and then increases with time. This water age distribution exists for any flux of water leaving a reservoir or the catchment. Inside a reservoir S , the water age distribution is noted as $S(T, t)$ or $p_S(T, t)$ (absolute or pdf respectively). The catchments overall age distribution corresponds to the residence time distribution (RTD) of water in the catchment. The basic concept of water transit time distributions can be illustrated by representing water as a population growing older as it moves through the catchment until leaving it and being renewed by fresh rainfall entering the catchment (Rinaldo et al., 2015; Sprenger et al., 2019).

Early approaches to track transit times through hydrological catchments include steady-state TTD which assume a time-invariant mathematical shape (e.g. exponential or gamma distribution) for the TTD (McGuire and McDonnell, 2006; Małoszewski and Zuber, 1982; Kirchner et al., 2000, 2001). The parameters of this distribution were calibrated against observed tracer time series in system outflow. Different modifications have been made to these TTD in order to account for non-steady state conditions, e.g. by presenting the TTD as a function of cumulative flow volume instead of time (Niemi, 1977; Rodhe et al., 1996) assuming time-invariant flow-paths but allowing time variant flow.

An elegant way to avoid having to adapt rigid TTD to time-variant conditions is to define the age selectivity of a catchment or reservoir instead of the TTD. This approach was invented by Botter et al. (2011) and is today well-known as StoreAge Selection (SAS) functions (Rinaldo et al., 2015; Hrachowitz et al., 2016; Sprenger et al., 2019). SAS functions define the relation between water age distributions in a reservoir and in a flux leaving the reservoir in a spatially integrated manner. They can be described as the equivalent of the advection-dispersion equation along the dimension of age, integrated over space (Rinaldo et al., 2015; Ginn et al., 2009; Fiori and Russo, 2008). They were

initially defined by Botter et al. (2011) under the name of mixing functions as

$$\omega_Q(T, t) = \frac{p_Q(T, t)}{p_S(T, t)} \quad (5.1)$$

Coming back to the parallel with a population (the reservoir S), a SAS function defines the probability of an individual of a certain age to die, instead of fixing the age distribution of individuals that die per year. Thereby, SAS functions compensate for the demographics of water present in the reservoir (if a population has more aged individuals, the fraction of aged individuals in those dying is higher). Therefore, SAS functions are more adaptive to varying conditions than defining a TTD. Water fluxes in between the different reservoirs and out of them have different probabilities to take older versus younger water, very much as in most populations, mortality changes with age. In the case of water transfer this can be due to the location of the water in the reservoir (eg. on a vertical axis, along a hillslope, in smaller versus larger pores of the soil, closer or further from plant roots, etc.).

While for any flux a real SAS function exists, in hydrological modeling mathematical functions that can be parameterized to reproduce tracer observations are used to approximate them. SAS functions are well adapted for implementation in conceptual models as they represent the spatial heterogeneity of hydrologic features of the critical zoneⁱ by integrating their functionality without a need to explicitly specify them (Botter et al., 2011).

In order to be more representative of real-world conditions, SAS functions can be made time-variant as a function of the current conditions. For example, the age preference can depend on the amount of water in the reservoir (Harman, 2015). These time-variant SAS functions are mostly used to represent the hypothesis that increased humidity activates more preferential flow paths and therefore creates a stronger young water preference through bypassing of the slower components of the reservoir (Harman, 2015).

A more physically and spatially explicit way of tracking water age is to track water particles throughout spatially distributed hydrologic models (Davies et al., 2013; Maxwell et al., 2016; Danesh-Yazdi et al., 2018; Remondi et al., 2018; Yang et al., 2018; Weill et al., 2019). These models are more demanding in terms of computational power and detailed data, but in return can give spatially distributed insights in water transfer dynamics.

5.1.2 Goals of transit time tracing within the PhD

Within this PhD project, an age tracking model is used in order to estimate the transit time distributions as well as new water fractions (nwf) and young water fractions (ywf) (Kirchner, 2016, 2019). We define nwf and ywf as the portion of water in streamflow of an age of less than one day and less than 30 days respectively. This serves to evaluate, under what hydrological conditions water from recent precipitation can rapidly be found in the streams, carrying the contaminants it had just washed out from the fields. As many of the pharmaceutical contaminants investigated in this study have strong sorption coefficients (see Chapter 3), we assume that water transiting the critical zone for periods

ⁱ The critical zone is the zone at the earth's surface in which interactions between atmosphere, geosphere, hydrosphere and biosphere take place and generally spans from the tree canopy to the bedrock

longer than one day to a few days will potentially "lose" those contaminants via sorption to reactive surfaces of the soil and stream bed sediment. Furthermore, over longer periods of time, degradation will take place. Ivermectin (IVM) for example is easily photodegradable, whereas biodegradation takes longer time (see Chapter 4). Due to those factors, particularly the sorption, very young water reaching the stream would represent the highest risk of contaminating surface water, which is particularly sensitive to antiparasitic drugs, as explained in subsection 4.1.2.3. The questions to be answered in this chapter are:

1. In which conditions and which seasons, are there significant fractions of the discharge in the Claduègne that are less than one day old?
2. How high are these fractions?

In order to answer these questions, hypotheses about the catchment functioning are established. Through the process of model calibration and evaluation through observations of discharge and tracers, the following question will be treated:

3. Can our simplified hypotheses of catchment functioning reproduce discharge and tracer dynamics at the outlet?

The decreased mobility observed for IVM after drying of cow dung (see Chapter 4 and Wohde et al. (2016)) is expected to lead to an important influence of the time between treatment and a rain event with the potential to flush these contaminants into surface water bodies. A similar behavior is expected for other PhAC used in the Claduègne catchment. Thus, after identifying periods and hydro-meteorological conditions that favor rapid transfer of event water into the stream, those periods are compared to treatment periods and grazing seasons in order to evaluate the risk of transfer of veterinary pharmaceuticals toward the streams.

We chose to construct a semi-distributed hydrological model that consists mainly of a saturated and an unsaturated zone reservoir for each of the two geological units of the catchment and that traces transit times via SAS functions. The term semi-distributed refers to the fact that there is no full, highly resolved spatial distribution, but different spatial units are defined (the two geological units with saturated and unsaturated zone each). This model has a small number of spatial units and most of the spatial variability is treated in an integrated way. Accordingly, it can be considered on the 'lower edge' of semi-distributed models toward lumped models. The model's hydrological behavior and age preferences are calibrated with the aid of observed dissolved silica concentrations at the catchment outlet and deuterium ratio of the water molecule in precipitation and stream-flow. Part of the basic model structure and some of the equations are oriented after a model presented by Markus Hrachowitz during the autumn school "Water Ages in the Hydrological Cycle" in October 2019 in Freudenstadt, Germany, similar to the model used by Hrachowitz et al. (2015, 2014); Fovet et al. (2014). In the following, this model will be referred to as the "example model" in order to identify the parts taken from there.

The choice to use a relatively simple conceptual model that integrates processes over large spatial units of the catchment was made for several reasons: The available spatially distributed information is not sufficiently precise to use a fully distributed model with high spatial resolution and physical

process representation without calibration with confidence. Furthermore, we are interested in the temporal component of water transfer and physically based hypotheses of hydrological functioning could be made and conceptualized on the scale of the catchment. These hypotheses are physically and chemically sound and based on observations of discharge and several tracers. Therefore, the construction of a numerical conceptual model based on these hypotheses on the scale of the Claduègne catchment seemed to be the best adapted approach according to the objectives and available resources and data.

5.2 Methods

This section starts with an explanation of the choice of the two tracers used in the hydrological model. Then the sampling strategy is detailed as well as the chemical analyses performed on those samples and the results of this monitoring are presented. Based on these results and prior knowledge of the catchment behavior, some assumptions are formulated on which the model structure is based, before detailing the model architecture and calibration procedure.

5.2.1 Dataset description

Fig. 5.1 shows the location of sampling sites throughout the catchment. Hydrological monitoring and regular water sampling took place at two stations: the outlet of the Claduègne catchment (CLA) as well as the outlet of the Gazel subcatchment (GAZ). For the hydrological modeling however, in a first approach we only considered the water flow and tracer concentrations at CLA. All water sampling sites are listed in Table 5.1.

5.2.1.1 Tracer choice and sampling strategy

Different kinds of tracers were under consideration. As this PhD study is interested in the fate of agricultural contaminants entering the system through diffuse input onto natural soils, we needed to use tracers that are not too heavily influenced by other anthropogenic sources such as chloride. The goal of the model being to trace transit times through the catchment, we also needed tracers to either have a measurable, time-variant signal in precipitation and conserve it throughout their transit through the catchment, or to gain this signal as a function of time passed in the catchment. Furthermore, taking into account the contrasted geology of the catchment and the dominance of cattle breeding on the Coiron plateau (upper part of the catchment), we needed the tracers to have a strong signal from this basaltic region that is not masked throughout the transit of the lower part of the catchment on sedimentary geology, as would be the case with calcium for example. We decided to analyze major and trace elements using inductively coupled plasma - optical emission spectrometry (ICP), major anions using ion chromatography (IC) and water stable isotopes using an induction module cavity ring-down spectroscope (IM-CRDS). We then selected two tracers that work in two different ways. Stable water isotopes are used as a conservative tracer of the rainwater. We analyzed the isotopic signature of rainwater and assume that all water keeps this signature during transit through the catchment. This way the isotopic signature of the stream water leaving the catchment can be modeled and compared to analyzed stream water samples. Hereby we neglect isotopic fractionation during transit of the

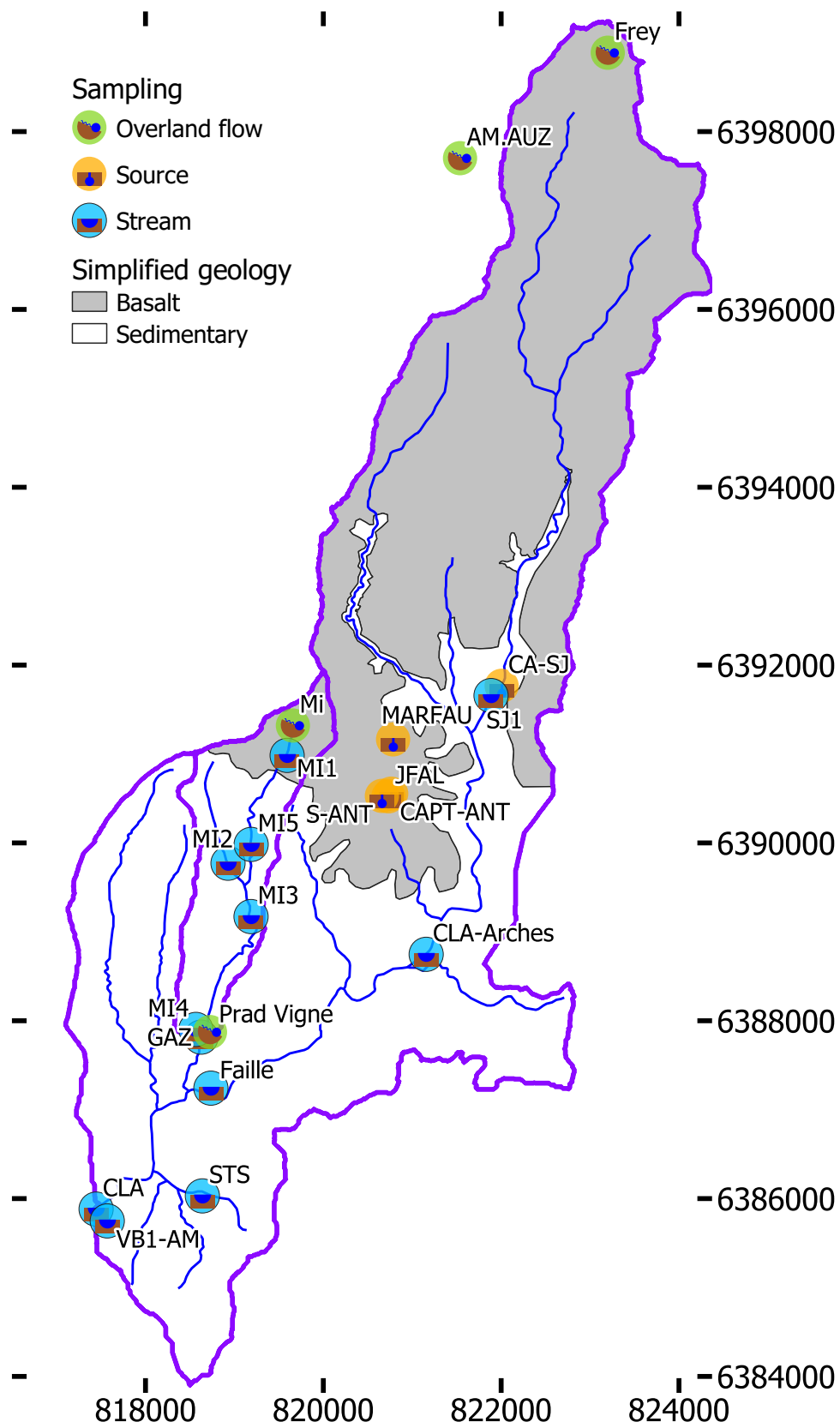


FIGURE 5.1: Sampling sites in the Claduegne catchment. Coordinates are in Lambert 93.

TABLE 5.1: List of water sampling sites for tracer analysis. X_{L93} and Y_{L93} are easting and northing in Lambert 93. OF is overland flow. The point "STS" is on sedimentary geology at the outlet of the waste water treatment plant.

Name	Type	Geology	X_{L93}	Y_{L93}
AM.AUZ	OF	basalt	821537.5	6397701
Frey	OF	basalt	823199.3	6398887
Mi	OF	basalt	819657.6	6391320
Prad Vigne	OF	sedimentary	818725	6387872
CAPT-ANT	source	basalt	820763.1	6390554
CA-SJ	source	mixed	822005.3	6391767
JFAL	source	basalt	820732.3	6390524
MARFAU	source	basalt	820784.4	6391164
S-ANT	source	basalt	820658.5	6390529
CLA	stream	mixed	817444	6385881
CLA-Arches	stream	mixed	821156.6	6388747
Faille	stream	sedimentary	818735.3	6387241
GAZ	stream	mixed	818625	6387815
MI1	stream	basalt	819592.8	6390984
MI2	stream	mixed	818927.7	6389771
MI3	stream	mixed	819186.8	6389171
MI4	stream	sedimentary	818566.2	6387902
MI5	stream	mixed	819187.9	6389983
SJ1	stream	mixed	821886.1	6391657
STS	stream	sed-WWTP	818639.5	6386030
VB1-AM	stream	sedimentary	817569.6	6385748

catchment. The second tracer, dissolved silica is not present in rain water (confirmed by analyses) but dissolves slowly in contact with rock and soil minerals. The concentration of dissolved silica in water therefore depends on the contact time and contact surface between water and silica-containing minerals. Silica has several advantages as compared to the major ions and many trace element that we analyzed as well. Silica has no charge which makes the assumption of conservative transfer with water more realistic. Furthermore, its dissolution is slow, meaning that it does not reach saturation but progressively increases in concentration (as opposed to Calcium for example). Saturation would obliterate the age-information carried in the concentration, as once the water is saturated the concentration is no longer impacted by dissolution and therefore no longer depends on contact time. Another large advantage of silica is its dominant source being the basaltic plateau with less of it originating from the downstream sedimentary area, meaning that the signal originating from the basaltic area is not covered during transit through the sedimentary area.

Rain water samples have been taken using a *Teledyne ISCO 3700* automated sampler starting in November 2019. The sampler was controlled by a *Campbell CR800* datalogger and the sampling container was changed after either (a) it contained at least 5 mm of precipitation or (b) it contained at least 2 mm of precipitation and no precipitation was observed for 3 hours. In general, stream and rain water samples were brought to the laboratory and filtered within one to four weeks after sampling. However, due to travel limitations during the COVID-19 sanitary crisis, some samples stayed in the sampler for two months. We decided not to exclude these rain water samples from the model as this

would have meant a large lack in the model input and interpolating over such a long period would be even less realistic. As a consequence, particular care needs to be taken when interpreting the modeled and observed data from march 2020.

Stream water samples have been taken at the outlet of the Claduègne catchment at variable frequency. Stream water sampling was conducted from June 2019 to summer 2021, but only samples until December 2020 will be shown and discussed, as thereafter discharge data has not yet been quality controlled. During sporadic field trips, stream water samples have been taken manually and an *ISCO 1680* water sampler has been programmed to take a sample every 12 h over the course of two weeks following each field trip. In addition, during flood events (exceedance of a seasonally adapted threshold in water level and turbidity), samples were taken at a higher frequency (every 30 min) by a *Teledyne ISCO 3700* automated sampler. A very similar sampling strategy was conducted at the Gazel outlet, with a sample every 20 min during flood events and repeated sampling during low flow periods.

We also conducted several spatial sampling campaigns. Figure 5.1 and Table 5.1 resume the sampling sites. There are several points in the stream and its tributaries on both geologies that had been sampled manually repeatedly. In addition, we sampled different sources throughout the catchment during the driest part of the year in order to have an overview of the signature of the deep reservoirs.

5.2.1.2 Water analysis

All water samples were filtered at 0.45 μm with *Sartorius Minisart NML* cellulose acetate filters. Stream water and source samples were filtered into 10 mL amber glass bottles for stable isotope analysis, 15 mL metal-free polypropylene tubes for ICP analysis and 15 mL polypropylene tubes for IC analysis. Rain water samples were only filtered into 10 mL amber glass bottles for stable isotope analysis. After filtration, samples were stocked in a dark refrigerator at 4 °C.

The ^{18}O and deuterium (^2H) isotope ratios in the water molecule ($\delta^{18}\text{O}$ and $\delta^2\text{H}$) were analyzed using a *Picarro L2120-i* isotopic water analyzer. Before analysis, samples were transferred from the 10 mL amber glass bottles to 2 mL glass analysis vials with PTFE septum within 72 h before analysis and stocked in a refrigerator at 4 °C until transfer onto the auto-sampler tray. Standards were analyzed in the beginning and end as well as every 19 samples. We used two home-made standards: MQ-01 and EGRIP-01. MQ-01 was obtained from purified Grenoble tap water and EGRIP-01 is melted ice from EGRIP borehole on the Greenland ice sheet. The standards were stocked in a 10 L HDPE container and analyzed at the Laboratoire des Sciences du Climat et de l'Environnement (LSCE) at Paris Saclay University using a Finnigan MAT252 mass spectrometer. We used six injections per sample in high precision mode (9.5 min per injection, of which 4 min were retained as measurement). In order to compensate for the memory effect, a $v_{raw} = a/n_{inj} + b$ relation was fitted between the raw measured values v_{raw} and the injection number n_{inj} . Then the functions asymptote b was kept as memory-corrected measured isotope ratio (before calibration). This method was developed as a simple compensation of the instrument's memory effect, which was observed to persist during more than ten sample injections during some tests. An article describing this method and including a validation was submitted to *MethodsX* and is currently under review. It is included in Appendix E. For

calibration, a linear relation was fitted to known vs. measured isotope ratio of the two standards at each measure of the standards. Then, in order to compensate for instrument drift, the two parameters of this linear calibration relation (slope and intercept) were interpolated between each set of standards. Real sample isotope values were predicted by applying the corresponding calibration to each sample's measured value.

In addition, stream water samples were analyzed for the concentration of 14 major and trace elements (Al, Ba, Ca, Cu, Fe, K, Mg, Mn, Mo, Na, P, S, Si, Sr) using a Varian 720ES ICP-OES (Inductively Coupled Plasma - Optical Emission Spectrometer) at ISTerre laboratory, Grenoble. Briefly, the samples are ionized using a plasma of Argon gas. When the elements recombine with electrons they lost during the process, they emit light of a specific wavelength. The intensity of the emitted light is measured at each specific wavelength and can be related to the amount of that element in the sample using known standards. The elements can have multiple characteristic wavelengths. A wavelength that has high sensitivity and little interference with other elements is chosen. The wavelengths that were used are summarized in Table 5.2. We used squared and linear calibration functions according to the observed relation between measured intensity and real concentrations of the standard as summarized in Table 5.2.

TABLE 5.2: Wavelength used for each element in ICP analysis and calibration function applied.

Element	Wavelength [nm]	calibration
Al	396.152	squared
Ba	455.403	linear
Ca	315.887	squared
Cu	327.395	squared
Fe	238.204	squared
K	769.897	linear
Mg	285.213	squared
Mn	259.372	squared
Mo	202.032	linear
Na	589.592	squared
P	213.618	linear
S	181.972	linear
Si	251.611	squared
Sr	216.596	squared

The samples were also analyzed for major anion concentrations using an ion chromatograph (IC, *Metrohm modular systems 732-733*). Briefly, the sample is pumped through a positively charged anion exchanger column and anions are exchanged between the liquid and adsorbed phase. This slows down their transfer through the column by different factors depending on their charge and size and thereby separates the different anions. The electric conductivity of the solution leaving the anion exchanger column is continuously measured and increases with the anion concentration, leading to one peak per anion. The integrated surface of each peak is converted to the actual concentration by analyzing a known standard (*Roth Rotistar multi-element IC-Standard-Solution*, pure as well as

diluted by factors 10 and 100) and calibrating the relation between measured surface and known concentration through sequential linear relations between the different standard concentrations.

5.2.1.3 Synthesis of results / data

In this subsection, the results of major anions, major and trace elements and water stable isotope analyses are presented and discussed and some assumptions on the catchment functioning are formulated. In addition to the stream water samples, a few precipitation samples were analyzed for ions and elements. No detectable concentration was found. The presented ions and elements are therefore considered not to be present in precipitation.

Major and trace elements and anions Different discharge-concentration relationships can be identified for the different elements and ions at the Claduègne outlet. Figure 5.2 shows a selection of them. All analyzed elements and ions are displayed in Fig. D.1. Most elements and ions show a dilution tendency for the highest discharge values (decrease in concentration with increase in discharge). This can be explained by a dilution of enriched ground water with less concentrated event water during rainfall events. Sometimes this tendency concerns the highest discharge values only, as is the case for calcium. Given the fast dissolution kinetic of calcium carbonate (Morse, 1983) rapidly reaching equilibrium, this may indicate that only during flood events, when very young event water reaches the streams the concentration decreases and in other cases, Ca quickly reaches equilibrium concentration again in recent water before it reaches the stream. For other elements, e.g. silicon and chloride, this tendency covers most of the range of discharge values, indicating a slower dissolution (Si) or a limited reservoir or input (Cl). Some elements' concentrations rather tend to increase with higher discharge, as is the case for iron and aluminum. These metallic cations are known to form complexes with organic matter (OM), which play the role of a transport vector (Jansen et al., 2004; Reuter and Perdue, 1977). Their concentration increase during flood events can thus be explained by increased mobilization of OM during these periods. In addition, some nutrients show a similar dynamic of increase during flood events (potassium, phosphorus, nitrogen, sulfur), but only during some of the flood events (Fig. 5.3 for the example of potassium). This can be explained by the activation of flow paths during flood events (e.g. overland flow and other preferential flow), are not contributing to stream flow during low-flow periods and that wash out nutrients from the fields after artificial application. Figure 5.3 shows the temporal evolution of a selection of anion and element concentrations at the Claduègne outlet over the observation period and one selected event, together with precipitation and discharge at the Claduègne outlet. The remaining solutes are shown in Figs. D.2 to D.5. Most concentrations are lower during the wet period in winter 2019-2020 and rise over the summer months of 2020 until autumn (e.g. Si and K in Fig. 5.3 a)). However, some elements behave differently: Calcium only presents lower concentrations during flood events and reaches its initial concentration rapidly after each flood event. This can be seen by looking at the 'baseline' of Ca concentrations in Fig. 5.3 a), which does not show significant seasonal variations like Si does. This can be explained by the rapid dissolution kinetics of calcium carbonate which make it reach saturation / equilibrium rapidly as discussed above. Some metallic cations and nutrients (Al, Fe, K, P) peak during flood events, however over the year they follow the same tendency as most other elements with lower concentrations in autumn / winter and higher concentrations in summer (see K

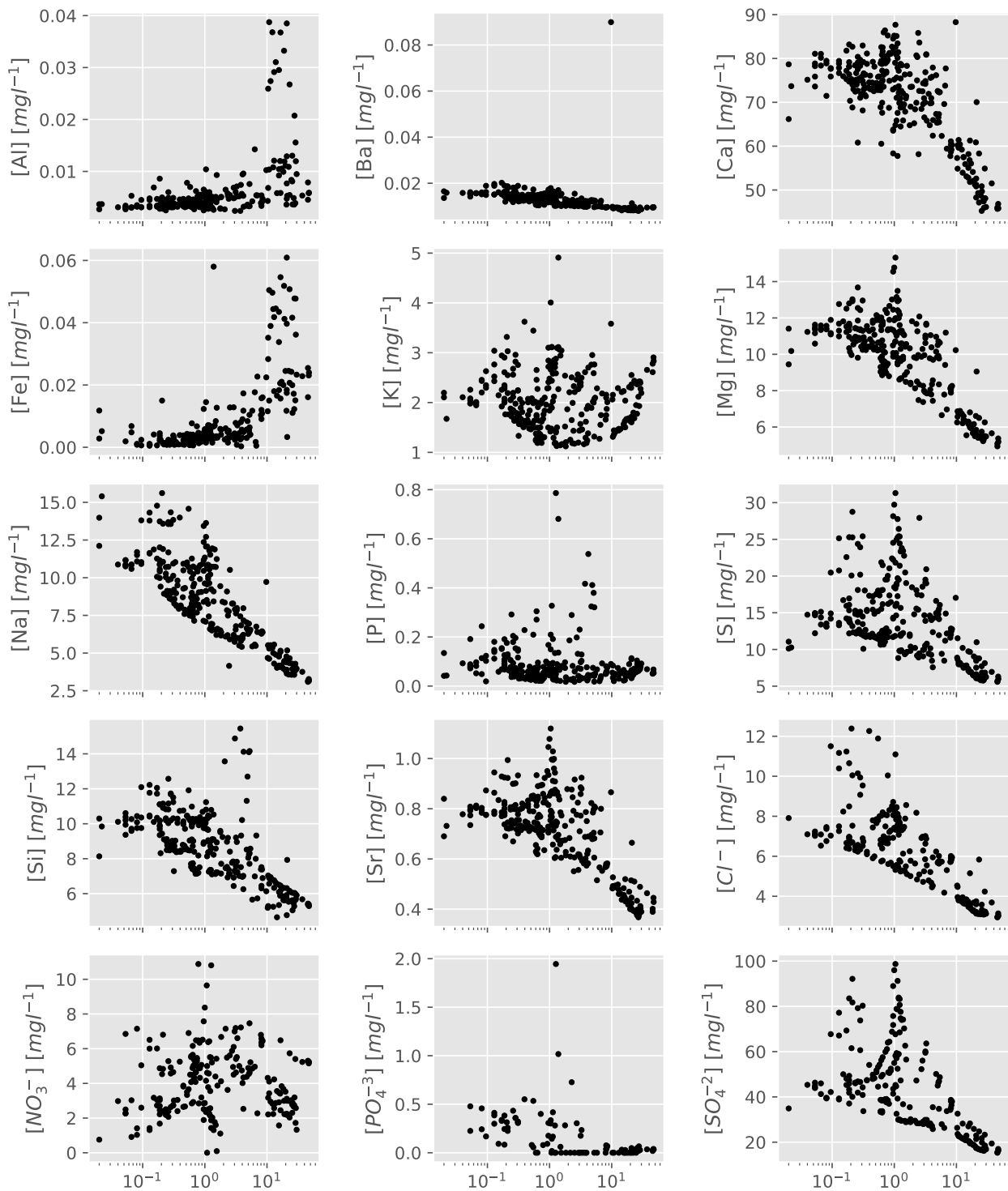


FIGURE 5.2: Concentration - discharge relationship of a selection of elements and ions from water samples from the Claduègne outlet. Note the logarithmic scale on the x-axis.

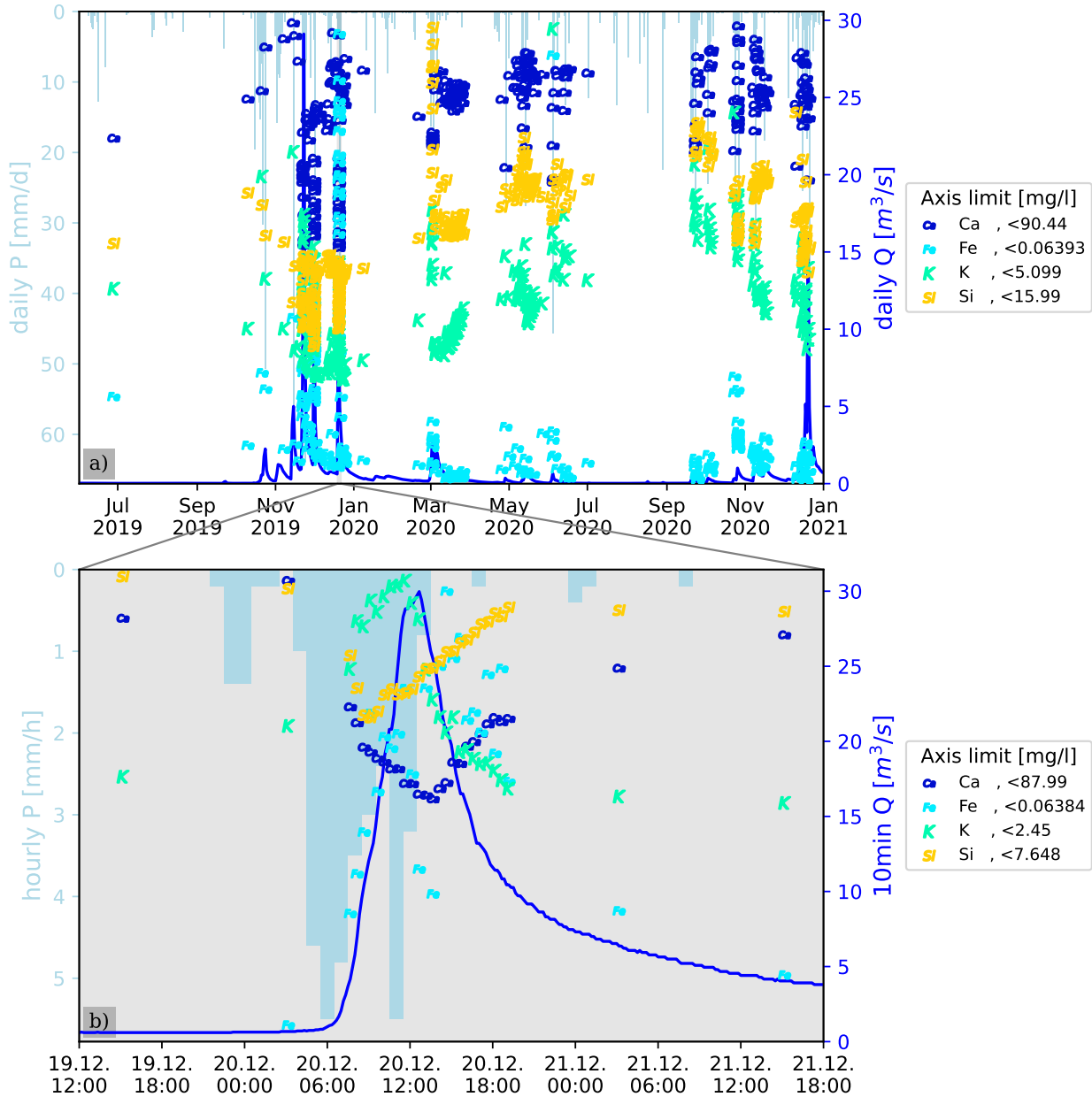


FIGURE 5.3: Precipitation, discharge and concentration time-series of a selection of elements and ions from water samples from the Claduegne outlet for the whole observation period (a) and one selected event (b). For each element and ion the y-axis is scaled from zero to just above the maximum concentration. The upper axis limit for each element is shown in the legend.

in Fig. 5.3 b) and a) respectively for flood and seasonal evolution). Silica is discussed in detail in the next section.

Silica Figure 5.4 a) resumes the silicaⁱⁱ concentrations at the different sampling sites, grouped by geology and source type. The large majority of samples belong to the group of streams with

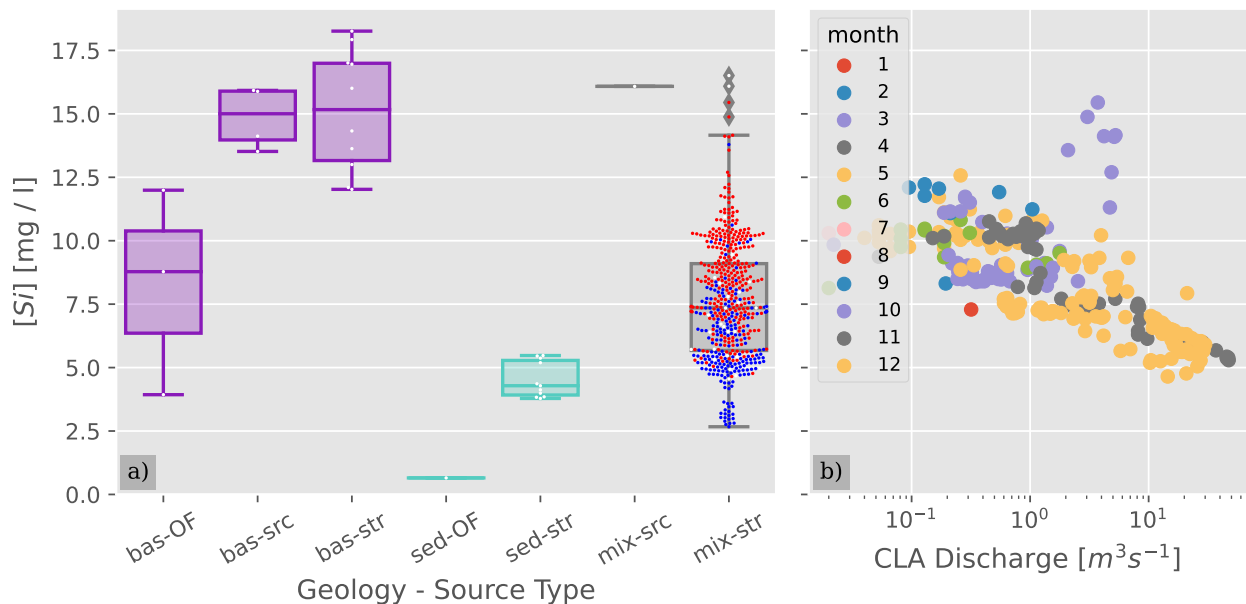


FIGURE 5.4: Synthesis of silica concentrations. a) Boxplot of all observed silica concentrations, grouped by geology and source type. The colors indicate the geology: purple for basalt (bas), turquoise for sedimentary (sed) and gray for mixed geological origin (mix). The source types are as follows: OF = overland flow, src = groundwater source, str = stream. Each sample is additionally represented by a white dot. The two outlets of Gazel and Claduègne are included in the streams of mixed origin and represented by blue and red dots respectively. b) Silica concentrations as a function of discharge at the Claduègne outlet, colored by the month. Note the logarithmic x-axis.

mixed geological origin, however even with few samples in the other groups, some clear contrasts can be seen. The dissolved silica concentration is generally higher in water from basaltic than from sedimentary geology. This is consistent, despite the higher concentration of SiO_2 in the sedimentary soils (Section 2.7). We assume a different mineralogy to be the cause of a more rapid dissolution of silica in the basaltic soils, but further investigations on the reasons are beyond the scope of this work. The sub-groups are small, but values are generally lower in overland flow samples than in stream- and groundwater. All stream water samples except at the two hydrometrical stations had been taken outside of major flood periods, when a majority of stream water comes from ground water. Generally, the streams of mixed geological origin have an intermediate Si signature. The Claduègne outlet (red points) shows slightly higher Si concentrations than the Gazel outlet (blue points) which can be explained by the higher basaltic proportion of the catchment (47 % vs. 23 %). The two highest outliers of mixed streams correspond to the points "SJ1" and "CLA-Arches" for both of which the large majority

ⁱⁱ We analyze the total concentration of silicon (Si) and assume it to be present in a dissolved form of silica (e.g. orthosilicic acid, $Si(OH)_4$). Concentrations are given as mgSi/L

of the drained surface is on basaltic geology. The only ground water source on mixed geology (mixed in Fig. 5.4 a)) has a high dissolved silica concentration like the basaltic ground water sources. It is situated just downhill of the basaltic part and therefore most likely drains basaltic groundwater. The two outlets (Claduègne and Gazel) have been sampled in varied conditions. They span a wide range of values from the order of basaltic base flow to below sedimentary base flow. This indicates the dependence of dissolved silica concentrations on flow conditions, which is summarized in Fig. 5.4 b). As a general tendency, dissolved silica concentrations decrease with higher discharge. This trend persists over the whole range of discharge values. It can be interpreted as an effect of the increase in dissolved silica concentration with transit time. New water from recent precipitation that did not have sufficient time to dissolve large quantities of silica would lead to a decrease of $[Si]$ in the discharge. The negative correlation would then indicate shorter transit times in periods with higher discharge. This figure also shows, that discharge alone does not explain all of the variation in dissolved silica concentration ($[Si]$ is not precisely predicted by discharge alone). We will try and obtain more insight into the transit times from the modeling. The solubility of amorphous silica in water in environmental pH ranges where orthosilicic acid is the dominant species is 40 mgSi/L and 60 mgSi/L at 10 °C and 30 °C respectively (calculated from the relation given by Gunnarsson and Arnórsson (2000)). All observed stream concentrations are well below this solubility, indicating that Si dissolution with time is not limited by solubility, which would limit the use of dissolved silica as transit time tracer.

Figure 5.5 shows the temporal evolution of dissolved silica concentration at the outlet of the Claduègne catchment together with discharge and precipitation. Figure 5.5 a) shows the whole observation period from June 2019 to December 2020 and Fig. 5.5 b) shows a zoom on one flood event in December 2019. On Fig. 5.5 a) we can observe an overall trend of lower dissolved silica concentrations and higher discharge during winter season and higher Si concentrations and lower discharge during summer season, which corresponds to the trend visible in Fig. 5.4. This observation is coherent with the assumption that $[Si]$ is not solubility-limited but controlled by dissolution kinetics. In Fig. 5.5 b) we can observe a pattern that occurs during several flood events: There are two main precipitation events (on the 13th and 20th of December) that both cause a decline in dissolved silica concentration of low amplitude over a period of about seven days. The second event additionally causes a second superposed decline in concentration of much higher amplitude but lasting only a few hours. This abrupt decline is finished before the slower one even reached its minimum. These two declines can be conceptualized as two independent mechanisms. One slower mechanism of dilution of a reservoir and one faster mechanism that may represent a direct contribution of event water, low in dissolved silica, to discharge. Looking at the seasonal scale (Fig. 5.5) we can distinguish a third, much slower reservoir that changes its signature on this seasonal scale with lower concentrations in the wettest season (November to December) and higher concentrations at the end of the dry period in September. These distinct mechanisms inspire the basic structure of the model with one slow and one fast reservoir that will be presented below. Briefly, the slow reservoir can be interpreted as ground water and serves to reproduce the seasonality. The faster reservoir represents the unsaturated zone and serves to reproduce the rapid reaction on the event-scale. Ideally, the slower response on the event-scale would also be reproduced through the ground water reservoir.

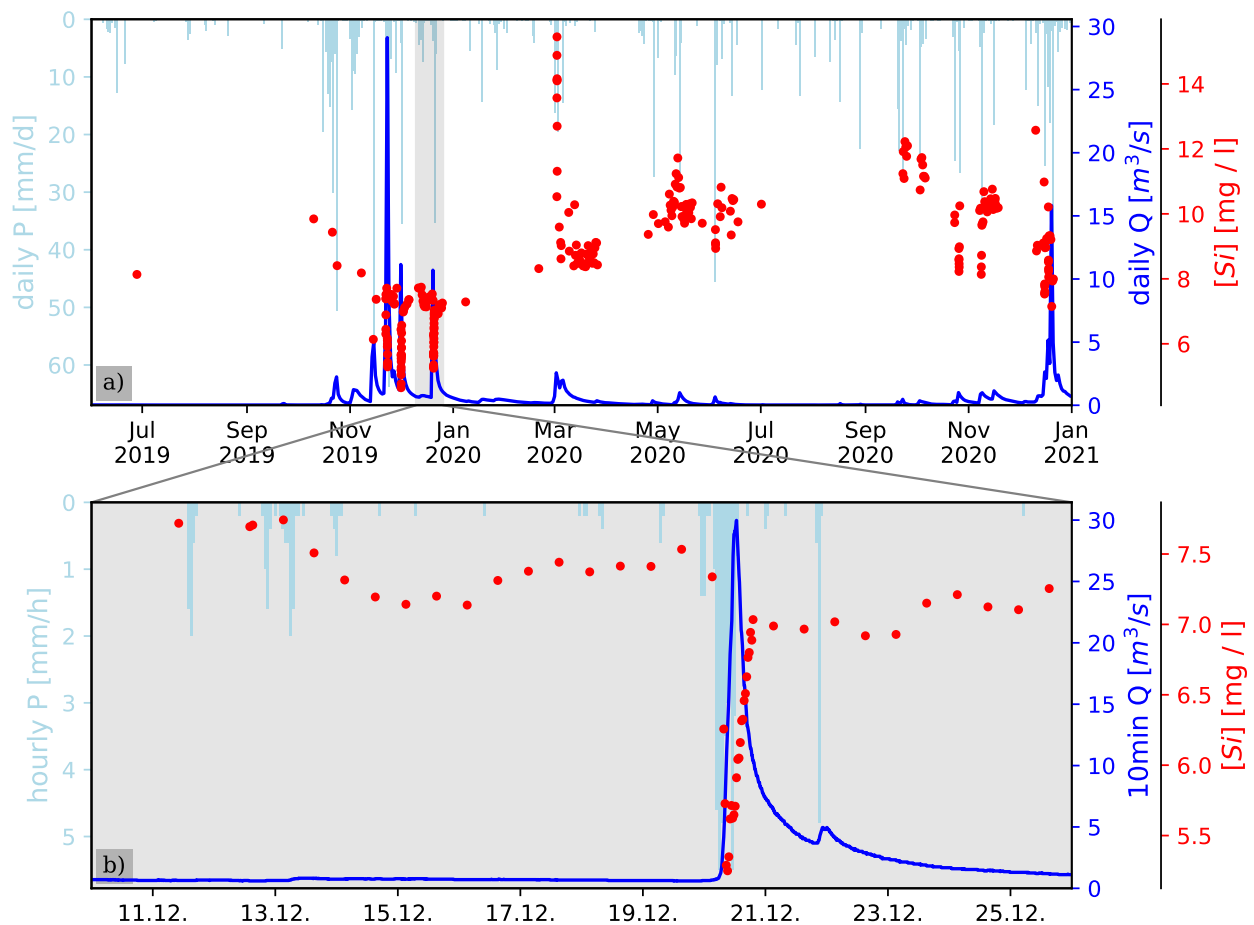


FIGURE 5.5: Time series of dissolved silica concentration and discharge at the Cladugne outlet as well as precipitation. a) covers the whole sampling period while b) zooms into one flood event, highlighted in golden in a).

Another mechanism can be observed in some of the spring and summer events, particularly the event in March 2020 (Fig. 5.5 a): Here the concentration increases strongly together with the peak of the flood event. We interpret this as the activation of a reservoir that has increased its dissolved silica concentration over a period of little rainfall due to dissolution of silica and concentration through evaporation of water leaving silica behind. This reservoir would be the non-saturated zone, which, below a threshold of soil water content would stop contributing to stream flow but continue to dissolve silica and contribute to evapotranspiration and thus further concentrate silica. In the end of summer this effect is less pronounced, which may be due to a very low amount of water remaining in the unsaturated zone leading to supersaturation and precipitation of silica. Therefore, in the end of summer, the amount of dissolved silica that could be mobilized by activation of the reservoir is too small to lead to a strong increase of stream $[Si]$. This mechanism also inspired the structure of the model. Another important information that we obtained from this data is the rapidity of the catchment's reactions, that makes it necessary to consider at least an hourly model time step in order to be able to represent some essential mechanisms. This corresponds to previous studies in the catchment.

Hachgenei (2018) estimated a time of concentration of 4.5 h for the Cladugne and 2.5 h for the Gazel.

Water stable isotope ratios Isotopes of an element have the same number of protons but a different number of neutrons and therefore a different elementary mass. A stable isotope does not spontaneously undergo radioactive decay. Both elements of the water molecule, hydrogen and oxygen have a largely dominant isotope (^1H and ^{16}O respectively). Hydrogen has one heavier stable isotope (^2H , deuterium) and oxygen has two heavier stable isotopes (^{17}O and ^{18}O). In hydrology, ^2H and ^{18}O are the most widely studied isotopes and often referred to as water stable isotopes (or stable water isotopes). In the following, we focus on these two isotopes. The abundance of stable isotopes can be expressed as the ratio of the rare isotope to the abundant isotope, e.g. $R_{2\text{H}} = \frac{^2\text{H}}{^1\text{H}}$ and $R_{18\text{O}} = \frac{^{18}\text{O}}{^{16}\text{O}}$. The international norm is to report those ratios as a normalized difference to an international standard, the Vienna Standard Mean Ocean Water (VSMOW), which is a mixture of ocean water sample from different locations on the planet. The samples normalized difference to VSMOW is expressed as $\delta^2\text{H}$ and $\delta^{18}\text{O}$ respectively in ‰, where $\delta^2\text{H} = \frac{R_{2\text{H SAMP}} - R_{2\text{H STD}}}{R_{2\text{H STD}}}$ (Craig, 1961b), with $R_{2\text{H SAMP}}$ and $R_{2\text{H STD}}$ being the sample's and standard's (VSMOW) isotopic ratio. For simplicity, in the following, the term isotope ratio is used for these isotope ratio normalized differences as compared to VSMOW.

During phase changes such as evaporation and condensation, isotopes become enriched in one phase and depleted in the other. This process is called isotopic fractionation. The isotopic fractionation of water is governed by two factors: (i) heavier isotopes prefer phases with stronger bonds (solid>liquid>gaseous) and (ii) the diffusion of heavier isotopes is slower Sodemann (2006). Therefore, atmospheric water vapor that evaporated from the ocean is usually depleted in heavy isotopes as compared to ocean water. Precipitation that condensed from this atmospheric water is enriched as compared to the atmospheric water. If the contact between the phases is sufficiently long and there is no immediate export of one of the phases, an equilibrium is reached between the phases' isotope ratios. This equilibrium is described by the fractionation factor α . For the liquid (subscript l) to vapor (subscript v) fractionation of $R_{2\text{H}}$, $\alpha_{v/l}^{2\text{H}}$ is defined as (Sodemann, 2006)

$$\alpha_{v/l}^{2\text{H}} = \frac{R_{2\text{H } v}}{R_{2\text{H } l}} \quad (5.2)$$

Generally, $\alpha_{v/l}$ is very close to 1 and its distance to 1 indicates the strength of fractionation. An important factor influencing $\alpha_{v/l}$ is air temperature. At higher temperature, $\alpha_{v/l}$ is higher (closer to 1), meaning less fractionation. Due to its smaller size and lower binding energy, the fractionation of ^2H is generally about eight times stronger than that of ^{18}O , meaning that $1 - \alpha_{v/l}$ is eight-fold. This governs the $\delta^2\text{H} = f(\delta^{18}\text{O})$ relationship in precipitation, which is generally aligned along a straight line with a slope of 8. As an example, at 20 °C, $\alpha_{v/l}^{2\text{H}} = 0.922$ and $\alpha_{v/l}^{18\text{O}} = 0.990$ (Majoube, 1971). In nature, fractionation cannot always reach equilibrium. This is the case if one of the phases is exported rapidly. In a non-equilibrium fractionation process the isotopic ratios can deviate from the 1 : 8 ratio, as the slower diffusing H_2^{18}O molecules will be further from equilibrium than the H^2HO molecules. This deviation from equilibrium is quantified as deuterium excess $d = \delta^2\text{H} - 8 \cdot \delta^{18}\text{O}$ in ‰ (Dansgaard, 1964). It is often interpreted in terms of conditions during evaporation, such as

the gradient in relative humidity above the water surface or air and water temperature (Merlivat and Jouzel, 1979; Cappa, 2003), but can as well be influenced by other atmospheric processes such as phase changes in clouds (Ciais and Jouzel, 1994).

For the use of stable water isotopes in hydrology, it is not necessary to get into more detail of the physical processes of isotopic fractionation in the atmosphere. In general, we use the isotopic signature of precipitation as it reaches the soil surface as input information. This signal is then transferred through a hydrological model as conservative tracer and model output can be compared to observations in stream water samples in order to validate the transfer of water through the model. The essential prerequisite for this approach to work is a strong signal in precipitation meaning a large range of isotope ratios. The higher the amplitude of variations of the isotopic signal in precipitation, the higher the chance to observe a clear signal in the stream response even after some mixing.

As the isotope ratio in precipitation is determined by multiple phase changes under different conditions, it can be very variable with location and time. Generally, the isotope-ratio (heavy vs. dominant isotope) in atmospheric water and therefore in precipitation is higher (closer to ocean water) in summer than in winter and higher at low elevation than at high elevation due to weaker isotopic fractionation at higher temperature. It can also vary on shorter time scales even within one single rainfall event, due to variable conditions during formation of rainfall. While δ^2H and $\delta^{18}O$ can be very variable, the relation $\delta^2H = f(\delta^{18}O)$ tends to be linear for most precipitation waters with a slope close to eight as explained above and an intercept above zero representing the deuterium excess from non-equilibrium. This relation is called meteoric water line and is relatively consistent over the planet. This global meteoric water line GMWL was initially defined by Craig (1961a). The GMWL was later refined by Rozanski et al. (1993), based on a large global dataset. Local deviations from the GMWL exist due to different climatic conditions and local phenomena. This is why local meteoric water lines (LMWL) have been defined for different regions of the world (e.g. Rozanski et al. (1993); Ladouche et al. (2009); Gat and Carmi (1970)).

In addition to the atmospheric processes mentioned above, isotopic fractionation may also occur within the critical zone during evaporation. The evaporation fractionation depends on antecedent precipitation volumes and, to a lesser degree on temperature and evaporation rates (Sprenger et al., 2018).

In the following, the results from this study are presented. The stable isotope ratios range from -18.8‰ to 1.2‰ for $\delta^{18}O$ and from -137‰ to 10‰ for δ^2H in precipitation. In stream water they range from -10.1‰ to -4.8‰ for $\delta^{18}O$ and from -67‰ to -31‰ for δ^2H . These ranges are similar to values observed by Gallart et al. (2020) for precipitation in a small (0.56 km^2) Mediterranean catchment in the Pyrenees, while they observed a larger range of values in stream flow. Figure 5.6 shows all rain and stream water samples and compares their $\delta^{18}O - \delta^2H$ relation to the global meteoric water line GMWL (Rozanski et al., 1993) and different local meteoric water lines from literature for the French Gard and Hérault department (Ladouche et al., 2009; Payne, 1992) as well the East Mediterranean (Gat and Carmi, 1970). The precipitation and stream water samples from the Claduègne catchment align with the Gard meteoric water line (Ladouche et al., 2009; Payne, 1992). This is also the data from the closest site to the Claduègne that could be identified in literature. A linear

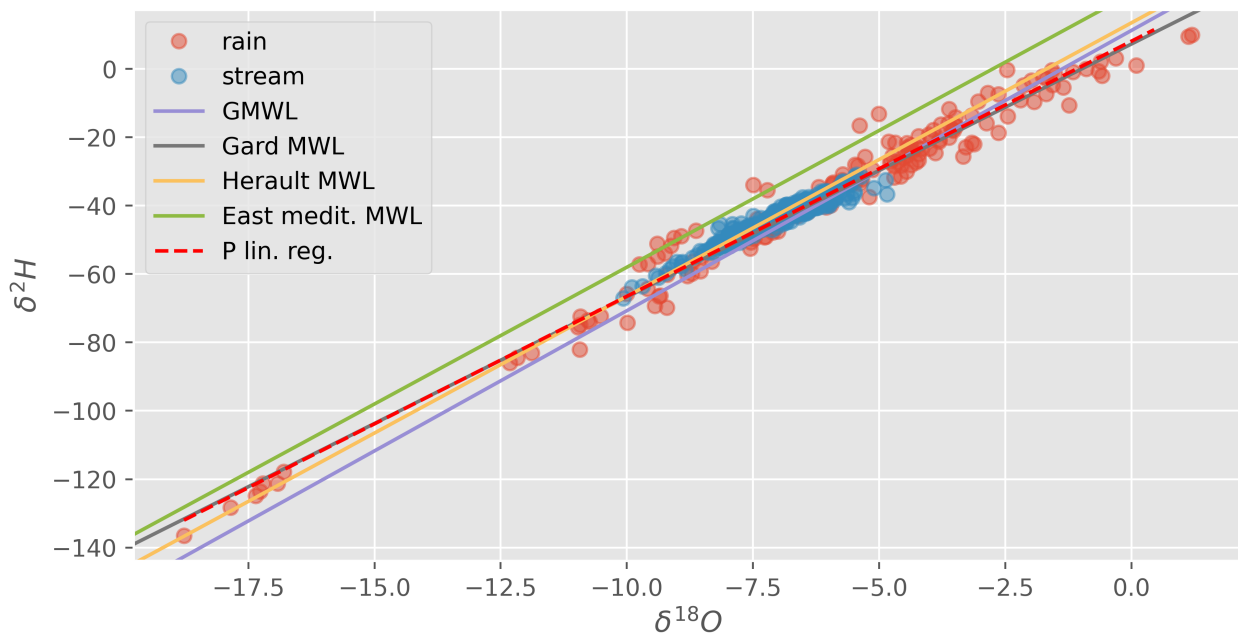


FIGURE 5.6: Water stable isotope ratios of all rain and stream water samples from the Claduègne catchment, δ^2H vs. $\delta^{18}O$, compared to the global and different local meteoric water lines. The red dashed line is a linear regression performed on the precipitation samples.

regression of the Claduègne precipitation samples gave the relation $\delta^2H = 7.46 \cdot \delta^{18}O + 8.13\text{‰}$ which is close to the Gard MWL $\delta^2H = 7.4 \cdot \delta^{18}O + 7.3\text{‰}$.

Figure 5.7 shows the temporal evolution of stable isotopes in precipitation in the Claduègne catchment over the seasons and at the scale of one precipitation event. The precipitation samples are more depleted in heavy isotopes in autumn and winter and less depleted in summer (Fig. 5.7 a)). There is a high intra-event variability in the isotopic signature, with generally higher values in the beginning of the event and with low precipitation intensities and lower values toward the end of the event and at higher intensities (Fig. 5.7 b)). The same was observed by Bouvier et al. (2018) in a catchment under Mediterranean climate. This corresponds to the "amount effect", first observed by Dansgaard (1964), as a negative correlation between mean isotope ratio and total amount of precipitation on a monthly time scale.

5.2.2 The model

We developed and use a semi-distributed hydrological model that tracks water throughout the catchment, from the moment it enters the system as rainfall until it leaves the catchment through the outlet. The unique identification of each volume of water is its age, i.e. the time passed since the moment it entered the catchment in form of effective precipitation onto the soil surface. The model is semi-distributed as it integrates hydrological processes over each of the two geological entities of the Claduègne catchment: The Coiron plateau on basaltic geology (upstream) and the lower parts on sedimentary geology (marl and limestone). Within each geological entity, there are two non-linear

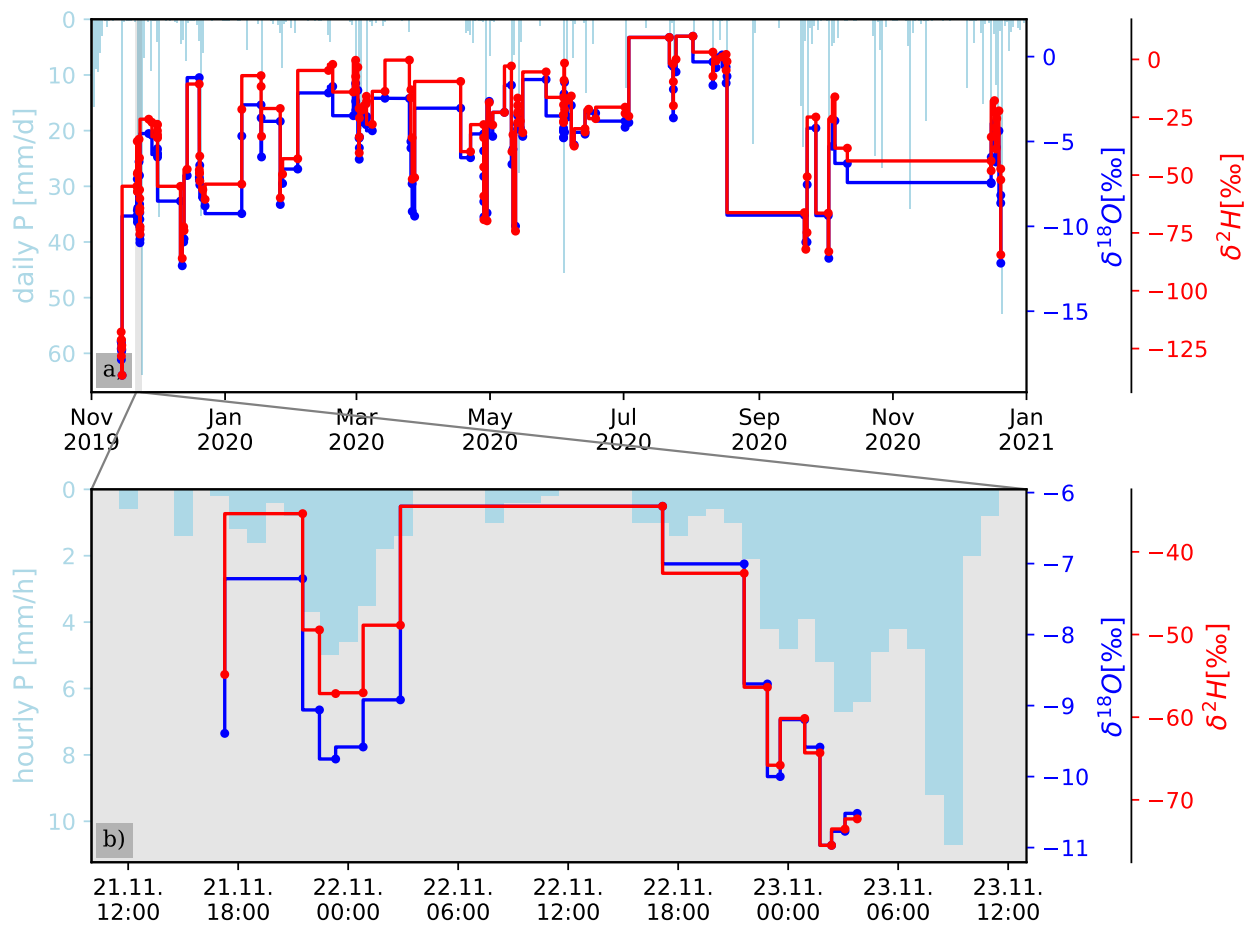


FIGURE 5.7: Evolution of water stable isotope ratios in precipitation with time over the observation period (a) and throughout one storm event (b) that corresponds to the period highlighted in golden in a).

reservoirs and a small interception reservoir. Water fluxes in between and out of the reservoirs are calculated as a function of the amount of water in the reservoir. The reservoirs conceptually correspond to vertical parts of the critical zone (from the canopy to groundwater). They should be seen as functional rather than positional units. Each reservoir has at least one flux entering it and one flux leaving it. In both, the reservoirs and the fluxes, the age of each volume of water is tracked and each flux can have a preference for younger or older water, implemented via SAS-functions. The model is run with a set of parameters and the forcing data which consists of a time-series of precipitation and potential evapotranspiration (E_p) for each of the geological entities as well as precipitation δ^2H . Observed discharge Q at the catchment's outlet as well as tracer concentrations (δ^2H and $[Si]$) are used to evaluate the model performance. Once the model performs well, the age distributions of discharge at any time during the modeled period can be obtained. The model time step is one hour.

In the following, we define the data that is used to run and evaluate the model. Then the model's reservoir structure is presented as well as the calculation of water fluxes out of each reservoir. Thereupon, the representation of age within the reservoirs is explained as well as the age selectivity of the different fluxes, followed by the use of tracers inside the model. In the end, the algorithm that is used

to calibrate the model is presented. The model is written in Python 3 (Van Rossum and Drake, 2009). Calculations are performed using NumPy (Harris et al., 2020) and Pandas (McKinney, 2010) is used for the treatment of time series data.

5.2.2.1 Forcing and calibration data

The model input data consists of a continuous hourly timeseries from 2017 to 2020 of the following variables: (i) P_{BER} and P_{MIR} are observed hourly precipitation obtained from the Berzème-RAD and Mirabel-SA rain gauges managed by Météo France. They are used as precipitation input for the Coiron plateau and the sedimentary part respectively. (ii) PET_{BER} and PET_{MIR} are E_p for the Coiron plateau and the sedimentary part respectively. (iii) δ^2H_P is the precipitation deuterium isotopic ratio. This is obtained from samples of every 5 mm of precipitation as described above (subsection 5.2.1) for the period from October 2019 to December 2020. The measured δ^2H of a precipitation sample was assigned to the period the sampler was positioned to let precipitation flow into this sample at a 1 min resolution. Then δ^2H_P was averaged to hourly resolution. Missing samples (due to technical failure) were filled with the value of the next valid sample. For the period before October 2019 (used as spin-up), monthly averages of the observation period (Oct 2019 - Dec 2020) are used as we do not possess any samples from this period.

In addition, the dataset contains observations of the following three variables, that are used to evaluate the model performance during the calibration process: (i) Q_{OBS} is the measured discharge at the Claduègne outlet, averaged over 1 h. (ii) δ^2H_S and (iii) Si_S are the observed stream deuterium isotopic ratio [‰] and dissolved silica concentration (expressed in mg Si per L) from samples taken at variable temporal resolution (see above). Hours without a sample are assigned NAN, hours with two samples are assigned the average of the two samples. All hourly data represent the mean (discharge and concentrations) or cumulated value (precipitation and evapotranspiration) of the preceding hour.

5.2.2.2 Model structure

Each of the two geological entities of the catchment contains three reservoirs: an interception, unsaturated and saturated reservoir. The overall structure is shown in Fig. 5.8. All volumes and fluxes are treated internally in mm and mm h^{-1} respectively, where the reference area in the reservoirs is the geological unit and the reference area in the Claduègne is the whole catchmentⁱⁱⁱ. Snow does not play a significant role in the study site and is not considered. The three reservoirs and associated fluxes are as follows:

1. The **interception reservoir** S_i represents surfaces that are wetted by rainfall without transmitting the water into the soil until evaporated. A typical example is the tree canopy. In the model, S_i has a limited capacity I_{max} (in mm) and receives all precipitation until full. All further precipitation (effective precipitation P_e) goes directly to the unsaturated reservoir S_u . For simplicity, P_e

ⁱⁱⁱ The volume of water is expressed as volume per surface area in units of height ($1 \text{ mm} = 1 \text{ L m}^{-2}$). From precipitation into the reservoirs the respective surface does not change. Once water enters stream flow and water from both geological entities is mixed, the reference surface becomes the whole catchment area. Therefore, water volumes need to be multiplied by the proportion of the whole catchment surface that lies on the respective geological entity. An illustrative example with numbers: 100 mm of water from the basaltic part (which makes 46.8% of the catchment area) will only represent 46.8 mm in the Claduègne (corresponding to the same volume of water spread over the whole catchment).

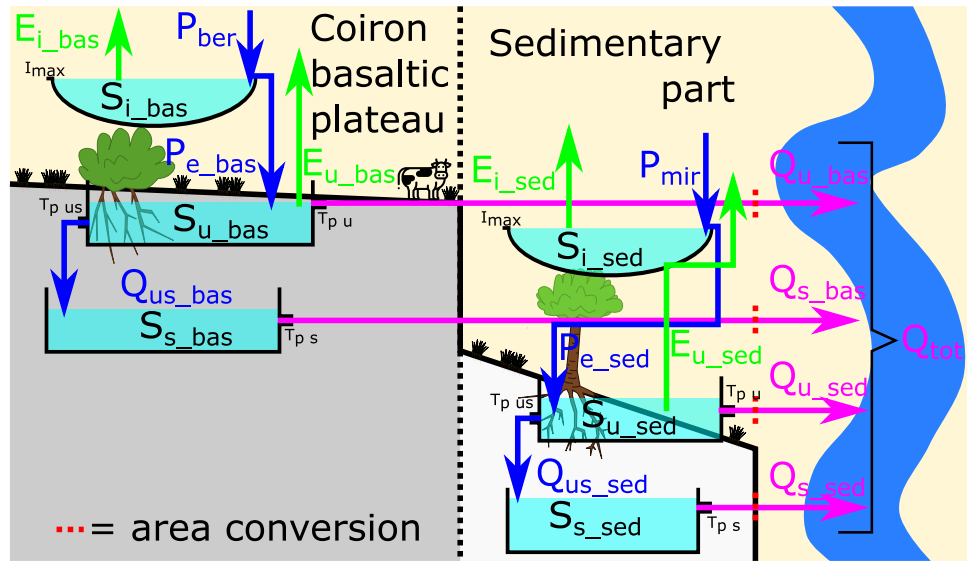


FIGURE 5.8: Reservoirs and fluxes in the conceptual model of the Claduègne catchment.

is not mixed with the water in S_i . Water from S_i never reaches the soil. The only flux leaving S_i is evaporation E_i .

2. The **unsaturated reservoir** S_u represents the unsaturated zone. This includes the soil matrix as well as rapid flow paths such as macropores and overland flow. No differentiation is made between rapid flow at the soil surface and below, as this would add to model complexity without the possibility of verification. S_u receives P_e . There are three fluxes leaving S_u : actual evapotranspiration E_u , preferential stream flow Q_u which contributes to total streamflow Q_{tot} , and groundwater recharge Q_{us} which feeds into the saturated reservoir S_s .
3. The **saturated reservoir** S_s represents the catchments ground water reservoir. It receives Q_{us} and produces groundwater flow Q_s which contributes to total streamflow Q_{tot} .

In order to keep the number of symbols reasonable, the symbol of each reservoir (e.g. S_u) and flux (e.g. Q_u) is used with two meanings according to the context: (i) It can describe the reservoir / flux itself and (ii) it can represent the amount of water in it in mm of water height for reservoirs or mm h^{-1} for the fluxes.

The fluxes in between and out of the reservoirs are calculated as follows: For evapotranspiration we make the simple assumption that as long as there is water in S_i , E_i accounts for 50% of E_p and the remainder can be taken from S_u . This assumption is taken from the "example model". This assumes that the interception reservoir covers approximately half of the surfaces and bare soil evaporation as well as plant transpiration will still continue even if there is water in S_i . This assumption might not be precise, but is fixed in order to limit the number of calibrated parameters because it is not expected to have significant impact on the result. As long as sufficient water is available in S_u , the full remainder will be evaporated from S_u as actual evapotranspiration E_u , which is integrating plant transpiration and bare soil evaporation. If insufficient water is available (less than water stress threshold W_s [mm]), plants are under water stress and E_u is progressively limited by water availability. This is done over

the following relation (modified after the "example model"):

$$E_u = \begin{cases} E_p - E_i & \text{if } S_u \geq W_s \\ (E_p - E_i) \cdot \frac{S_u}{W_s} & \text{otherwise} \end{cases} \quad (5.3)$$

Regarding the other fluxes Q_u , Q_{us} and Q_s (in mm h^{-1}), an empirical formula is used that depends on three parameters which are calibrated. We allow for a passive part in each reservoir, that can be different for each flux leaving it. The formula is taken from the "example model" except that T_p was added, allowing to have a different threshold for different fluxes. Passive storage was treated differently in the "example model". For example, at a certain amount of water remaining in the unsaturated reservoir, there might be no more preferential stream flow, while ground water recharge and evapotranspiration still take place. This is represented by a threshold (or passive volume) T_p in mm. Besides this there are two parameters to describe the relation between volume of water in the reservoir (S in mm) and water flux leaving it (Q in mm h^{-1}): K [mm h^{-1}] is a linear factor: the higher K , the faster the reservoir is emptying. A [-] is a parameter describing the non-linearity of the response. $A = 1$ corresponds to a linear relation between S and Q . $A > 1$ means the more water is in the storage, the more an additional volume of water will increase the discharge. This would be typical in the unsaturated zone, where at low water content water moves slowly through small pores and added water volumes would move much faster through larger pores creating a stronger response in runoff. Each of these parameters exists for each of the three fluxes (Q_u , Q_{us} and Q_s) but is kept identical for the two geological entities to limit the number of calibrated parameters. Q is calculated as follows:

$$Q = \begin{cases} \frac{S - \left((-K \cdot ts + K \cdot ts \cdot A + (S - T_p)^{1-A})^{\frac{-1}{A-1}} + T_p \right)}{ts} & \text{if } S > T_p \\ 0 & \text{otherwise} \end{cases} \quad (5.4)$$

Where ts is the model time step in [h], which is 1 h in our case. This formula only works for $A \neq 1$, but represents a quasi-linear reservoir for values of A close to 1. Therefore, if $A = 1$ it is replaced with 1.0000000001. Inside the model, the water flux is mostly treated in units of water height as $Q \cdot ts$ in [mm] instead of units of a specific discharge [mm h^{-1}], which in our case have the same value due to the model timestep $ts = 1$ h. In the following equations and calculation steps this is indicated by a multiplication of Q with ts .

As the basaltic part of the catchment is at a certain distance from the outlet, an additional parameter was tested, called bas_{delay} . This parameter represents an additional delay between generation of discharge from the basalt and its arrival at the outlet. During calibration the values 0 h and 1 h were tested.

5.2.2.3 Age of water

Water enters the catchment through the unsaturated reservoir via effective precipitation and then ages one hour every time step. Accordingly, the water in each reservoir $S(T, t)$ at any time step t is a mix of water of different age T that entered the system as effective precipitation T time steps before. We assume water of different age to be distributed unevenly throughout the reservoir. Taking

the unsaturated zone as an illustration, we would expect older water to be found lower in the soil column as it had more time to infiltrate and potentially in smaller pores inside the soil matrix as this is where water will be replaced at the slowest pace. Younger water from a recent rain event would be expected closer to the soil surface and along the more rapid flow paths. Figure 5.9 illustrates this storage age distribution on a simplified example of a part of the unsaturated zone with colored patches representing volumes of water of different ages. The spatial representation of water ages in

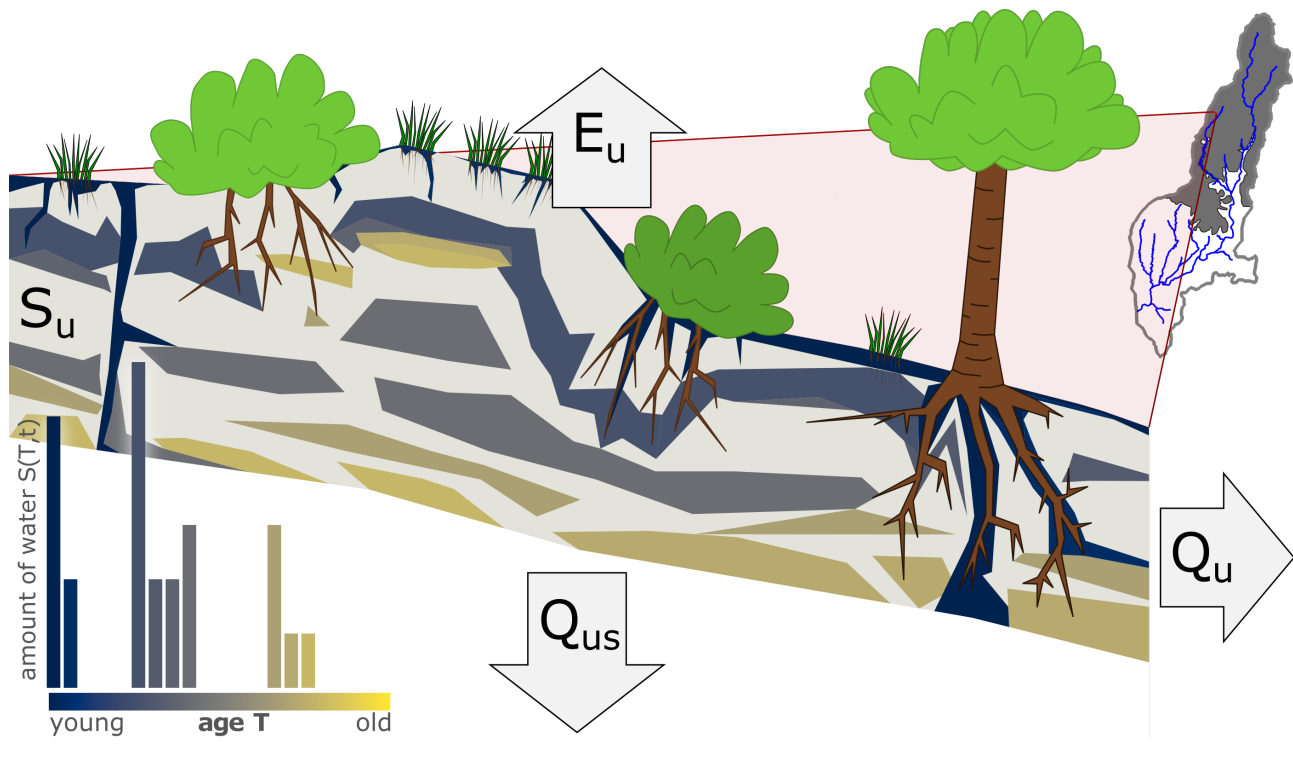


FIGURE 5.9: Schematic illustration of storage age distribution on the example of the unsaturated zone reservoir S_u . The graphic illustrates a transect through the unsaturated zone in a small part of the catchment (e.g. the short red line in the catchment silhouette). Colored patches represent water of different age.

Fig. 5.9 is purely illustrative. Inside the model, no spatial distribution of water ages is simulated. In order to track water ages throughout the model, these ages need to be stored. Practically, at any time t , this is represented by an array $S(T, t)$ with one value for each past model time step containing the amount of water (in mm) of this age T contained in the reservoir. Because only the amount of water of each age is modeled and no spatial representation of these ages, one age does not represent a fixed volume of porespace neither one particular location in the 'real-world' soil column but can very well be distributed throughout the soil column. On each iteration, the water in the reservoirs ages one time step (one hour) by advancing one position in $S(T, t)$, before water is transferred into and out of the reservoir. All volumes of water conserve their age when being transferred via one of the fluxes. The age distribution inside a water flux however, does not need to equal the age distribution of water in the reservoir. This is where StorageAge selection functions are required.

StoreAge Selection functions As the distribution of age is not uniform throughout the reservoir, we assume that the water fluxes leaving a reservoir are not necessarily a representative mixture

of the reservoir's age distribution but may have a higher proportion of younger or older water than the reservoir. Figure 5.9 helps visualizing this age-selectivity: Concerning Q_{us} , a preference for old water would be the case if celerity (pressure wave propagation) was the dominant mechanism, where water entering the reservoir would 'push' older water out of the reservoir. A preference for young water would typically represent a dominance of preferential flow with young water directly contributing to the flux leaving the reservoir via bypassing of older water in the reservoir. Numerically this is represented by StoreAge Selection (SAS) functions associated with each flux, that represent the preference of that flux for older vs. younger water from the storage. In our model, the SAS function is a unitless distribution between 0 and 1 that has an integral of 1. The application of an example SAS function to the fictive unsaturated reservoir from Fig. 5.9 is illustrated in Fig. 5.10. Figure 5.10 a) shows the initial amount of water of each age in the storage (the reservoir's absolute water age distribution $S(T, t)$). Figure 5.10 b) shows three different SAS functions with no age preference (black), young preference (orange) and no preference (green). The SAS function is then used to calculate the age distribution of the flux leaving the reservoir. In simple words, the reservoir's water age distribution $S(T, t)$ (Fig. 5.10 a) is divided by the total amount of water in the reservoir $S(t)$ and multiplied with the SAS function (orange line in Fig. 5.10 b) and the total outflux volume $Q(t) \cdot ts$ to obtain the water age distribution of the outflux $Q(T, t) \cdot ts$ (orange bars in Fig. 5.10 f). The calculated $Q(T, t) \cdot ts$ is subtracted from $S(T, t)$ to obtain the remaining water age distribution $S(T, t+1)$ (blue part of the bars in Fig. 5.10 f)).

We follow a procedure proposed by Van Der Velde et al. (2012) that consists of expressing the SAS function $\omega_Q(T, t)$ as a function of the cumulative water age distribution in the storage instead of the age. This was also used in the "example model". We will call this formulation $\omega_Q^*(P_S(T, t), t)$. Mathematically, this approach corresponds to replacing the age T with the cumulative water age distribution in the storage $P_S(T, t)$ in Eq. (5.1), changing it into

$$\omega_Q^*(P_S(T, t), t) = \frac{p_Q(P_S(T, t), t)}{p_S(P_S(T, t), t)} \quad (5.5)$$

This avoids having to correct for the highly variable amounts of water of each age including 'empty ages' (ie. ages from times without rainfall, meaning there is no water of this age) while using a smooth, mathematically defined function for the SAS-function. Furthermore it can be considered more realistic to have a preference for eg. the youngest x percent of water instead of water being exactly x months old.

In the model, the SAS function is defined as a beta-distribution (adopted from the "example model") with the two shape parameters a and b . b is fixed to one in order to keep the distribution's tail flat and reduce the number of calibration parameters. a is calibrated for each reservoir and each of the geological units and called SAS_α in the following. The beta-distribution was chosen as it is defined for the interval $[0, 1]$ and its integral is 1 which makes it convenient to use. Furthermore, its first shape parameter a allows to have a strong preference or disfavor for young water while the effect on older water is less steep. A beta function representing a young and old water preference ($a=0.6$ & $a=1.5$ respectively) are illustrated in Fig. 5.10 b) (pdf) and c) (cumulative distribution function (cdf)). The beta distributions pdf of a variable x is defined as (Dormann, 2013):

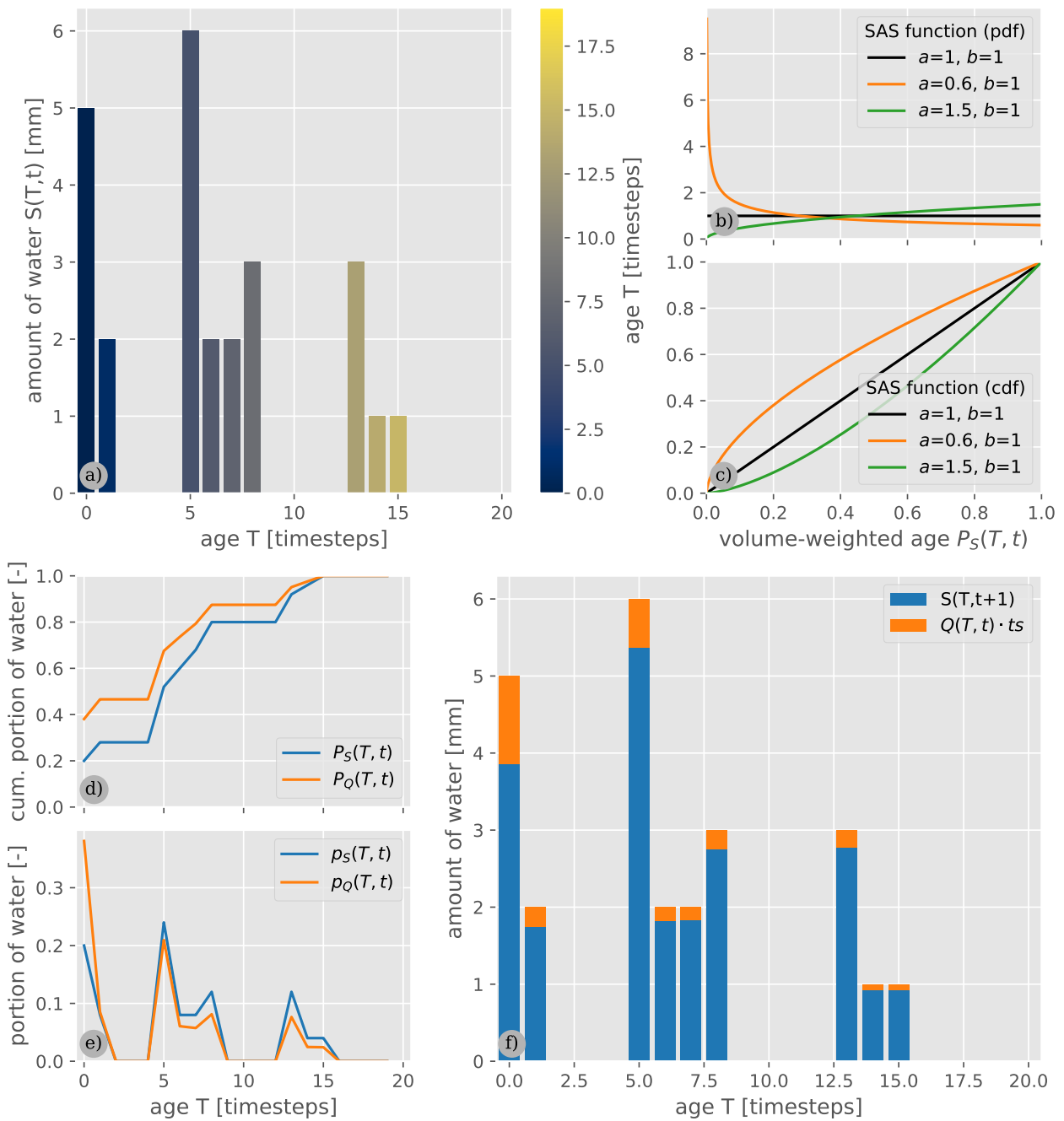


FIGURE 5.10: Schematic illustration of SAS function application to a reservoir and flux with fictive numbers. **a)** shows the reservoirs water age distribution $S(T, t)$ (i.e. the amount of water of each age T in the reservoir at a time t). **b)** shows the probability density functions (pdf) of three different possible SAS functions that can be applied with no age preference (black), young water preference (orange) and old water preference (green). **c)** shows the cumulative distribution function (cdf) of these. **d)** shows the cdf of the water age distribution of the storage (blue) and the outflux (orange), using the SAS function with young water preference. **e)** shows the pdf of those age distributions. **f)** shows the resulting water age distributions of outflux ($Q(T, t) \cdot ts$, orange part of the bars) and the water remaining in the storage ($S(T, t + 1)$, blue part of the bars) after subtraction of $Q(T, t) \cdot ts$.

$$f(x, a, b) = \frac{\Gamma(a + b) \cdot x^{a-1} \cdot (1 - x)^{b-1}}{\Gamma(a) \cdot \Gamma(b)} \quad (5.6)$$

where Γ is the gamma function

$$\Gamma(z) = \int_0^{\infty} y^{z-1} \cdot e^{-y} dy \quad (5.7)$$

Mathematically, SAS sampling is conducted as follows (see Fig. 5.10 for illustration):

1. The pdf of the reservoir's water age distribution $p_S(T, t)$ (blue line in Fig. 5.10 e) is calculated as reservoir water age distribution $S(T, t)$ (Fig. 5.10 a)), divided by the total amount of water in the reservoir S_{tot} . It is then cumulated to obtain its cdf $P_S(T, t)$ (blue line in Fig. 5.10 d)).
2. $P_S(T, t)$ is weighted by the fluxes age preference by obtaining the values of a cumulative beta-distribution with the parameters $a = SAS_{\alpha}$ and $b = 1$ (SAS function cdf; Fig. 5.10 c)) for each value in $P_S(T, t)$. This results in the cdf of the water age distribution in the flux leaving the storage $P_Q(T, t)$ (orange line in Fig. 5.10 d) for beta-distribution with $a=0.6$ & $b=1$).
3. The derivative of $P_Q(T, t)$, $p_Q(T, t)$ (orange line in Fig. 5.10 e)) is the pdf of the outfluxes age distribution.
4. The outfluxes age distribution $Q(T, t) \cdot ts$ containing the amount of water in the flux of each age T is calculated as the product of $p_Q(T, t)$ and the total outflux volume $Q \cdot ts$ (Fig. 5.10 f)).
5. The remaining water in the storage is $S(T, t + 1) = S(T, t) - Q(T, t) \cdot ts$ (Fig. 5.10 f)).

A beta distribution with a small a and $b = 1$ returns very high values for very small x -values (i.e. it has a very high preference for the youngest water volumes). In some cases, with a small amount of water of the youngest age and a high overall Q leaving the reservoir, this can lead to a $Q \cdot ts > S$ for those youngest ages. Due to the short time step of the model, this is more likely to occur in this model than in models on a daily time step like the "example model". In order to avoid extracting more water from one age class than available, a correction is applied. In simple words, all ages where more water than available would be taken, this is limited to available water. The missing water that could not be taken from these ages is then taken from the following ages, until all the difference is balanced. For all older ages, the initially calculated amount is extracted.

In the following, this correction is described in detail. Figure 5.11 illustrates the problem as well as the applied compensation on fictive data. In the following description, the letters a)-h) refer to the sub-figures of Fig. 5.11. If a SAS function with a very strong young water preference (b) is applied to a reservoir with a tiny portion of its water in the youngest age classes (a)), this can lead to the calculated amount of water to extract from this age class (d)) being higher than the available amount (a)) and therefore leaving a negative amount of water to remain in the reservoir at these young age classes (c)). The following steps correct for this, without modifying the total amount of extracted water $Q \cdot ts$. First, the uncorrected cumulative age distribution of water remaining in the storage (e)) is calculated. The corrected remaining water in the reservoir (g)) is set to 0 wherever the uncorrected cumulative age distribution (e)) is below zero. At the first age where the uncorrected cumulative age distribution (e)) is above zero (the age 4 in our example), the corrected remaining water in the reservoir (g)) is set to the value of the uncorrected cumulative age distribution. For all remaining ages, the values of the uncorrected age distribution (c)) are kept. Sub-figure e) compares the corrected and uncorrected

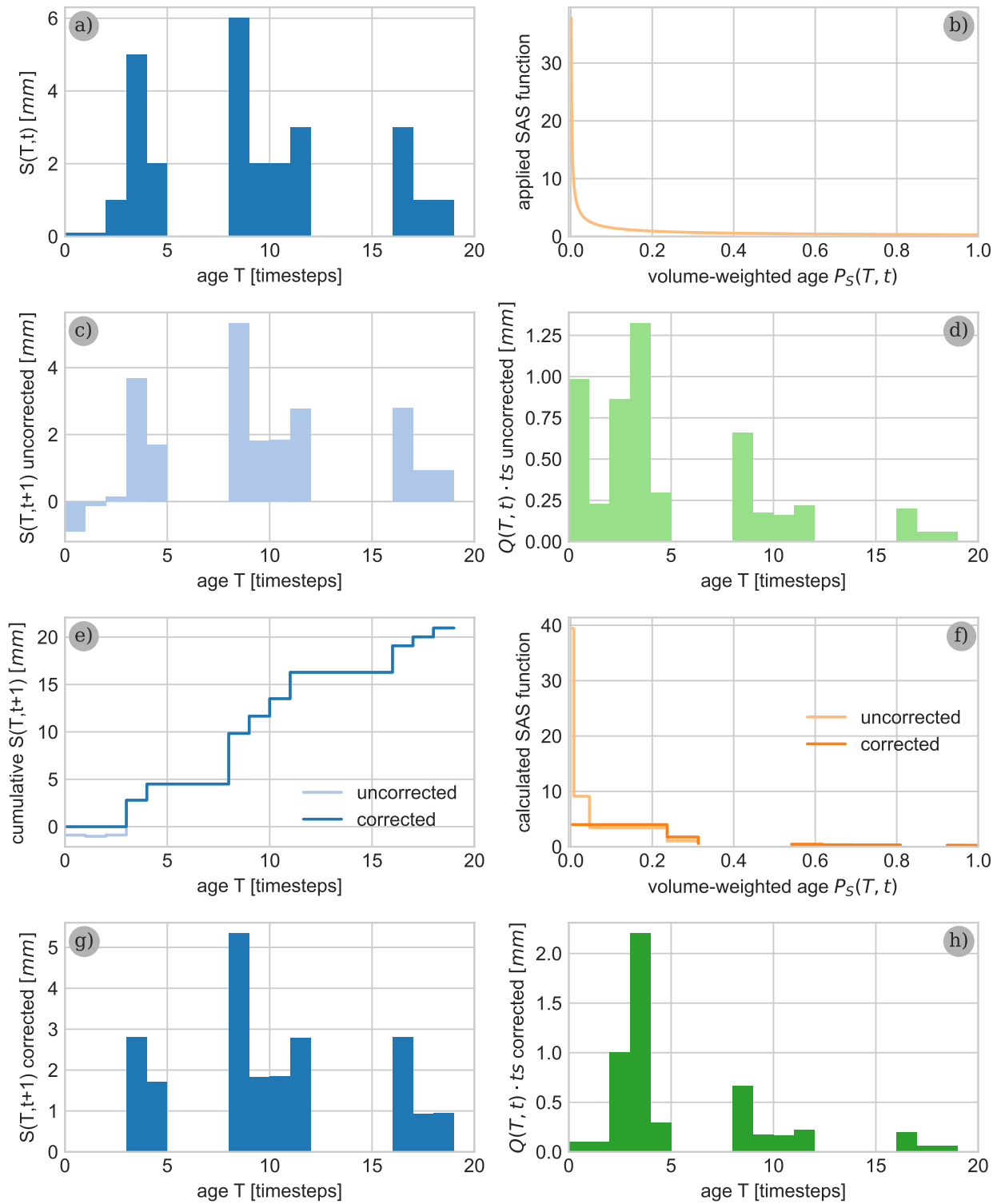


FIGURE 5.11: Schematic illustration of the compensation of a young water preference that extracts more water from an age class than available. This illustration uses fictive data. See the description in the text for details. Note the different y-axis scales. In this example $S(t) = 26.2$ mm and $Q(t) \cdot ts = 5.24$ mm.

cumulative age distribution, showing that the correction only affects the youngest ages. Sub-figure h) shows the corrected age distribution in Q . Sub-figure f) compares the SAS-functions $\omega_Q^*(P_S(T, t), t)$ recalculated from the corrected and uncorrected data (Eq. (5.5)).

For E_u and Q_s , the SAS functions are assumed constant with time and SAS_α is calibrated directly. This corresponds to the application of SAS functions in the "example model", and was done this way because too little is known to formulate advanced hypotheses on time-variant SAS-functions for these fluxes. For Q_u and Q_{us} , time-variant SAS-functions are implemented, as the age-preference of fluxes out of the unsaturated zone is assumed to depend on the amount of water inside the unsaturated zone (Harman, 2015). This dependence is illustrated in Fig. 5.12. For both Q_u and Q_{us} , we assume a

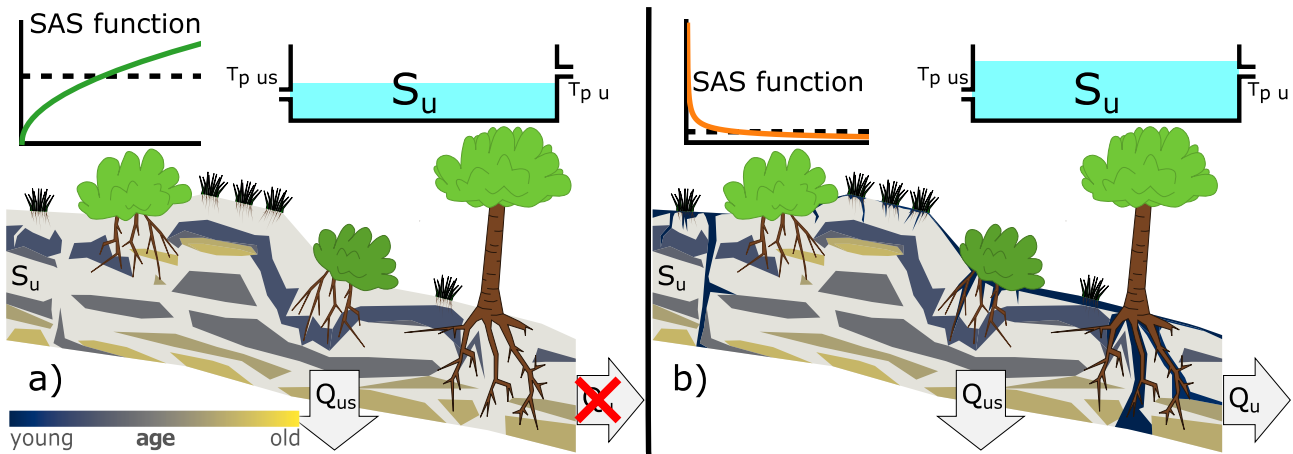


FIGURE 5.12: Schematic illustration of time-variant SAS functions in the unsaturated reservoir. a) shows a drier condition where matrix flow with old water preference is dominant. b) shows a wetter condition with preferential flow and a young water preference.

young water preference as long as there is preferential flow ($S_u > T_{p u}$). This young water preference is assumed to be stronger, the higher the amount of water in S_u . If there is no preferential flow, (i.e. $S_u < T_{p u}$), matrix flow is expected to be the dominant flow mechanism, which can be considered to have an old water preference according to the expected vertical distribution of water ages throughout the unsaturated zone (Fig. 5.9). Therefore, the time-variant SAS_α for Q_u and Q_{us} is calculated at each time-step as follows:

$$SAS_\alpha = \begin{cases} 1 - \frac{S_u - T_{p u}}{SAS_{stretch}} & \text{if } 1 - \frac{S_u - T_{p u}}{SAS_{stretch}} > 0.2 \\ 0.2 & \text{otherwise} \end{cases} \quad (5.8)$$

where $SAS_{stretch}$ is a calibrated factor in mm that defines how strongly SAS_α depends on S_u . SAS_α is limited to a minimum of 0.2 in order to avoid too extreme shapes of the SAS function. $SAS_{stretch}$ is calibrated for the basaltic and sedimentary part separately due to the contrasted nature of their soils, but assumed to be the same for Q_u and Q_{us} in order to limit the number of calibrated parameters. With this, Q_u is guaranteed to have a young water preference whereas Q_{us} has an old water preference when $S_u < T_{p u}$.

Using SAS functions in a semi-distributed conceptual model with serial^{iv} reservoirs comes with a challenge. SAS functions for a flux out of a reservoir define the preference for water as a function of the time passed in the reservoir. In the end however, we are interested in the overall time, the water spent inside the catchment. These two age distributions are not the same as soon as water is passed from one reservoir into another one and therefore need to be treated separately. The catchment age is used in order to estimate the overall TTD while the storage age is used to apply the SAS function. Treating them independently adds a second dimension to the water age distribution for any reservoir receiving water that has a distribution of ages already. In the "example model", this problem is avoided by not applying SAS functions to reservoirs that receive water from another reservoir. In our case this concerns the two saturated reservoirs S_s . The addition of another time dimension strongly increases the consumed computer memory and computation time. This problem was partially solved by the use of two separate models: One for modeling the tracer transfer that is used for calibration and another one for the actual age tracking. The tracer model conserves age throughout each reservoir and resets the age to zero for water and tracers when entering a new reservoir. This corresponds to only modeling the storage age without keeping track of the catchment age. The second model is used to track the overall water age throughout the catchment. In this age tracking model, the age distribution is kept in two dimensions within each of the two saturated reservoirs. The age tracking model is run one time only on the optimized set of parameters, so a longer calculation time is acceptable. Furthermore, the memory consumption of the age tracking model is lower as only water and no tracers are modeled. In this model, the overall age distribution (since catchment entry) is conserved and keeps evolving, while transfer selection is executed along a second dimension tracking the time since storage entry. No preference exists along the overall age dimension, however the two age dimensions are correlated, so the selectivity along the storage age leads to a certain selectivity along the overall age. Fluxes of water leaving the reservoir are summed over the storage age dimension resulting in a 1D age distribution along the catchment age dimension. In order to limit memory and computational demand, age distributions were stored to an age of one year. All water of an age >1 yr is stored as having an age of 1 yr. We would anyways not expect a good precision of the model beyond an age of one year. Over the course of one year a large number of different tracer signals are integrated. We use this argument to justify the use of one integrated signal for all water beyond one year of age. As the SAS functions are applied to cumulative water-volume corrected age, this does not influence their application. Furthermore, the beta function with the parameters $b = 1$ and $a = SAS_\alpha$ being calibrated has a flat tail meaning little selectivity between the highest water ages. This also does not influence the interpretation of the results in terms of nwf (< 1 d) and ywf (< 30 d), which are the primary focus of this study.

Calculated age parameters Resulting TTD for a flux Q , corresponding to $p_Q(T, t)$ are calculated at each time t as a function of age T as follows:

$$p_Q(T, t) = \frac{Q(T, t)}{Q(t)} \quad (5.9)$$

^{iv} The term "serial reservoirs" refers to one reservoir receiving water from another reservoir.

Equivalently, RTD for a reservoir S (corresponding to $p_S(T, t)$) are calculated as follows:

$$p_S(T, t) = \frac{S(T, t)}{S(t)} \quad (5.10)$$

It should be noted, that in the results, all ages refer to time since catchment entry and not time since storage entry. Therefore, for the two groundwater reservoirs S_s , this is not the residence time inside the reservoir, but the residence time inside the catchment for water in this reservoir.

For the whole observation period, volume-weighted average TTD and RTD called master transit time distribution (mTTD) and master residence time distribution (mRTD) can be calculated as follows:

$$mTTD = \frac{\sum_{t=0}^{nt-1} Q(T, t)}{\sum_{t=0}^{nt-1} Q(t)} \quad (5.11)$$

$$mRTD = \frac{\sum_{t=0}^{nt-1} S(T, t)}{\sum_{t=0}^{nt-1} S(t)} \quad (5.12)$$

where nt is the number of time steps. The mTTD and mRTD can be calculated over the whole observation period as shown above or for a sub-period (e.g. a season or an event). The mRTD can be calculated for the whole catchment or a specific reservoir. The mTTD can be calculated for overall stream flow or a specific flux.

The overall or master SAS function of a flux or overall catchment discharge ($\omega_m(T)$) can be calculated from model output as follows:

$$\omega_m(T) = \frac{mTTD}{mRTD} \quad (5.13)$$

To match the way, SAS-functions are applied in this study, the SAS function is also shown as a function of the cumulative mRTD in the result section.

5.2.2.4 Tracers

As described above, time series of δ^2H in precipitations and streamflow as well as $[Si]$ in streamflow are used in this model in order to verify its age selectivity. They are the key to not only getting quantitative dynamics of water flow right, but also its TTD. The model is split into two separate modules: One "tracer version", which is modeling the age distribution inside each storage with regards to the time of entry into the storage for water and both tracers, but not keeping track of the history of the age distributions of previous time steps throughout the catchment in order to run more efficiently. This version is used for calibration to determine the best set of parameter values and in order to evaluate the model hypotheses. A second "age tracking version" is then run on the selected set of parameter values. In the age tracking version, tracers are not modeled, but the history of water age distributions is tracked on the catchment scale throughout the model and saved for each reservoir and streamflow at each time step. In the following, the way the tracers are used in the tracer model is explained.

Tracer concentrations are a property of each volume of water in each age class that strictly stay with this water volume in this age class. They age with their water and are transferred with their water. The two tracers δ^2H and $[Si]$ are used in the following way: For δ^2H , the precipitation signature is used as model input and every volume of water conserves its δ^2H throughout the model all the way to the streamflow. This is different for silica, as $[Si] = 0$ in precipitation (verified in a few precipitation samples). The water receives silica from dissolution of minerals in the saturated and non-saturated zone. A first order dissolution kinetic from an infinite reservoir is assumed. The saturated and non-saturated zone of each of the two geologies each have a dissolution rate constant k , which governs the dissolution velocity. The mass of Si at a time t , $m_{Si}(t)$ in mg m^{-2} ^v is calculated from the mass and concentration of Si at the previous time step, $m_{Si}(t-1)$ and $[Si](t-1)$ and the dissolved silica concentration at saturation $[Si]_{sat}$ as follows:

$$m_{Si}(t) = m_{Si}(t-1) + k \cdot t_s \cdot \left(1 - \frac{[Si](t-1)}{[Si]_{sat}}\right) \quad (5.14)$$

where k is a dissolution rate constant that is calibrated for each reservoir and t_s is the time step (1 h). This assumes that the contact surface between water and minerals (which governs the speed of dissolution) does not significantly vary with water content in a reservoir, as a certain mass of Si is added each time step, independently of the amount of water in the reservoir. This assumption is made because the less water there is in total, the more it will be held in smaller pores with a much larger specific contact surface. Therefore, the contact surface is not assumed to significantly decrease with the amount of water in the reservoir. Silica dissolution is applied to each individual age class in the storage. As these age classes do not physically correspond to a fixed volume of pore space but occupy variable fractions of the total pore space, Eq. (5.14) is divided by the total storage volume S_{tot} and thus applied to the concentration rather than mass of dissolved silica in each age class as follows:

$$[Si](T, t) = [Si](T-1, t-1) + \frac{k \cdot t_s \cdot \left(1 - \frac{[Si](T-1, t-1)}{[Si]_{sat}}\right)}{S_{tot}(t-1)} \quad (5.15)$$

This assumes no difference in contact surface per water volume between the different ages. This might not be totally realistic but is kept this way for simplicity. With regards to transfer, dissolved silica is considered to be conservative, thus $[Si]$ in each flux and each age equals to $[Si]$ in the corresponding age in the reservoir it comes from. The only exception is evapotranspiration: $[Si]$ in E_u is set to zero and the mass of dissolved silica remains in S_u , increasing the concentration. For empty ages in a reservoir, $[Si]$ is set to zero. This is important in the case where certain ages in S_u are emptied through E_u . Physically this corresponds to precipitation of the remaining silica. Note that according to Eq. (5.15), over-saturation in some ages due to evapotranspiration causes precipitation of silica.

^v As water volumes in the model are area-normalized (as water height), this is also true for tracer mass obtained as product of concentration and water height. Nevertheless, the term mass is used for this "mass per area" in order to avoid confusion.

5.2.2.5 Model calibration

In order to well parametrize the described processes in the model, a set of 20 parameters was calibrated. We defined their ranges (minimum and maximum values) as well as the kind of expected distribution they are chosen from (uniform or log-uniform). The ranges were estimated from manual testing, prior assumptions and first calibration runs with wider parameter ranges. The calibration is performed by running the model 61943 times (corresponding to four times 48 h on a 32-core node) and choosing the best set of parameters in terms of goodness of fit of the model's predicted $Q(t)$, $[Si](t)$ and $\delta^2H(t)$ time series to observed values. The calibration was performed on the period from 01.12.2019 to 31.12.2020. The process is described in more detail in the following.

Table 5.3 summarizes the calibrated parameters and their ranges and distributions. The parameters

TABLE 5.3: List of calibrated parameters of the model with unit, range and type of distribution (uni = uniform; log = uniform in logarithmic space; int = interger). Abbreviations used in the description: Unsat. = unsaturated; res. = reservoir; pref. = preferential; sat. = saturated; dis. const. = dissolution rate constant

Parameter	Description	unit	min	max	distr.
I_{max}	Size of interception reservoir	mm	0	3	uni
W_s	Water stress threshold	mm	50	200	uni
K_u	Unsat. res. pref. flow reactivity	mm h ⁻¹	5×10^{-6}	2×10^{-4}	log
A_u	Unsat. res. pref. flow non-linearity	–	2	4.8	uni
$T_{p u}$	Unsat. res. pref. flow threshold	mm	50	150	uni
K_{us}	Unsat. res. recharge reactivity	mm h ⁻¹	7×10^{-6}	1×10^{-4}	log
A_{us}	Unsat. res. recharge non-linearity	–	2	4	uni
$T_{p us}$	Unsat. res. recharge threshold	mm	40	100	uni
K_s	Sat. res. streamflow reactivity	mm h ⁻¹	3×10^{-7}	1×10^{-5}	log
A_s	Sat. res. streamflow non-linearity	–	2	4	uni
$T_{p s}$	Sat. res. streamflow threshold	mm	200	1200	uni
$SAS_{\alpha Eu}$	Unsat. res. ET SAS function	–	0.5	1	uni
$SAS_{stretch u bas}$	Unsat. res. SAS stretch basalt	mm	30	100	uni
$SAS_{stretch u sed}$	Unsat. res. SAS stretch sedimentary	mm	10	60	uni
$SAS_{\alpha s}$	Sat. res. streamflow SAS function	–	0.5	1.5	uni
$k_{Su bas}$	Unsat. res. basalt silica dis. const.	mg m ⁻² h ⁻¹	0.07	7	log
$k_{Su sed}$	Unsat. res. sedimentary silica dis. const.	mg m ⁻² h ⁻¹	0.006	0.6	log
$k_{Ss bas}$	Sat. res. basalt silica dis. const.	mg m ⁻² h ⁻¹	0.1	10	log
$k_{Ss sed}$	Sat. res. sedimentary silica dis. const.	mg m ⁻² h ⁻¹	0.01	1.0	log
bas_{delay}	Delay from basalt to outlet	h	0	1	int

are calibrated by maximizing the Nash-Sutcliffe Efficiency (NSE) of Q , $[Si]$ and δ^2H in the Cladu-ègne stream at the outlet. NSE is a common criterion to evaluate model performance by comparing modeled to observed data as follows:

$$NSE = 1 - \frac{\sum_{t=1}^{nt} (V_m(t) - V_o(t))^2}{\sum_{t=1}^{nt} (V_o(t) - \bar{V}_o)^2} \quad (5.16)$$

where $V_m(t)$ and $V_o(t)$ are modeled and observed values of the variable at time t , \bar{V}_o is its average and nt is the number of time steps (Nash and Sutcliffe, 1970). The NSE of the three variables is

maximized by minimizing the Euclidean distance ED between each NSE values and one.

$$ED = \sqrt{(1 - NSE(Q))^2 + (1 - NSE([Si]))^2 + (1 - NSE(\delta^2 H))^2} \quad (5.17)$$

The optimization is done using Sequential Model-Based Optimization (SMBO). SMBO is a technique to evaluate a costly fitness function (the model) by the use of a surrogate function that is cheaper to evaluate (less computationally demanding). This surrogate function relates tested parameter values to obtained goodness of fit of the model. It is used in order to chose the set of parameter values to be evaluated next by the model. After each model run, the surrogate function is updated with the results. The model starts with a random choice of a set of parameter values and then the history of parameter values and resulting goodness of fit is evaluated in order to determine the surrogate function proposing the next parameter set to evaluate. More specifically, Python's hyperopt module is used with a Tree-structured Parzen Estimator approach (TPE) (Bergstra et al., 2013, 2011). Briefly, TPE separates the past model runs into good versus bad runs based on an adaptive threshold on the loss (ED in our model). It then estimates the probability distributions of good and bad results using kernel density estimation^{vi} for each parameter. The ratio of those two probability distributions is then used to select the parameter value with the highest probability to lead to a good result for each parameter. As most optimization algorithms, TPE evaluates the parameters independently which is not ideal for interdependent parameters. There is no perfect solution for optimization of twenty partially interdependent parameters of a costly fitness function and hyperopt allowed a simple implementation and produced good parameter sets in less time than pure random search.

For each parameter, the range and expected kind of distribution are defined before calibration (see Table 5.3). Parameters are expected to be either uniformly distributed within their range (uni), uniformly distributed on a logarithmic scale within the range (log) or an integer within their range (int, also uniformly distributed). This last option is used for bas_{delay} as it needs to be a delay in full time steps. The log option is chosen for parameters that can span multiple orders of magnitude and where the order of magnitude needs to be determined, which is the case for dissolution rate constants and the flow reactivity parameter.

One run of the tracer model takes about 4 min on a single core of a recent portable PC. In order to speed up the calibration process which requires many model runs, we used ray tune (Liaw et al. (2018), version 1.6.0). This allowed us to run the parameter optimization on a node of the GRI-CAD (Grenoble alpes Recherche Infrastructure de Calcul intensif et de Données) computer cluster speeding up the process by a factor 30 by running the calibration on 32 cores on parallel. Ray tune manages the distribution of the model runs on different cores, with each core running the model on one set of parameters. As soon as one core finishes its model run it reports back the obtained loss (ED) and gets assigned the next set of parameters to run. In the meantime, hyperopt estimates the next set of parameters to assign to the next core that finishes.

^{vi} kernel density estimation is a method to estimate a continuous probability distribution from discrete values without prior definition of the distribution's shape

Once the parameters are calibrated, the model can be run in its "age tracking version", where tracers are not modeled, but the water age distribution is tracked on catchment scale throughout the model and saved for each reservoir and streamflow at each time step.

Validation As the idea to develop this model including tracer choice, sampling strategy and installation of the samplers formed over the course of the PhD project, the data span a relatively short period. In addition, isotopic precipitation data is missing for the beginning of 2021 and the discharge of 2021 had not been quality controlled at the time of writing. Therefore, the only data that could be used as a partial validation is a flood event in November 2019. It had been excluded from the calibration, because precipitation sampling was started just before this event and the model therefore does not have robust precipitation isotope information for this period. Nevertheless this event is used as a partial validation concerning Q and $[Si]$ and the results of δ^2H will also be shown for this uncalibrated event.

5.2.2.6 Initial conditions

Due to the long spin-up period, the sensitivity of the model result to the initial conditions was very low. The initial conditions were set for the water volumes and tracer concentrations as follows: for both geological entities $S_i = 0$ mm, $S_u = 50$ mm, $S_s = 500$ mm, $\delta^2H(\text{all reservoirs}) = -45\text{‰}$ and $[Si](S_u) = 5 \text{ mg L}^{-1}$. $[Si](S_s)$ was 15 mg L^{-1} for the basalt and 10 mg L^{-1} for the sedimentary part. Regarding boundary conditions, there were no other fluxes than those presented before.

5.3 Results

5.3.1 Model fit

Figures 5.13 and 5.14 show the time series of modeled versus observed $[Si]$ and δ^2H respectively, plotted on modeled versus observed Q and observed precipitation. Figure 5.15 shows the time-series of the streamflow discharge residuals. It shows that the discharge in the beginning of a flood event tends to be underestimated and the discharge during the recession tends to be overestimated. The absolute residuals are highest during the major flood events when the variations in absolute discharge are the strongest and fastest. The figure shows that relatively high residuals occur during some of the smaller flood events in the summer and beginning of autumn (May-June and October-November 2020). During July and August, the modeled discharge continues to decrease while the observed discharge remains at a low but constant baseflow (about 20 L s^{-1}) with some small spikes during rain events that represent small total water volumes. Figure 5.16 summarizes the relations between modeled and observed values of Q , $[Si]$ and δ^2H . The retained values for the calibrated parameters are presented and discussed in subsection 5.4.1. The NSE of Q , $[Si]$ and δ^2H are 0.719, 0.634 and 0.504 respectively for the calibration period (highlighted in green on Figures 5.13 and 5.14 a)) and 0.828, 0.631 and 0.495 for the whole presented period, including the period highlighted in red, that had not been considered for calibration. This indicates that the uncalibrated flood event is similarly well represented as the calibrated event with regards to $[Si]$ and δ^2H and the fit of Q is even better for the uncalibrated event than for the calibration period. It should be mentioned, however, that

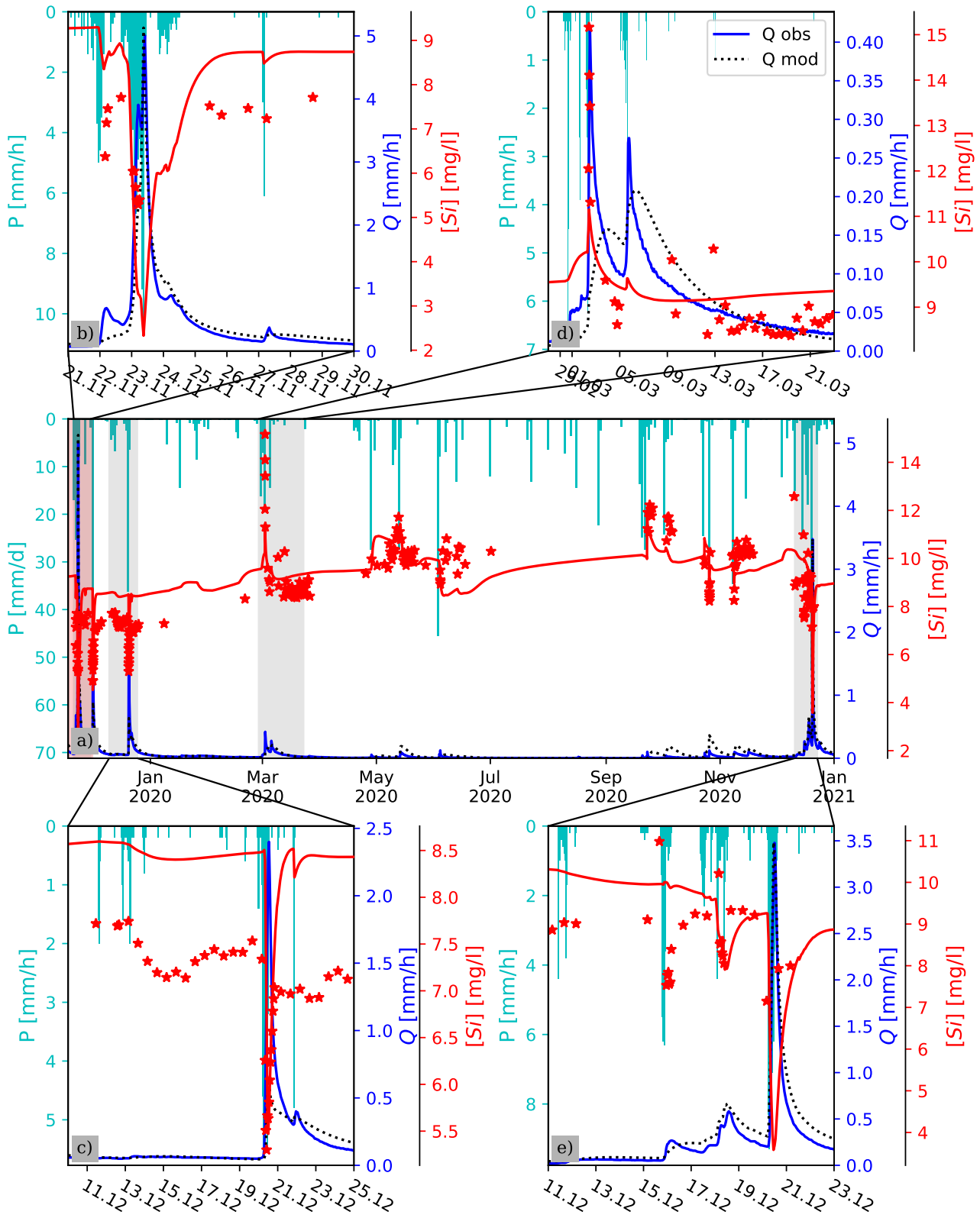


FIGURE 5.13: Time series of precipitation (P) modeled vs. observed discharge (Q) and Si concentration ($[Si]$) at the Claduègne outlet. Stars are observed and lines are modeled $[Si]$. a) is the whole period, the part highlighted in red was not calibrated. b) to e) show zooms on different events which are highlighted in gray in a). Hourly and daily precipitation intensity are shown at an hourly and daily resolution respectively.

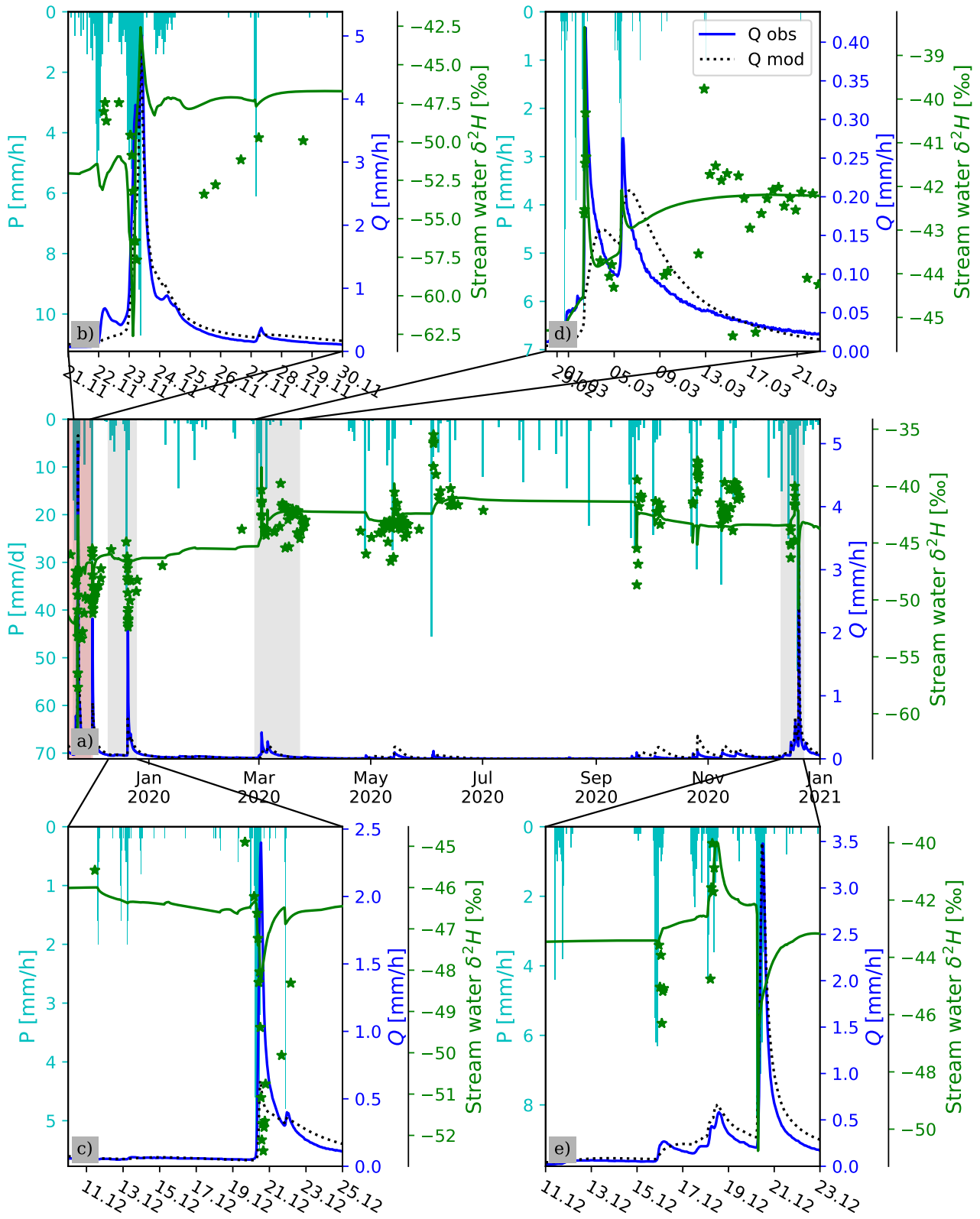


FIGURE 5.14: Time series of precipitation (P) modeled vs. observed discharge (Q) and stream deuterium ratio (δ^2H) at the Claduègne outlet. Stars are observed and lines are modeled δ^2H . a) is the whole period, the part highlighted in red was not calibrated. b) to e) show zooms on different events which are highlighted in gray in a). Hourly and daily precipitation intensity are shown at an hourly and daily resolution respectively.

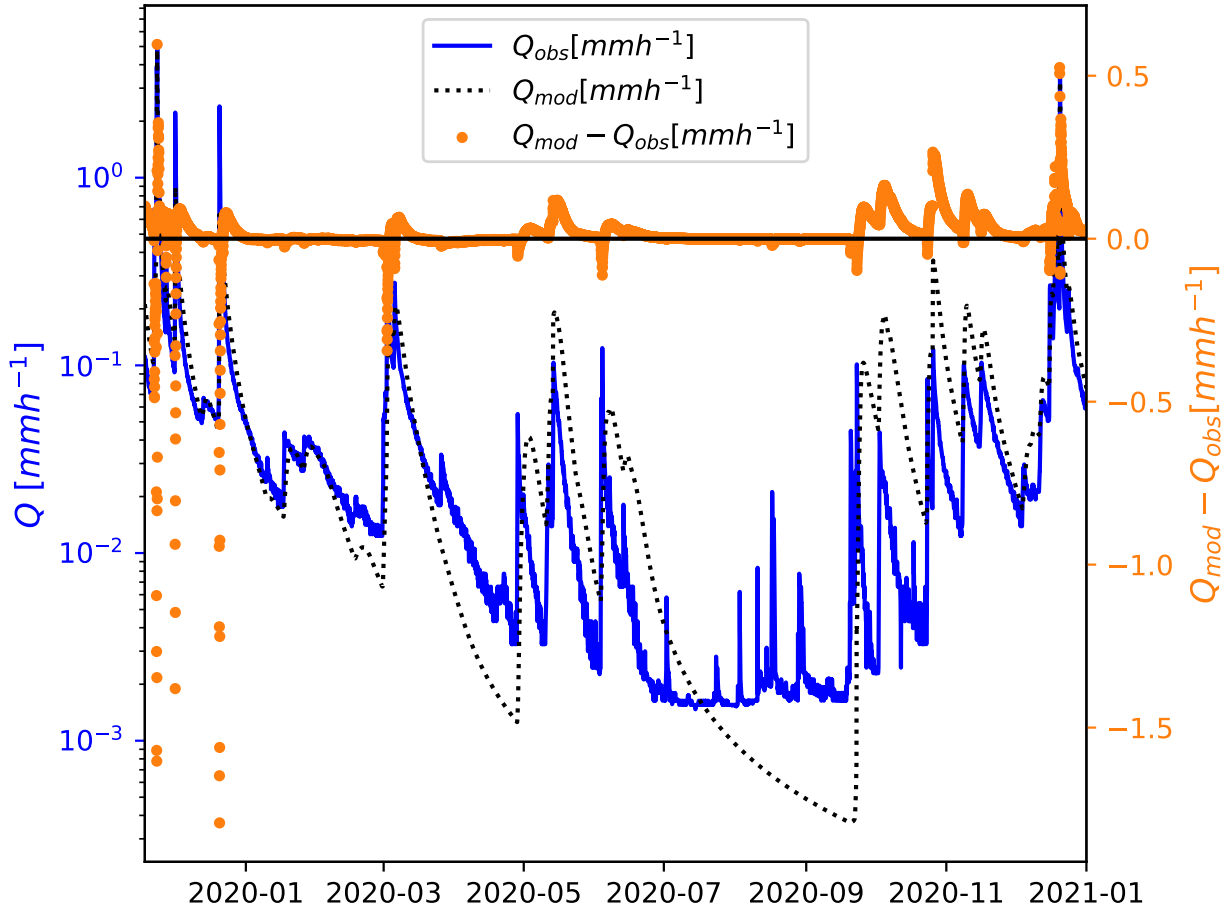


FIGURE 5.15: Residuals of streamflow discharge (observed - modeled).

due to the definition of NSE (Eq. (5.16)) it is easier to obtain a high NSE-value with more dynamic discharge (Moriassi et al., 2015). After Moriassi et al. (2015), for hydrological models on daily resolution concerning Q , a good fit is NSE between 0.7 and 0.8 and a value above 0.8 represents a very good fit. The obtained model fit would therefore translate to a good to very good fit for Q . Optimizing only Q during calibration (and not $[Si]$ and δ^2H), a NSE above 0.9 could be reached. Moriassi et al. (2015) also class NSE values for the solutes N and P. For N they classify as a good fit values of NSE between 0.4 and 0.55 and a very good fit above 0.55. After this classification we obtained a very good fit for $[Si]$ and a good fit for δ^2H . All the cited values are for daily models, which is the highest resolution they consider. However, the thresholds increase with lower resolution, indicating that for an hourly time step thresholds should rather be lower. In addition, calculated values for the coefficient of determination R^2 are shown in Fig. 5.16, calculated according to Krause et al. (2005) as:

$$R^2 = \left[\frac{\sum_{t=0}^{nt} (V_o(t) - \bar{V}_o)(V_m(t) - \bar{V}_m)}{\sqrt{\sum_{t=0}^{nt} ((V_o(t) - \bar{V}_o)^2) \sum_{t=0}^{nt} ((V_m(t) - \bar{V}_m)^2)}} \right]^2 \quad (5.18)$$

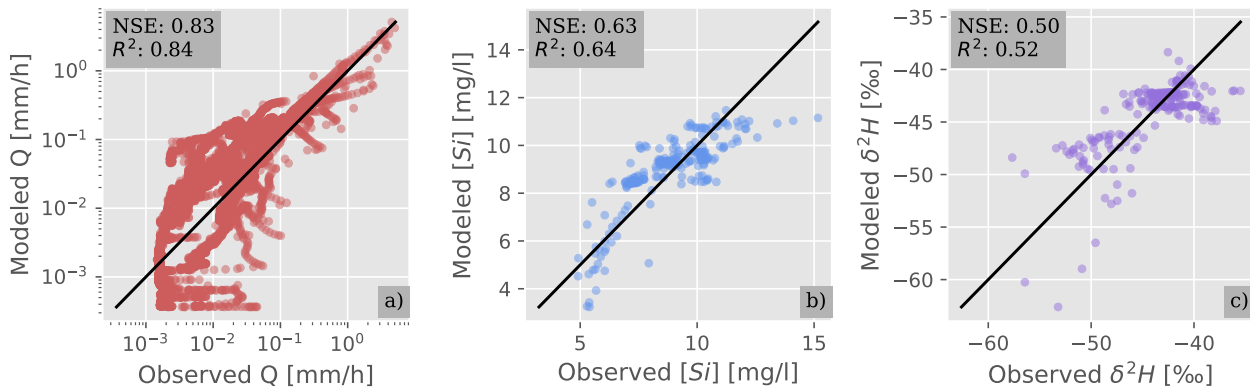


FIGURE 5.16: Summary of modeled versus observed discharge (Q , a)), Si concentration ($[Si]$, b)) and stream deuterium ratio (δ^2H , c)). The black lines are $y=x$. Note the log-log scale in a).

Concerning Q , the model reproduces the dynamic and amplitude of most of the largest flood events well. Most of the smaller flood events are well represented with regards to their amplitude, except the first autumn floods in 2020, the amplitude of which is overestimated (Fig. 5.13 a)). The model however fails to well reproduce the dynamic of flood events on drier soil: The model reaction is too slow (e.g. Fig. 5.13 d)). Figure 5.16 a) shows that this behavior is persistent over many of the small to medium events where the peak flow is underestimated (spikes to the right of the 1:1 line) and the recession flow is overestimated (roundish shapes to the left of the 1:1 line). Looking into the contributions of the different reservoirs (data not shown here), this is due to an absence of preferential flow, because the unsaturated reservoir is not filled above the threshold for preferential flow. See in the discussion section for more detail on the cause of this. Figure 5.16 a) also shows that the largest flood events are relatively well-represented being approximately parallel to the 1:1 line. Another interesting insight from Fig. 5.16 a) is that the model underestimates the lowest discharge values which occur during the summer months.

The general patterns of $[Si]$ are well reproduced by the model. The flood events for which a dilution of $[Si]$ was observed follow this trend (Fig. 5.13 b), c), and e) as well as others in a)). During flood events for which an increase of $[Si]$ was observed, this pattern is also reproduced by the model (Fig. 5.13 d)) and the summer and early autumn events in a)). The amplitude of $[Si]$ variations is sometimes overestimated (Fig. 5.13 e)) or underestimated (Fig. 5.13 d)). In Fig. 5.13 a) it can be noticed that the baseline of the winter-concentration is overestimated, while in summer it matches well with the observations. Figure 5.16 b) shows that the model slightly underestimates the lowest $[Si]$ while significantly underestimating the highest $[Si]$, corresponding to the event depicted in Fig. 5.13 d).

Concerning δ^2H , the seasonal variations are well captured (Fig. 5.14 a)). The dynamic and amplitude of short variations in δ^2H are however not always well covered. Figure 5.14 d) shows an example of a flood event that is well covered. The event in Fig. 5.14 c) has an insufficient amplitude. It should be remembered that stable water isotope sampling in precipitation was started in November 2019, which is why the event in Fig. 5.14 b) was excluded from calibration. It should be noted as well that

in winter 2020/2021 the precipitation sampler had some technical defects, so the model input δ^2H is of lower quality.

5.3.1.1 Goodness of fit interdependence

Figure 5.17 shows the relation between overall goodness of fit (ED) and individual NSE of each of Q , $[Si]$ and δ^2H for individual model runs. Looking at the overall trend (Fig. 5.17 a)), we can observe

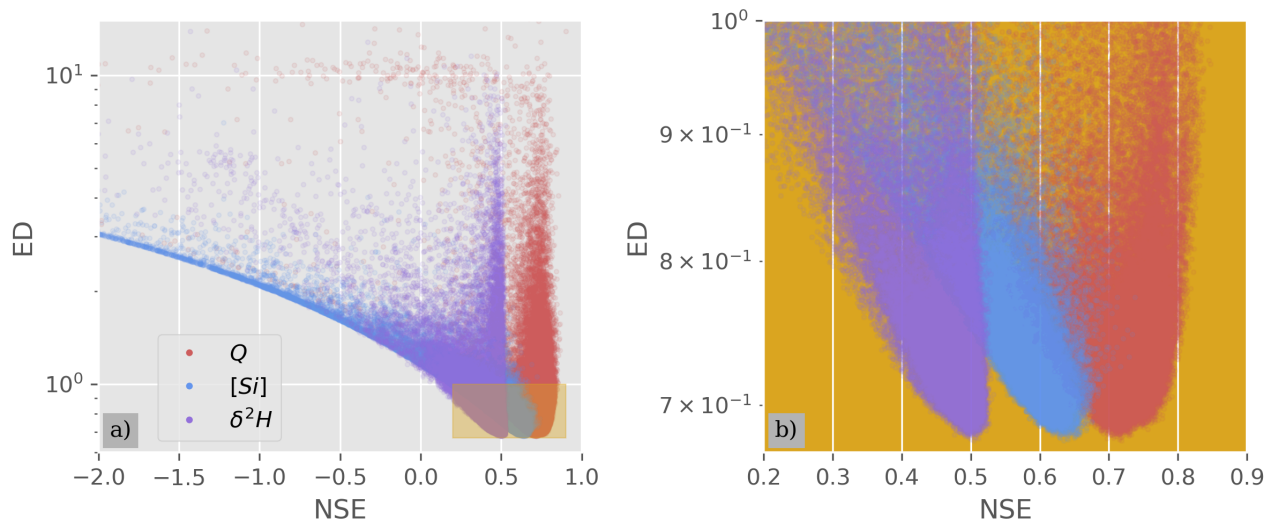


FIGURE 5.17: Individual goodness of fit (NSE) for Q (red), $[Si]$ (blue) and δ^2H (purple) versus overall goodness of fit (ED). b) is a zoom into the highlighted area in a).

that the NSE of $[Si]$ is well correlated with ED, while Q and δ^2H show this correlation only for a part of the model runs, whereas other runs seem nearly uncorrelated (the almost vertical lines in Fig. 5.17 a)). This is due to the calibration of the dissolution rate constants k which impacts the fit of $[Si]$ but not the fit of Q and δ^2H . The same is true for the parametrization of the SAS functions, which affect $[Si]$ and δ^2H but not Q . Regarding the relations close to the optimal fit (Fig. 5.17 b)), we can see that for all the best runs with the lowest ED, the NSE was better for $Q > [Si] > \delta^2H$. Due to the quadratic formulation of ED, this means that δ^2H generally weighs heavier in the goodness of fit evaluation than Q . This is presumably why the model run with the lowest ED has almost the highest NSE for δ^2H , while it has a much below the optimum NSE for Q .

5.3.2 Transit times

The modeled temporal evolution of the ywf and nwf are illustrated in Fig. 5.18 together with observed precipitation and modeled and observed discharge. As a reminder, ywf and nwf are the unitless fractions of discharge that are younger than 30 d and 1 d respectively. The ywf is mostly between 0% and 20% in summer and between 10% and 30% during large parts of the winter season (Fig. 5.18 a)). It can reach over 80% for short peaks during the major flood events, caused by intense precipitation on previously wet soil. The nwf is 0 the majority of time but rises up to 60% during these major flood

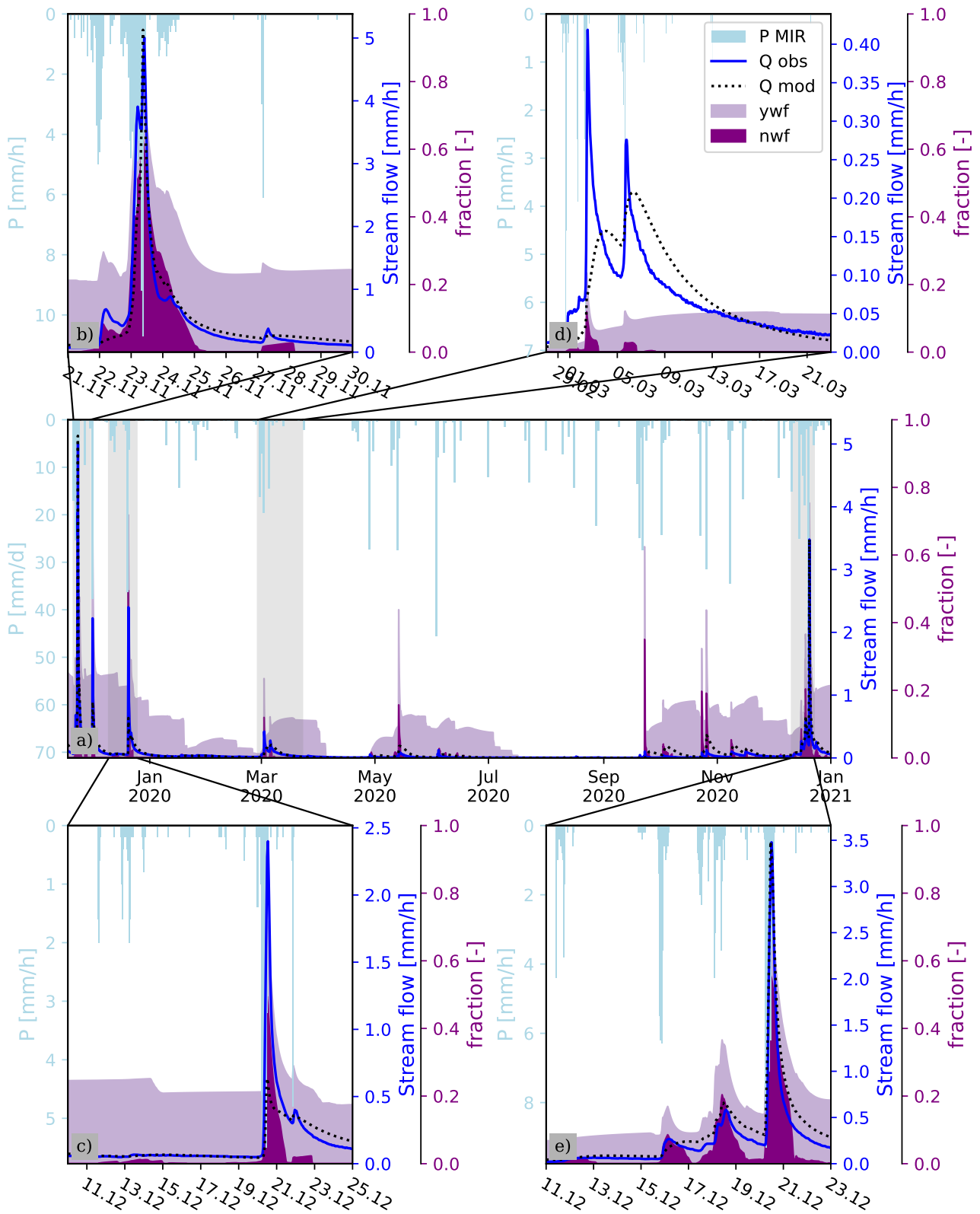


FIGURE 5.18: Time series of modeled new water fraction (nwf) and young water fraction (ywf) with precipitation (P) and modeled vs. observed discharge (Q). a) is the whole period. b) to e) show zooms on different events.

events (Fig. 5.18 b), c), e)) and shows some lower spikes about 20 % during smaller flood events in spring and summer (Fig. 5.18 a) and d)).

Figure 5.19 shows a hydrograph separation into seven age classes extracted from the modeled transit time distributions. It shows both an increase in base flow of old water during flood events as well as a sharp increase in event water. During the peak flow of the major flood events there is a strong contribution of water of less than five hours of age.

Figure 5.20 shows the temporal evolution of TTD (subfigure a)). As a reminder, we use the backward TTD which corresponds to the age distribution of water in streamflow of the Claduègne $p_Q(T, t)$ at any moment t . Data has been aggregated to daily resolution (over both, time and age axes) and plotted on a logarithmic scale. Due to the long period, in this overview only the water volumes from major flood events are visible. As they are aging (moving from top to bottom) over time (moving from left to right), their contributions diminishes (darker color). The TTD of a specific moment in time corresponds to the color along a vertical line from the corresponding position on the x-axis. The mTTD in Fig. 5.20 b) shows that in average 48 % of the water in discharge has spent more than 1 yr within the catchment while in average 70 % of the water stored in the catchment is older than 1 yr. Within the water less than 1 yr of age which is shown in Fig. 5.20 b), there is a strong dominance of shorter transit times and a slight dominance of shorter residence times. Furthermore, Figure 5.20 a) shows that precipitation fallen during the driest period from July to August 2020 does not reach the stream until more precipitation moistens the unsaturated zone in September and connects it to stream flow (corresponding to the appearance of the contribution of water of different ages in the end of September 2020). Figure 5.20 d) shows a zoom into a period of eight days in December 2020 and an age < 3 d. It shows that precipitation from the events on the 15th and 17th of December lead to small contributions of a few percent. The precipitation from the 20th of December then leads to a very strong contribution (> 30 %) of event water throughout this event. Over several hours after the end of precipitation, water from this event still makes about 15 % of the discharge at the outlet. Water from this event remains an important contributor to discharge over the following days. It can also be seen that following this event, water from the end of the event is preferred over water from the beginning of the event (the brightest color is the furthest to the top of the water from this event). This is due to the shape of the beta function becoming very steep close to zero and is not necessarily representative of reality. The mTTD over these eight days (Fig. 5.20 e)) shows that 5.6 % of the discharge of this period came from precipitation that fell within the same hour. 25.8 % of the total discharge during these eight days were less than 3 d old.

Figure 5.21 shows the mTTD, mRTD and recalculated SAS-functions for each of the fluxes. Figure 5.21 a) shows the cumulative mTTD of total discharge as well as the different individual discharges. Globally, 2.5 %, 8.3 %, and 25 % of discharge are younger than 1 h, 1 d and 30 d respectively. Preferential flow Q_u is much younger than ground water flow Q_s . In Q_u , the fraction younger than 30 d is 77 % and 89 % for the basaltic and sedimentary part respectively. In Q_s , this fraction is 15 % and 16 % respectively for the basaltic and sedimentary part. Figure 5.21 b) separates the global mTTD into the contributions of the different fluxes. It shows that over the year the contributions of the unsaturated parts are small (13.4 % together), but account for a large part of the young water (89 %, 62 %, and 45 % of water younger than 1 d, 7 d, and 30 d respectively). Regarding residence times, a similar

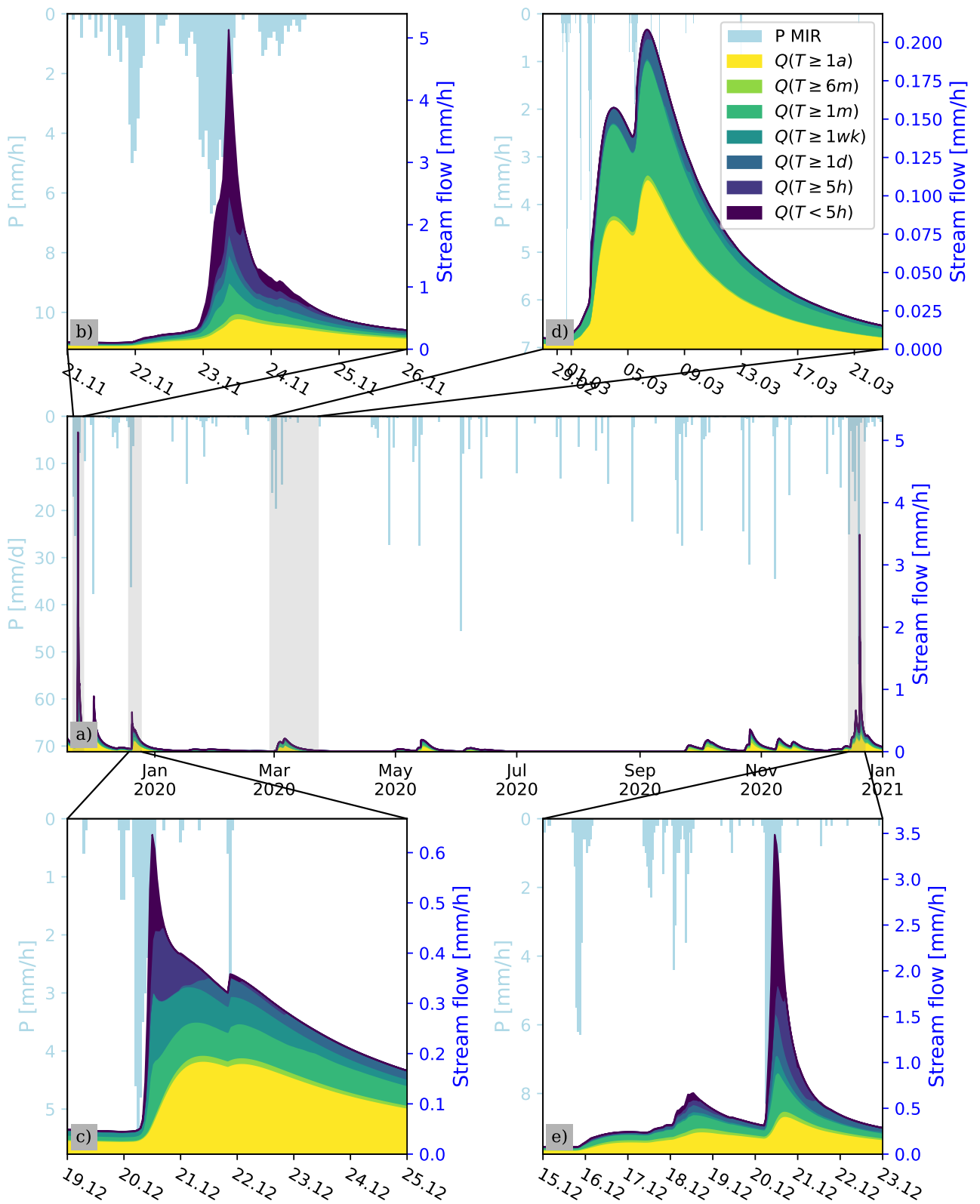


FIGURE 5.19: Time series of modeled discharge (Q) split into age classes (see color scale) with precipitation (P). a) is the whole period. b) to e) show zooms on different events.

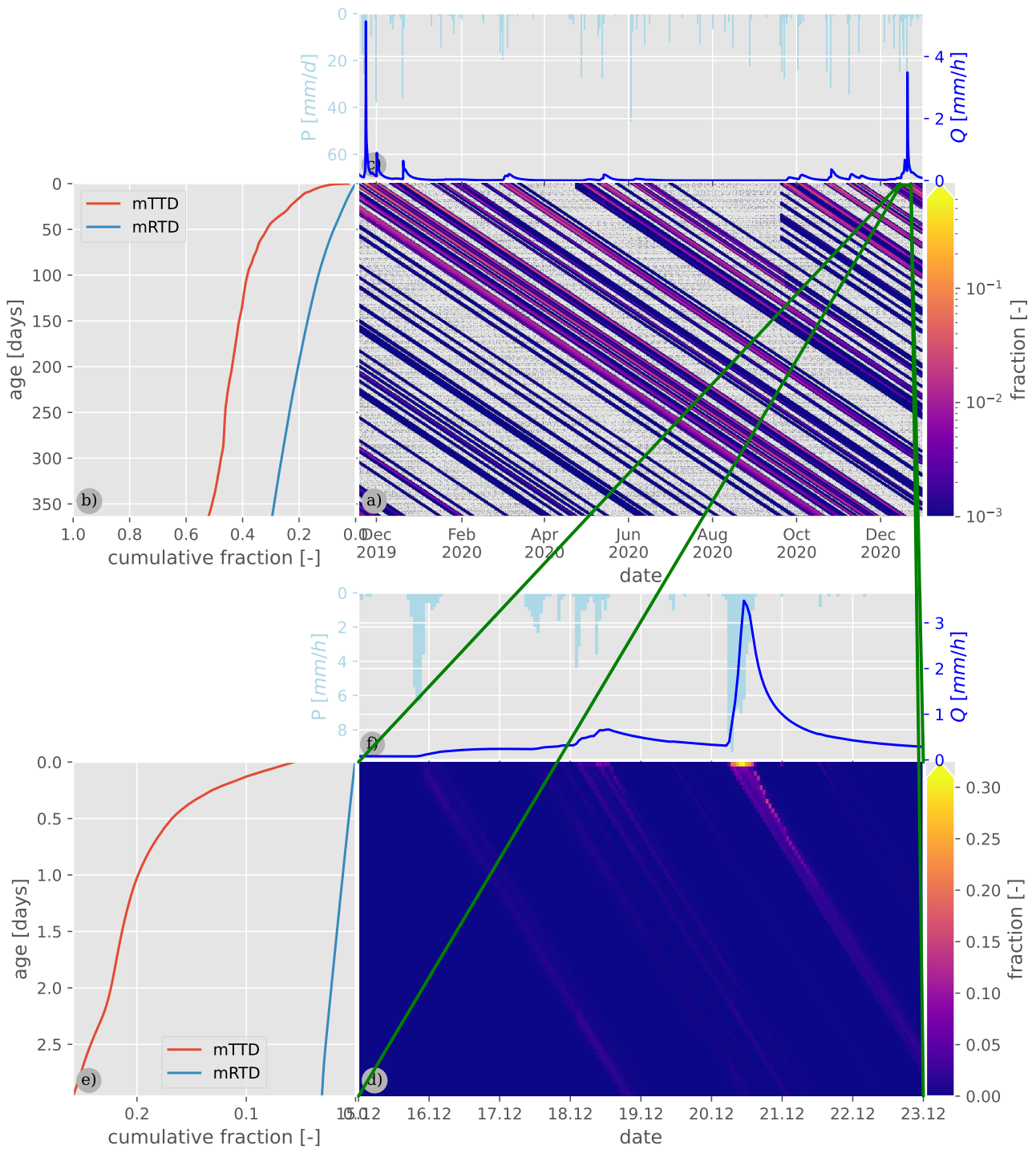


FIGURE 5.20: Temporal evolution of transit time distribution over the whole observation period (a) and a zoom into an 8 d period in december 2020 regarding ages < 8 d (d), green lines and rectangle indicate the location of d in a)). Discharge is plotted along the time-axis (c and f) and the cumulative master transit time distribution (mTTD) in discharge and master residence time distribution (mRTD) of the catchment for the respective period are plotted along the age-axis (b and e). Note the logarithmic scale on the colorbar of a).

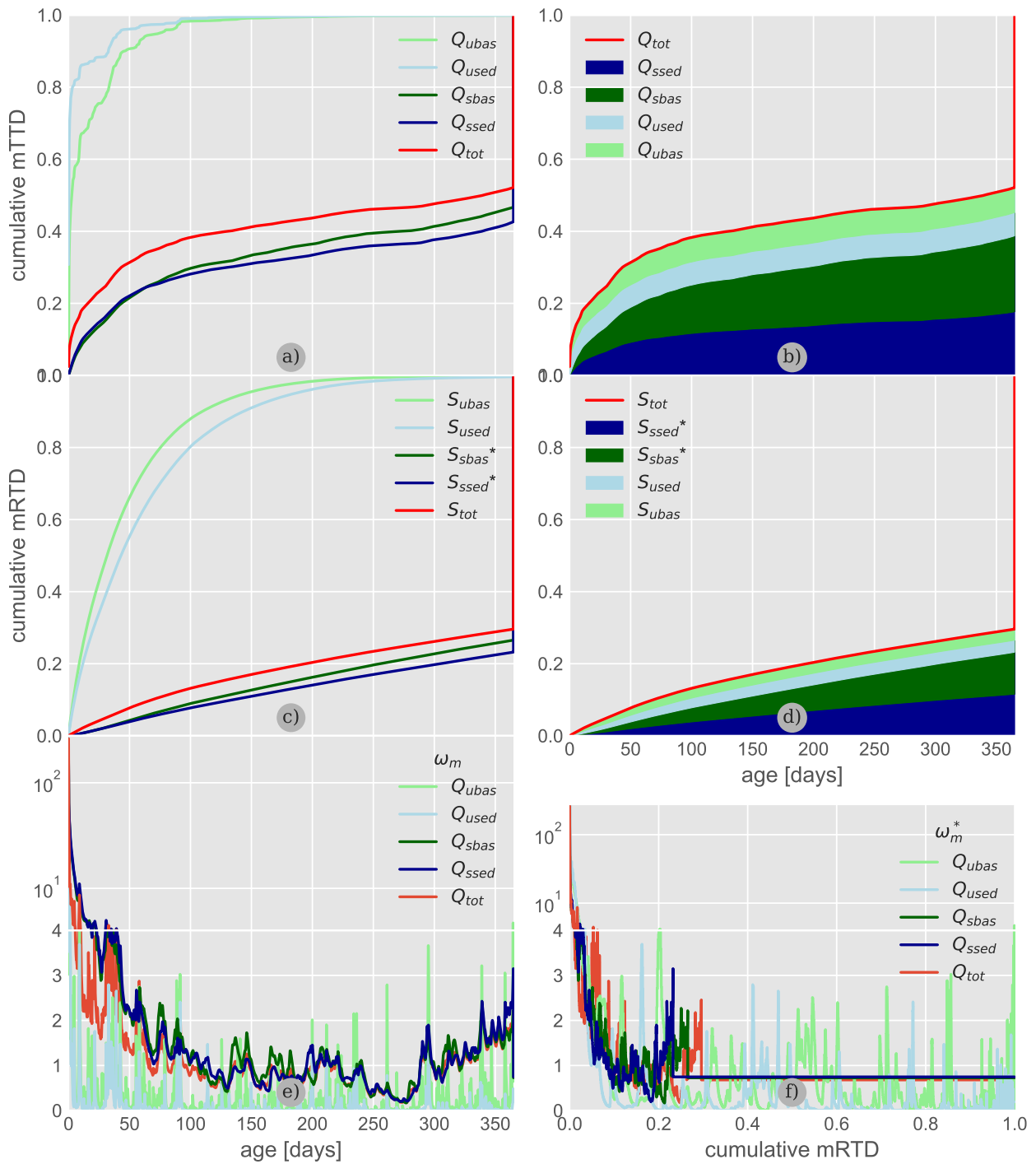


FIGURE 5.21: Cumulative master transit time distributions (mTTD, a) and b)) and master residence time distribution (mRTD, c) and d)) for the catchment and each flux (mTTD) and reservoir (mRTD). Subfigures a) and c) show individual distributions for each flux / reservoir and subfigures b) and d) show the contribution of each flux / reservoir to the catchments mTTD / mRTD. *Residence times are expressed in age since catchment entry, which does not correspond to the age since storage entry for the two groundwater reservoirs S_s . Subfigures e) and f) show the overall SAS-functions of the total discharge and each flux as a function of age (e), ω -notation) and as a function of cumulative storage age distribution (f), ω^* -notation). Note the cut axis in e) and f) with a logarithmic scale on the upper part.

distribution can be seen (Fig. 5.21 c) and d)). The mRTD are generally older than the mTTD. This is particularly true for the groundwater reservoirs S_s . It should be noted that the mRTD and mTTD for the ground water reservoirs and flows are calculated on age since catchment entry and not since reservoir entry. Therefore, they describe rather catchment residence and transit times of water in this reservoir and passing through it respectively. 70 % of the water stored in the catchment are older than one year. This percentage is higher in the groundwater reservoirs while water in the unsaturated zone is generally younger than 1 yr. Figure 5.21 d) shows that the unsaturated reservoirs account for most of the catchments young water, while they only store 6.4 % of all the water in the catchment. They account for 89 %, 73 %, and 57 % of the water younger than 1 d, 7 d, and 30 d respectively. The calculated SAS functions in Fig. 5.21 e) and f) show a strong young water preference in all fluxes (Fig. 5.21 f)).

5.4 Discussion

5.4.1 Calibrated parameters

In this section, the parameters retained after the calibration are presented. Their realism and importance is discussed. Table 5.4 lists the parameter values. All fluxes have a non-linearity ($A > 1$),

TABLE 5.4: List of the retained values of the calibrated parameters of the model including the description and unit (as mentioned in Table 5.3). Abbreviations used in the description: Unsat. = unsaturated; res. = reservoir; pref. = preferential; sat. = saturated; dis. const. = dissolution rate constant

Parameter	Description	value	unit
I_{max}	Size of interception reservoir	2.47	mm
W_s	Water stress threshold	200	mm
K_u	Unsat. res. pref. flow reactivity	7.23×10^{-6}	mm h ⁻¹
A_u	Unsat. res. pref. flow non-linearity	3.43	–
$T_{p u}$	Unsat. res. pref. flow threshold	103	mm
K_{us}	Unsat. res. recharge reactivity	9.68×10^{-6}	mm h ⁻¹
A_{us}	Unsat. res. recharge non-linearity	2.58	–
$T_{p us}$	Unsat. res. recharge threshold	56.0	mm
K_s	Sat. res. streamflow reactivity	8.43×10^{-6}	mm h ⁻¹
A_s	Sat. res. streamflow non-linearity	4.00	–
$T_{p s}$	Sat. res. streamflow threshold	1054	mm
$SAS_{\alpha Eu}$	Unsat. res. ET SAS function	0.875	–
$SAS_{stretch u bas}$	Unsat. res. SAS stretch basalt	92.0	mm
$SAS_{stretch u sed}$	Unsat. res. SAS stretch sedimentary	22.7	mm
$SAS_{\alpha s}$	Sat. res. streamflow SAS function	0.550	–
$k_{Su bas}$	Unsat. res. basalt silica dis. const.	1.44	mg m ⁻² h ⁻¹
$k_{Su sed}$	Unsat. res. sedimentary silica dis. const.	0.0236	mg m ⁻² h ⁻¹
$k_{Ss bas}$	Sat. res. basalt silica dis. const.	0.123	mg m ⁻² h ⁻¹
$k_{Ss sed}$	Sat. res. sedimentary silica dis. const.	0.467	mg m ⁻² h ⁻¹
bas_{delay}	Delay from basalt to outlet	0	h

meaning the more water is in the reservoir, the higher the increase in discharge caused by an additional volume of water. This seems to be realistic behavior as additional water will usually occupy

more concentrated and rapid flow paths. The preferential flow threshold $T_{p,u}$ is above that of recharge $T_{p,us}$, which complies to the assumptions made beforehand, that ground water recharge can still take place through the soil matrix when preferential flow stopped. The calibrated water stress threshold W_s (the amount of water in the unsaturated zone below which evapotranspiration is limited by water availability) is double the preferential flow threshold $T_{p,u}$, which may not be realistic. If the unsaturated zone is filled well above the threshold of preferential flow, plant transpiration should not be limited by water availability. This might however just indicate that the actual evapotranspiration is much lower than the potential evapotranspiration obtained from *Système d'Analyse des Renseignements Adaptés à la Nivologie (SAFRAN)* reanalysis most of the time, to a greater extent than the simple relation in Eq. (5.3) would account for. In this case, increasing W_s is the way the calibration could account for this. Furthermore, this could show that without taking into account isotopic fractionation during evapotranspiration from the unsaturated zone, this process cannot correctly be represented in the model. This hypothesis is supported by Fig. 5.22, which compares the goodness of fit of each parameter as compared to the value of W_s . It shows that the effect of W_s on ED (a) almost completely comes from

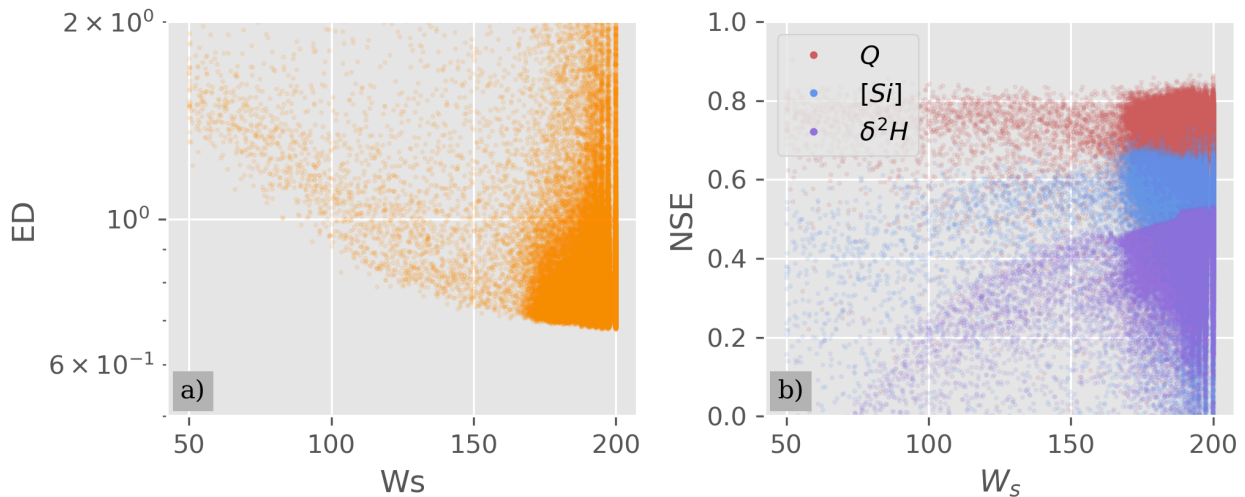


FIGURE 5.22: a) dependence of ED on values for W_s , b) dependence of the NSE for Q (red), $[Si]$ (blue) and δ^2H (purple) on values for W_s .

δ^2H (b, purple). The NSE of Q does not significantly depend on W_s and the NSE of $[Si]$ is slightly higher for a lower W_s (about 170 mm).

The SAS_α is more variable as a function of the amount of water in the unsaturated zone in the sedimentary than in the basaltic part. The sedimentary part has more clayey soils with drying cracks as obvious preferential flow paths. This could potentially explain a higher contrast in age preference between dry and wet conditions (= smaller value of $SAS_{stretch}$). However, when looking at the effect of variable values for $SAS_{stretch}$ (not shown here), the effect of some variation of this parameter on the NSE of the tracers is not very strong.

Concerning the saturated reservoir, there is a hydraulically passive part of 1054 mm and the reservoir has a young water preference. It is difficult to give a robust estimation of the passive volume from this

model. This volume per definition does not influence flow, and its influence on tracer concentrations is by increasing the residence time and therefore contributing older water to streamflow. Seasonal tracers like δ^2H are not sensitive to water older than a year (Kirchner, 2016) and the effect of longer transit times on $[Si]$ is calibrated through calibration of the silica dissolution rate constant. This parameter (T_{p_s}) should therefore not be interpreted in a physical sense.

Figure 5.23 shows the dependence of the NSE for $[Si]$ on the silica dissolution rate constants of the four reservoirs. The calibrated silica dissolution rate constants follow the order $k_{Su\ bas} > k_{Ss\ sed} >$

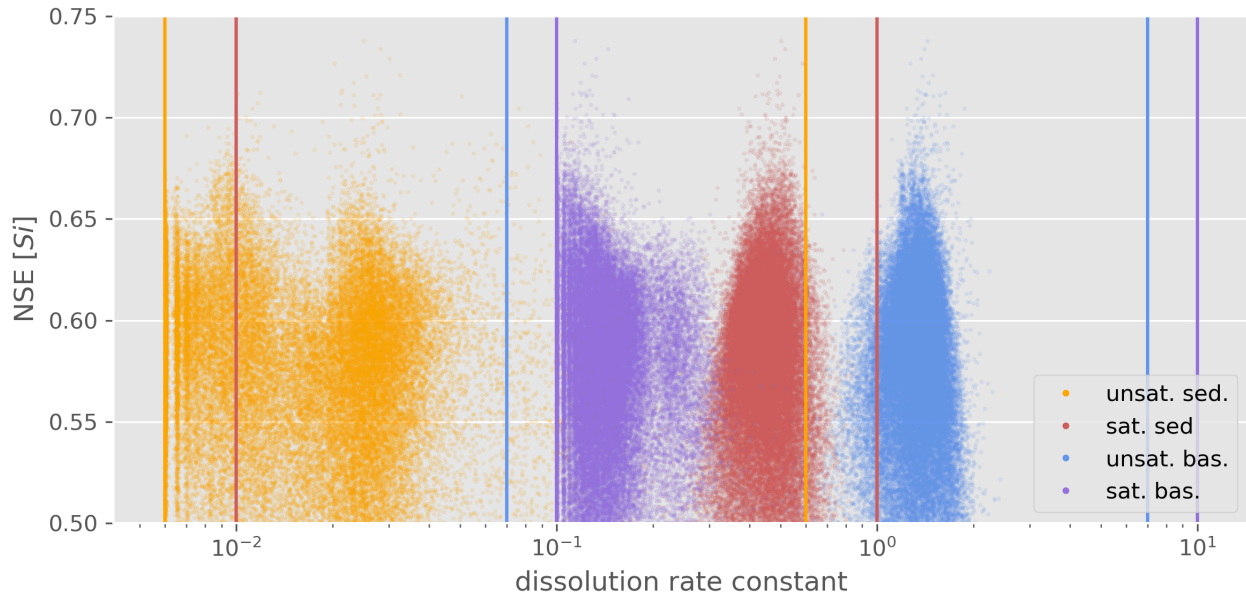


FIGURE 5.23: Dependence of the NSE for $[Si]$ on values for the four silica dissolution rate constants. The points show all points with a $NSE([Si]) > 0.5$. Vertical lines are the calibration ranges for each constant. Note the logarithmic scale on the x-axis.

$k_{Ss\ bas} > k_{Su\ sed}$. Having the highest silica dissolution in the unsaturated zone of the basaltic geology fits well to the observations from spatial sampling campaigns. The much lower dissolution rate constants for the saturated reservoir of the basaltic part might be explained by a very low contact surface between water and minerals in the fissured rock aquifer. They allow for a large passive reservoir enabling mixing and a smoother signature over the year while limiting the increase in $[Si]$. The saturated zone of the sedimentary part has a very similar dissolution rate constant to that of the basaltic part, even though the parent bedrock contains less silica. This may be explained by a higher water - mineral contact surface due to more weathered bedrock as compared to the basalt. The value of the unsaturated zone in the sedimentary part is the lowest. This may be explained by the significantly lower contact surface (due to a smaller reservoir size) as compared to the saturated zone, as well as a probably less easily dissolvable form of silica in the sedimentary parent material as compared to the basaltic part. Furthermore, due to the small order of magnitude, the exact value does not have a strong influence on the result (stream $[Si]$, Fig. 5.23). The dissolution rate constants correspond to a theoretical maximum dissolved silica "production" of 29.81 kg h^{-1} , 2.53 kg h^{-1} , 0.55 kg h^{-1} ,

and 10.94 kg h^{-1} for $S_{u \text{ bas}}$, $S_{s \text{ bas}}$, $S_{u \text{ sed}}$ and $S_{s \text{ sed}}$ respectively in the theoretical case of a $[Si]$ of 0 mg L^{-1} .

When evaluating the results of the large number of calibration runs, it can be observed that the optimum values for some of the parameters are close for Q and $[Si]$ but different for δ^2H . This is illustrated in Fig. 5.24: While high NSE values of $[Si]$ coincide with relatively high values of $NSE(Q)$ (Fig. 5.24 a)), this does not seem to be the case for Q and δ^2H : Fig. 5.24 c) has an obtuse angle where no model run produces a high NSE for both δ^2H and Q). This might indicate a problem with δ^2H . A possible reason is the quality of the isotopic data. There were some technical issues with the precipitation sampler leading to missing samples and some of the samples remained in the sampler for a relatively long period as explained in subsection 5.2.1. Another possible reason is the neglect of isotopic fractionation through evapotranspiration from the unsaturated zone reservoir. This could be added with reasonable effort, and might allow to improve the parameterization of the model.

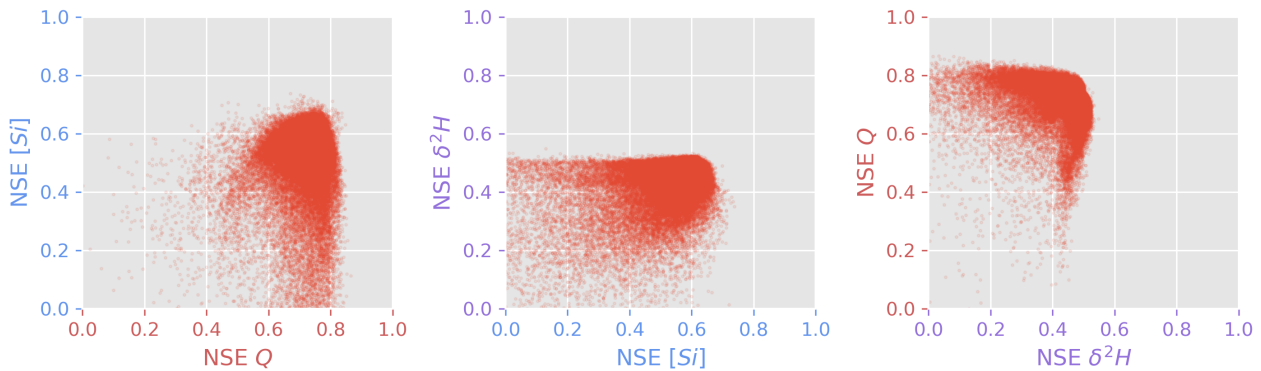


FIGURE 5.24: Relation between the NSE values for Q (red), $[Si]$ (blue) and δ^2H (purple).

Some of the parameters did not substantially impact the calibration result, meaning that equally good fits of all three parameters and the overall ED could be obtained over the whole range of values. This was the case for I_{max} , $SAS_{\alpha \text{ Eu}}$ and bas_{delay} . These could be set to fixed values in order to reduce the number of calibrated parameters.

5.4.1.1 Implications on catchment functioning

We could show that during wet conditions, more bypassing of the reservoirs through preferential flow is likely to take place. This stands in contrast to observations at the scale of the soil mesocosms (Chapter 4), where a stronger piston flow effect pushing out old water occurred under wet conditions and more rapid discharge of event water took place under dry condition. This shows that mechanisms controlling water flow on one scale do not necessarily need to be of importance on another scale. On the other hand, the mechanisms observed in Chapter 4, leading to rapid discharge of event water under dry conditions could play a role at the catchment-scale, by being responsible for the smaller rapid reactions of the catchment observed under dry conditions that are not well represented by the model.

5.4.2 Discussion and implications of the modeled transit time distributions

The age tracking results themselves cannot be validated like the tracer data, as the age distribution of stream water is not a physical or chemical parameter that could be measured. For those periods where tracer observations are well reproduced by the model, the age tracking results may be considered a realistic solution, provided that the observation-based assumptions on catchment functioning and tracer behavior are valid. However, these results cannot be proven to be correct or very precise. Generally, the variations of the proportions of the youngest ages are those having the strongest impact on the tracers and can be considered with the most confidence (Kirchner, 2016). For periods where discharge and tracer data are less well reproduced, a qualitative interpretation of the missing mechanisms and their effect on transit time distributions is done, but without quantitative estimation of transit time distributions. This is the case for the smaller flood events on relatively dry soil (e.g. Fig. 5.18 d)).

The results of the transit time tracing confirm hypotheses of large amounts of event water reaching the stream rapidly during flood events. The model helped to give a quantitative estimation of nwf and ywf and their evolution with time. The high temporal resolution of the model allows to combine both seasonal and event-scale dynamics, which are both well-represented by the model for most cases. In general, a large portion of the discharge (48 %) is older than 1 yr (Fig. 5.20 b)). In the end of summer, the Claduègne almost exclusively carries water older than 30 d (Fig. 5.18 a)), with most of it being older than 1 yr (data not shown). However, the frequent flood events regularly lead to event water contributions (nwf) between 10 % and 30 % for short periods of time (Fig. 5.18 a)). In autumn and winter, the ywf remains between 10 % and 30 % most of the time while rising to 80 % during major floods (Fig. 5.18 b) and e)). During these events, the nwf rises above 60 %. This is in accordance with field observations large-scale overland flow (OF) on the Coiron plateau during a flood event in October 2013 (Fig. 4.21).

Gallart et al. (2020) estimate young water fractions, which they define by an age < 2 to 3 mo, for a small (0.56 km^2) Mediterranean catchment in the Pyrenees via direct calculation from comparing the amplitude of the isotopic signals of stream flow and precipitation. They obtain very variable values ranging from 0 to 1 which is also in accordance with the results from the Claduègne catchment despite the difference in size.

These results indicate, that there is a particular risk of flushing of contaminants from soils into the streams in autumn and winter, as these are the periods with the highest event water fractions in streamflow (Fig. 5.18), but even flood events in summer carry this risk. The model generally underestimates the reactivity of the catchment under dry conditions (Fig. 5.15). The model produces no or very limited preferential flow Q_u under these conditions (data not shown). If we interpret this difference between model and observation as presence of preferential flow that is not represented by the model, the nwf and therefore the risk of contaminant mobilization under these conditions are likely to be higher in reality than expected from the model results. This would match the strong preferential flow leading to discharge of event water under dry conditions that has been observed on the scale of soil mesocosms even before the soil was well moistened (Chapter 4). The small spikes in flow that

can be observed during July and August represent small total water volumes that might be explained by direct precipitation on streams or roads, a process that is not taken into account in the model.

The main seasons for medical treatment of livestock are autumn and spring (Chapter 3). For those livestock that remain outside in autumn and winter, the autumn treatment may cause a serious risk of pollution of the streams. Those cattle that are brought inside for winter (a large part of the beef), are usually treated just before bringing them in. Therefore, the PhAC would be expected to be found in the manure, which is applied to the fields in different seasons, but usually not when strong rainfall is predicted in the following days. Concerning the treatment in spring, it is usually applied at the moment of bringing the cattle outside. This may signify a serious risk of contamination of the streams during spring storm events, which are not the major event type in the catchment but still occur regularly. The underestimation of the temporal dynamic of these events by the model is likely to indicate an underestimation of the portion of event water. The results of Chapter 4 indicate that during this type of intense precipitation on relatively dry soil, water and contaminants may easily bypass the soils through OF and subsurface storm flow on the plot scale, while the significance of this effect on the catchment scale could not be proven.

5.4.3 Constraints, limitations and possible improvements

A general limitation of the model design that can be observed throughout all of the different calibration runs, is that events on dry soil cannot be reproduced correctly in their dynamic. For these events, the total amount of precipitation is insufficient to fill the unsaturated reservoir up to preferential flow threshold, and the modeled hydrologic response therefore passes through the saturated reservoir and is relatively slow. In reality, a rapid increase in discharge of limited amplitude can be observed for several events in late summer and autumn (Fig. 5.15). It may be realistic that the unsaturated zone does not get close to saturation during these events. However, overland flow may still occur through exceedance of infiltration capacity, if the precipitation intensity is high enough. This is particularly true if the infiltration capacity is temporarily impacted by soil water repellency as observed in Chapter 4. This phenomenon can explain the rapid response of low amplitude observed in discharge during some events on dry soil. It is currently not implemented in the model. It is not an option to lower or remove the threshold on preferential flow in order to reproduce this behavior, as then the model cannot reproduce the strong difference in the amplitude of flood events between dry and wet condition that can be seen in Fig. 5.13 a) on a seasonal scale (spring/summer vs. autumn/winter) and in Fig. 2.8 on the event scale. In order to represent the catchment's rapid response to flood events on dry soils in the model without neglecting the importance of the catchments initial hydric condition for its overall reaction, Q_u would need to depend not only on S_u but also a parameter on a shorter time-scale like the precipitation intensity itself or the amount of water in S_u that is younger than a certain threshold (one or a few hours).

The idea for this part of the PhD was developed during the PhD project, including the selection of potentially adapted tracers, establishment of the sampling strategy and the sampling itself. At the moment of writing, the discharge data has not yet been quality controlled for 2021 and precipitation data from Meteo France for this period is not accessible yet. Sample collection was continued in 2021, but the precipitation sampler suffered an elongated technical failure and damage by game animals

in the beginning of 2021. Therefore, the dataset spans a limited period, not allowing to exclude a long independent period from the calibration in order to validate the model on. The flood event in November 2019 (Fig. 5.14 b)) was excluded from calibration because the collection of precipitation stable isotope data was started just before and is therefore not considered to be a robust input for the model. It can however be used to evaluate the model parametrization on Q and $[Si]$ and the model seems to perform well for these two. However, for a full, robust model validation, an elongated period of validation data including variable hydrological conditions would be necessary. Fortunately, this task can be performed at least on Q and $[Si]$ as soon as precipitation and discharge data become available.

Assuming δ^2H to be a perfectly conservative tracer is not fully realistic, at least for the unsaturated zone, due to isotopic fractionation (Sprenger et al., 2018), mostly during evaporation and plant transpiration. This assumption was made in order to keep the model at reasonable simplicity. Including isotopic fractionation should be one of the first steps in order to improve the model.

In a model like the one presented, many different sets of parameters can produce similarly good results. The approach to limit this equifinality was to constrain the model architecture as well as the parameter ranges according to our knowledge of the catchment. As an example, the range of silica dissolution rate constants k was set higher for the basaltic part of the catchment than for the sedimentary part of the catchment, according to the observations presented in subsection 5.2.1. Otherwise, the model could probably obtain a similarly well fit with higher silica dissolution in the sedimentary part and lower Si dissolution in the basaltic part.

Calibrating both silica dissolution rate constants and water age parameters on observed stream silica may also cause an equifinality problem as both transit time and dissolution rate constant positively affect $[Si]$. Unfortunately, it is very difficult to estimate such a parameter experimentally on the scale of a catchment or for the different reservoirs of the model, and a physical definition would require knowledge of the absolute contact surface between water and mineral SiO_2 . Fortunately however, δ^2H already restrains the model parametrization with regards to transfer times. Furthermore, the dynamic of $[Si]$ gives precious information on the dynamic of transfer on different time-scales, as discussed in subsection 5.2.1. The intra-event dynamic and more generally the nwf and ywf should be less prone to these equifinality problems, as on these time-scales the silica dissolution is limited. On the other hand, estimates of passive storage volumes and old water fractions from this model are considered imprecise.

In order to estimate the importance of this equifinality for the age results, four resulting water age parameters were compared between the retained model run, optimized on ED as well as three other parameter sets. These three parameter sets were selected from the 3026 calibration model runs with an $ED < 0.7$, choosing those with the best NSE for Q , δ^2H and Si respectively. Table 5.5 shows the results of this comparison. No substantial difference between the resulting age parameters can be observed. The master ywf and nwf vary by 7% and 13% respectively while their maximum values vary by only 3%. This shows that similar results are obtained with regards to water age if choosing different parameter sets. Therefore, the modeled age results are not expected to be extremely sensitive to the equifinality in model parametrization.

TABLE 5.5: Sensitivity of age results to different parameter sets. The table shows the values of the overall fraction of water younger than 30 days (master ywf) and 1 day (master nwf), as well as the highest observed fraction of water younger than 30 days (ywf_{max}) and younger than 1 day (nwf_{max}). These values are compared for model parameter sets optimized on ED , as well as the NSE of Q , Si and δ^2H . COV is the covariance between the different results.

	ED	Q	Si	$2H$	COV
master ywf	0.246	0.284	0.251	0.244	7.2%
master nwf	0.083	0.105	0.079	0.085	13.2%
ywf_{max}	0.788	0.801	0.753	0.799	2.8%
nwf_{max}	0.630	0.634	0.602	0.650	3.2%

The selection of parameters to calibrate the model is important. Generally the less parameters are calibrated and the more parameters are fixed using knowledge of the system, the higher the chances to get the right results for the right reason and to be able to obtain a robust model that also works in uncalibrated conditions (e.g. a period without tracer observations). Twenty parameters is a large number already, so several decisions were taken to keep the number the lowest possible. As silica is used as tracer and large differences in $[Si]$ were observed between the two geological units, those units had to be parametrized separately. In addition, the observed dynamic in solute concentrations suggested to separate saturated and unsaturated zone, which considering the results seems to have been key to represent the hydrological processes and reproduce observed tracer dynamics. The decisions made to restrict the number of parameters include neglecting isotopic fractionation during evapotranspiration from the unsaturated zone as well as limiting each SAS function to one single calibrated parameter. It was nevertheless possible to include a time-variant SAS-function for the unsaturated zone with only one calibrated parameter, that is restrained by hypotheses and improved the model as compared to the use of a fixed SAS_{α} . Another crucial restriction that has been made to limit the number of calibration parameters is to use identical flow thresholds and reservoir reactivities for the two geological entities. This is an unrealistic hypothesis, but calibrating these parameters separately for each geological unit would add nine calibration parameters (three parameters times three fluxes). If this should be changed in a future version of the model, it would be advisable to use fixed values for a part of the parameters or fix some of them relative to another one.

As mentioned in subsection 5.2.2, we do not consider the age information beyond an age of 1 yr, as the tracers are not expected to carry sufficient information beyond this age and it is beyond our scale of interest, which focuses on nwf and ywf. Kirchner (2016) elaborates on why seasonal tracers like water stable isotopes can only be used in order to compute this kind of water age fractions but not in order to calculate mean transit times.

5.4.4 SAS functions and reactive transport

As the PhD project focuses on the transfer of pharmaceuticals, the question whether this kind of model may be used directly for modeling these compounds in future came up many times. Therefore, some thoughts on the potential opportunities of reactive transport modeling through SAS functions in a semi-distributed hydrological model are noted in the following.

SAS functions are a useful tool for understanding the temporal dynamic of water and conservative tracers through different hydrologic systems without the need for detailed geospatial datasets and spatial representation of the processes and associated computational demand. However, their application to reactive transport modeling is limited. The implementation of a retardation through sorption to soil or any other process where the modeled compound (e.g. a contaminant) is separated from its water volume and passed on to another one seems difficult, at least in a differentiated way, as the water volumes inside a storage are represented by their age only and do not have any spatial equivalence inside the model. However, one could think of applications of SAS functions to reactive transport modeling in an integrative way. For example, if we assume older water to be deeper in the soil matrix and younger water to be in larger percentage in preferential flow paths, this would have direct implementations to adsorption and desorption kinetics due to different contact surfaces. A conceptual model with SAS functions for each storage like the one presented in this study could be adapted for doing this. One single adsorbed contaminant reservoir could be associated with each storage (again, without specifying its spatial distribution inside the reservoir) and the exchange kinetics would be more rapid for older than for younger water. This way, as long as contaminants are in solution, they would remain in their respective water volume, but after adsorption they would start approaching an equilibrium between adsorbed and dissolved phase. The huge drawback of doing this in a spatially integrative way would be the presumable very heterogenic spatial distribution of adsorbed contaminants inside the system that is not directly linked to the spatial distribution of residence times of water. Degradation would be rather simple to implement in such a model. For this kind of model, the data obtained from the interviews presented in Chapter 3, specifically on the treatment seasons and relative amounts used could provide valuable model input. The experiments presented in Chapter 4 could help define the concentrations in incoming water, however some calibration of input-concentrations at catchment-scale seems inevitable due to the very different spatial scales.

Alltogether, I do not consider this kind of model to be adapted for reactive transport modelling. For this kind of modeling, various tools are available and spatially distributed models are generally more adapted. The power of SAS-functions lies in the capability of reproducing the transfer of water in a spatially integrated but temporally explicit manner. This does not work in the same way for non-conservative reactive contaminants.

5.5 Conclusion

A tracer model with age tracking functionality was established for the Claduègne catchment on a high temporal resolution of 1 h, using two tracers with different mechanisms. The creation of a second age dimension allowed to account for both, age since storage entry for the application of SAS-functions and age since catchment entry for overall age-tracking through the serial reservoirs. Using this second age dimension only in the age tracking version and not in the tracer model version that is run for calibration kept computation efficient.

This chapter shows that the hypotheses about catchment functioning constructed from the discharge and tracer data presented in Section 2.5 and subsection 5.2.1 can be formulated into a conceptual hydrological model that correctly reproduces observed discharge and tracer concentrations at the

Claduègne outlet. The model generally works well in the reproduction of discharge and tracer values on the seasonal scale as well as during the major flood events. It also reproduces well a major flood event in November 2019 that the model has not been calibrated against. This suggests, that the basic concepts this model is built on, correctly represent the catchment's functioning with regards to the seasonal contrast and the dynamic of major flood events. These hypotheses include the need for a large amount of water in the unsaturated reservoir in order to produce a major flood event. In order to obtain such a large amount of water, intense precipitation on a pre-filled reservoir from recent precipitation is needed. Furthermore, in order to represent the evolution of dissolved silica concentrations, a slow, continuous dissolution of mineral silica is needed to reproduce the seasonal signal. In order to represent the evolution during flood events, two counteracting phenomena need to be in balance: (i) the arriving event water is poor in dissolved silica and therefore leads to a dilution of stream silica concentration. (ii) the arrival of new water in the unsaturated zone mobilizes some older water from the unsaturated zone that had previously been enriched in dissolved silica through dissolution and evapotranspiration. The SAS function is what balances between these two components in order to reproduce the observed evolution of stream silica concentration at the outlet. The evolution of discharge is well reproduced on the seasonal scale as well as on the intra-event scale during the major flood events. During events under dry conditions, the dynamic of discharge is not well-reproduced by the model. The overall tendencies of dissolved silica concentration and deuterium isotopic ratio are well reproduced, whereas this is not always the case for their amplitude.

We could reproduce the observations with an unsaturated zone that recharges the groundwater above 56 mm and produces preferential flow above 103 mm and a saturated zone with a passive part of 1054 mm. We could show that the evolution of tracer concentrations can be well reproduced with a young water preference in the saturated reservoir that indicates a not well mixed reservoir with a passive part that contributes little to the water flowing out of the reservoir. For the unsaturated reservoir, the mechanism that worked best is a time-variant SAS-function, that has an increasing young water preference with increased amount of water indicating increased preferential flow (including overland flow). Below the preferential flow threshold, an old water preference was present in ground water recharge, corresponding to matrix flow.

The high temporal resolution allowed an insight into the intra-event dynamics of nwf and ywf of flood events that are typically much shorter than a day. We could show that nwf and ywf are particularly high during large flood events and ywf are generally higher over the autumn months. The estimated transit times are very variable from a dominance of event water of a few hours of age during major flood events to an exclusive contribution of old water during the summer season. During the smaller summer flood events, event water contributions are likely to be underrepresented due to an underestimated reactivity of the model. The most likely explanation of the reactivity of the catchment during these dry conditions is water repellent soil leading to preferential flow (including overland flow) bypassing the soil without moistening it. This mechanism is not represented in the model. In general, during the autumn and winter season, fractions of new (< 1 d) and young (< 30 d) water are highest indicating the highest risk of transfer of contaminants into the streams.

6

General conclusion & perspectives

6.1 Conclusion

We identified 14 pharmaceutically active compounds (PhAC) that are systematically used in livestock breeding under Mediterranean climate in our study region, the Claduègne catchment. 10 of them were antiparasitic drugs, whereas antibiotics were rarely used. One of these antiparasitics, Ivermectin (IVM), was chosen in order to study its mobilization from contaminated cow dung on soil at the temporal scale of short intense precipitation events. The highest risk of mobilizing larger quantities of IVM was through overland flow (OF). While the soils from the foothills on sedimentary geology tend to efficiently filter out IVM from water flowing through the soil, this is less the case for soils from the Coiron plateau which produce strong preferential flow due to soil water repellency (SWR). In addition, these soils tend to produce stronger overland flow, which matches observations made in the field. At this scale, the transfer of IVM through and over the soils was significantly reduced under initially moist conditions. It seems that SWR limits adsorption of IVM on soil through limited soil-water interaction. The observations suggest that SWR has a substantial positive impact on both overland flow generation and rapidity of transfer of event water through the soil on both soils, but is stronger on the soils from the Coiron plateau. In addition, cracks from retraction of clay minerals during drying of the soils led to more rapid transfer of event water through the soils from the sedimentary foothills under dry conditions.

While these mechanisms may have an effect on the catchment scale, a direct transfer of their effect from one scale to another is not possible. A good example for this is the age preference of water fluxes on the scale of the soil mesocosms (Chapter 4) versus the catchment scale (Chapter 5). While

the drainage flow at the scale of the soil mesocosms showed a stronger piston flow effect pushing out old water first under wet conditions and more rapid discharge of event water under dry condition, the inverse worked best for overall flow at the integrated catchment-scale applying an increasing young-water preference with increased wetness. This can be explained by differences between the dominant mechanisms on different scales. Preferential flow due to SWR observed on the scale of the soil mesocosms may in large parts not be connected all the way to the streams on the scale of the hillslope and catchment due to the large saturation deficit of the soil infiltrating the water at some place. In addition, saturation overland flow, which was not accounted for in the mesocosm experiments, may occur at the scale of the hillslope and catchment.

On the spatial scale of the Claduègne catchment, hypotheses on the transfer of water were formulated based on observations of geochemical tracers, discharge and precipitation at high resolution. These hypotheses were translated into a conceptual model with age tracking functionality. The model was evaluated on Q , $[Si]$ and δ^2H and could correctly reproduce their evolution at the outlet of the Claduègne catchment with regards to their seasonality and intra-event evolution over the major flood events. For small flood events on dry soil, the model failed to reproduce the observed high dynamic of the hydrological response. In the model, discharge depends on the amount of water in the different reservoirs and the unsaturated zone was one single reservoir including soil matrix and preferential flow paths. The strong effect of water repellency that was observed during the plot-scale experiments is therefore not represented in the model at all. The catchment-scale effect of this water repellency is likely to explain the difference between the high observed and low modeled reactivity of the Claduègne during flood events on dry soil.

The Cévennes-Vivarais Mediterranean Hydrometeorological Observatory (OHM-CV), which the Claduègne catchment is part of was initially focused on understanding the hydro-meteorological and hydrological processes and conditions that generate flash floods. Therefore a large effort had been made to understand the conditions leading to the strongest hydrological responses. This work also focuses on the strong contrast between major flood events and low-flow conditions. The results of this study however suggest, that in order to better understand the transfer of residues of veterinary pharmaceuticals from dung in the fields toward the stream, smaller flood events may be of interest as well. More precisely, intense precipitation events on initially dry soil leading to a rapid hydrological response should be investigated. While the observations from the plot-scale experiments cannot directly be transferred to the scale of the Claduègne catchment, it is possible that the observed mechanisms have an impact on this scale. As these conditions are often observed in spring, which is one of the main treatment seasons and also the season when cattle are brought outside, there might be some serious risk of contaminant transfer over this period.

At the outlet of the Gazel subcatchment, the highest concentrations of Fenbendazole (FBZ), a pork antiparasitic drug, were observed under this condition of intense precipitation on dry soil, reaching 28.4 ng L^{-1} . This observation is based on a limited number of samples covering only a small part of the year and not allowing to draw a robust conclusion, but it would justify closer investigations on this specific condition for the transfer of hydrophobic molecules like some of the most toxic systematically used veterinary pharmaceuticals in the Claduègne catchment.

The results of this study show that for adsorbing diffuse agricultural contaminants, the export into streams is extremely variable with hydrometeorological conditions. For the understanding of the transfer of these contaminants, low frequency sampling that would be likely to miss most short flood events is of very limited use. The mobilization of these contaminants almost exclusively takes place under intense precipitation and on a rather short time scale. In addition to the hydro-meteorology, other environmental factors are of crucial importance for the transfer of these contaminants such as soil properties (structure, grain sizes, organic matter (OM) content, minerology) and condition (water content, water repellency).

A more applied conclusion of this study would be that if practicable from an agricultural point of view, cattle should be kept inside during the weeks after treatment and the dung from this period should be treated separately and applied only to fields that are on flat terrain far from surface water bodies and on well infiltrating, hydrophilic soils. This however is a relatively theoretical suggestion, as in many cases the treatment needs to be done just before letting the cattle outside in order to avoid parasite infestations on the fields. In this case it is advisable to keep the cattle on fields with well infiltrating soil, a small slope and at a distance from surface water bodies over the weeks following treatment. In addition, cattle should not be treated if precipitation is announced. All these suggestions however need to be practicable for the farmer.

6.2 Perspectives

A four-year research project of INRAe (Lyon) in collaboration with IGE (Grenoble), funded by the Agence Nationale de la Recherche (ANR) named CHYPSTER is currently starting. The project is in parts based on results of this PhD study and will pursue some of the investigations from this PhD. In brief, the project uses an interdisciplinary approach that includes the identification of anthropogenic contaminant sources, advanced passive sampling for contaminant analysis, biogeochemical fingerprinting and distributed hydrological modeling for the prediction of future trajectories of water quality scenarios, linked with changes in human activity, land use and climate. The approach will be applied to the Claduègne as well as the Yzeron catchment which encompasses the Claduègne.

If I was to give advise on future pharmaceutical sampling strategies, I would recommend to search for the 14 molecules systematically used at high frequency during smaller flood events caused by intense precipitations on dry soils in spring, summer and the beginning of autumn and compare the concentration values to those of a few samples taken before and after these flood events. Ideally, some additional sampling in the streams on the Coiron plateau would be advisable. Furthermore, a screening analysis of the polar organic compound integrative sampler (POCIS) employed during this work could be performed, looking for any of the 89 identified molecules. In addition analysis of sediment from the streams could give an idea of the present molecules, as the hydrophobic molecules are expected to be present in higher concentrations adsorbed to the sediment.

This study demonstrates the importance of high-quality long-term hydro-meteorological and geochemical datasets as produced by the OHM-CV and other observatories of the French Critical Zone Observatories Research Infrastructure (OZCAR-RI). It shows one of the many possible applications of these data. A few suggestions can be drawn from the additional water sampling that was started

over the course of this PhD. The quality of the isotopic water analyses was not satisfactory. Due to strong heat over the summer month, evaporation from the samplers is likely to be significant, even over short periods. In order to avoid this, simple measures could be installed such as described by Von Freyberg et al. (2020). There was repeated damage through game animals leading to the loss of a large number of samples, which could be avoided by installation of a protective barrier. The stream water sampling strategy applied in this study using two automated samplers revealed to be very useful. One sampler was controlled by the data logger to sample at high frequency during flood events and allowed to cover the intra-event evolution of concentrations while a second sampler was systematically activated to take samples on a lower frequency (every twelve hours), in order to select a few samples posterior that allowed to cover the evolution before and after flood events. These pre-event samples are crucial in order to get the full picture and were often missing in previous sampling, and still were missing in the pharmaceutical samples of this study, as the used samplers did not have glass containers.

In order to verify the hypotheses of flow behavior during dry and wet conditions from the soil transfer study (Fig. 4.22), short rainfall simulation experiments of a few minutes using dye tracer like Hardie et al. (2011) would be very useful. These experiments should be performed on initially dry as well as initially moist soil to compare the occurrence of preferential flow. In addition, these experiments could help to verify the absence of preferential flow along the sidewalls of the sampling frames.

The X-ray tomography images of the Coiron soils (Fig. 4.8) will be used in future to estimate a K_{HS} value through numerical flow simulation through the soil columns. These could be used to compensate for the fact that no values of K_{HS} could be estimated during infiltration experiments due to SWR.

A factor that is expected to be important for the transfer of IVM is the intensity of precipitation. It would be the next logical step to compare our results to experiments on the same soils with lower precipitation intensity over a longer period. In order to obtain more realistic rainfall characteristics, a different nozzle producing larger drops could be used, for example the Spraying Systems Fulljet HH50WSQ as used by J. B. Humphry et al. (2002). In addition, a higher distance between nozzle and soil surface could allow the raindrops to reach their final velocity and thus carry a more realistic kinetic energy. A higher kinetic energy of the raindrops would however be expected to modify the soil surface limiting the possibility to compare the results of subsequent rain events.

In order to answer another important question, 'How is the export of IVM re-partitioned between dissolved and sorbed phase (on suspended particulate matter)?' analyses of IVM on suspended sediment samples are needed. Unfortunately, the samples collected for this purpose could not be analyzed within the time limits of the PhD. These analyses could be done in future with the objective of publishing the experiments. The variable concentrations of the internal standard during IVM analysis will be the subject of an internship starting in April 2022.

There are several possible ways of improving the catchment-scale hydrological model. There are multiple indications that including isotopic fractionation could substantially improve the result. This could be done by implementing a liquid to vapor fractionation factor $\alpha_{v/l}$. This could be a fixed value from literature in order to avoid adding any calibration parameters. Another aspect that should be

improved in order to obtain more robust new water fraction (nwf) and young water fraction (ywf) is the occurrence of preferential flow on relatively dry soil, that cannot correctly be reproduced by the model. A solution to this could either be the implementation of an additional preferential flow as a function of effective precipitation or as a function of the amount of water in the S_u younger than a couple of hours. This however would add at least one calibration parameter. Another possibly important improvement of the model would be a different parametrization of the two geologies with regards to some of the parameters that are still the same on both geologies at the moment. However, in order to keep the number of parameters reasonable, some of the parameters should be set to fixed values.

Glossary

BCF The bioconcentration factor (BCF) is the concentration of a contaminant in an organism divided by the concentration in the surrounding medium (e.g. water). 61

critical zone The critical zone is the zone at the earth's surface in which interactions between atmosphere, geosphere, hydrosphere and biosphere take place and generally spans from the tree canopy to the bedrock. 10, 120, 134

DEM A digital elevation model (DEM) is a 2D raster image of surface elevation. 10

GABA γ -amino butyric acid (GABA) is a neuro-transmitter. 60

LiDAR Light detection and ranging (LiDAR) is a method to determine distances via a laser beam. 23

LOEC The lowest observed effect concentration (LOEC) is the lowest concentration of a contaminant at which an effect on a test organism could be observed. 42, 61

nwf The new water fraction (nwf) is the fraction of water that is younger than 24 hours. 120, 174

PEC A predicted environmental concentration (PEC) of a contaminant is the concentration expected to be found in the environment, usually obtained from modeling. 52

PNEC The predicted no effect concentration (PNEC) of a contaminant is the concentration below which no adverse effect is expected for environmental organisms. ii, 39, 114

po Pour-on (po) application of a drug is a topical application to the skin, which is common for beef, usually on the back. 37, 62

SAFRAN The Système d'Analyse des Renseignements Adaptés à la Nivologie (SAFRAN) is a re-analysis model from Météo France. 16, 161

sc Subcutaneous (sc) injection is an injection into the tissue between skin and muscle. 37, 62

SPE Solid phase extraction is a method to preconcentrate a sample before analysis by adsorbing the substance of interest from a large volume of water onto a solid phase and then elute it with a small volume of solvent. 41, 76

srb A sustained-release bolus (srb) is an intraruminal bolus continuously releasing a medicament over time. 62

voxel A voxel is a point in a three-dimensional raster image. 86, 89

ywf The young water fraction (ywf) is the fraction of water that is younger than 30 days. 120, 174

References

- Accinelli, C., Dinelli, G., Vicari, A., and Catizone, P.: Atrazine and metolachlor degradation in subsoils, *Biology and Fertility of Soils*, 33, 495–500, <https://doi.org/10.1007/s003740100358>, 2001.
- Agence nationale du médicament vétérinaire (ANMV): Index des Médicaments vétérinaires autorisés en France, URL <http://www.ircp.anmv.anses.fr/>, 2015.
- Aitkenhead, J. A. and McDowell, W. H.: Soil C:N ratio as a predictor of annual riverine DOC flux at local and global scales, *Global Biogeochemical Cycles*, 14, 127–138, <https://doi.org/10.1029/1999GB900083>, 2000.
- Allen, R. G., Pereira, L. S., Raes, D., and Smith, M.: FAO Irrigation and Drainage Paper No. 56 - Crop Evapotranspiration, Rome: Food and Agriculture Organization of the United Nations, 56, 1998.
- Alvinerie, M., Sutra, J., Galtier, P., Lifschitz, A., Virkel, G., Sallovitz, J., and Lanusse, C.: Persistence of ivermectin in plasma and faeces following administration of a sustained-release bolus to cattle, *Research in Veterinary Science*, 66, 57–61, <https://doi.org/10.1053/rvsc.1998.0240>, 1998.
- Ankley, G., Hoff, D., Mount, D., Lazorchak, J., Beaman, J., Linton, T., and Erickson, R.: Aquatic Life Criteria for Contaminants of Emerging Concern, 2008.
- ANMV: Base de données publique des médicaments vétérinaires autorisés en France - data.gouv.fr, URL <https://www.data.gouv.fr/fr/datasets/base-de-donnees-publique-des-medicaments-veterinaires-autorises-en-france-1/>, 2020.
- ANSM: Répertoire des Spécialités Pharmaceutiques, URL <http://agence-prd.ansm.sante.fr/php/ecodex/index.php><http://agence-prd.ansm.sante.fr/php/ecodex/telecharger/telecharger.php>, 2020.
- Arganda-Carreras, I., Kaynig, V., Rueden, C., Eliceiri, K. W., Schindelin, J., Cardona, A., and Seung, H. S.: Trainable Weka Segmentation: A machine learning tool for microscopy pixel classification, *Bioinformatics*, 33, 2424–2426, <https://doi.org/10.1093/bioinformatics/btx180>, 2017.
- Arnold, J. G., Srinivasan, R., Muttiah, R. S., and Williams, J. R.: LARGE AREA HYDROLOGIC MODELING AND ASSESSMENT PART I: MODEL DEVELOPMENT, *Journal of the American Water Resources Association*, 34, 73–89, <https://doi.org/10.1111/j.1752-1688.1998.tb05961.x>, 1998.

- aus der Beek, T., Weber, F. A., Bergmann, A., Hickmann, S., Ebert, I., Hein, A., and Küster, A.: Pharmaceuticals in the environment-Global occurrences and perspectives, *Environmental Toxicology and Chemistry*, 35, 823–835, <https://doi.org/10.1002/etc.3339>, 2016.
- Bachmair, S. and Weiler, M.: Interactions and connectivity between runoff generation processes of different spatial scales, *Hydrological Processes*, 28, 1916–1930, <https://doi.org/10.1002/hyp.9705>, 2014.
- Bair, D. A., Popova, I. E., Tate, K. W., and Parikh, S. J.: Transport of oxytetracycline, chlortetracycline, and ivermectin in surface runoff from irrigated pasture, *Journal of Environmental Science and Health - Part B Pesticides, Food Contaminants, and Agricultural Wastes*, 52, 631–640, <https://doi.org/10.1080/03601234.2017.1330069>, 2017.
- Baken, K. A., Sjerps, R. M., Schriks, M., and van Wezel, A. P.: Toxicological risk assessment and prioritization of drinking water relevant contaminants of emerging concern, *Environment International*, 118, 293–303, <https://doi.org/10.1016/j.envint.2018.05.006>, 2018.
- Bártíková, H., Podlipná, R., and Skálová, L.: Veterinary drugs in the environment and their toxicity to plants, *Chemosphere*, 144, 2290–2301, <https://doi.org/10.1016/j.chemosphere.2015.10.137>, 2016.
- Behera, P., Patro, B. K., Singh, A. K., Chandanshive, P. D., Ravikumar, S. R., Pradhan, S. K., Pentapati, S. S. K., Batmanabane, G., Mohapatra, P. R., Padhy, B. M., Bal, S. K., Singh, S. R., and Mohanty, R. R.: Role of ivermectin in the prevention of SARS-CoV-2 infection among health-care workers in India: A matched case-control study, *PLoS ONE*, 16, 1–12, <https://doi.org/10.1371/journal.pone.0247163>, 2021.
- Benettin, P., Rinaldo, A., and Botter, G.: Tracking residence times in hydrological systems: Forward and backward formulations, *Hydrological Processes*, 29, 5203–5213, <https://doi.org/10.1002/hyp.10513>, 2015.
- Bergstra, J., Bardenet, R., Bengio, Y., and Kégl, B.: Algorithms for hyper-parameter optimization, *Advances in Neural Information Processing Systems 24: 25th Annual Conference on Neural Information Processing Systems 2011, NIPS 2011*, pp. 1–9, 2011.
- Bergstra, J., Yamins, D., and Cox, D. D.: Hyperopt : A Python Library for Optimizing the Hyperparameters of Machine Learning Algorithms, in: *Proceedings of the 12th Python in Science Conference*, pp. 13–19, 2013.
- Bergström, S.: The HBV model-its structure and applications, *SMHI Reports Hydrology*, 4, 32, 1992.
- Beuerle, A.: Implémentation d'un modèle conceptuel distribué pour simuler l'effet de la variabilité spatiale de la pluie sur les transferts de surface, *Tech. rep.*, ENSE3, G-INP Université Grenoble Alpes, Grenoble, France, 2021.
- Beven, K. and Germann, P.: Macropores and water flow in soils, *Water Resources Research*, 18, 1311–1325, <https://doi.org/10.1029/WR018i005p01311>, 1982.

- Beven, K. and Germann, P.: Macropores and water flow in soils revisited, *Water Resources Research*, 49, 3071–3092, <https://doi.org/10.1002/wrcr.20156>, 2013.
- Beven, K. J. and Kirkby, M. J.: A physically based, variable contributing area model of basin hydrology, *Hydrological Sciences Bulletin*, 24, 43–69, <https://doi.org/10.1080/02626667909491834>, 1979.
- Bloom, R. A. and Matheson, J. C.: Environmental assessment of avermectins by the US food and drug administration, *Veterinary Parasitology*, 48, 281–294, [https://doi.org/10.1016/0304-4017\(93\)90163-H](https://doi.org/10.1016/0304-4017(93)90163-H), 1993.
- Blöschl, G.: Scaling in hydrology, *Hydrological Processes*, 15, 709–711, <https://doi.org/10.1002/hyp.432>, 2001.
- Blum, A., Chery, L., Barbier, J., Baudry, D., and Petelet-Giraud, E.: Contribution à la caractérisation des états de références géochimiques des eaux souterraines. Outils et méthodologie., Tech. rep., BRGM RP-51549-FR, 2002.
- Botter, G., Bertuzzo, E., and Rinaldo, A.: Catchment residence and travel time distributions: The master equation, *Geophysical Research Letters*, 38, 1–6, <https://doi.org/10.1029/2011GL047666>, 2011.
- Boudevillain, B., Delrieu, G., Galabertier, B., Bonnifait, L., Bouilloud, L., Kirstetter, P.-E., and Mosini, M.-L.: The Cévennes-Vivarais Mediterranean Hydrometeorological Observatory database, *Water Resources Research*, 47, 1–6, <https://doi.org/10.1029/2010WR010353>, 2011.
- Boudevillain, B., Delrieu, G., Wijbrans, A., and Confoland, A.: A high-resolution rainfall re-analysis based on radar–raingauge merging in the Cévennes-Vivarais region, France, *Journal of Hydrology*, 541, 14–23, <https://doi.org/10.1016/j.jhydrol.2016.03.058>, 2016.
- Bouvier, C., Patris, N., Freydier, R., Guilhe-Batiot, C., Seidel, J. L., Taupin, J. D., Brunet, P., and Remes, A.: The Floodscale experiment in the small catchment of Valescure, France: An overview of the isotopic and geochemical data base, *Geoscience Data Journal*, 5, 14–27, <https://doi.org/10.1002/gdj3.57>, 2018.
- Bouyer, M.: La paramétrisation des sols dans le modèle CVN-P : modèle hydrologique semi-distribué à base physique., Tech. rep., Agrocampus Ouest, 2014.
- Boxall, A., Fogg, L., Blackwell, P., Kay, P., Pemberton, E., and Croxford, A.: Veterinary Medicines in the Environment, *Rev Environ Contam Toxicol*, 180, 1–91, 2004.
- Braud, I. and Vandervaere, J.-P.: Infiltration campaign Claduègne catchment, Ardèche, France, <https://doi.org/10.6096/MISTRALS-HyMeX.1321>, 2015.
- Braud, I., Ayrat, P. A., Bouvier, C., Branger, F., Delrieu, G., Le Coz, J., Nord, G., Vandervaere, J. P., Anquetin, S., Adamovic, M., Andrieu, J., Batiot, C., Boudevillain, B., Brunet, P., Carreau, J., Confoland, A., Didon-Lescot, J. F., Domergue, J. M., Douvinet, J., Dramais, G., Freydier, R., G??ard, S., Huza, J., Leblois, E., Le Bourgeois, O., Le Boursicaud, R., Marchand, P., Martin, P., Nottale, L., Patris, N., Renard, B., Seidel, J. L., Taupin, J. D., Vannier, O., Vincendon, B., and Wijbrans, A.:

- Multi-scale hydrometeorological observation and modelling for flash flood understanding, *Hydrology and Earth System Sciences*, 18, 3733–3761, <https://doi.org/10.5194/hess-18-3733-2014>, 2014.
- Braud, I., Andrieu, J., Bouvier, C., Branger, F., Delrieu, G., Douvinet, J., Freydier, R., Leblois, E., Coz, J. L., Nord, G., Perez, S., Renard, B., Anquetin, S., Batiot, C., Besson, A., Bonnet, S., Bouyer, M., Brunet, P., Chen, S., Confoland, A., Coussot, C., Dramais, G., Grard, N., Huza, J., Bourgeois, O. L., Boursicaud, R. L., Mansanarez, V., Marchand, P., Nottale, L., Ollagnier, M., Rebolho, C., Tangwouo, A., Vannier, O., Vincendon, B., and Wijbrans, A.: FloodScale : Observation et modélisation hydro-météorologique multi-échelles pour la compréhension et la simulation des crues éclairées Rapport scientifique final du projet, Tech. rep., ANR, 2016.
- Braud, I., Desprats, J.-f., Ayral, P.-a., Bouvier, C., and Vandervaere, J.-p.: Mapping topsoil field-saturated hydraulic conductivity from point measurements using different methods, *Journal of Hydrology and Hydromechanics*, 65, 264–275, <https://doi.org/10.1515/johh-2017-0017>, 2017.
- Campbell, W. C.: Ivermectin and Abamectin, Springer-Verlag, New York, https://doi.org/10.1007/978-1-4612-3626-9_5, 1989.
- Cappa, C. D.: Isotopic fractionation of water during evaporation, *Journal of Geophysical Research*, 108, 4525, <https://doi.org/10.1029/2003JD003597>, 2003.
- Caracciolo, R., Escher, B. I., Lai, F. Y., Nguyen, T. A., Le, T. M. T., Wiberg, K., Tröger, R., König, M., Schlichting, R., Némery, J., Wiberg, K., Nguyen, P. D., and Baduel, C.: Impact of a megacity on a tropical estuary assessed with a combination of chemical analysis and in vitro bioassays, in preparation.
- Carrega, P.: Les inondations azuréennes du 3 octobre 2015 : un lourd bilan lié à un risque composite, *Pollution atmosphérique*, 228, 1–26, <https://doi.org/10.4267/pollution-atmospherique.5475>, 2016.
- Ccancapa, A., Masiá, A., Andreu, V., and Picó, Y.: Spatio-temporal patterns of pesticide residues in the Turia and Júcar Rivers (Spain), *Science of the Total Environment*, 540, 200–210, <https://doi.org/10.1016/j.scitotenv.2015.06.063>, 2016.
- Charuaud, L.: Résidus de médicaments vétérinaires dans les eaux destinées à la consommation humaine en zone d'élevage intensif, Ph.D. thesis, Université de Rennes 1, URL <http://www.theses.fr/2018REN1B066>, 2018.
- Charuaud, L., Jardé, E., Jaffrézic, A., Liotaud, M., Goyat, Q., Mercier, F., and Le Bot, B.: Veterinary pharmaceutical residues in water resources and tap water in an intensive husbandry area in France, *Science of the Total Environment*, 664, 605–615, <https://doi.org/10.1016/j.scitotenv.2019.01.303>, 2019a.
- Charuaud, L., Jarde, E., Jaffrezic, A., Thomas, M. F., and Le Bot, B.: Veterinary pharmaceutical residues from natural water to tap water: Sales, occurrence and fate, *Journal of Hazardous Materials*, 361, 169–186, <https://doi.org/10.1016/j.jhazmat.2018.08.075>, 2019b.

- Chen, J., Yang, L., Chen, X., Ripp, S., Radosevich, M., and Zhuang, J.: Bacterial mobility facilitated by soil depth and intact structure, *Soil and Tillage Research*, 209, 104911, <https://doi.org/10.1016/j.still.2020.104911>, 2021.
- Chiu, S. H. L., Green, M. L., Baylis, F. P., Eline, D., Rosegay, A., Meriwether, H., and Jacob, T. A.: Absorption, Tissue Distribution, and Excretion of Tritium-Labeled Ivermectin in Cattle, Sheep, and Rat, *Journal of Agricultural and Food Chemistry*, 38, 2072–2078, <https://doi.org/10.1021/jf00101a015>, 1990.
- Ciais, P. and Jouzel, J.: Deuterium and oxygen 18 in precipitation: Isotopic model, including mixed cloud processes, *Journal of Geophysical Research*, 99, 16793, <https://doi.org/10.1029/94JD00412>, 1994.
- Cleuvers, M.: Mixture toxicity of the anti-inflammatory drugs diclofenac, ibuprofen, naproxen, and acetylsalicylic acid, *Ecotoxicology and Environmental Safety*, 59, 309–315, [https://doi.org/10.1016/S0147-6513\(03\)00141-6](https://doi.org/10.1016/S0147-6513(03)00141-6), 2004.
- Comber, S. D.: Abiotic persistence of atrazine and simazine in water, *Pesticide Science*, 55, 696–702, [https://doi.org/10.1002/\(SICI\)1096-9063\(199907\)55:7<696::AID-PS11>3.0.CO;2-7](https://doi.org/10.1002/(SICI)1096-9063(199907)55:7<696::AID-PS11>3.0.CO;2-7), 1999.
- Cook, D. F., Dadour, I. R., and Ali, D. N.: Effect of diet on the excretion profile of ivermectin in cattle faeces, *International Journal for Parasitology*, 26, 291–295, [https://doi.org/10.1016/0020-7519\(95\)00132-8](https://doi.org/10.1016/0020-7519(95)00132-8), 1996.
- Craig, H.: Isotopic variations in meteoric waters, *Science*, 133, 1702–1703, <https://doi.org/10.1126/science.133.3465.1702>, 1961a.
- Craig, H.: Standard for Reporting Concentrations of Deuterium and Oxygen-18 in Natural Waters, *Science*, 133, 1833–1834, <https://doi.org/10.1126/science.133.3467.1833>, 1961b.
- Crump, A. and Ōmura, S.: Ivermectin, ‘Wonder drug’ from Japan: the human use perspective, *Proceedings of the Japan Academy, Series B*, 87, 13–28, <https://doi.org/10.2183/pjab.87.13>, 2011.
- Danesh-Yazdi, M., Klaus, J., Condon, L. E., and Maxwell, R. M.: Bridging the gap between numerical solutions of travel time distributions and analytical storage selection functions, *Hydrological Processes*, 32, 1063–1076, <https://doi.org/10.1002/hyp.11481>, 2018.
- Dansgaard, W.: Stable isotopes in precipitation, *Tellus*, 16, 436–468, <https://doi.org/10.3402/tellusa.v16i4.8993>, 1964.
- Darcy, H.: *Les fontaines publiques de la ville de Dijon: exposition et application*, Victor Dalmont, 1856.
- Dasenaki, M. E. and Thomaidis, N. S.: Multi-residue determination of 115 veterinary drugs and pharmaceutical residues in milk powder, butter, fish tissue and eggs using liquid chromatography-tandem mass spectrometry, *Analytica Chimica Acta*, 880, 103–121, <https://doi.org/10.1016/j.aca.2015.04.013>, 2015.

- Davies, I. M., McHenery, J. G., and Rae, G. H.: Environmental risk from dissolved ivermectin to marine organisms, *Aquaculture*, 158, 263–275, [https://doi.org/10.1016/S0044-8486\(97\)00209-3](https://doi.org/10.1016/S0044-8486(97)00209-3), 1997.
- Davies, J. and Davies, D.: Origins and Evolution of Antibiotic Resistance, *Microbiology and Molecular Biology Reviews*, 74, 417–433, <https://doi.org/10.1128/MMBR.00016-10>, 2010.
- Davies, J., Beven, K., Rodhe, A., Nyberg, L., and Bishop, K.: Integrated modeling of flow and residence times at the catchment scale with multiple interacting pathways, *Water Resources Research*, 49, 4738–4750, <https://doi.org/10.1002/wrcr.20377>, 2013.
- Delrieu, G., Nicol, J., Yates, E., Kirstetter, P.-E., Creutin, J.-D., Anquetin, S., Obled, C., Saulnier, G.-M., Ducrocq, V., Gaume, E., Payrastré, O., Andrieu, H., Ayrat, P.-A., Bouvier, C., Neppel, L., Livet, M., Lang, M., Du-Châtelet, J. P., Walpersdorf, A., and Wobrock, W.: The Catastrophic Flash-Flood Event of 8–9 September 2002 in the Gard Region, France: A First Case Study for the Cévennes–Vivarais Mediterranean Hydrometeorological Observatory, *Journal of Hydrometeorology*, 6, 34–52, <https://doi.org/10.1175/JHM-400.1>, 2005.
- Di Guardo, A., Calamari, D., Benfenati, E., Halling-Sørensen, B., Zuccato, E., and Fanelli, R.: Pharmaceuticals as Environmental Contaminants: Modelling Distribution and Fate, in: *Pharmaceuticals in the Environment*, pp. 183–194, Springer Berlin Heidelberg, Berlin, Heidelberg, https://doi.org/10.1007/978-3-662-09259-0_15, 2004.
- Dibner, J. J. and Richards, J. D.: Antibiotic growth promoters in agriculture: History and mode of action, *Poultry Science*, 84, 634–643, <https://doi.org/10.1093/ps/84.4.634>, URL <http://dx.doi.org/10.1093/ps/84.4.634>, 2005.
- Doerr, S. H.: On standardizing the 'water drop penetration time' and the 'molarity of an ethanol droplet' techniques to classify soil hydrophobicity: a case study using medium textured soils, *Earth Surface Processes and Landforms*, 23, 663–668, [https://doi.org/10.1002/\(SICI\)1096-9837\(199807\)23:7<663::AID-ESP909>3.0.CO;2-6](https://doi.org/10.1002/(SICI)1096-9837(199807)23:7<663::AID-ESP909>3.0.CO;2-6), 1998.
- Doerr, S. H., Shakesby, R. A., and Walsh, R. P.: Soil water repellency: Its causes, characteristics and hydro-geomorphological significance, *Earth Science Reviews*, 51, 33–65, [https://doi.org/10.1016/S0012-8252\(00\)00011-8](https://doi.org/10.1016/S0012-8252(00)00011-8), 2000.
- Doong, R. A., Sun, Y. C., Liao, P. L., Peng, C. K., and Wu, S. C.: Distribution and fate of organochlorine pesticide residues in sediments from the selected rivers in Taiwan, *Chemosphere*, 48, 237–246, [https://doi.org/10.1016/S0045-6535\(02\)00066-8](https://doi.org/10.1016/S0045-6535(02)00066-8), 2002.
- Dormann, C. F.: *Parametrische Statistik*, Springer Berlin, Heidelberg, 2013.
- Doube, M., Klosowski, M. M., Arganda-Carreras, I., Cordelières, F. P., Dougherty, R. P., Jackson, J. S., Schmid, B., Hutchinson, J. R., and Shefelbine, S. J.: BoneJ: Free and extensible bone image analysis in ImageJ, *Bone*, 47, 1076–1079, <https://doi.org/10.1016/j.bone.2010.08.023>, 2010.
- Ducrocq, V., Drobinski, P., Lambert, D., Molinié, G., and Llasat, C.: Preface: Forecast and projection in climate scenario of Mediterranean intense events: Uncertainties and propagation on

- environment (the MEDUP project), *Natural Hazards and Earth System Sciences*, 13, 3043–3047, <https://doi.org/10.5194/nhess-13-3043-2013>, 2013.
- Duplus, T.: Enquete sur l'utilisation de produits chimiques dans un bassin versant rural - le cas de la Claduègne (Ardèche), Tech. rep., Université Grenoble Alpes, 2017.
- ECHA: EC inventory, URL <https://echa.europa.eu/de/information-on-chemicals/ec-inventory>, 2022.
- Eggen, R. I. L., Hollender, J., Joss, A., Schärer, M., and Stamm, C.: Reducing the Discharge of Micropollutants in the Aquatic Environment: The Benefits of Upgrading Wastewater Treatment Plants, *Environmental Science and Technology*, 48, 7683–7689, <https://doi.org/10.1021/es500907n>, 2014.
- Estrada-Mondragon, A. and Lynch, J. W.: Functional characterization of ivermectin binding sites in $\alpha 1\beta 2\gamma 2L$ gaba(A) receptors, *Frontiers in Molecular Neuroscience*, 8, 1–13, <https://doi.org/10.3389/fnmol.2015.00055>, 2015.
- European Medicines Agency: European Surveillance of Veterinary Antimicrobial Consumption (ES-VAC) Sales Data and Animal Population Data Collection Protocol (Version 3), 2019.
- Eurostat: Production and consumption of chemicals by hazard class, URL https://ec.europa.eu/eurostat/databrowser/view/env_chmhaz/default/table?lang=en, 2021.
- FDA: USP Therapeutic Categories Model Guidelines, URL <https://www.fda.gov/regulatory-information/fdaaa-implementation-chart/usp-therapeutic-categories-model-guidelines>, 2018.
- Fernández, C., Porcel, M. A., Alonso, A., Andrés, M. S., and Tarazona, J. V.: Semifield assessment of the runoff potential and environmental risk of the parasiticide drug ivermectin under Mediterranean conditions, *Environmental Science and Pollution Research*, 18, 1194–1201, <https://doi.org/10.1007/s11356-011-0474-8>, 2011.
- Fiori, A. and Russo, D.: Travel time distribution in a hillslope: Insight from numerical simulations, *Water Resources Research*, 44, 1–14, <https://doi.org/10.1029/2008WR007135>, 2008.
- Flury, M., Flühler, H., Jury, W. A., and Leuenberger, J.: Susceptibility of soils to preferential flow of water: A field study, *Water Resources Research*, 30, 1945–1954, <https://doi.org/10.1029/94WR00871>, 1994.
- Fovet, O., Ruiz, L., Hrachowitz, M., Faucheux, M., and Gascuel-Odoux, C.: Hydrological hysteresis in catchments and its value for assessing process consistency in conceptual models, *Hydrology and Earth System Sciences Discussions*, 11, 5663–5707, <https://doi.org/10.5194/hessd-11-5663-2014>, 2014.
- Frain de La Gaulayrie, P. S.: Le volcanisme du massif du Coiron (Ardèche), Ph.D. thesis, Université de Paris VI - Pierre et Marie Curie, 1973.

- Freeze, R. A.: Streamflow generation, <https://doi.org/10.1029/RG012i004p00627>, 1974.
- Fu, Z., Hu, W., Beare, M. H., Müller, K., Wallace, D., and Wai Chau, H.: Contributions of soil organic carbon to soil water repellency persistence: Characterization and modelling, *Geoderma*, 401, 115312, <https://doi.org/10.1016/j.geoderma.2021.115312>, 2021.
- Gallart, F., Valiente, M., Llorens, P., Cayuela, C., Sprenger, M., and Latron, J.: Investigating young water fractions in a small Mediterranean mountain catchment: Both precipitation forcing and sampling frequency matter, *Hydrological Processes*, 34, 3618–3634, <https://doi.org/10.1002/hyp.13806>, 2020.
- Garric, J., Vollat, B., Duis, K., Péry, A., Junker, T., Ramil, M., Fink, G., and Ternes, T. A.: Effects of the parasiticide ivermectin on the cladoceran *Daphnia magna* and the green alga *Pseudokirchneriella subcapitata*, *Chemosphere*, 69, 903–910, <https://doi.org/10.1016/j.chemosphere.2007.05.070>, 2007.
- Gat, J. R. and Carmi, I.: Evolution of the isotopic composition of atmospheric waters in the Mediterranean Sea area, *Journal of Geophysical Research*, 75, 3039–3048, <https://doi.org/10.1029/JC075i015p03039>, 1970.
- Gaume, E., Livet, M., Desbordes, M., and Villeneuve, J. P.: Hydrological analysis of the river Aude, France, flash flood on 12 and 13 November 1999, *Journal of Hydrology*, 286, 135–154, <https://doi.org/10.1016/j.jhydrol.2003.09.015>, 2004.
- Geiss, F., Del Bino, G., Blech, G., Norager, O., Orthmann, E., Mosselmans, G., Powell, J., Roy, R., Smyrniotis, T., and Town, W. G.: The EINECS inventory of existing chemical substances on the EC market, *Toxicological and Environmental Chemistry*, 37, 21–33, <https://doi.org/10.1080/02772249209357850>, 1992.
- Geyer, J., Gavrilova, O., and Petzinger, E.: Brain penetration of ivermectin and selamectin in *mdr1a,b* P-glycoprotein- and *bcrp* - deficient knockout mice, *Journal of Veterinary Pharmacology and Therapeutics*, 32, 87–96, <https://doi.org/10.1111/j.1365-2885.2008.01007.x>, 2009.
- Ginn, T. R., Haeri, H., Massoudieh, A., and Foglia, L.: Notes on groundwater age in forward and inverse modeling, *Transport in Porous Media*, 79, 117–134, <https://doi.org/10.1007/s11242-009-9406-1>, 2009.
- Glaser, B., Jackisch, C., Hopp, L., and Klaus, J.: How Meaningful are Plot-Scale Observations and Simulations of Preferential Flow for Catchment Models?, *Vadose Zone Journal*, 18, 1–18, <https://doi.org/10.2136/vzj2018.08.0146>, 2019.
- González Canga, A., Sahagún Prieto, A. M., José Diez Liébana, M., Martínez, N. F., Vega, M. S., and Vieitez, J. J.: The pharmacokinetics and metabolism of ivermectin in domestic animal species, *Veterinary Journal*, 179, 25–37, <https://doi.org/10.1016/j.tvjl.2007.07.011>, 2009.
- Goss, M. J., Ehlers, W., and Unc, A.: The role of lysimeters in the development of our understanding of processes in the vadose zone relevant to contamination of groundwater aquifers, *Physics and Chemistry of the Earth*, 35, 913–926, <https://doi.org/10.1016/j.pce.2010.06.004>, 2010.

- Gothwal, R. and Shashidhar, T.: Antibiotic Pollution in the Environment: A Review, *Clean - Soil, Air, Water*, 43, 479–489, <https://doi.org/10.1002/clen.201300989>, 2015.
- Grabowski, T., Jaroszewski, J. J., and Piotrowski, W.: Correlations between no observed effect level and selected parameters of the chemical structure for veterinary drugs, *Toxicology in Vitro*, 24, 953–959, <https://doi.org/10.1016/j.tiv.2010.01.003>, 2010.
- Grenni, P., Ancona, V., and Barra Caracciolo, A.: Ecological effects of antibiotics on natural ecosystems: A review, *Microchemical Journal*, 136, 25–39, <https://doi.org/10.1016/j.microc.2017.02.006>, 2018.
- Grillot, J.-C.: Contribution à l'étude géologique et hydrogéologique du Massif des Coirons (Partie Occidentale) (Ardèche), Ph.D. thesis, Université des Sciences et Techniques du Languedoc, URL <https://tel.archives-ouvertes.fr/tel-01004598>, 1971.
- Gunnarsson, I. and Arnórsson, S.: Amorphous silica solubility and the thermodynamic properties of H_4SiO_4 in the range of 0 ° to 350 °C at P(sat), *Geochimica et Cosmochimica Acta*, 64, 2295–2307, [https://doi.org/10.1016/S0016-7037\(99\)00426-3](https://doi.org/10.1016/S0016-7037(99)00426-3), 2000.
- Haas, C., Gerke, H. H., Ellerbrock, R. H., Hallett, P. D., and Horn, R.: Relating soil organic matter composition to soil water repellency for soil biopore surfaces different in history from two Bt horizons of a Haplic Luvisol, *Ecohydrology*, 11, 1–11, <https://doi.org/10.1002/eco.1949>, 2018.
- Hachgenei, N.: Study of the distributed hydrologic response of the Claduègne catchment (Ardèche) using dense networks of rain and water level gauges, Tech. rep., Université Grenoble-Alpes, 2018.
- Hachgenei, N., Nord, G., Spadini, L., Mora, H., Courvoisier, F., Sutra, J.-F., Vandervaere, J.-P., Legoût, C., Morel, M.-C., Martins, J., Lespine, A., and Duwig, C.: A device to simulate contaminant transfer and surface and subsurface flow through intact soil monoliths, *Vadose Zone Journal*, 21, <https://doi.org/10.1002/vzj2.20184>, 2022a.
- Hachgenei, N., Vaury, V., Nord, G., Spadini, L., and Duwig, C.: Faster and more precise isotopic water analysis of discrete samples by predicting the repetitions' asymptote instead of averaging last values, *MethodsX*, 9, 101656, <https://doi.org/10.1016/j.mex.2022.101656>, 2022b.
- Halley, B. A., Jacob, T. A., and Lu, A. Y.: The environmental impact of the use of ivermectin: environmental effects and fate, *Chemosphere*, 18, 1543–1563, [https://doi.org/10.1016/0045-6535\(89\)90045-3](https://doi.org/10.1016/0045-6535(89)90045-3), 1989a.
- Halley, B. A., Nessel, R. J., and Lu, A. Y. H.: Environmental Aspects of Ivermectin Usage in Livestock: General Considerations, *Ivermectin and Abamectin*, pp. 162–172, https://doi.org/10.1007/978-1-4612-3626-9_11, 1989b.
- Halley, B. A., VandenHeuvel, W. J., and Wislocki, P. G.: Environmental effects of the usage of avermectins in livestock, *Veterinary Parasitology*, 48, 109–125, [https://doi.org/10.1016/0304-4017\(93\)90149-H](https://doi.org/10.1016/0304-4017(93)90149-H), 1993.

- Hansch, C., Hoekman, D., Leo, A., Zhang, L., and Li, P.: The expanding role of quantitative structure-activity relationships (QSAR) in toxicology, *Toxicology Letters*, 79, 45–53, [https://doi.org/10.1016/0378-4274\(95\)03356-P](https://doi.org/10.1016/0378-4274(95)03356-P), 1995.
- Hardie, M. A., Cotching, W. E., Doyle, R. B., Holz, G., Lisson, S., and Mattern, K.: Effect of antecedent soil moisture on preferential flow in a texture-contrast soil, *Journal of Hydrology*, 398, 191–201, <https://doi.org/10.1016/j.jhydrol.2010.12.008>, 2011.
- Harman, C. J.: Time-variable transit time distributions and transport: Theory and application to storage-dependent transport of chloride in a watershed, *Water Resources Research*, 51, 1–30, <https://doi.org/10.1002/2014WR015707>, 2015.
- Harris, C. R., Millman, K. J., van der Walt, S. J., Gommers, R., Virtanen, P., Cournapeau, D., Wieser, E., Taylor, J., Berg, S., Smith, N. J., Kern, R., Picus, M., Hoyer, S., van Kerkwijk, M. H., Brett, M., Haldane, A., del Río, J. F., Wiebe, M., Peterson, P., Gérard-Marchant, P., Sheppard, K., Reddy, T., Weckesser, W., Abbasi, H., Gohlke, C., and Oliphant, T. E.: Array programming with NumPy, *Nature*, 585, 357–362, <https://doi.org/10.1038/s41586-020-2649-2>, 2020.
- Hartmann, A., Golet, E. M., Gartiser, S., Alder, A. C., Koller, T., and Widmer, R. M.: Primary DNA damage but not mutagenicity correlates with ciprofloxacin concentrations in german hospital wastewaters, *Archives of Environmental Contamination and Toxicology*, 36, 115–119, <https://doi.org/10.1007/s002449900449>, 1999.
- Hayat, R., Ali, S., Amara, U., Khalid, R., and Ahmed, I.: Soil beneficial bacteria and their role in plant growth promotion: A review, *Annals of Microbiology*, 60, 579–598, <https://doi.org/10.1007/s13213-010-0117-1>, 2010.
- Heimfarth, L., Santos, V. S., Araújo, A. A. d. S., Quintans-Júnior, L. J., and Martins-Filho, P. R.: Letter to the editor: Ivermectin: Panacea or true promise for covid-19?, *EXCLI Journal*, 19, 1517–1519, <https://doi.org/10.17179/excli2020-3022>, 2020.
- Hempel, H., Scheffczyk, A., Schallnaß, H. J., Lumaret, J. P., Alvinerie, M., and Römbke, J.: Toxicity of four veterinary parasiticides on larvae of the dung beetle *Aphodius constans* in the laboratory, *Environmental Toxicology and Chemistry*, 25, 3155–3163, <https://doi.org/10.1897/06-022R2.1>, 2006.
- Herd, R. P., Sams, R. A., and Ashcraft, S. M.: Persistence of ivermectin in plasma and faeces following treatment of cows with ivermectin sustained-release, pour-on or injectable formulations, *International Journal for Parasitology*, 26, 1087–1093, [https://doi.org/10.1016/S0020-7519\(96\)80007-5](https://doi.org/10.1016/S0020-7519(96)80007-5), 1996.
- Horton, R. E.: The role of infiltration in the hydrologic cycle, *Eos, Transactions American Geophysical Union*, 14, 446–460, 1933.
- Horvat, A. J., Babić, S., Pavlović, D. M., Ašperger, D., Pelko, S., Kaštelan-Macan, M., Petrović, M., and Mance, A. D.: Analysis, occurrence and fate of anthelmintics and their transformation products in the environment, *TrAC - Trends in Analytical Chemistry*, 31, 61–84, <https://doi.org/10.1016/j.trac.2011.06.023>, 2012.

- Hrachowitz, M. and Clark, M. P.: HESS Opinions: The complementary merits of competing modelling philosophies in hydrology, *Hydrology and Earth System Sciences*, 21, 3953–3973, <https://doi.org/10.5194/hess-21-3953-2017>, 2017.
- Hrachowitz, M., Fovet, O., Ruiz, L., Euser, T., Gharari, S., Nijzink, R., Freer, J., Savenije, H. H., and Gascuel-Oudou, C.: Process consistency in models: The importance of system signatures, expert knowledge, and process complexity, *Water Resources Research*, 50, 7445–7469, <https://doi.org/10.1002/2014WR015484>, 2014.
- Hrachowitz, M., Fovet, O., Ruiz, L., and Savenije, H. H.: Transit time distributions, legacy contamination and variability in biogeochemical $1/f\alpha$ scaling: How are hydrological response dynamics linked to water quality at the catchment scale?, *Hydrological Processes*, 29, 5241–5256, <https://doi.org/10.1002/hyp.10546>, 2015.
- Hrachowitz, M., Benettin, P., van Breukelen, B. M., Fovet, O., Howden, N. J., Ruiz, L., van der Velde, Y., and Wade, A. J.: Transit times—the link between hydrology and water quality at the catchment scale, *Wiley Interdisciplinary Reviews: Water*, 3, 629–657, <https://doi.org/10.1002/wat2.1155>, 2016.
- Huza, J., Teuling, A. J., Braud, I., Grazioli, J., Melsen, L. A., Nord, G., Raupach, T. H., and Uijlenhoet, R.: Precipitation, soil moisture and runoff variability in a small river catchment (Ardèche, France) during HyMeX Special Observation Period 1, *Journal of Hydrology*, 516, 330–342, <https://doi.org/10.1016/j.jhydrol.2014.01.041>, 2014.
- IGN: Registre parcellaire graphique, URL <https://www.data.gouv.fr/fr/datasets/registre-parcellaire-graphique-rpg-contours-des-parcelles-et-ilots-cultureaux-et-leur-groupe-de-cultures-majoritaire/>, 2019.
- IGN: Registre parcellaire graphique 2020, URL <https://geoservices.ign.fr/rpg#telechargement>, 2021.
- Inoue, K. and Higashi, T.: Al- and Fe-humms complexes in Andisols, in: *Proceedings of the 9th International Soil Classification Workshop*, edited by Kinloch, D. I., Shoji, S., Beinroth, F. M., and Eswaran, H., pp. 535–546, Japanese Committee for 9th International Soil Classification Workshop and Soil Management Support Services, Washington, D.C., Japan, 1988.
- INSEE: Recensement 2017, URL <https://www.insee.fr/fr/statistiques/zones/2011101?debut=0>, 2017.
- J. B. Humphry, T. C. Daniel, D. R. Edwards, and A. N. Sharpley: A Portable Rainfall Simulator for Plot–Scale Runoff Studies, *Applied Engineering in Agriculture*, 18, 199–204, <https://doi.org/10.13031/2013.7789>, 2002.
- Jackson, H. C.: Ivermectin as a Systemic Insecticide, *Parasitology Today*, 5, 146–156, 1989.
- Jansen, B., Nierop, K. G., and Verstraten, J. M.: Mobilization of dissolved organic matter, aluminium and iron in podzol eluvial horizons as affected by formation of metal-organic complexes and interactions with solid soil material, *European Journal of Soil Science*, 55, 287–297, <https://doi.org/10.1111/j.1365-2389.2004.00598.x>, 2004.

- Jaynes, D. B., Ahmed, S. I., Kung, K.-J. S., and Kanwar, R. S.: Temporal Dynamics of Preferential Flow to a Subsurface Drain, *Soil Science Society of America Journal*, 65, 1368–1376, <https://doi.org/10.2136/sssaj2001.6551368x>, 2001.
- Jochmann, R. and Blanckenhorn, W. U.: Non-target effects of ivermectin on trophic groups of the cow dung insect community replicated across an agricultural landscape, *Basic and Applied Ecology*, 17, 291–299, <https://doi.org/10.1016/j.baae.2016.01.001>, 2016.
- Josse, J.: Identification et cartographie des sources potentielles de pollutions diffuses en milieu agricole : utilisation combinée d'enquêtes de terrain et de série temporelle d'images Sentinel-2, Tech. rep., Cermosem, laboratoire Pacte UMR 5194 CNRS-Université Grenoble Alpes, 2021.
- Jurin, J.: II. An account of some experiments shown before the Royal Society; with an enquiry into the cause of the ascent and suspension of water in capillary tubes., *Philosophical Transactions of the Royal Society of London*, 30, 739–747, 1718.
- Kaushik, C. P., Sharma, H. R., Jain, S., Dawra, J., and Kaushik, A.: Pesticide residues in river Yamuna and its canals in Haryana and Delhi, India, *Environmental Monitoring and Assessment*, 144, 329–340, <https://doi.org/10.1007/s10661-007-9996-4>, 2008.
- Kay, P., Blackwell, P. A., and Boxall, A. B.: Column studies to investigate the fate of veterinary antibiotics in clay soils following slurry application to agricultural land, *Chemosphere*, 60, 497–507, <https://doi.org/10.1016/j.chemosphere.2005.01.028>, 2005a.
- Kay, P., Blackwell, P. A., and Boxall, A. B.: A lysimeter experiment to investigate the leaching of veterinary antibiotics through a clay soil and comparison with field data, *Environmental Pollution*, 134, 333–341, <https://doi.org/10.1016/j.envpol.2004.07.021>, 2005b.
- Kilmartin, J., Cazabon, D., and Smith, P.: Investigations of the toxicity of ivermectin for salmonids, *Bulletin of the European Association of Fish Pathologists (United Kingdom)*, 17, 58–61, 1996.
- Kim, S., Chu, K. H., Al-Hamadani, Y. A., Park, C. M., Jang, M., Kim, D. H., Yu, M., Heo, J., and Yoon, Y.: Removal of contaminants of emerging concern by membranes in water and wastewater: A review, *Chemical Engineering Journal*, 335, 896–914, <https://doi.org/10.1016/j.cej.2017.11.044>, 2018.
- King, P. M.: Comparison of methods for measuring severity of water repellence of sandy soils and assessment of some factors that affect its measurement, *Australian Journal of Soil Research*, 19, 275–285, <https://doi.org/10.1071/SR9810275>, 1981.
- Kirchner, J. W.: Getting the right answers for the right reasons: Linking measurements, analyses, and models to advance the science of hydrology, *Water Resources Research*, 42, 1–5, <https://doi.org/10.1029/2005WR004362>, 2006.
- Kirchner, J. W.: Aggregation in environmental systems-Part 1: Seasonal tracer cycles quantify young water fractions, but not mean transit times, in spatially heterogeneous catchments, *Hydrology and Earth System Sciences*, 20, 279–297, <https://doi.org/10.5194/hess-20-279-2016>, 2016.

- Kirchner, J. W.: Quantifying new water fractions and transit time distributions using ensemble hydrograph separation: Theory and benchmark tests, *Hydrology and Earth System Sciences*, 23, 303–349, <https://doi.org/10.5194/hess-23-303-2019>, 2019.
- Kirchner, J. W., Feng, X., and Neal, C.: Fractal chemistry and its implications for contaminant transport in catchments, *Nature*, 403, 524–527, <https://doi.org/10.1038/35000537>, 2000.
- Kirchner, J. W., Feng, X., and Neal, C.: Catchment-scale advection and dispersion as a mechanism for fractal scaling in stream tracer concentrations, *Journal of Hydrology*, 254, 82–101, [https://doi.org/10.1016/S0022-1694\(01\)00487-5](https://doi.org/10.1016/S0022-1694(01)00487-5), 2001.
- Klein, E. Y., Van Boeckel, T. P., Martinez, E. M., Pant, S., Gandra, S., Levin, S. A., Goossens, H., and Laxminarayan, R.: Global increase and geographic convergence in antibiotic consumption between 2000 and 2015, *Proceedings of the National Academy of Sciences of the United States of America*, 115, E3463–E3470, <https://doi.org/10.1073/pnas.1717295115>, 2018.
- Kollet, S. J. and Maxwell, R. M.: Demonstrating fractal scaling of baseflow residence time distributions using a fully-coupled groundwater and land surface model, *Geophysical Research Letters*, 35, 1–6, <https://doi.org/10.1029/2008GL033215>, 2008.
- Konstantinou, I. K., Hela, D. G., and Albanis, T. A.: The status of pesticide pollution in surface waters (rivers and lakes) of Greece. Part I. Review on occurrence and levels, *Environmental Pollution*, 141, 555–570, <https://doi.org/10.1016/j.envpol.2005.07.024>, 2006.
- Krause, P., Boyle, D. P., and Bäse, F.: Comparison of different efficiency criteria for hydrological model assessment, *Advances in Geosciences*, 5, 89–97, <https://doi.org/10.5194/adgeo-5-89-2005>, 2005.
- Krogh, K., Søbørg, T., Brodin, B., and Halling-Sørensen, B.: Sorption and Mobility of Ivermectin in Different Soils, *Journal of Environment Quality*, 37, 2202, <https://doi.org/10.2134/jeq2007.0592>, 2008a.
- Krogh, K. A., Björklund, E., Loeffler, D., Fink, G., Halling-Sørensen, B., and Ternes, T. A.: Development of an analytical method to determine avermectins in water, sediments and soils using liquid chromatography-tandem mass spectrometry, *Journal of Chromatography A*, 1211, 60–69, <https://doi.org/10.1016/j.chroma.2008.09.081>, 2008b.
- Krogh, K. A., Jensen, G. G., Schneider, M. K., Fenner, K., and Halling-Sørensen, B.: Analysis of the dissipation kinetics of ivermectin at different temperatures and in four different soils, *Chemosphere*, 75, 1097–1104, <https://doi.org/10.1016/j.chemosphere.2009.01.015>, 2009.
- Kumar, K., C. Gupta, S., Chander, Y., and Singh, A. K.: Antibiotic Use in Agriculture and Its Impact on the Terrestrial Environment, *Advances in Agronomy*, 87, 1–54, [https://doi.org/10.1016/S0065-2113\(05\)87001-4](https://doi.org/10.1016/S0065-2113(05)87001-4), 2005.
- Kummerer, K.: Significance of antibiotics in the environment, *Journal of Antimicrobial Chemotherapy*, 52, 5–7, <https://doi.org/10.1093/jac/dkg293>, 2003.

- Kümmerer, K., ed.: *Pharmaceuticals in the Environment - Sources, Fate, Effects and Risks*, Springer, 3 edn., https://doi.org/10.1007/978-3-662-04634-0_1, 2008.
- Kung, K.-J. S., Steenhuis, T. S., Klavivko, E. J., Gish, T. J., Bubbenzer, G., and Helling, C. S.: Impact of Preferential Flow on the Transport of Adsorbing and Non-Adsorbing Tracers, *Soil Science Society of America Journal*, 64, 1290–1296, <https://doi.org/10.2136/sssaj2000.6441290x>, 2000.
- Ladouche, B., Luc, A., and Nathalie, D.: Chemical and isotopic investigation of rainwater in Southern France (1996-2002): Potential use as input signal for karst functioning investigation, *Journal of Hydrology*, 367, 150–164, <https://doi.org/10.1016/j.jhydrol.2009.01.012>, 2009.
- Laffont, C. M., Alvinerie, M., Bousquet-Mélou, A., and Toutain, P. L.: Licking behaviour and environmental contamination arising from pour-on ivermectin for cattle, *International Journal for Parasitology*, 31, 1687–1692, [https://doi.org/10.1016/S0020-7519\(01\)00285-5](https://doi.org/10.1016/S0020-7519(01)00285-5), 2001.
- Laffont, C. M., Bousquet-Mélou, A., Bralet, D., Alvinerie, M., Fink-Gremmels, J., and Toutain, P.-L.: A pharmacokinetic model to document the actual disposition of topical ivermectin in cattle, *Veterinary Research*, 34, 445–460, <https://doi.org/10.1051/vetres:2003014>, 2003.
- Lange, I. G., Daxenberger, A., Schiffer, B., Witters, H., Ibarreta, D., and Meyer, H. H.: Sex hormones originating from different livestock production systems: Fate and potential disrupting activity in the environment, *Analytica Chimica Acta*, 473, 27–37, [https://doi.org/10.1016/S0003-2670\(02\)00748-1](https://doi.org/10.1016/S0003-2670(02)00748-1), 2002.
- Latron, J., Llorens, P., and Gallart, F.: The hydrology of Mediterranean mountain areas, *Geography Compass*, 3, 2045–2064, <https://doi.org/10.1111/j.1749-8198.2009.00287.x>, 2009.
- Lecompte, V., Brelot, E., and Patois, L.: Effluents hospitaliers et stations d'épuration urbaines : caractérisation, risques et traitabilité, Tech. rep., GRAIE - Groupe de Recherche Rhône-Alpes sur les Infrastructures et l'Eau, URL <http://www.graie.org/Sipibel/publications/sipibel-synthese-effluentshospitaliersmedicaments-oct16.pdf>, 2016.
- Leelamanie, D. A., Karube, J., and Yoshida, A.: Characterizing water repellency indices: Contact angle and water drop penetration time of hydrophobized sand, *Soil Science and Plant Nutrition*, 54, 179–187, <https://doi.org/10.1111/j.1747-0765.2007.00232.x>, 2008.
- Lemnitz, C., Kuhnert, M., Bens, O., Güntner, A., Merz, B., and Hüttl, R. F.: Spatial and temporal variations of actual soil water repellency and their influence on surface runoff, *Hydrological Processes*, 22, 1976–1984, <https://doi.org/10.1002/hyp.6782>, 2008.
- Li, S. W. and Lin, A. Y. C.: Increased acute toxicity to fish caused by pharmaceuticals in hospital effluents in a pharmaceutical mixture and after solar irradiation, *Chemosphere*, 139, 190–196, <https://doi.org/10.1016/j.chemosphere.2015.06.010>, 2015.
- Liaw, R., Liang, E., Nishihara, R., Moritz, P., Gonzalez, J. E., and Stoica, I.: Tune: A Research Platform for Distributed Model Selection and Training, arXiv preprint arXiv:1807.05118, URL <http://arxiv.org/abs/1807.05118>, 2018.

- Liebig, M., Fernandez, Á. A., Blübaum-Gronau, E., Boxall, A., Brinke, M., Carbonell, G., Egeler, H., Fenner, K., Fernandez, C., Fink, G., Garric, J., Halling-Sørensen, B., Knacker, T., Krogh, K. A., Küster, A., Dirk Löffler, Cots, M. Á. P., Pope, L., Prasse, C., Römbke, J., Rönnefahrt, I., Schneider, M. K., Schweitzer, N., Tarazona, J. V., Ternes, T. A., Traunspurger, W., Wehrhan, A., and Duisy, K.: Environmental risk assessment of ivermectin: A case study, *Integrated Environmental Assessment and Management*, 6, 567–587, <https://doi.org/10.1002/ieam.96>, 2010.
- Lifschitz, A., Virkel, G., Sallovitz, J., Sutra, J. F., Galtier, P., Alvinerie, M., and Lanusse, C.: Comparative distribution of ivermectin and doramectin to parasite location tissues in cattle, *Veterinary Parasitology*, 87, 327–338, [https://doi.org/10.1016/S0304-4017\(99\)00175-2](https://doi.org/10.1016/S0304-4017(99)00175-2), 2000.
- Lumaret, J. P., Alvinerie, M., Hempel, H., Schallnaß, H. J., Claret, D., and Römbke, J.: New screening test to predict the potential impact of ivermectin- contaminated cattle dung on dung beetles, *Veterinary Research*, 38, 15–24, <https://doi.org/10.1051/vetres:2006041>, 2007.
- Lustigman, S. and McCarter, J. P.: Ivermectin resistance in *Onchocerca volvulus*: Toward a genetic basis, *PLoS Neglected Tropical Diseases*, 1, 1–3, <https://doi.org/10.1371/journal.pntd.0000076>, 2007.
- Majoube, M.: Fractionnement en oxygène 18 et en deutérium entre l'eau et sa vapeur, *Journal de Chimie Physique*, 68, 1423–1436, <https://doi.org/10.1051/jcp/1971681423>, 1971.
- Małozzewski, P. and Zuber, A.: Determining the turnover time of groundwater systems with the aid of environmental tracers. 1. Models and their applicability, *Journal of Hydrology*, 57, 207–231, [https://doi.org/10.1016/0022-1694\(82\)90147-0](https://doi.org/10.1016/0022-1694(82)90147-0), 1982.
- Mandaric, L., Kalogianni, E., Skoulikidis, N., Petrovic, M., and Sabater, S.: Contamination patterns and attenuation of pharmaceuticals in a temporary Mediterranean river, *Science of the Total Environment*, 647, 561–569, <https://doi.org/10.1016/j.scitotenv.2018.07.308>, 2019.
- Maron, D. F., Smith, T. J., and Nachman, K. E.: Restrictions on antimicrobial use in food animal production: An international regulatory and economic survey, *Globalization and Health*, 9, <https://doi.org/10.1186/1744-8603-9-48>, 2013.
- Marschner, P. and Rengel, Z.: *Nutrient Cycling in Terrestrial Ecosystems*, vol. 23, Springer Berlin, Heidelberg, 2007.
- Martins, J., Nord, G., Morel, C., Spadini, L., Hachgenei, N., Mao, P., Robinet, N., Margoum, C., Daval, A., Mathon, B., and Liger, L.: Origine et devenir des contaminants PHARMaceutiques dans les Bassins Versants agricoles. Le cas de la Claduègne (Ardèche)., Tech. rep., Institut des Géosciences de l'environnement, 2019.
- Maxwell, R. M.: A terrain-following grid transform and preconditioner for parallel, large-scale, integrated hydrologic modeling, *Advances in Water Resources*, 53, 109–117, <https://doi.org/10.1016/j.advwatres.2012.10.001>, URL <http://dx.doi.org/10.1016/j.advwatres.2012.10.001>, 2013.
- Maxwell, R. M., Condon, L. E., Kollet, S. J., Maher, K., Haggerty, R., and Forrester, M. M.: The imprint of climate and geology on the residence times of groundwater, *Geophysical Research Letters*, 43,

- 701–708, <https://doi.org/10.1002/2015GL066916>, URL <https://onlinelibrary.wiley.com/doi/10.1002/2015GL066916>, 2016.
- McGuire, K. J. and McDonnell, J. J.: A review and evaluation of catchment transit time modeling, *Journal of Hydrology*, 330, 543–563, <https://doi.org/10.1016/j.jhydrol.2006.04.020>, 2006.
- McKinney, W.: Data Structures for Statistical Computing in Python, in: *Proceedings of the 9th Python in Science Conference*, edited by van der Walt, S. and Millman, J., pp. 56–61, <https://doi.org/10.25080/Majora-92bf1922-00a>, 2010.
- Merlivat, L. and Jouzel, J.: Global climatic interpretation of the deuterium-oxygen 18 relationship for precipitation, *Journal of Geophysical Research*, 84, 5029, <https://doi.org/10.1029/JC084iC08p05029>, 1979.
- Mesa, L., Gutiérrez, M. F., Montalto, L., Perez, V., and Lifschitz, A.: Concentration and environmental fate of ivermectin in floodplain wetlands: An ecosystem approach, *Science of the Total Environment*, 706, 135 692, <https://doi.org/10.1016/j.scitotenv.2019.135692>, URL <https://doi.org/10.1016/j.scitotenv.2019.135692>, 2020.
- Mesa, L. M., Lindt, I., Negro, L., Gutierrez, M. F., Mayora, G., Montalto, L., Ballent, M., and Lifschitz, A.: Aquatic toxicity of ivermectin in cattle dung assessed using microcosms, *Ecotoxicology and Environmental Safety*, 144, 422–429, <https://doi.org/10.1016/j.ecoenv.2017.06.016>, URL <http://dx.doi.org/10.1016/j.ecoenv.2017.06.016>, 2017.
- Mestres, R. and Mestres, G.: Deltamethrin: Uses and Environmental Safety, *Journal of Environmental Contamination and Toxicology*, 124, 1–18, https://doi.org/10.1007/978-1-4612-2864-6_1, 1992.
- Ministere de la sante et de la protection sociale: Avis relatif à la suppression d'une autorisation de mise sur le marché de médicament vétérinaire., *Journal officiel "Lois et Décrets" - JORF*, 97, 7531, 2004.
- Molinié, G., Ceresetti, D., Anquetin, S., Creutin, J. D., and Boudevillain, B.: Rainfall regime of a mountainous mediterranean region: Statistical analysis at short time steps, *Journal of Applied Meteorology and Climatology*, 51, 429–448, <https://doi.org/10.1175/2011JAMC2691.1>, 2012.
- Montoya-Rodríguez, D. M., Ávila-Torres, Y., Serna-Galvis, E. A., and Torres-Palma, R. A.: Data on treatment of nafcillin and ampicillin antibiotics in water by sonochemistry, *Data in Brief*, 29, <https://doi.org/10.1016/j.dib.2020.105361>, 2020.
- Moreau-Guigon, E., Tamtam, F., Dinh, T. Q., Eurin, J., Labadie, P., Alliot, F., Chevreuil, M., Lavisson, G., Candido, P., Augustin, V., and Tournebize, J.: Sources et devenir des médicaments dans le bassin versant de la Seine, *Tech. rep.*, CNRS, URL http://www.sisyphe.upmc.fr/piren/?q=webfm_send/988, 2011.
- Moriasi, D. N., Gitau, M. W., Pai, N., and Daggupati, P.: Hydrologic and water quality models: Performance measures and evaluation criteria, *Transactions of the ASABE*, 58, 1763–1785, <https://doi.org/10.13031/trans.58.10715>, 2015.

- Morse, J. W.: Chapter 7. The KINETICS of CALCIUM CARBONATE DISSOLUTION and PRECIPITATION, in: Carbonates, July, pp. 227–264, De Gruyter, <https://doi.org/10.1515/9781501508134-011>, 1983.
- Mottier, M. L., Alvarez, L. I., Pis, M. A., and Lanusse, C. E.: Transtegumental diffusion of benzimidazole anthelmintics into *Moniezia benedeni*: Correlation with their octanol-water partition coefficients, *Experimental Parasitology*, 103, 1–7, [https://doi.org/10.1016/S0014-4894\(03\)00060-2](https://doi.org/10.1016/S0014-4894(03)00060-2), 2003.
- Mullins, C. E.: Magnetic Susceptibility of the Soil and Its Significance in Soil Science – a Review, *Journal of Soil Science*, 28, 223–246, <https://doi.org/10.1111/j.1365-2389.1977.tb02232.x>, 1977.
- Naidoo, V., Wolter, K., Cuthbert, R., and Duncan, N.: Veterinary diclofenac threatens Africa's endangered vulture species, *Regulatory Toxicology and Pharmacology*, 53, 205–208, <https://doi.org/10.1016/j.yrtph.2009.01.010>, 2009.
- Nash, J. E. and Sutcliffe, J. V.: River Flow Forecasting Through Conceptual Models Part I-a Discussion of Principles, *Journal of Hydrology*, 10, 282–290, [https://doi.org/10.1016/0022-1694\(70\)90255-6](https://doi.org/10.1016/0022-1694(70)90255-6), 1970.
- Nash, J. P., Kime, D. E., Van der Ven, L. T., Wester, P. W., Brion, F., Maack, G., Stahlschmidt-Allner, P., and Tyler, C. R.: Long-term exposure to environmental concentrations of the pharmaceutical ethynylestradiol causes reproductive failure in fish, *Environmental Health Perspectives*, 112, 1725–1733, <https://doi.org/10.1289/ehp.7209>, 2004.
- Niemi, A. J.: Residence time distributions of variable flow processes, *The International Journal of Applied Radiation and Isotopes*, 28, 855–860, [https://doi.org/10.1016/0020-708X\(77\)90026-6](https://doi.org/10.1016/0020-708X(77)90026-6), 1977.
- Nobel Media AB: The Nobel Prize in Physiology or Medicine 2015, URL <https://www.nobelprize.org/prizes/medicine/2015/summary/>, 2015.
- Nord, G., Boudevillain, B., Berne, A., Branger, F., Braud, I., Dramais, G., Gérard, S., Le Coz, J., Legouët, C., Molinié, G., Van Baelen, J., Vandervaere, J. P., Andrieu, J., Aubert, C., Calianno, M., Delrieu, G., Grazioli, J., Hachani, S., Horner, I., Huza, J., Le Boursicaud, R., Raupach, T. H., Teuling, A. J., Uber, M., Vincendon, B., and Wijbrans, A.: A high space-time resolution dataset linking meteorological forcing and hydro-sedimentary response in a mesoscale Mediterranean catchment (Auzon) of the Ardèche region, France, *Earth System Science Data*, 9, 221–249, <https://doi.org/10.5194/essd-9-221-2017>, 2017.
- Nuissier, O., Ducrocq, V., Ricard, D., Lebeaupin, C., and Anquetin, S.: A numerical study of three catastrophic precipitating events over southern France. I: Numerical framework and synoptic ingredients, *Quarterly Journal of the Royal Meteorological Society*, 134, 111–130, <https://doi.org/10.1002/qj.200>, 2008.
- Oaks, J. L., Gilbert, M., Virani, M. Z., Watson, R. T., Meteyer, C. U., Rideout, B. A., Shivaprasad, H. L., Ahmed, S., Chaudhry, M. J. I., Arshad, M., Mahmood, S., Ali, A., and Khan, A. A.: Diclofenac residues as the cause of vulture population decline in Pakistan, *Nature*, 427, 630–633, <https://doi.org/10.1038/nature02317>, 2004.

- Obimakinde, S., Fatoki, O., Opeolu, B., and Olatunji, O.: Veterinary pharmaceuticals in aqueous systems and associated effects: an update, *Environmental Science and Pollution Research*, 24, 3274–3297, <https://doi.org/10.1007/s11356-016-7757-z>, 2017.
- Ojogboro, J. O., Scrimshaw, M. D., and Sumpter, J. P.: Steroid hormones in the aquatic environment, *Science of the Total Environment*, 792, 148 306, <https://doi.org/10.1016/j.scitotenv.2021.148306>, URL <https://doi.org/10.1016/j.scitotenv.2021.148306>, 2021.
- Õmura, S. and Crump, A.: The life and times of ivermectin - A success story, *Nature Reviews Microbiology*, 2, 984–989, <https://doi.org/10.1038/nrmicro1048>, 2004.
- Osorio, V., Proia, L., Ricart, M., Pérez, S., Ginebreda, A., Cortina, J. L., Sabater, S., and Barceló, D.: Hydrological variation modulates pharmaceutical levels and biofilm responses in a Mediterranean river, *Science of the Total Environment*, 472, 1052–1061, <https://doi.org/10.1016/j.scitotenv.2013.11.069>, 2014.
- Palma, P., Fialho, S., Lima, A., Novais, M. H., Costa, M. J., Montemurro, N., Pérez, S., and de Alda, M. L.: Pharmaceuticals in a Mediterranean Basin: The influence of temporal and hydrological patterns in environmental risk assessment, *Science of the Total Environment*, 709, <https://doi.org/10.1016/j.scitotenv.2019.136205>, 2020.
- Payne, B.: On the statistical treatment of environmental isotope data in hydrology, in: *Isotope techniques in water resources development 1991*, pp. 273–290, International Atomic Energy Agency, Vienna, 1992.
- Popova, I. E., Bair, D. A., Tate, K. W., and Parikh, S. J.: Sorption, Leaching, and Surface Runoff of Beef Cattle Veterinary Pharmaceuticals under Simulated Irrigated Pasture Conditions, *Journal of Environmental Quality*, 42, 1167–1175, <https://doi.org/10.2134/jeq2013.01.0012>, 2013.
- Popp, M., Stegemann, M., Metzendorf, M. I., Gould, S., Kranke, P., Meybohm, P., Skoetz, N., and Weibel, S.: Ivermectin for preventing and treating COVID-19, *The Cochrane database of systematic reviews*, 7, CD015 017, <https://doi.org/10.1002/14651858.CD015017.pub2>, 2021.
- Prakash, V., Pain, D. J., Cunningham, A. A., Donald, P. F., Prakash, N., Verma, A., Gargi, R., Sivakumar, S., and Rahmani, A. R.: Catastrophic collapse of indian white-backed Gyps bengalensis and long-billed Gyps indicus vulture populations, *Biological Conservation*, 109, 381–390, [https://doi.org/10.1016/S0006-3207\(02\)00164-7](https://doi.org/10.1016/S0006-3207(02)00164-7), 2003.
- Pugajeva, I., Ikkere, L. E., Judjallo, E., and Bartkevics, V.: Determination of residues and metabolites of more than 140 pharmacologically active substances in meat by liquid chromatography coupled to high resolution Orbitrap mass spectrometry, *Journal of Pharmaceutical and Biomedical Analysis*, 166, 252–263, <https://doi.org/10.1016/j.jpba.2019.01.024>, 2019.
- Purdom, C. E., Hardiman, P. A., Bye, V. J., Eno, N. C., Tyler, C. R., and Sumpter, J. P.: Estrogenic Effects of Effluents from Sewage Treatment Works, *Chemistry and Ecology*, 8, 275–285, <https://doi.org/10.1080/02757549408038554>, 1994.

- Rabiet, M., Margoum, C., Gouy, V., Carluer, N., and Coquery, M.: Assessing pesticide concentrations and fluxes in the stream of a small vineyard catchment - Effect of sampling frequency, *Environmental Pollution*, 158, 737–748, <https://doi.org/10.1016/j.envpol.2009.10.014>, 2010.
- Raich-Montiu, J., Krogh, K., Granados, M., Jönsson, J., and Halling-Sørensen, B.: Determination of ivermectin and transformation products in environmental waters using hollow fibre-supported liquid membrane extraction and liquid chromatography–mass spectrometry/mass spectrometry, *Journal of Chromatography A*, 1187, 275–280, <https://doi.org/10.1016/j.chroma.2008.02.063>, 2008.
- Rath, S., Pereira, L. A., Bosco, S. M. D., Maniero, M. G., Fostier, A. H., and Guimarães, J. R.: Fate of ivermectin in the terrestrial and aquatic environment: mobility, degradation, and toxicity towards *Daphnia similis*, *Environmental Science and Pollution Research*, 23, 5654–5666, <https://doi.org/10.1007/s11356-015-5787-6>, 2016.
- Remondi, F., Kirchner, J. W., Burlando, P., and Fatichi, S.: Water Flux Tracking With a Distributed Hydrological Model to Quantify Controls on the Spatiotemporal Variability of Transit Time Distributions, *Water Resources Research*, 54, 3081–3099, <https://doi.org/10.1002/2017WR021689>, 2018.
- Reuter, J. H. and Perdue, E. M.: Importance of heavy metal-organic matter interactions in natural waters, *Geochimica et Cosmochimica Acta*, 41, 325–334, [https://doi.org/10.1016/0016-7037\(77\)90240-X](https://doi.org/10.1016/0016-7037(77)90240-X), 1977.
- Reynolds, W. D. and Elrick, D. E.: Determination of Hydraulic Conductivity Using a Tension Infiltrometer, *Soil Science Society of America Journal*, 55, 633–639, <https://doi.org/10.2136/sssaj1991.03615995005500030001x>, 1991.
- Richard, C.: Analyse risques / bénéfiques de l'utilisation des antiparasitaires en élevage en Région Wallonne, Tech. rep., Région Wallonne, 2011.
- Riedo, J., Wettstein, F. E., Rosch, A., Herzog, C., Banerjee, S., Buchi, L., Charles, R., Wachter, D., Martin-Laurent, F., Bucheli, T. D., Walder, F., and Van Der Heijden, M. G.: Widespread occurrence of pesticides in organically managed agricultural soils-The ghost of a conventional agricultural past?, *Environmental Science and Technology*, 55, 2919–2928, <https://doi.org/10.1021/acs.est.0c06405>, 2021.
- Rijal, J. B.: Method development and validation for the analysis of avermectins in water, soil and dung matrix using HPLC-FLD for the application to study the dissipation of organic micropollutants in the environment, Tech. rep., Université Claude Bernard Lyon 1, 2020.
- Rijal, J. B., Voiron, C., and Morel, M.-C.: Improvement and adaptation for routine environmental analysis of the method for the determination of Avermectin family compounds using high performance liquid chromatography and fluorescence detection: application to environmental samples, in: 14ème Congrès Francophone sur les Sciences Séparatives et les Couplages de l'AFSEP, 2021.
- Rinaldo, A., Benettin, P., Harman, C. J., Hrachowitz, M., McGuire, K. J., van der Velde, Y., Bertuzzo, E., and Botter, G.: Storage selection functions: A coherent framework for quantifying how catchments store and release water and solutes, *Water Resources Research*, 51, 4840–4847, <https://doi.org/10.1002/2015WR017273>, 2015.

- Robbez-masson, J., Barthes, J. P., and Bornand, M.: Bases de données pédologiques et systèmes d'informations géographiques. L'exemple de la région Languedoc Roussillon, forêt méditerranéenne, XXI, 2000.
- Roca, I., Akova, M., Baquero, F., Carlet, J., Cavaleri, M., Coenen, S., Cohen, J., Findlay, D., Gyssens, I., Heur, O. E., Kahlmeter, G., Kruse, H., Laxminarayan, R., Liébana, E., López-Cerero, L., MacGowan, A., Martins, M., Rodríguez-Baño, J., Rolain, J.-M., Segovia, C., Sigauque, B., Tacconelli, E., Wellington, E., and Vila, J.: The global threat of antimicrobial resistance: science for intervention I., *European Society of Clinical Microbiology and Infectious Diseases*, 6, 22–29, <https://doi.org/10.1016/j.nmni.2015.02.007>, 2015.
- Rodhe, A., Nyberg, L., and Bishop, K.: Transit Times for Water in a Small Till Catchment from a Step Shift in the Oxygen 18 Content of the Water Input, *Water Resources Research*, 32, 3497–3511, <https://doi.org/10.1029/95WR01806>, 1996.
- Römbke, J., Coors, A., Fernández, Á. A., Förster, B., Fernández, C., Jensen, J., Lumaret, J. P., Cots, M. Á. P., and Liebig, M.: Effects of the parasiticide ivermectin on the structure and function of dung and soil invertebrate communities in the field (Madrid, Spain), *Applied Soil Ecology*, 45, 284–292, <https://doi.org/10.1016/j.apsoil.2010.05.004>, 2010.
- Römbke, J., Duis, K., Egeler, P., Gilberg, D., Schuh, C., Herrchen, M., Hennecke, D., Hölzle, L. E., Hellemann-Thudium, B., Wohde, M., Wagner, J., and Düring, R.-A.: Comparison of the environmental properties of parasiticides and harmonisation of the basis for environmental assessment at the EU level, Tech. Rep. Project number: 3714644100, German Environment Agency, 2018.
- Roose-Amsaleg, C. and Laverman, A. M.: Do antibiotics have environmental side-effects? Impact of synthetic antibiotics on biogeochemical processes, *Environmental Science and Pollution Research*, 23, 4000–4012, <https://doi.org/10.1007/s11356-015-4943-3>, 2016.
- Roy, J. L. and McGill, W. B.: Assessing soil water repellency using the molarity of ethanol droplet (MED) test, *Soil Science*, 167, 83–97, <https://doi.org/10.1097/00010694-200202000-00001>, 2002.
- Rozanski, K., Araguás-Araguás, L., and Gonfiantini, R.: Isotopic Patterns in Modern Global Precipitation, *Geophysical Monograph-American Geophysical Union*, 78, 1–36, 1993.
- Samaniego, L., Kumar, R., and Attinger, S.: Multiscale parameter regionalization of a grid-based hydrologic model at the mesoscale, *Water Resources Research*, 46, 1–25, <https://doi.org/10.1029/2008WR007327>, 2010.
- Sanderson, H., Laird, B., Pope, L., Brain, R., Wilson, C., Johnson, D., Bryning, G., Peregrine, A. S., Boxall, A., and Solomon, K.: Assessment of the environmental fate and effects of ivermectin in aquatic mesocosms, *Aquatic Toxicology*, 85, 229–240, <https://doi.org/10.1016/j.aquatox.2007.08.011>, 2007.
- Sauvé, S. and Desrosiers, M.: A review of what is an emerging contaminant, *Chemistry Central Journal*, 8, 1–7, <https://doi.org/10.1186/1752-153X-8-15>, 2014.

- Schindelin, J., Arganda-Carreras, I., Frise, E., Kaynig, V., Longair, M., Pietzsch, T., Preibisch, S., Rueden, C., Saalfeld, S., Schmid, B., Tinevez, J. Y., White, D. J., Hartenstein, V., Eliceiri, K., Tomancak, P., and Cardona, A.: Fiji: An open-source platform for biological-image analysis, *Nature Methods*, 9, 676–682, <https://doi.org/10.1038/nmeth.2019>, 2012.
- Shaner, D. L. and Henry, W. B.: Field History and Dissipation of Atrazine and Metolachlor in Colorado, *Journal of Environmental Quality*, 36, 128–134, <https://doi.org/10.2134/jeq2006.0160>, 2007.
- Sherman, L. K.: Streamflow from rainfall by the unit-graph method, *Eng. News Record*, 108, 501–505, 1932.
- Šimůnek, J., Genuchten, M. T., and Šejna, M.: Development and Applications of the HYDRUS and STANMOD Software Packages and Related Codes, *Vadose Zone Journal*, 7, 587–600, <https://doi.org/10.2136/vzj2007.0077>, 2008.
- Sodemann, H.: Stable Isotopes of Water, Ph.D. thesis, Swiss Federal Institute of Technology, Zürich, <https://doi.org/https://doi.org/10.3929/ethz-a-005215132>, 2006.
- Sommer, C., Steffansen, B., Nielsen, B. O., Grønvold, J., Vagn Jensen, K. M., Brøchner Jespersen, J., Springborg, J., and Nansen, P.: Ivermectin excreted in cattle dung after subcutaneous injection or pour-on treatment: Concentrations and impact on dung fauna, *Bulletin of Entomological Research*, 82, 257–264, <https://doi.org/10.1017/S0007485300051804>, 1992.
- Soulsby, C., Rodgers, P., Smart, R., Dawson, J., and Dunn, S.: A tracer-based assessment of hydrological pathways at different spatial scales in a mesoscale Scottish catchment, *Hydrological Processes*, 17, 759–777, <https://doi.org/10.1002/hyp.1163>, 2003.
- Spellberg, B., Guidos, R., Gilbert, D., Bradley, J., Boucher, H. W., Scheld, W. M., Bartlett, J. G., and Edwards, J.: The Epidemic of Antibiotic-Resistant Infections: A Call to Action for the Medical Community from the Infectious Diseases Society of America, *Clinical Infectious Diseases*, 46, 155–164, <https://doi.org/10.1086/524891>, 2008.
- Sprenger, M., Tetzlaff, D., Buttle, J., Carey, S. K., McNamara, J. P., Laudon, H., Shatilla, N. J., and Soulsby, C.: Storage, mixing, and fluxes of water in the critical zone across northern environments inferred by stable isotopes of soil water, *Hydrological Processes*, 32, 1720–1737, <https://doi.org/10.1002/hyp.13135>, 2018.
- Sprenger, M., Stumpp, C., Weiler, M., Aeschbach, W., Allen, S. T., Benettin, P., Dubbert, M., Hartmann, A., Hrachowitz, M., Kirchner, J. W., McDonnell, J. J., Orlowski, N., Penna, D., Pfahl, S., Rinderer, M., Rodriguez, N., Schmidt, M., and Werner, C.: The Demographics of Water: A Review of Water Ages in the Critical Zone, *Reviews of Geophysics*, pp. 800–834, <https://doi.org/10.1029/2018rg000633>, 2019.
- Spycher, S., Mangold, S., Doppler, T., Junghans, M., Wittmer, I., Stamm, C., and Singer, H.: Pesticide Risks in Small Streams - How to Get as Close as Possible to the Stress Imposed on Aquatic Organisms, *Environmental Science and Technology*, 52, 4526–4535, <https://doi.org/10.1021/acs.est.8b00077>, 2018.

- Stoob, K., Singer, H. P., Mueller, S. R., Schwarzenbach, R. P., and Stamm, C. H.: Dissipation and transport of veterinary sulfonamide antibiotics after manure application to grassland in a small catchment, *Environmental Science and Technology*, 41, 7349–7355, <https://doi.org/10.1021/es070840e>, 2007.
- Stravs, M. A., Stamm, C., Ort, C., and Singer, H.: Transportable automated HRMS platform "MS2field" enables insights into water-quality dynamics in real time, *Environmental Science and Technology Letters*, 8, 373–380, <https://doi.org/10.1021/acs.estlett.1c00066>, 2021.
- Täumer, K., Stoffregen, H., and Wessolek, G.: Determination of repellency distribution using soil organic matter and water content, *Geoderma*, 125, 107–115, <https://doi.org/10.1016/j.geoderma.2004.07.004>, 2005.
- Tiseo, K., Huber, L., Gilbert, M., Robinson, T. P., and Van Boeckel, T. P.: Global trends in antimicrobial use in food animals from 2017 to 2030, *Antibiotics*, 9, 1–14, <https://doi.org/10.3390/antibiotics9120918>, 2020.
- Torn, M. S., Trumbore, S. E., Chadwick, O. A., Vitousek, P. M., and Hendricks, D. M.: Mineral control of soil organic carbon storage and turnover content were measured by horizon down to the depth at which, *Nature*, 389, 3601–3603, 1997.
- Uber, M.: Suspended sediment production and transfer in mesoscale catchments: a new approach combining flux monitoring, fingerprinting and distributed numerical modeling, Phd thesis, Université Grenoble Alpes, 2020.
- Uber, M., Vandervaere, J. P., Zin, I., Braud, I., Heistermann, M., Legoût, C., Molinié, G., and Nord, G.: How does initial soil moisture influence the hydrological response? A case study from southern France, *Hydrology and Earth System Sciences*, 22, 6127–6146, <https://doi.org/10.5194/hess-22-6127-2018>, 2018.
- Uber, M., Legout, C., Nord, G., Crouzet, C., Demory, F., and Poulénard, J.: Comparing alternative tracing measurements and mixing models to fingerprint suspended sediment sources in a mesoscale Mediterranean catchment, *Journal of Soils and Sediments*, 19, 3255–3273, <https://doi.org/10.1007/s11368-019-02270-1>, 2019.
- Van Boeckel, T. P., Brower, C., Gilbert, M., Grenfell, B. T., Levin, S. A., Robinson, T. P., Teillant, A., and Laxminarayan, R.: Global trends in antimicrobial use in food animals, *Proceedings of the National Academy of Sciences of the United States of America*, 112, 5649–5654, <https://doi.org/10.1073/pnas.1503141112>, 2015.
- van den Heuvel, W., Halley, B. A., Ku, C. C., Jacob, T. A., Wislocki, P. G., and Forbis, A.: Bioconcentration and depuration of avermectin B1a in the bluegill sunfish, *Environmental Toxicology and Chemistry*, 15, 2263–2266, 1996.
- Van Der Velde, Y., Torfs, P. J., Van Der Zee, S. E., and Uijlenhoet, R.: Quantifying catchment-scale mixing and its effect on time-varying travel time distributions, *Water Resources Research*, 48, 1–13, <https://doi.org/10.1029/2011WR011310>, 2012.

- van Hoek, A. H. A. M., Mevius, D., Guerra, B., Mullany, P., Roberts, A. P., and Aarts, H. J. M.: Acquired Antibiotic Resistance Genes: An Overview, *Frontiers in Microbiology*, 2, 104–108, <https://doi.org/10.3389/fmicb.2011.00203>, 2011.
- Van Rossum, G. and Drake, F. L.: *Python 3 Reference Manual*, CreateSpace, Scotts Valley, CA, <https://doi.org/10.5555/1593511>, 2009.
- Vannier, O.: Apport de la modélisation hydrologique régionale à la compréhension des processus de crue en zone méditerranéenne, Ph.D. thesis, Université de Grenoble, 2015.
- Ventola, C. L.: The antibiotic resistance crisis: part 1: causes and threats., *Pharmacy and Therapeutics*, 40, 277–283, URL <http://www.ncbi.nlm.nih.gov/pubmed/25859123>, 2015.
- Verdú, J. R., Cortez, V., Ortiz, A. J., González-Rodríguez, E., Martínez-Pinna, J., Lumaret, J. P., Lobo, J. M., Numa, C., and Sánchez-Piñero, F.: Low doses of ivermectin cause sensory and locomotor disorders in dung beetles, *Scientific Reports*, 5, 1–10, <https://doi.org/10.1038/srep13912>, 2015.
- Verdú, J. R., Lobo, J. M., Sánchez-Piñero, F., Gallego, B., Numa, C., Lumaret, J. P., Cortez, V., Ortiz, A. J., Tonelli, M., García-Teba, J. P., Rey, A., Rodríguez, A., and Durán, J.: Ivermectin residues disrupt dung beetle diversity, soil properties and ecosystem functioning: An interdisciplinary field study, *Science of the Total Environment*, 618, 219–228, <https://doi.org/10.1016/j.scitotenv.2017.10.331>, 2018.
- Verlicchi, P., Galletti, A., Petrovic, M., and Barceló, D.: Hospital effluents as a source of emerging pollutants: An overview of micropollutants and sustainable treatment options, *Journal of Hydrology*, 389, 416–428, <https://doi.org/10.1016/j.jhydrol.2010.06.005>, 2010.
- Vidal, D.: *Olivier de Serres, l'ardéchois , père de l'agriculture française, le dauphiné libéré*, Valence, France, 2019.
- Vidal, J. P., Martin, E., Franchistéguy, L., Habets, F., Soubeyroux, J. M., Blanchard, M., and Bailion, M.: Multilevel and multiscale drought reanalysis over France with the Safran-Isba-Modcou hydrometeorological suite, *Hydrology and Earth System Sciences*, 14, 459–478, <https://doi.org/10.5194/hess-14-459-2010>, 2010.
- Von Freyberg, J., L. A. Knapp, J., Rücker, A., and W. Kirchner, J.: Technical note: Evaluation of a low-cost evaporation protection method for portable water samplers, *Hydrology and Earth System Sciences*, 24, 5821–5834, <https://doi.org/10.5194/hess-24-5821-2020>, 2020.
- Walker, A. and Thompson, J. A.: The degradation of simazine, linuron and propyzamide in different soils, *Weed Research*, 17, 399–405, <https://doi.org/10.1111/j.1365-3180.1977.tb00500.x>, 1977.
- Wang, Z., Feyen, J., Van Genuchten, M. T., and Nielsen, D. R.: Air entrapment effects on infiltration rate and flow instability, *Water Resources Research*, 34, 213–222, <https://doi.org/10.1029/97WR02804>, 1998.
- Watson, C. L. and Letey, J.: Indices for Characterizing Soil-Water Repellency Based upon Contact Angle-Surface Tension Relationships, *Soil Science Society of America Journal*, 34, 841–844, <https://doi.org/10.2136/sssaj1970.03615995003400060011x>, 1970.

- Wei, R., Ge, F., Huang, S., Chen, M., and Wang, R.: Occurrence of veterinary antibiotics in animal wastewater and surface water around farms in Jiangsu Province, China, *Chemosphere*, 82, 1408–1414, <https://doi.org/10.1016/j.chemosphere.2010.11.067>, 2011.
- Weill, S., Lesparre, N., Jeannot, B., and Delay, F.: Variability of Water Transit Time Distributions at the Strengbach Catchment (Vosges Mountains, France) Inferred Through Integrated Hydrological Modeling and Particle Tracking Algorithms, *Water*, 11, 2637, <https://doi.org/10.3390/w11122637>, 2019.
- WHO: Anatomical Therapeutic Chemical (ATC) Classification, URL <https://www.who.int/tools/atc-ddd-toolkit/atc-classification>, 2021.
- Wijbrans, A., Delrieu, G., and Nord, G.: Within catchment spatial rainfall variability over a range of spatio-temporal scales in the Cévennes-Vivarais Region, France, 2015.
- Wohde, M., Blanckenhorn, W. U., Floate, K. D., Lahr, J., Lumaret, J. P., Römbke, J., Scheffczyk, A., Tixier, T., and Düring, R. A.: Analysis and dissipation of the antiparasitic agent ivermectin in cattle dung under different field conditions, *Environmental Toxicology and Chemistry*, 35, 1924–1933, <https://doi.org/10.1002/etc.3462>, 2016.
- Wolstenholme, A. J. and Rogers, A. T.: Glutamate-gated chloride channels and the mode of action of the avermectin/milbemycin anthelmintics, *Parasitology*, 131, <https://doi.org/10.1017/S0031182005008218>, 2005.
- Wolstenholme, A. J., Fairweather, I., Prichard, R., Von Samson-Himmelstjerna, G., and Sangster, N. C.: Drug resistance in veterinary helminths, *Trends in Parasitology*, 20, 469–476, <https://doi.org/10.1016/j.pt.2004.07.010>, 2004.
- Wooding, R. A.: Steady Infiltration from a Shallow Circular Pond, *Water Resources Research*, 4, 1259–1273, <https://doi.org/10.1029/WR004i006p01259>, URL <http://doi.wiley.com/10.1029/WR004i006p01259>, 1968.
- World Health Organization: Critically Important Antimicrobials for Human Medicine, Tech. rep., World Health Organization, Geneva, Switzerland, <https://doi.org/10.1017/CBO9781107415324.004>, 2011.
- World Health Organization: Global Health Estimates 2016: Deaths by Cause, Age, Sex, by Country and by Region, 2000-2016, URL <http://www.who.int/news-room/fact-sheets/detail/the-top-10-causes-of-death>, 2018.
- Wratten, S. D. and Forbes, A. B.: Environmental assessment of veterinary avermectins in temperate pastoral ecosystems, *Annals of Applied Biology*, 128, 329–348, <https://doi.org/10.1111/j.1744-7348.1996.tb07327.x>, 1996.
- Yan, C., Laverman, A. M., Mercier, B., Garnier, J., Cagin, V., Martinez, A., Dinh, Q. T., and Chevreuil, M.: Effets des concentrations environnementales des antibiotiques sur la dénitrification dans les sédiments de la Charmoise (bassin de l'Orge), URL http://www.sisyphe.upmc.fr/piren/?q=webfm_send/1000, 2011.

- Yang, J., Heidbüchel, I., Musolff, A., Reinstorf, F., and Fleckenstein, J. H.: Exploring the Dynamics of Transit Times and Subsurface Mixing in a Small Agricultural Catchment, *Water Resources Research*, 54, 2317–2335, <https://doi.org/10.1002/2017WR021896>, 2018.
- Zhang, S., Yan, L., Huang, J., Mu, L., Huang, Y., Zhang, X., and Sun, Y.: Spatial Heterogeneity of Soil C: N Ratio in a Mollisol Watershed of Northeast China, *Land Degradation and Development*, 27, 295–304, <https://doi.org/10.1002/ldr.2427>, 2016.
- Zhou, L. J., Ying, G. G., Liu, S., Zhang, R. Q., Lai, H. J., Chen, Z. F., and Pan, C. G.: Excretion masses and environmental occurrence of antibiotics in typical swine and dairy cattle farms in China, *Science of the Total Environment*, 444, 183–195, <https://doi.org/10.1016/j.scitotenv.2012.11.087>, 2013.

Appendix **A**

Interview guideline

Nom	
Adresse	
Téléphone	
Adresse mail	
Installé/e depuis quand ?	
Quelles parcelles ?	

Activité / type de bêtes (incl. Bio/conv. ; lait/viande)			
Depuis quand ?			
Surface par type de bêtes			
Nombre de bêtes			
Période de pâturage			
Traitement 1			
Traitement 2			
Traitement 3			

Epandage de fumiers → où et quand ?	
Vente des fumiers ? à qui ?	
Carnets de traitement	
Quel vétérinaire et où ?	
Puits / sources ?	
D'où vient l'eau pour leurs bêtes ?	
Photos des crues ?	
Suivi / carnet de traitement année prochaine	
Des contacts des autres éleveurs ?	

FIGURE A.1: Guideline for the semidirective interviews on the farmers use of pharmaceuticals

Appendix **B**

Additional pharmaceutical concentrations

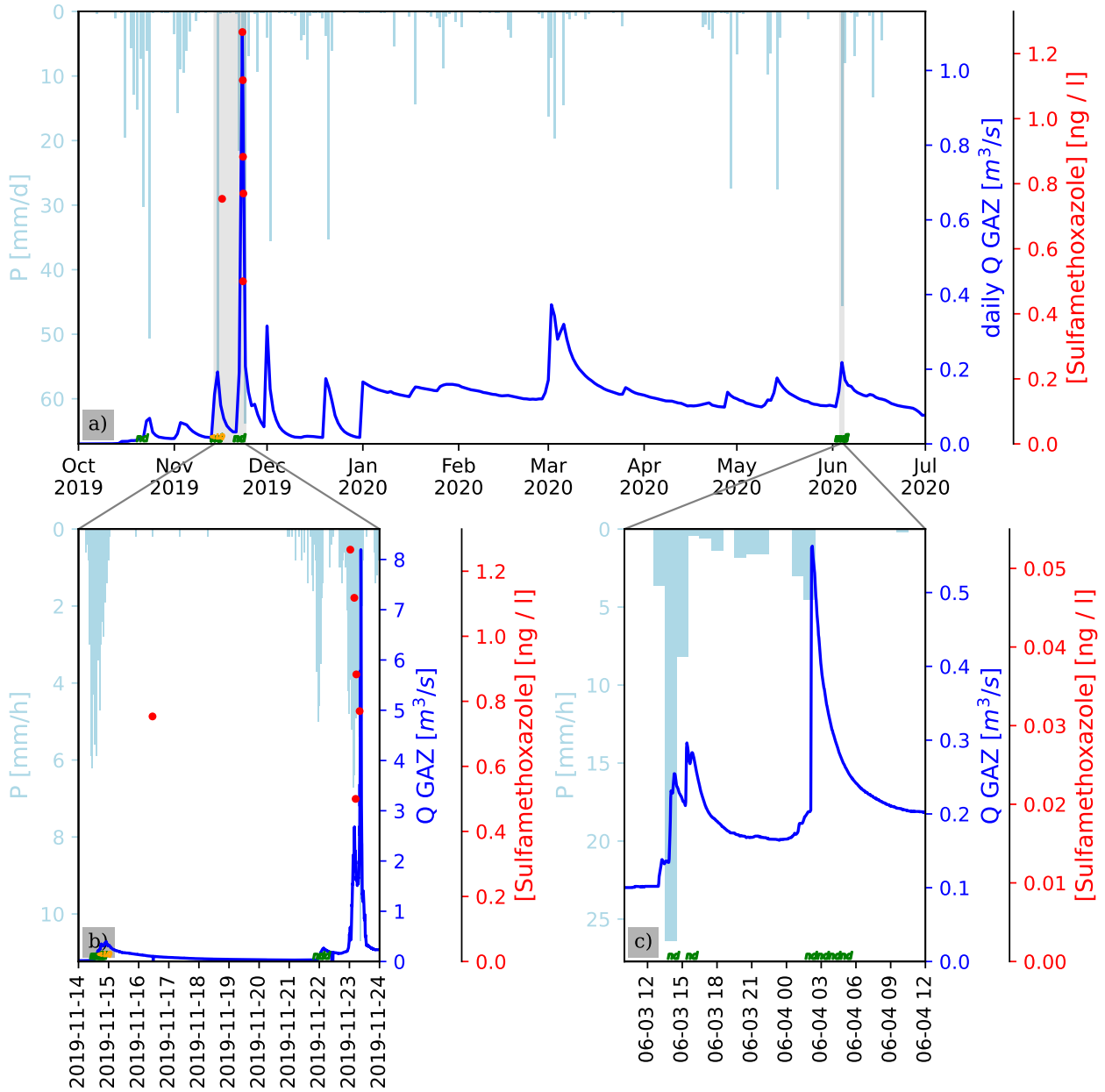


FIGURE B.1: Temporal evolution of the concentration of Sulfamethoxazole in grab samples from the Gazel outlet together with discharge (Q) and precipitation (P). Green 'nd' symbols at the bottom indicate samples without detectable concentration. Orange '< LQ' labels at the bottom of the plot indicate detection of a concentration below the limit of quantification (LQ). The discharge after 01.01.2020 has not been corrected and only serves to illustrate the rough evolution.

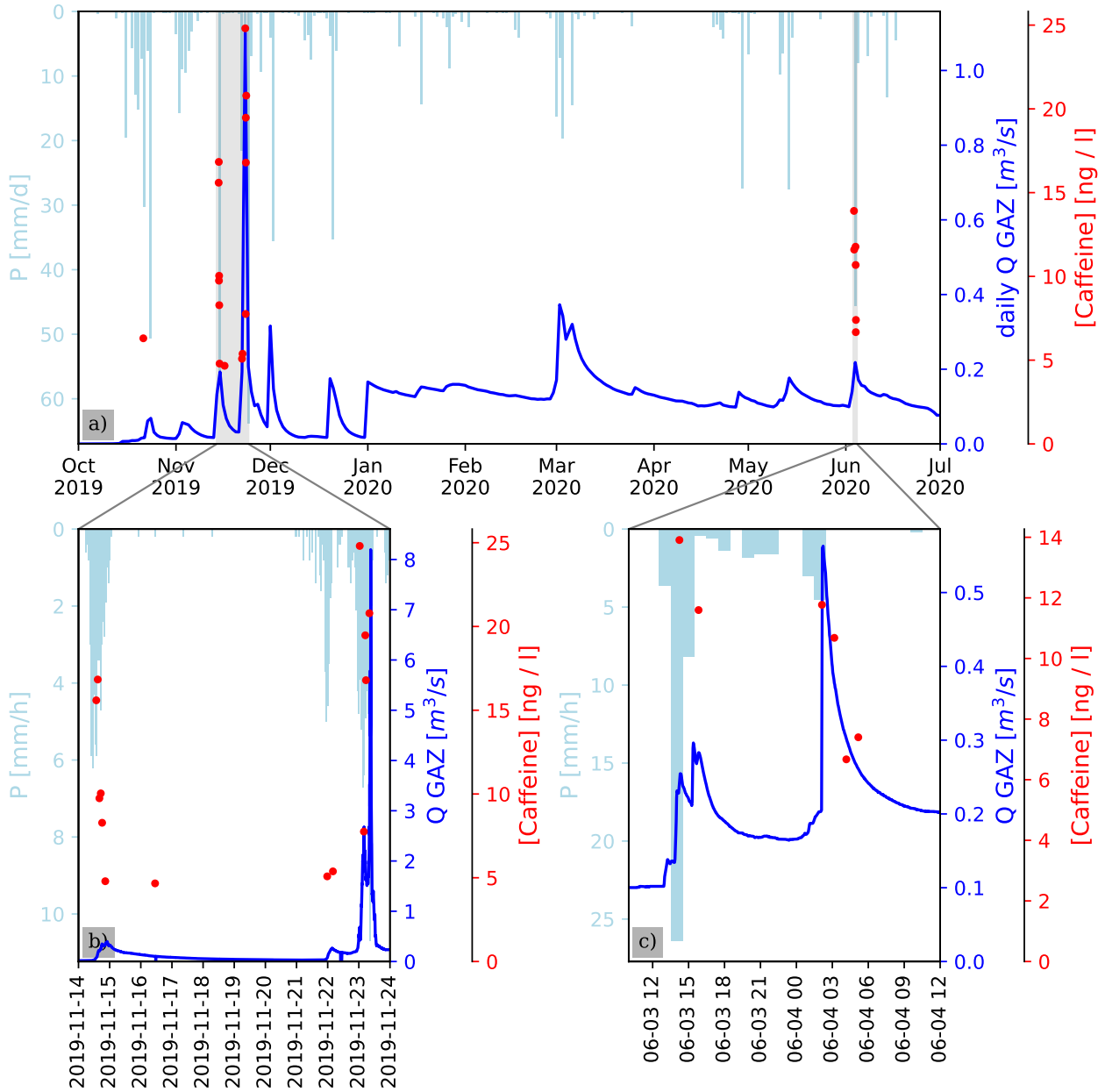


FIGURE B.2: Temporal evolution of the concentration of Caffeine in grab samples from the Gazel outlet together with discharge (Q) and precipitation (P). Green 'nd' symbols at the bottom indicate samples without detectable concentration. Orange '< LQ' labels at the bottom of the plot indicate detection of a concentration below the limit of quantification (LQ). The discharge after 01.01.2020 has not been corrected and only serves to illustrate the rough evolution.

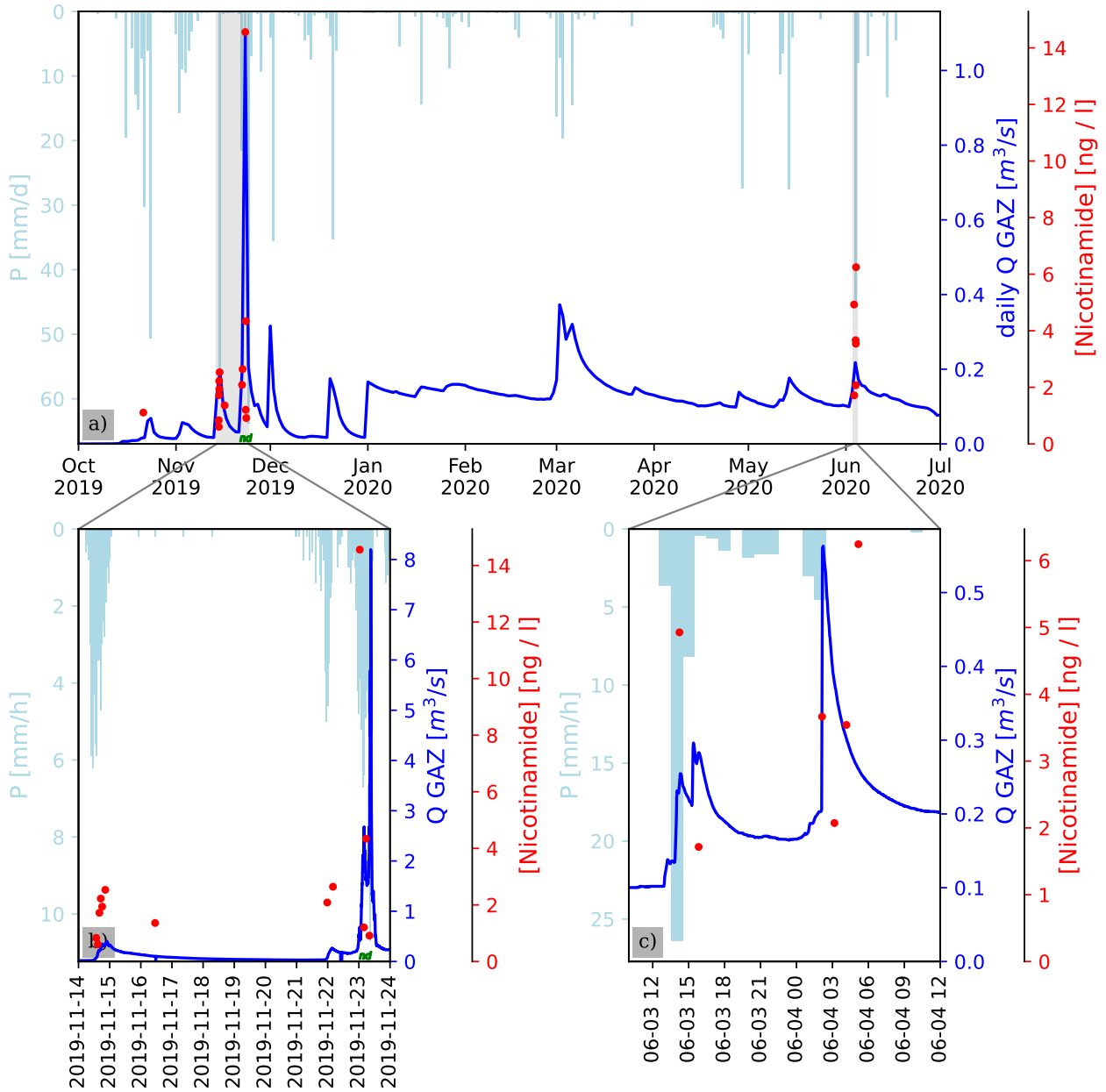


FIGURE B.3: Temporal evolution of the concentration of Nicotinamide in grab samples from the Gazel outlet together with discharge (Q) and precipitation (P). Green 'nd' symbols at the bottom indicate samples without detectable concentration. Orange '< LQ' labels at the bottom of the plot indicate detection of a concentration below the limit of quantification (LQ). The discharge after 01.01.2020 has not been corrected and only serves to illustrate the rough evolution.

Appendix **C**

Supplemental material soil sampling device

1

SUPPLEMENTAL MATERIAL

2

A device to simulate contaminant transfer and surface/subsurface flow through intact soil monoliths

3

4

Nico Hachgenei, Guillaume Nord, Lorenzo Spadini, Henri Mora, François Courvoisier, Jean-François-Sutra, Jean-Pierre Vandervaere, Cédric Legout, Marie-Christine Morel, Jean Martins, Anne Lespine, Céline Duwig

5

6

7

8

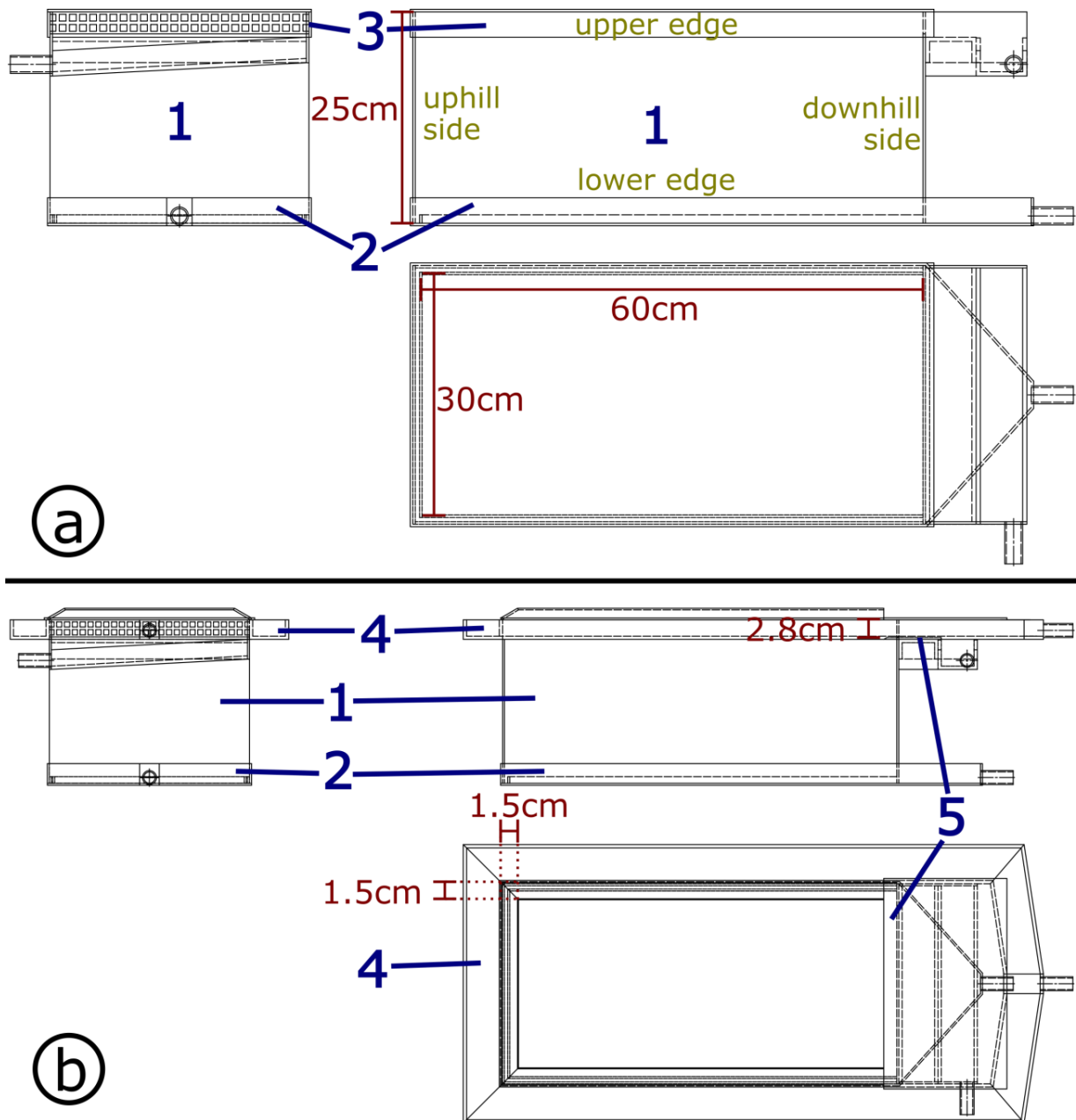
The provided supplemental material includes blueprints (Figure S1) and photos (Figures S2-3) of the sampling device as well as photos of the sampling steps (Figure S4). Furthermore, the chemical analysis of the test experiment is presented and the implications of the IVM concentrations obtained are discussed.

9

10

11

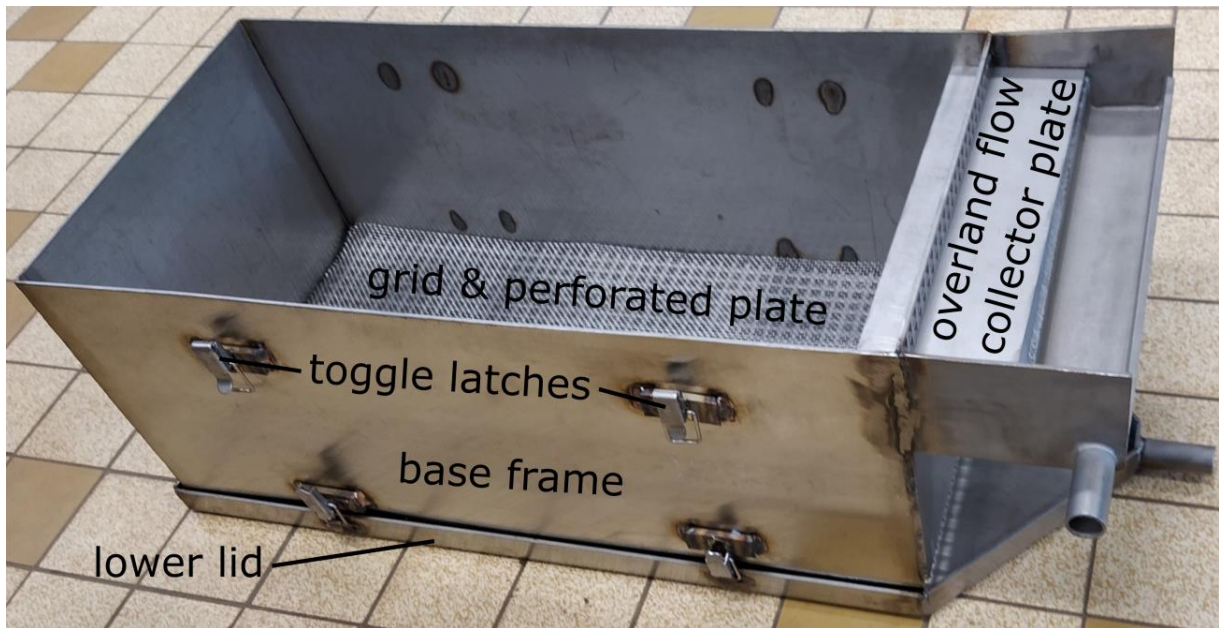
12



13

14 Supplemental Figure S1: Blueprints of the case in soil sampling mode (a) and in rainfall
 15 simulation mode (b). The numbered parts (in blue) are: 1: base frame, 2: lower lid, 3: upper lid,
 16 4: rain recovery frame, 5: overland flow collector plate. The grid and the perforated plate at the
 17 base are not shown for simplicity. The terms “upper”, “lower”, “uphill” and “downhill” as used
 18 in the article are depicted in olive. Dimensions are marked in red.

19



20

21 Supplemental Figure S2: Diagonal view of the sampling frame with lower lid, grids and overland
22 flow recovery plate in place



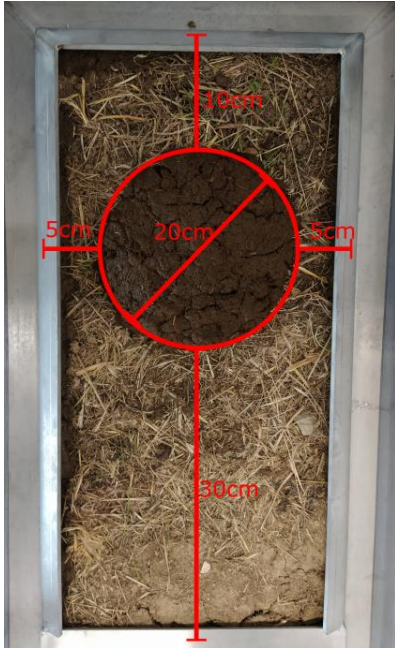
23

24 Supplemental Figure S3: Top view of lower lid (percolation collection)



25

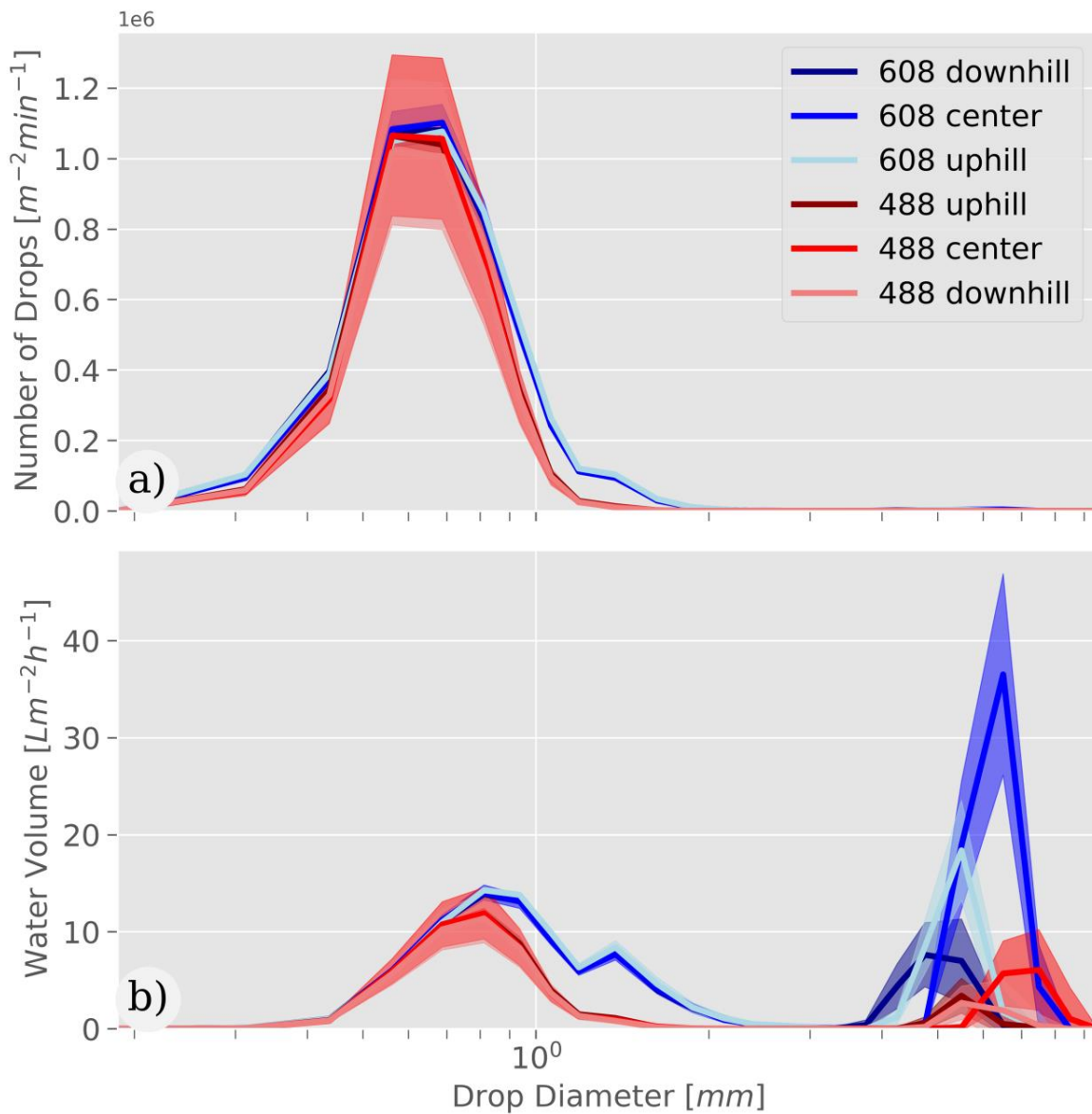
26 Supplemental Figure S4. Soil sampling steps. The numbers correspond to the steps in the
27 description of the sampling procedure in the main text (section "Procedure for sampling intact
28 soil in the field" of the description of the experimental device in the Material and methods
29 section).



30

31 Supplemental Figure S5. Position of the cow pat. This image shows a birds-eye view on the
32 setup with the rainfall collector covering the edges of the soil. The downhill side is at the
33 bottom of the image.

34



35

36 Supplemental Figure S6: Drop size distribution (mean +/- standard deviation) generated with
 37 the two presented sprinkler nozzles (490.608.30 and 490.488.30) measured with an OTT
 38 Parsivel disdrometer at the center, downhill third and uphill third of the soil surface. The
 39 reference is a horizontal plane traversed by the rain drops over a period and not a volume of air
 40 at one instant of time. a) shows the number of drops and b) the volume of water per size class
 41 traversing the horizontal plane. Note the logarithmic scale on the x-axis.

42

43

44 **Chemical analysis**

45 Major anion samples (including the Br⁻ tracer) were filtered (0.45µm, Sartorius Minisart
46 NML Cellulose Acetate) prior to analysis with a Metrohm modular IC 732 system. 50ml
47 subsamples for IVM analysis were poured (after mixing) into 55ml polypropylene centrifuge
48 tubes (Roth SA, France) and centrifuged for 15min at 7700 RCF (relative centrifugal force). The
49 supernatant was then concentrated by solid phase extraction (SPE, Supelclean LC-18 100mg
50 cartridges, Supelco, France) following a protocol used for biological samples (Lifschitz et al.,
51 2000) and adapted to water samples. Briefly, supernatants were spiked with 2.5 ng Doramectin
52 (VETRANAL analytical standard ≥95.0% from Sigma Aldrich, France), dissolved in Dimethyl
53 Sulfoxide to a concentration of 1gL⁻¹ and then diluted in water, as an internal standard,
54 extracted by SPE and eluted with 3ml acetonitrile (ACN). The SPE was performed within 24h
55 after sampling and samples were stored in the dark at 4°C in the meantime. Eluted samples
56 were stored in the dark at 4°C until analysis. Samples were then treated by derivatization and
57 analyzed by HPLC with fluorescence detection (HPLC-FLD) at INTHERES laboratory, Toulouse,
58 France (Lifschitz et al., 2000).

59

REFERENCES

60 Lifschitz, A., Virkel, G., Sallovitz, J., Sutra, J. F., Galtier, P., Alvinerie, M., & Lanusse, C. (2000).
61 Comparative distribution of ivermectin and doramectin to parasite location tissues in
62 cattle. *Veterinary Parasitology*, 87(4), 327–338. [https://doi.org/10.1016/S0304-](https://doi.org/10.1016/S0304-4017(99)00175-2)
63 [4017\(99\)00175-2](https://doi.org/10.1016/S0304-4017(99)00175-2)

64

Appendix **D**

Additional element / ion concentrations

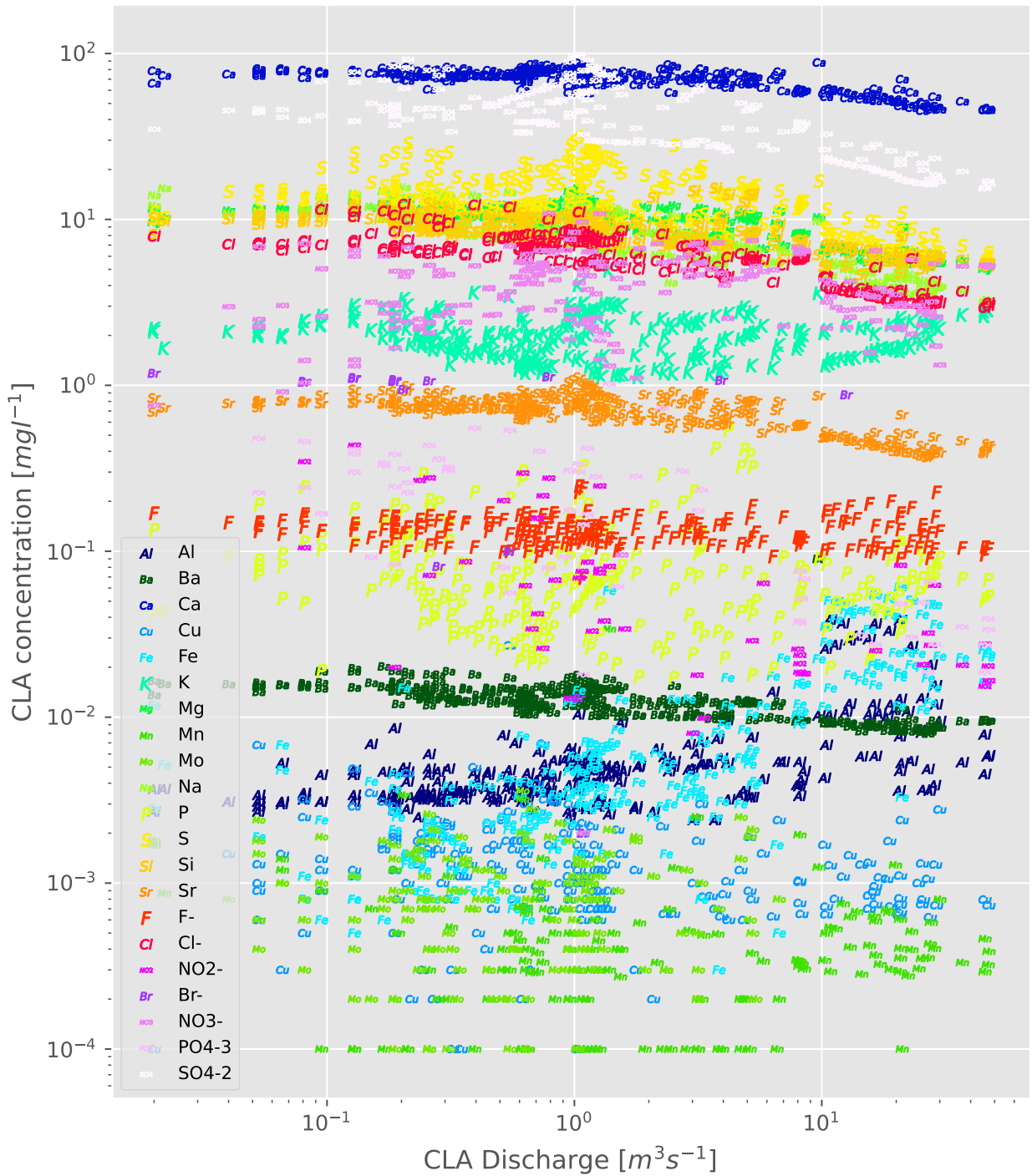


FIGURE D.1: Concentration - discharge relationship of all elements and ions from water samples from the Claduègne outlet. Note the logarithmic scale on both axes.

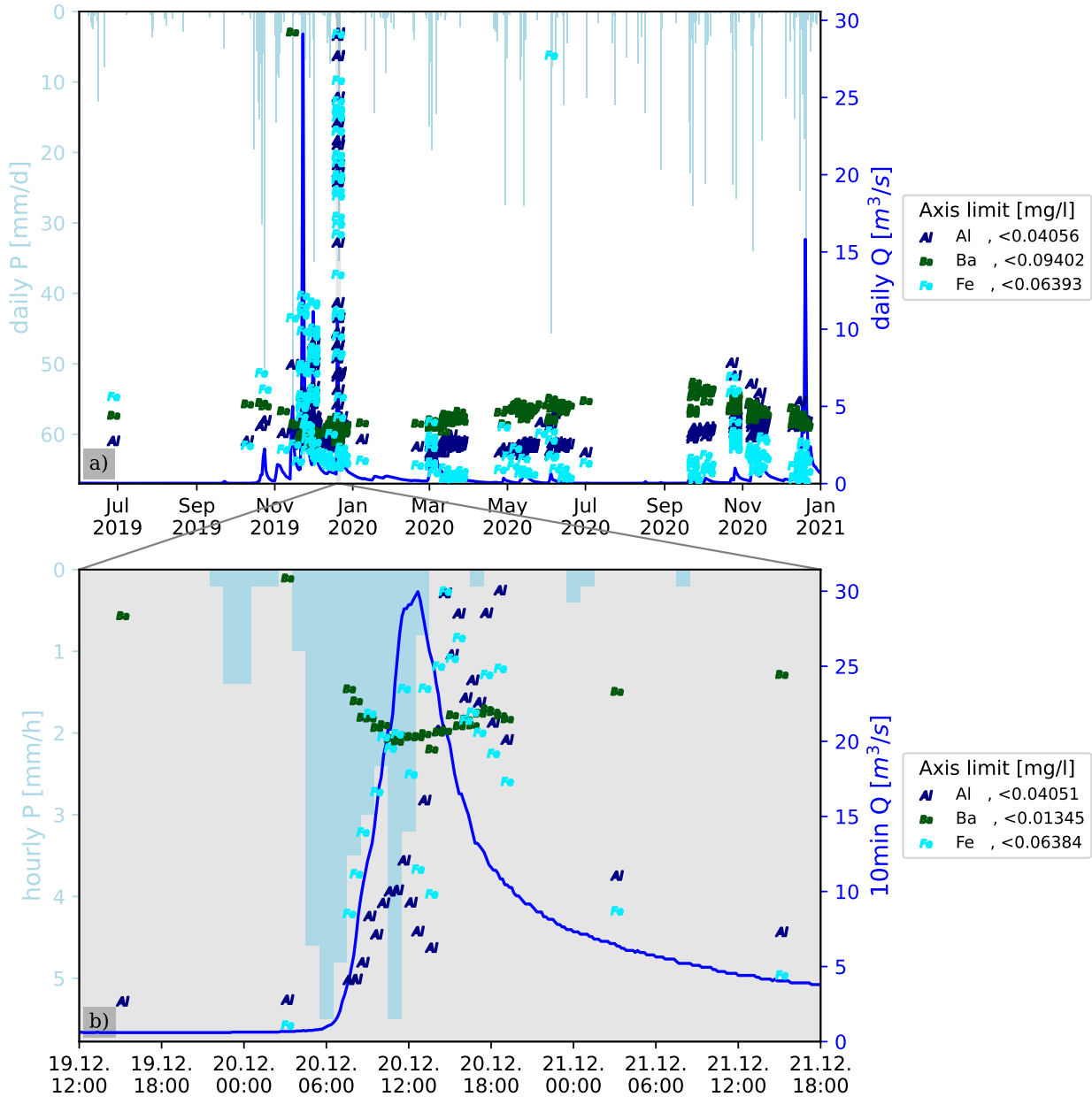


FIGURE D.2: Precipitation, discharge and concentration time-series of a selection of elements and ions from water samples from the Claduegne outlet for the whole observation period (a) and one selected event (b). For each element and ion the y-axis is scaled from zero to just above the maximum concentration. The upper axis limit for each element is shown in the legend.

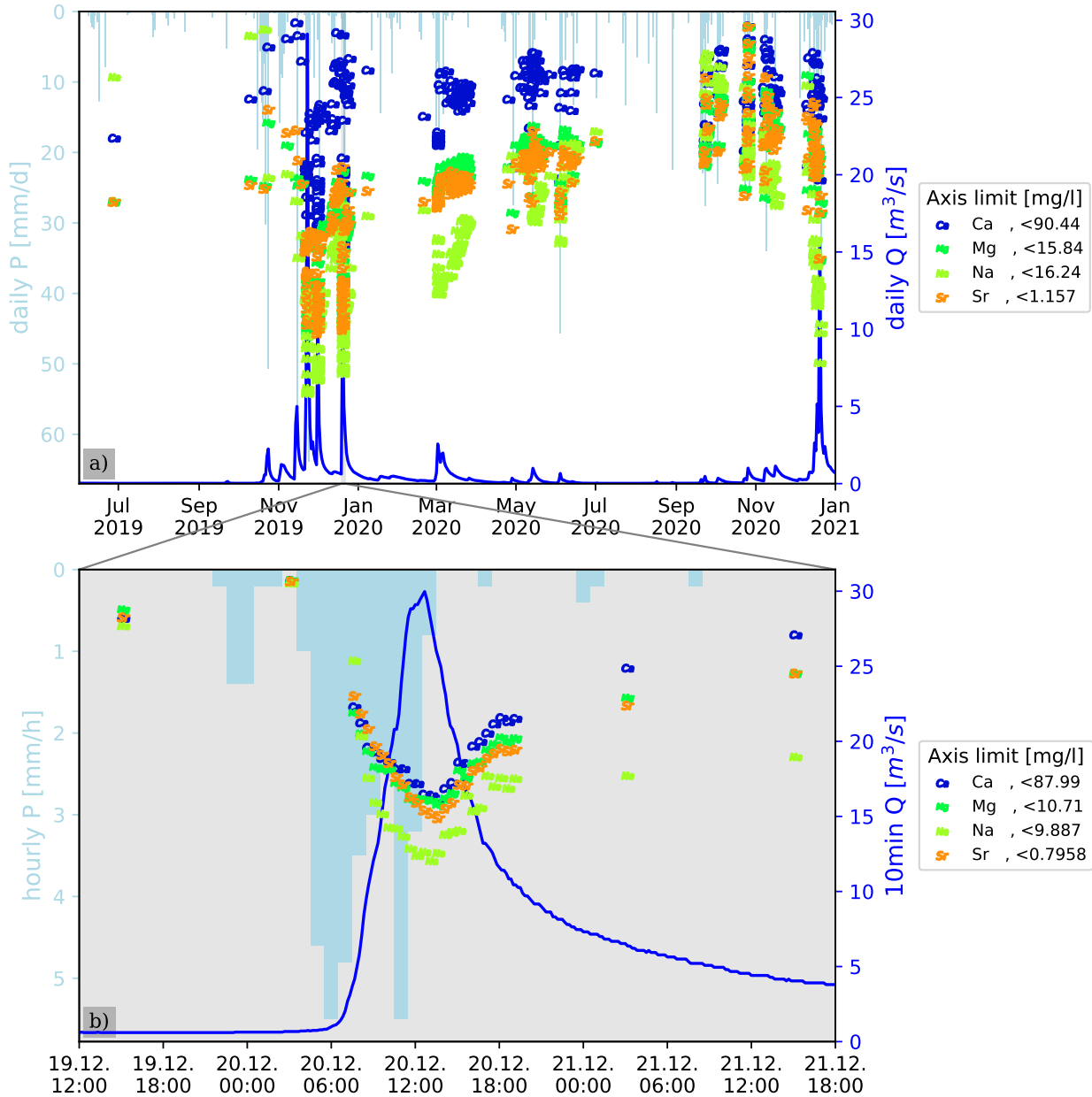


FIGURE D.3: Precipitation, discharge and concentration time-series of a selection of elements and ions from water samples from the Claduegne outlet for the whole observation period (a) and one selected event (b). For each element and ion the y-axis is scaled from zero to just above the maximum concentration. The upper axis limit for each element is shown in the legend.

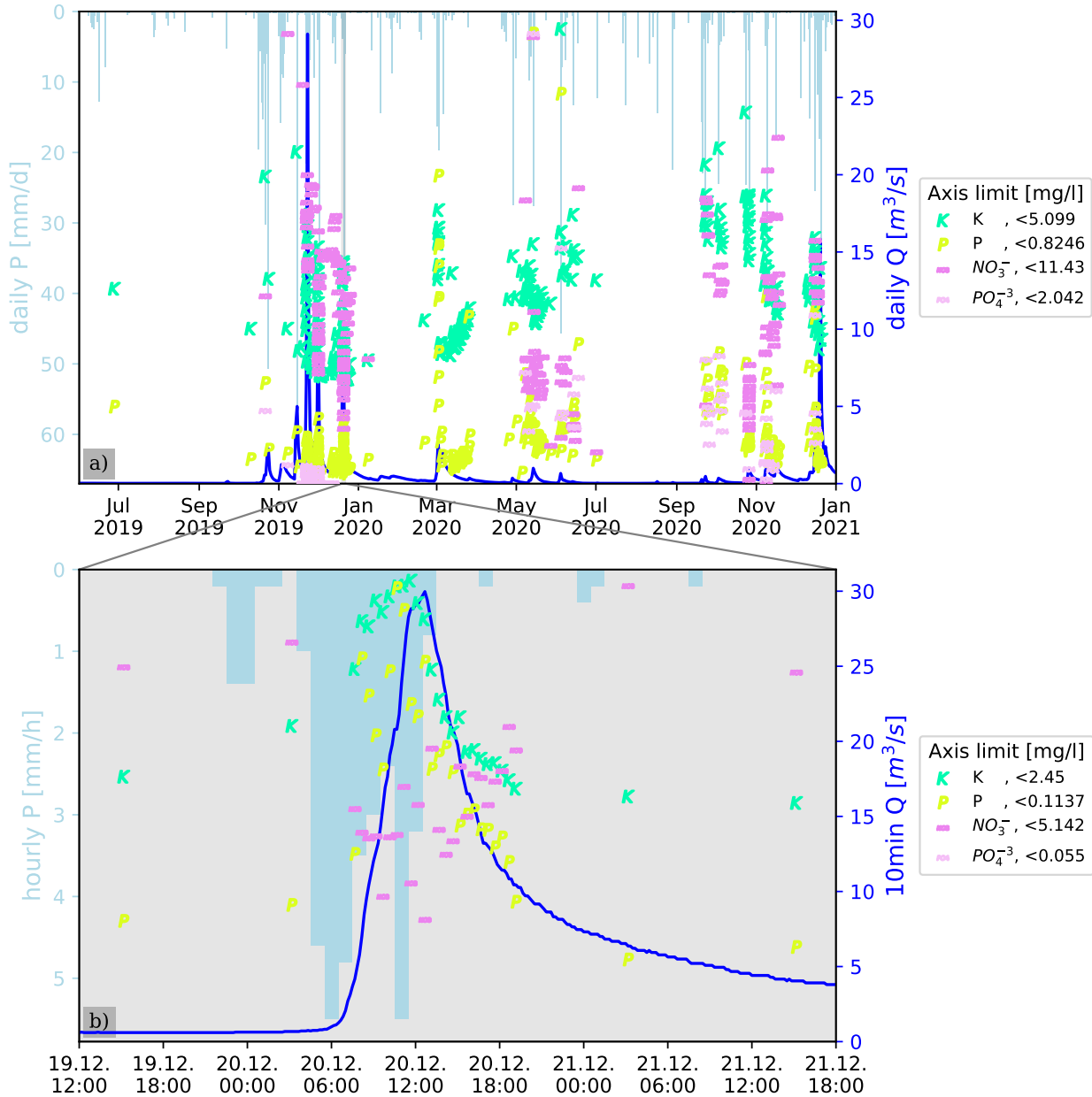


FIGURE D.4: Precipitation, discharge and concentration time-series of a selection of elements and ions from water samples from the Claduegne outlet for the whole observation period (a) and one selected event (b). For each element and ion the y-axis is scaled from zero to just above the maximum concentration. The upper axis limit for each element is shown in the legend.

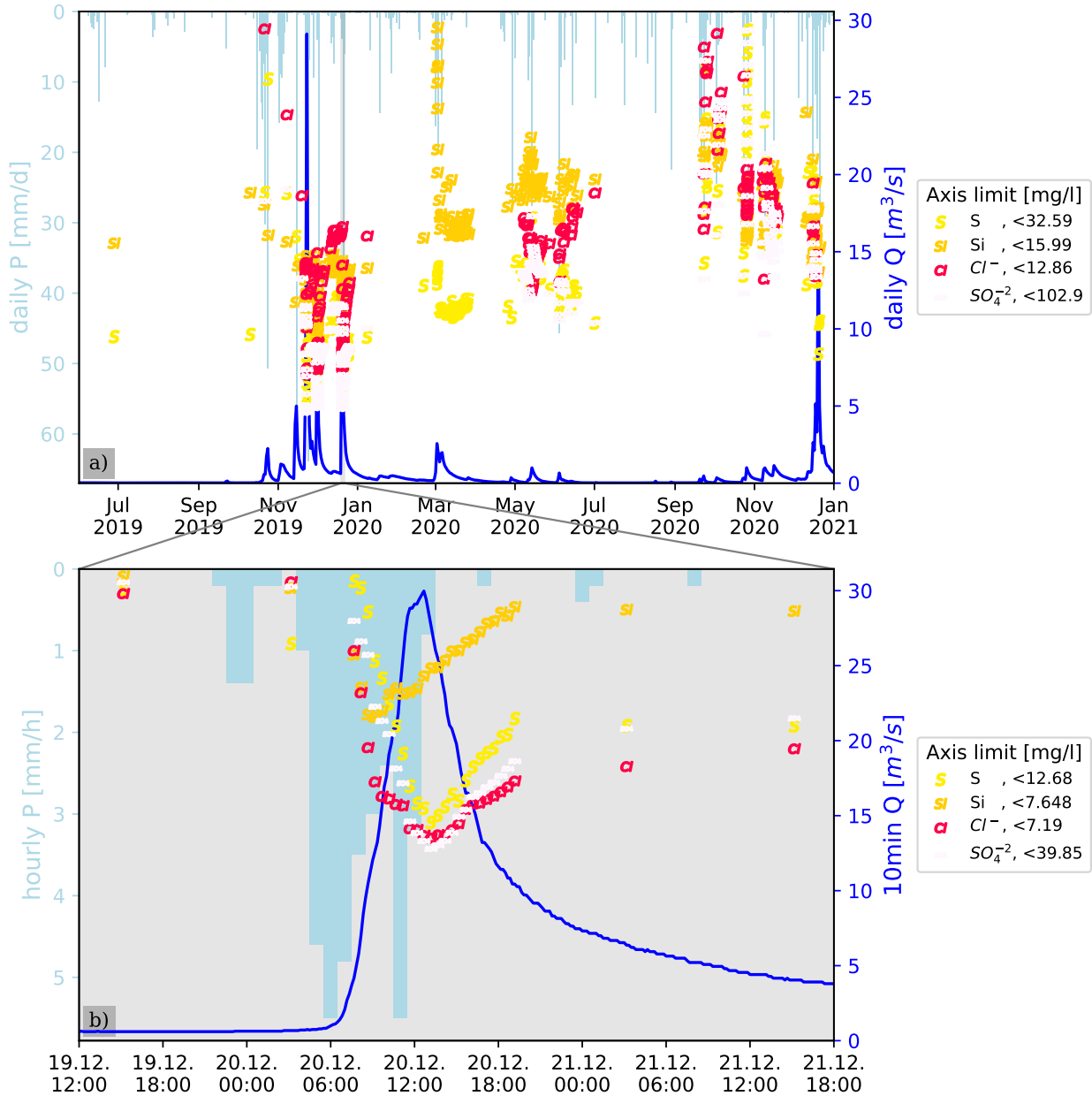


FIGURE D.5: Precipitation, discharge and concentration time-series of a selection of elements and ions from water samples from the Claduegne outlet for the whole observation period (a) and one selected event (b). For each element and ion the y-axis is scaled from zero to just above the maximum concentration. The upper axis limit for each element is shown in the legend.

Appendix E

**Method article: Stable isotope memory
effect correction (MEX, 2022)**

MethodsX 9 (2022) 101656



Contents lists available at ScienceDirect

MethodsX

journal homepage: www.elsevier.com/locate/mex

Method Article

Faster and more precise isotopic water analysis of discrete samples by predicting the repetitions' asymptote instead of averaging last values



Nico Hachgenei^{a,*}, Véronique Vaury^b, Guillaume Nord^a,
Lorenzo Spadini^a, Céline Duwig^a

^aIGE, Univ. Grenoble Alpes, CNRS, IRD, Grenoble INP, Grenoble, France

^biEES, Sorbonne Univ., Paris, France

A B S T R A C T

Water stable isotope analysis using Cavity Ring-Down Spectroscopy (CRDS) has a strong between-sample memory effect. The classic approach to correct this memory effect is to inject the sample at least 6 times and ignore the first two to three injections. The average of the remaining injections is then used as measured value. This is in many cases insufficient to completely compensate the memory effect. We propose a simple approach to correct this memory effect by predicting the asymptote of consecutive repeated injections instead of averaging over them. The asymptote is predicted by fitting a $y = \frac{a}{x} + b$ relation to the sample repetitions and keeping b as measured value. This allows to save analysis time by doing less injections while gaining precision. We provide a Python program applying this method and describe the steps necessary to implement this method in any other programming language. We also show validation data comparing this method to the classical method of averaging over the last couple of injections. The validation suggests a gain in time of a factor two while gaining in precision at the same time. The method does not have any specific requirements for the order of analysis and can therefore also be applied to an existing set of analyzes in retrospect.

- We fit a simple $y = \frac{a}{x} + b$ relation to the sample repetitions of Picarro L2130-i isotopic water analyzer, in order to keep the asymptote (b) as measured value instead of using the average over the last couple of measurements.
- This allows a higher precision in the measured value with less repetitions of the injection saving precious time during analysis.
- We provide a sample code using Python, but generally this method is easy to implement in any automated data treatment protocol.

© 2022 The Author(s). Published by Elsevier B.V.

This is an open access article under the CC BY license (<http://creativecommons.org/licenses/by/4.0/>)

Abbreviations: aol, average of the last injections; exp, method fitting an exponential function $y = a \cdot e^{-bx} + c$ to repeated injections; inv, method fitting $y = \frac{a}{x} + b$ to repeated injections.

* Corresponding author.

E-mail address: nico.hachgenei@univ-grenoble-alpes.fr (N. Hachgenei).

<https://doi.org/10.1016/j.mex.2022.101656>

2215-0161/© 2022 The Author(s). Published by Elsevier B.V. This is an open access article under the CC BY license (<http://creativecommons.org/licenses/by/4.0/>)

ARTICLE INFO

Method name: Asymptotic Approximation Calibration in Cavity Ring-Down Spectroscopy (CRDS)

Keywords: Picarro, Water stable isotopes, Cavity ring-down spectroscopy (CRDS), Calibration, Hydrology, Tracer

Article history: Received 26 November 2021; Accepted 27 February 2022; Available online 3 March 2022

Specifications table

Subject Area:	
More specific subject area:	Environmental tracers
Method name:	Asymptotic Approximation Calibration in Cavity Ring-Down Spectroscopy (CRDS)
Name and reference of original method:	Picarro L2130-i manual [3]
Resource availability:	A Python program applying this method is provided in the Supplementary Material, as well as a validation dataset

Introduction

Cavity Ring-Down Spectroscopy (CRDS) such as the *Picarro L2130-i Isotopic Water Analyzer* is an inexpensive, easy to use and relatively precise method for the analysis of stable isotope ratios of the water molecule. However, this method is subject to a strong between-sample memory effect (or carryover) as well as drift with time [1,5,8]. The memory-effect is caused by residual water of previous samples inside the sampling syringe, transfer path or the cavity itself [2,8]. In their *L2130-i Isotopic Water Analyzer* manual [3], Picarro states that in order to ‘completely eliminate memory effects’, each sample should be injected 6 times (p. I-14) and the first two to three values should be ignored. Then the average of the last couple of injections is retained as measured value. This method will be referred to as aol (average of last samples) in the following. Laboratories using CRDS like the *Picarro L2130-i Isotopic Water Analyzer* often either use this approach, sometimes with a higher number of injections if precision is of importance, or rely on custom programs to try and correct for the memory effect. When analyzing contrasted samples (e.g., the standards or contrasted environmental samples like rain water), a clear, monotonous trend may still be visible in the repetitions, even beyond 10 injections [1,2]. Vallet-Coulomb et al. [5] detected a memory effect after up to 45 injections of the same sample.

There have been other publications with different approaches to try and correct the memory effect via software solutions, sometimes combined with the analysis of a particular sequence of known standards. These approaches have been grouped differently by different authors (e.g., [4,6]). The simplest solution is averaging over the last couple of injections and ignoring the first injections (aol). This assumes that enough injections were performed for the value to stabilize. As mentioned above, many injections are often necessary to reach stabilization of measured values. This method is simple to apply and therefore still largely used and recommended by Picarro, even though it requires many injections making it money- and time-consuming and in reality stabilization is often not reached, creating a bias in the result. More advanced approaches include the application of correction coefficients that quantify the memory effect as a function of the difference between the current and previous sample [1,6,8]. These correction coefficients correspond to the proportion of residual water vapor from the previous sample. Wassenaar et al. [8] propose a particular order of analysis and a software (Lims for Lasers) which allow to quantify the memory effect in between two samples by comparing the result of a standard analyzed after a contrasting standard to the result of a repeated analysis of the same standard. They use the average of non-ignored injections as only information for each sample. Gröning [1] proposes an excel-based software-tool estimating the memory effect for each injection of the sample analysis by estimating the effect of the previous sample on each injection of the following sample for each pair of two consecutive samples. Van Geldern & Barth [6] use a similar approach, estimating memory coefficients from a series of known standards and update these memory coefficients using daily repetition of the series of standards. Guidotti et al. [2] argue that there are multiple pools of residual water of different size that are mixed with the sample over different periods of time. Therefore, they propose to use one exponential model for each pool’s contribution to the overall memory effect. This method has a solid physical

base in the assumption of different pools, the isotopic signature of which changes exponentially with subsequent injections. The model parametrization remains empirical as the pools are not physically defined and the parameters are calibrated from repeated analyzes of known standards. The most rapid pool would change its signature to the new sample's signature almost instantly with the first injection while the signature of the slowest pool would remain far from the samples signature even over many consecutive injections. Therefore, their memory correction algorithm considers not only the previous sample but all previously injected samples since the start of the series. This is a very complete and physically sound approach however requiring prior assumptions on the number of pools contributing to the memory effect as well as the calibration of two parameters per pool in addition to the initial conditions (initial isotopic signature of each pool).

Vallet-Coulomb et al. [5] perform a detailed comparison of different memory correction methods on the same sequence of standards and samples treating known standards as unknown samples with ten injections each. Firstly, they apply an aol method by ignoring the first six samples and averaging over the remaining four. Secondly, they use one method where for each sample the residual vapor has the signature of the previous sample and its contribution decreases with the number of injections. This resembles the methods used by Gröning [1] and Van Geldern & Barth [6]. Thirdly they use the method presented by Guidotti et al. [2] using two residual water pools. Finally, they developed a simplified version of the method proposed by Guidotti et al. [2], where the exchange between the sample and the residual vapor is constant, but the signature of the residual vapor changes with every injection and depends on the four previous samples. Instead of assuming the number of contributing pools and calibrating parameters of multiple exponential functions to mathematically approximate the evolution of the isotopic signature of each pool, they use measured memory correction coefficients obtained beforehand from subsequent series of 50 injections of known standards. The aol method overestimated the sample values as they were preceded by a high sample. The method from Guidotti et al. [2] also overestimated the sample values, which the authors explain with the method being developed for extremely contrasted artificially spiked samples and not adapted for environmental waters. The method only depending on the previous sample's value overcorrected the result and the method developed by the authors produced the best results with a slight overcorrection.

We propose a simple approach to correct the memory effect that can be implemented in any programming language that is used for data treatment and we provide a ready-to-use Python implementation together with the validation data. This approach works in a different way than those developed by others that are presented above. Instead of estimating the memory effect from previous samples and then correcting the value of each injection for it, we consider each sample individually and predict the asymptote of repeated injections from the trend observed through the injections. The application of this approach does not require profound knowledge of the analytical system and is hardly more complex than averaging over the last samples but adds precision and requires less injections per sample.

In addition to the memory effect, the instrument's drift over time needs to be corrected for. In contrast to the memory effect, this correction is relatively straight forward and does not differ much between the different studies. It is estimated by regularly measuring known standards and quantifying their trend over time and can then be corrected through linear approximation. A simple drift correction is also briefly described at the end of the methods section and included in the Python program provided with this article.

Method details

In this section, the principle of the proposed memory correction method is introduced, including a step-by-step description. Thereafter, the whole workflow of the provided calibration program is presented briefly including the calibration and drift correction. This workflow was applied to three Picarro standards and a few natural stream water samples. The stream water samples will not be further presented in this article. In the following validation section, different tests were performed to compare the proposed method to the use of the classical aol method as well as an exponential approximation.

Assuming the asymptote of the measured value per injection to be the ‘ideal’ measured value (i.e. unaffected by the memory effect), an average over the last measured values is biased toward the precedent sample as long as the data present a trend. Therefore, we aimed to directly estimate the asymptote from the trend in the repeated injections. This method uses the information from all injections in order to predict the asymptote instead of eliminating this valuable information and only using the last measured values. It does not have particular requirements on the order of analysis and can deal with variable number of injections (e.g. if more injections are used for the standards than for the samples). Different asymptotic functions may be used to try and reproduce this trend. We found $y = \frac{a}{x} + b$ (called *inv* hereafter) to give good results. y is the measured isotope ratio, x is the number of injection, a and b are parameters that are optimized to fit the data points, where a is a scale factor and b is the asymptote. Fitting an exponential function $y = a \cdot e^{-b \cdot x} + c$ (called *exp* hereafter) did not significantly improve the calibration compared to the *aol* method (see method validation section for details).

The procedure of the *inv* method is to optimize a and b to obtain a good fit for measured value vs. injection number for each of the analyzed samples. We use Python’s *scipy* module and its *optimize.curve_fit* function [7]. The program is provided in the supplementary material.

This method is applied to any analyzed sample (i.e. standards and unknown samples). The memory correction can be combined with any calibration workflow. See the end of this section for details on the full workflow of the provided Python program.

No matter which programming language is used, we strongly recommend either fitting a linear function to $1/x$ -transformed data or using increasing weight/decreasing uncertainty with number of injection when fitting directly on the data-scale. If all points are equally weighted, the first injections have a stronger influence on the fit as they are further away from the mean and thus weigh stronger in the fitting algorithms cost function. We obtain this weighting in *scipy.optimize.curve_fit* through the *sigma* argument, which describes the uncertainty of each data point and corresponds to the inverse of each point’s weight. The cost function is $chisq = \sum (\frac{y-f(x)}{\sigma})^2$. *Sigma* should thus decrease with number of injection in order to increase the weight. We used $\sigma(x) = \frac{1}{1+0.5 \cdot x}$ in order to have a weight of $1 + 0.5 \cdot x$ for the x^{th} injection. Varying this parameter slightly (e.g. using $\sigma(x) = \frac{1}{x}$ or $\sigma(x) = \exp(-0.2x)$) did not significantly impact the results presented in the method validation section.

We also recommend to verify the existence of a trend in the measured values vs. injection number (and thus presence of a memory effect) before fitting the *inv* function. If the data does not present a trend (too little difference between first and last value) which happens, if the sample is very close to the previous sample and the memory effect does not affect the measured value, we use the classic method of averaging over the last injections. A minimum difference between first and last value of 0.15 for $\delta^{18}\text{O}$ and 0.4 for $\delta^2\text{H}$ worked well in our case. If no satisfying fit can be found (e.g. there is a difference between start and end, but due to noise with no clear trend), again, the *aol* method should be used. In our program, the *curve_fit* function produces a runtime error if no fit can be found and the *aol* method is used. It is recommended to plot each series of injections with the fit in order to visually verify the fit by scrolling through the figures.

The procedure of memory correction can be summarized with the following steps to be applied to each analyzed sample, one by one.

1. Verify if the difference between first and last value is larger than a threshold, if so continue to step 2, else do *aol*.
2. Try to fit a $y = \frac{a}{x} + b$ function to measured value vs. injection number by optimizing a and b to minimize the cost function $chisq = \sum (\frac{y-f(x)}{\sigma})^2$, where *sigma* prevents overfitting to the first injections. If this fails use *aol*, else continue to step 3.
3. Retain b as the measured value of the sample.

Given that each injection in high precision mode takes about 8 min and that *inv* seems to yield a higher precision after only six injections compared to *aol* after 12 injections (see method validation section), analysis could be sped up a factor two using this method while gaining in precision. Taking into account the necessity of regularly reanalyzing the standards due to possible drift of the device,

Table 1

Values and uncertainties of the standards used. (Picarro Lot #0517-12-06.x, Certificate C0350).

Name	$\delta^{18}\text{O}$ [‰]	Uncertainty	$\delta^2\text{H}$ [‰]	Uncertainty
PICARRO ZERO	0.3	± 0.2	1.8	± 0.9
PICARRO MID	-20.6	± 0.2	-159.0	± 1.3
PICARRO DEPL	-29.6	± 0.2	-235.0	± 1.8

the time gain is increased as more samples may be analyzed in between two repetitions of the standards.

The step-by-step calibration workflow of the provided Python program is as follows:

1. For each set of standards (in our example data there is one in the beginning and one in the end).
 - a. Inv method is applied to estimate each standard's measured value.
 - b. A calibration is performed by fitting a linear relation to real vs. measured values of the standards.
 - c. The two fitted parameters (intersection and slope) are saved together with the central time of analysis of this set of standards (i.e. the middle time between first injection of the first standard and last injection of the last standard).
2. The calibration parameters (interception and slope) are interpolated to each sample's central measurement time (i.e. the middle time between first and last injection), using the two neighboring sets of standards in order to obtain one individual set of calibration parameters for each sample that is corrected for the instrument's drift. The parameters are interpolated along the time-axis, assuming that instrument drift is linear with time for the duration between each two sets of standards.
3. The measured value of each sample is calculated by applying the inv method to its repeated injections.
4. The predicted isotopic ratio of each sample is calculated by applying its individual calibration parameters to the measured value.

This workflow is applied to $\delta^{18}\text{O}$ and $\delta^2\text{H}$ in parallel independently. The program is written in Python 3 and tested on version 3.8, but should be compatible with near future versions.

Method validation

For validation, we compare the method of fitting an asymptotic function to the method officially recommended by Picarro (aol). We used 3 different standards: PICARRO ZERO, MID and DEPL. They were stored in sealed glass ampoules, opened on the day of analysis and directly transferred into analysis vials. Their concentrations and uncertainties are given in Table 1. We also analyzed IAEA VSMOW2 (Vienna Standard Mean Ocean Water) and SLAP2 (Standard Light Antarctic Precipitation) (see supplementary material), however they were not used for calibration or verification as they had been opened beforehand and stored in a recipient containing air. We did 12 injections of each standard in high precision mode (8 min per injection). The order of analysis was as follows.

1. Tap water
2. PICARRO DEPL
3. PICARRO MID
4. Tap water
5. PICARRO ZERO

In order to estimate the number of injections necessary to obtain acceptable precision, we dropped the results from the last injections and repeated the calibration on this reduced data in order to

simulate an analysis using less injections. This way we could compare the results of doing 2, 3, 4, 5, 6, 7, 8, 9, 10, 11 and 12 injections. For the aol we chose to average over the last 5, 4, 3, 2, 1 injections when there were at least 9, 7, 5, 3, 2 injections respectively in total.

Fig. 1 illustrates the application of aol and inv for different numbers of injections (uncalibrated raw measurement). The result of inv does not vary much (between 2.58 and 2.81 for this standard), while aol varies much more (from -0.64 to $+1.93$). We also note that even after 12 injections, the ranges of values obtained by the two methods do not overlap. This can be explained by the trend that still persists after 12 injections, indicating that the measurements have not yet reached their asymptote. The average remains thus biased towards the previously measured sample. The exp method generally results in values close to aol. It either fits the first couple of injections or the last ones but it fails to reproduce the overall shape. This is in accordance with Guidotti et al. [2] who state that there are multiple residual water pools with different exponentially evolving signatures. The combined effect of these pools can therefore not be covered by one single exponential function. The inv function however seems to be able to match the combined effect of these different pools.

After extracting each standard's measured value with the different methods, a calibration is performed over the three standards by fitting a linear relation between measured and real values. In order to estimate the improvement from using an asymptotic estimation instead of averaging over the last couple of values, we calculated the coefficient of determination R^2 of this calibration function. According to the manual of the *Picarro L2130-i* [3], the relationship between the machines signal and the real isotopic ratio of the sample is perfectly linear. Therefore, a higher R^2 of the calibration indicates a more precise estimation of each standard's measured value on the scale of the instruments raw estimation.

A calibration was performed for each method and each number of injections Fig. 2. shows the R^2 for $\delta^{18}\text{O}$ and $\delta^2\text{H}$ as a function of the total number of injections for the three tested methods (aol, inv, exp). It can be seen that R^2 improves with the number of injections for all of the methods. R^2 was higher when applying inv method to estimate the measured value from repeated injections, indicating a more linear relation between measured and real values with less noise and thus a better calibration. The lower R^2 of the calibration based on the aol method can be explained by the memory effect causing an overestimation of PICARRO DEPL and underestimation of PICARRO MID & ZERO leading to a less linear relation between measured and real values. Exp produces very similar results as aol, while inv produces a good fit even with very few injections. As little as four injections seem to produce acceptable results, however we strongly recommend to do at least six injections. With only six injections, the calibration fit using inv method is better than that using aol method with twelve injections. This indicates, that the approximation method removes a significant part of the bias in measurement caused by the previous sample through memory effect.

Fig. 3 shows the two parameters (slope and intercept) of the retained calibration (real standard value = f (measured value)). For aol, the effect of using too few injections is a higher slope and a higher intercept (for both isotopes). This translates to a lower maximum and higher minimum measured value, indicating that the 'extreme' standards are 'pulled' toward the middle (or toward the previously measured value). This trend continues all the way to our maximum of 12 injections, indicating a potential of improvement even beyond 12 injections.

The exp method remains close to the aol method. This is because an exponential function that well represents the strong difference between the first injections too rapidly approaches zero thereafter. Thus, the exponential function tends to have its asymptote somewhere between the last couple of injections without extrapolating their trend into the future. The calibration results of the inv method are much less sensitive to the number of injections. The inv method produces relatively constant intersection and slope after four ($\delta^{18}\text{O}$) to six ($\delta^2\text{H}$) injections.

Fitting an exponential function would correspond to the hypothesis of one residual water pool with a first order mixing with water from the new sample, diluting it by the same factor with each new injection. This hypothesis can be rejected, as the exponential function underestimates the projected memory effect. In reality, the memory effect has a longer 'tail' (i.e. seems to be more time-persistent) than a first order dilution. As mentioned above, this may be explained by the existence of multiple exponential pools, the combined effect of which cannot be reproduced by one single exponential relation [2]. This longer 'tail' can be reproduced by the inv method.

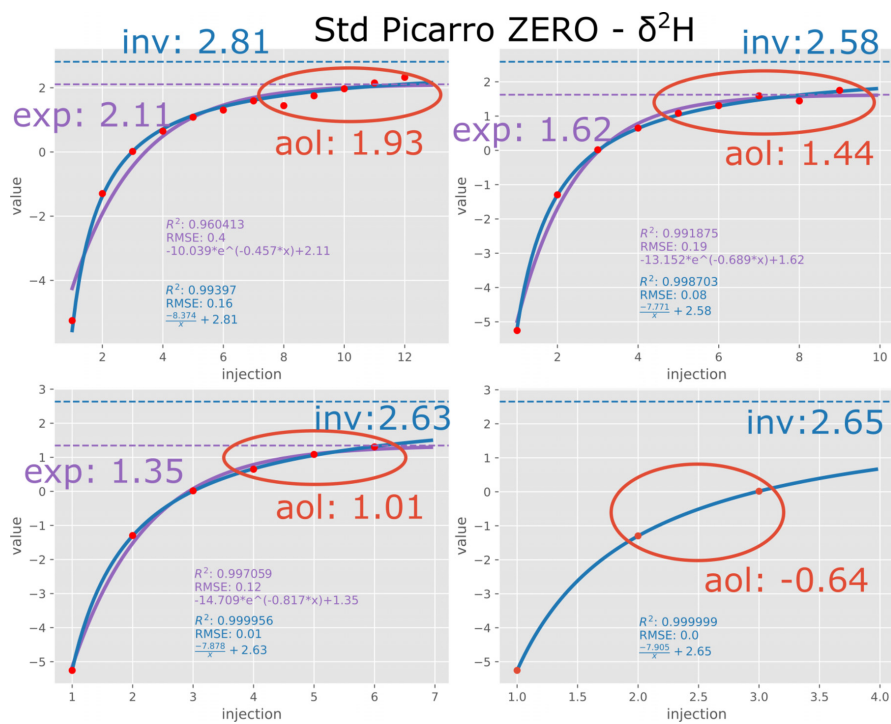


Fig. 1. Application of aol, inv and exp to $\delta^2\text{H}$ of Picarro ZERO standard after 12, 9, 6 and 3 injections respectively. Red dots are measurements, the blue curves are inv function fits and the purple curves are exp function fits. Dashed lines are corresponding asymptotes.

8

N. Hachgenei, V. Vaury and G. Nord et al./MethodsX 9 (2022) 101656

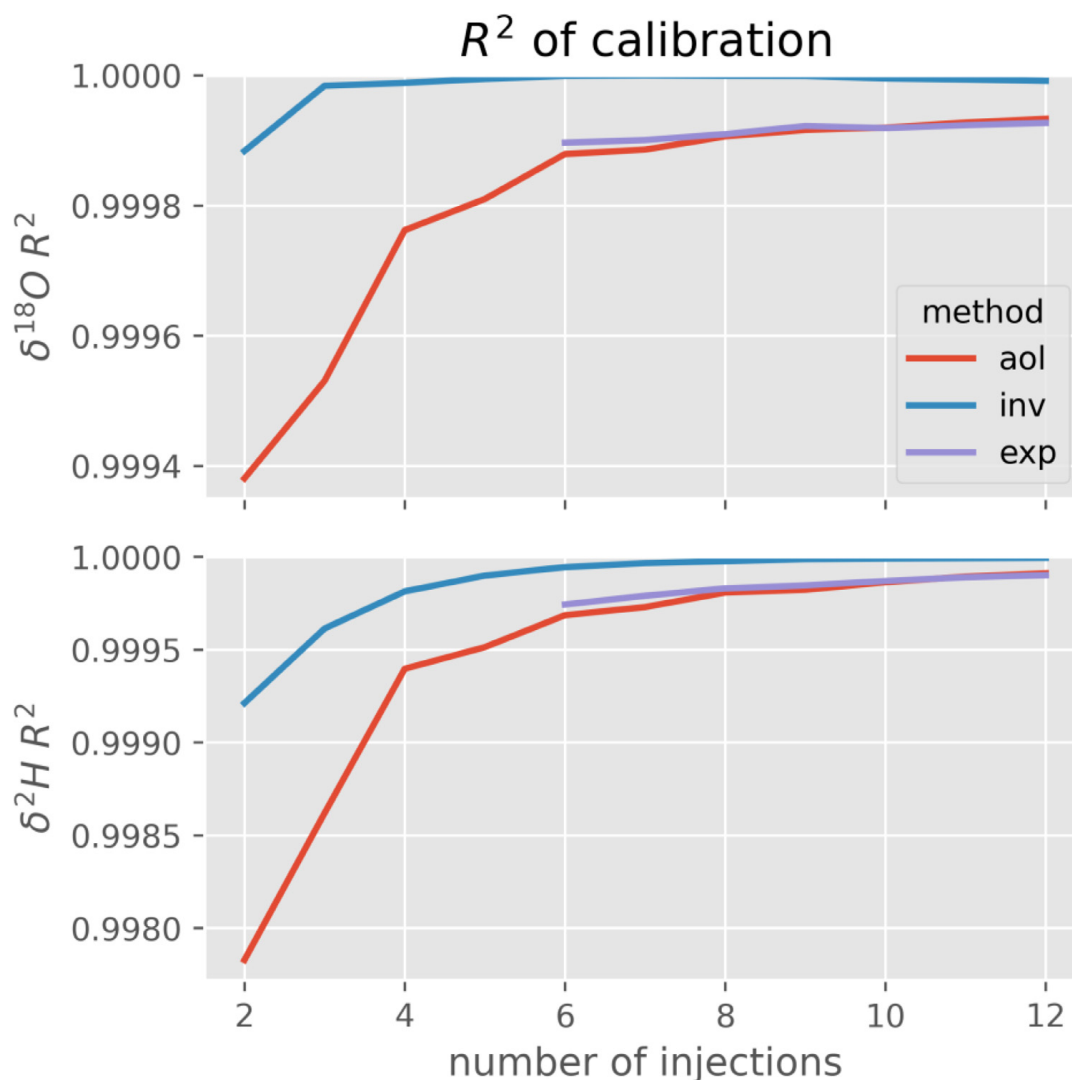


Fig. 2. Goodness of fit (R^2) of the calibration curve obtained from the three standards for the three presented methods as a function of the number of injections.

As an additional validation of the method we performed a calibration on the two extreme standards only (PICARRO DEPL and ZERO) and predicted the concentration of the intermediate standard (PICARRO MID) using this calibration. We did this for 2 to 12 injections again to verify the potential of the method to reduce the number of injections necessary in order to obtain acceptable results Fig. 4. shows the predicted value of PICARRO MID as a function of the number of injections for the three methods. The aol and exp methods do not reach within one standard deviation of the real value even after 12 injections for both isotopes. The inv method gets within uncertainty bounds with 3 injections ($\delta^{18}\text{O}$) or 7 injections ($\delta^2\text{H}$).

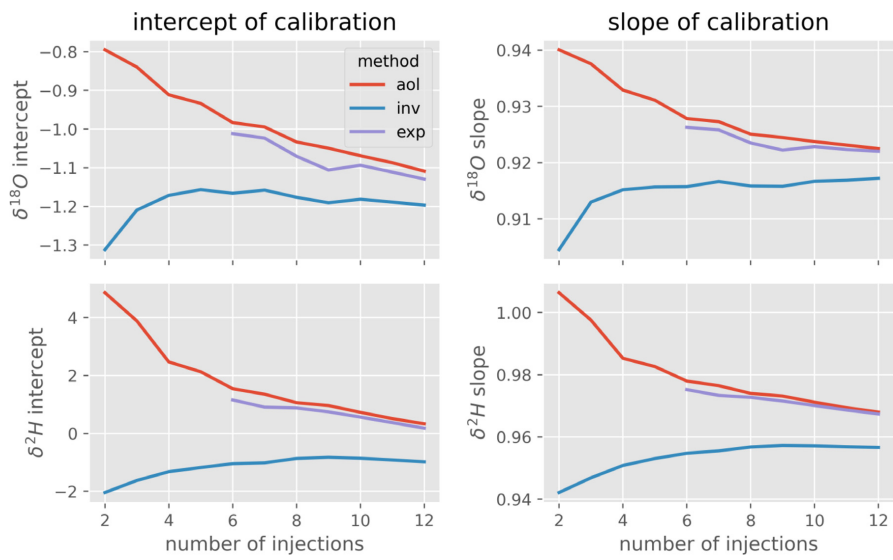


Fig. 3. Effect of the number of injections on the two parameters of the calibration function (slope and intercept) for the three methods.

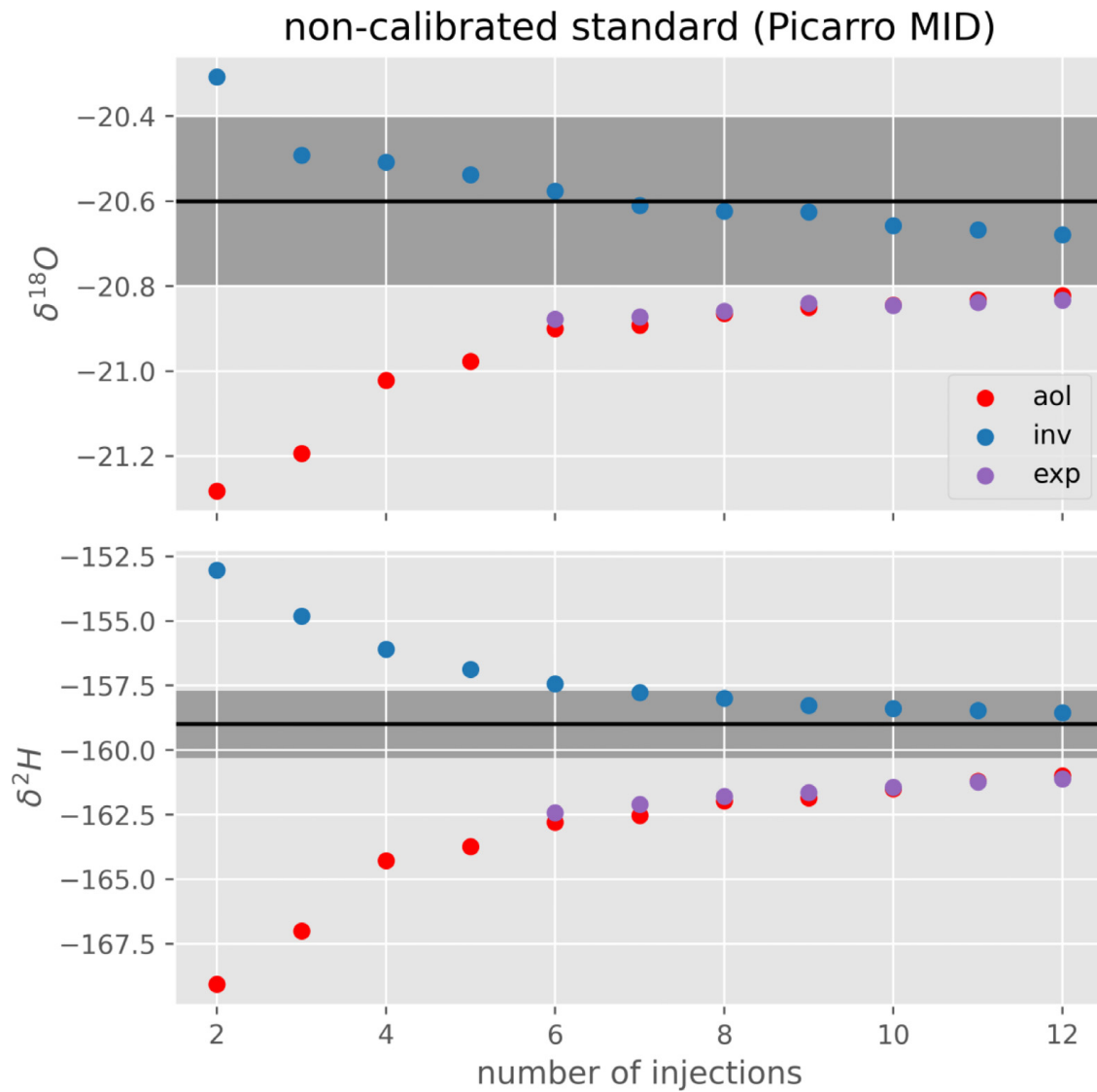


Fig. 4. Prediction of the intermediate standard, that for this example has not been used for calibration. Measured using the three methods calibrated on the two remaining standards (DEPL and ZERO). The black line represents the actual value of the standard. The shaded area corresponds to the uncertainty of the standard as given by Picarro. The points are prediction from the three different methods calibrated on x injections and measuring the sample with the same number of injections.

Declaration of Competing Interest

The authors declare that they have no known competing financial interests or personal relationships that could have appeared to influence the work reported in this paper.

Acknowledgment

We would like to thank Niels Munksgaard for sharing some of his expertise. We also thank Mathieu Sebilo for enabling us to do the analyzes. The analyzes were funded by OHMCV observatory, which is part of OZCAR Research Infrastructure (<https://www.ozcar-ri.org/>) that is supported by the French Ministry of Research, French Research Institutions and Universities. We thank three anonymous reviewers for their constructive comments.

Supplementary materials

Supplementary material associated with this article can be found, in the online version, at doi:[10.1016/j.mex.2022.101656](https://doi.org/10.1016/j.mex.2022.101656).

References

- [1] M. Gröning, Improved water $\delta^2\text{H}$ and $\delta^{18}\text{O}$ calibration and calculation of measurement uncertainty using a simple software tool, *Rapid Commun. Mass Spectrom.* 25 (19) (2011) 2711–2720, doi:[10.1002/rcm.5074](https://doi.org/10.1002/rcm.5074).
- [2] S. Guidotti, H.G. Jansen, A.T. Aerts-Bijma, B.M.A.A. Verstappen-Dumoulin, G. Van Dijk, H.A.J. Meijer, Doubly labelled water analysis: preparation, memory correction, calibration and quality assurance for $\delta^2\text{H}$ and $\delta^{18}\text{O}$ measurements over four orders of magnitudes, *Rapid Commun. Mass Spectrom.* 27 (9) (2013) 1055–1066, doi:[10.1002/rcm.6540](https://doi.org/10.1002/rcm.6540).
- [3] PicarroL2130-i Analyzer for Isotopic H₂O User's Guide, Rev A, Part Number 40027, Picarro, 2014, https://www.enviscid.com/uploads/5/6/3/8/56382687/l2130-i_users_manual_rev_a.pdf.
- [4] A. Pierchala, K. Rozanski, M. Dulinski, Z. Gorczyca, M. Marzec, R. Czub, High-precision measurements of $\delta^2\text{H}$, $\delta^{18}\text{O}$ and $\delta^{17}\text{O}$ in water with the aid of cavity ring-down laser spectroscopy, *Isotopes Environ. Health Stud.* 55 (3) (2019) 290–307, doi:[10.1080/10256016.2019.1609959](https://doi.org/10.1080/10256016.2019.1609959).
- [5] C. Vallet-Coulomb, M. Couapel, C. Sonzogni, Improving memory effect correction to achieve high-precision analysis of $\delta^{17}\text{O}$, $\delta^{18}\text{O}$, $\delta^2\text{H}$, 17O-excess and D-excess in water using cavity ring-down laser spectroscopy, *Rapid Commun. Mass Spectrom.* 35 (14) (2021), doi:[10.1002/rcm.9108](https://doi.org/10.1002/rcm.9108).
- [6] R. Van Geldern, J.A.C. Barth, Optimization of instrument setup and post-run corrections for oxygen and hydrogen stable isotope measurements of water by isotope ratio infrared spectroscopy (IRIS), *Limnol. Oceanogr. Methods* 10 (2012) 1024–1036 DECEMBER, doi:[10.4319/lom.2012.10.1024](https://doi.org/10.4319/lom.2012.10.1024).
- [7] P. Virtanen, R. Gommers, T.E. Oliphant, M. Haberland, T. Reddy, D. Cournapeau, E. Burovski, P. Peterson, W. Weckesser, J. Bright, S.J. Van Der Walt, M. Brett, J. Wilson, K.J. Millman, N. Mayorov, A.R.J. Nelson, E. Jones, R. Kern, ... E. Larson, SciPy 1.0: fundamental algorithms for scientific computing in python, *Nat. Methods* 17 (2020) 261–272, doi:[10.1038/s41592-019-0686-2](https://doi.org/10.1038/s41592-019-0686-2).
- [8] L.I. Wassenaar, T.B. Coplen, P.K. Aggarwal, Approaches for achieving long-term accuracy and precision of $\delta^{18}\text{O}$ and $\delta^2\text{H}$ for waters analyzed using laser absorption spectrometers, *Environ. Sci. Technol.* 48 (2) (2014) 1123–1131, doi:[10.1021/es403354n](https://doi.org/10.1021/es403354n).